

**Measurement of the transverse momentum  
spectrum of  $W$  bosons produced at  $\sqrt{s} = 7$  TeV  
using the ATLAS detector**

A dissertation presented  
by  
Ben Campbell Smith  
to  
The Department of Physics  
in partial fulfillment of the requirements  
for the degree of  
Doctor of Philosophy  
in the subject of  
Physics

Harvard University  
Cambridge, Massachusetts  
May 2011

©2011 - Ben Campbell Smith

All rights reserved.

Thesis advisor

Author

**Masahiro Morii**

**Ben Campbell Smith**

## **Measurement of the transverse momentum spectrum of $W$ bosons produced at $\sqrt{s} = 7$ TeV using the ATLAS detector**

### **Abstract**

$W$  boson production at the Large Hadron Collider provides a fertile ground for testing predictions of the Standard Model. This thesis presents a measurement of the transverse momentum spectrum of  $W$  bosons produced via proton-proton collisions at  $\sqrt{s} = 7$  TeV using the ATLAS detector. The results are found to be in good agreement with predictions made by PYTHIA Monte Carlo tuned to match the  $W$  and  $Z$  transverse momentum spectra observed in proton-antiproton collisions at  $\sqrt{s} = 1.96$  TeV at the Tevatron.

125k  $W \rightarrow \mu\nu$  and 105k  $W \rightarrow e\nu$  candidates were selected from data recorded in late 2010, totaling  $30\text{ pb}^{-1}$  in the muon channel and  $33\text{ pb}^{-1}$  in the electron channel. Background subtraction was performed using data driven techniques to estimate the background from multijet events, and Monte Carlo to estimate the background from  $W \rightarrow \tau\nu$ ,  $Z \rightarrow \ell\ell$ , and top backgrounds.

A data driven approach was used to estimate the calorimeter response to hadronic activity from the recoil of the  $W$  boson.  $Z \rightarrow \ell\ell$  ( $\ell = e, \mu$ ) decays were selected in data, and deviations between the leptonic and hadronic transverse momenta were

used to correct  $W$  signal Monte Carlo. The corrected response matrix was used to unfold the observed  $W$  transverse momentum spectrum to the truth level using an iterative technique called Bayesian unfolding. The unfolded spectrum was then corrected for selection efficiency and normalized to produce a shape suitable for tuning Monte Carlos.

# Contents

Title Page . . . . .	i
Abstract . . . . .	iii
Table of Contents . . . . .	v
List of Figures . . . . .	viii
List of Tables . . . . .	xiv
Acknowledgments . . . . .	xvi
<b>1 Introduction</b>	<b>1</b>
<b>2 Background</b>	<b>2</b>
2.1 The Standard Model . . . . .	3
2.2 Electroweak physics . . . . .	4
2.2.1 W/Z Production at Hadron Colliders . . . . .	6
2.2.2 W/Z Decays . . . . .	7
2.3 Quantum Chromodynamics . . . . .	10
2.3.1 Parton Distribution Functions . . . . .	12
2.3.2 Soft QCD . . . . .	14
2.3.3 Jet Production . . . . .	15
2.4 Previous measurements . . . . .	16
<b>3 Detector</b>	<b>21</b>
3.1 Coordinate Systems . . . . .	22
3.2 The Large Hadron Collider . . . . .	25
3.3 Inner Detector . . . . .	30
3.3.1 Pixel Detector . . . . .	34
3.3.2 Semiconductor Tracker . . . . .	34
3.3.3 Transition Radiation Tracker . . . . .	35
3.4 Calorimeter . . . . .	36
3.4.1 Electromagnetic Calorimeter . . . . .	40
3.4.2 Hadronic Calorimeter . . . . .	43
3.5 Muon Spectrometer . . . . .	44

---

3.5.1	Monitored Drift Tubes . . . . .	45
3.5.2	Cathode Strip Chambers . . . . .	51
3.5.3	Resistive Plate Chambers . . . . .	54
3.5.4	Thin Gap Chambers . . . . .	54
3.6	Magnet System . . . . .	55
3.6.1	Solenoid . . . . .	56
3.6.2	Toroids . . . . .	56
3.7	Combined Muon Tracking . . . . .	60
3.8	Trigger . . . . .	62
3.8.1	Level 1 Trigger . . . . .	64
3.8.2	Level 2 Trigger . . . . .	64
3.8.3	Event Filter . . . . .	65
3.8.4	Trigger Menu and Performance . . . . .	66
<b>4</b>	<b>Software</b>	<b>69</b>
4.1	ATLAS Computing Model . . . . .	69
4.2	Production Software . . . . .	71
4.2.1	Trigger Navigation Slimming . . . . .	72
4.2.2	Trigger Object Matching . . . . .	75
Object Retrieval . . . . .	76	
Distance Definition . . . . .	79	
4.2.3	Muon ID Ntuple Makers . . . . .	80
4.3	ROOT Reader Framework . . . . .	81
4.3.1	Objects . . . . .	82
4.3.2	Readers . . . . .	85
4.3.3	Analysis . . . . .	87
4.3.4	Batch Support . . . . .	89
4.3.5	Skimming and Slimming . . . . .	90
4.3.6	Cut Flows . . . . .	91
<b>5</b>	<b><math>Wp_T</math></b>	<b>93</b>
5.1	Data and Simulation Samples . . . . .	96
5.1.1	Data Quality and Luminosity . . . . .	96
5.1.2	Trigger Requirements . . . . .	97
5.1.3	Simulation Samples . . . . .	98
5.1.4	Monte Carlo Corrections . . . . .	100
5.2	Event Selection . . . . .	101
5.2.1	Muon Event Selection . . . . .	102
5.2.2	Electron Event Selection . . . . .	105
5.2.3	Fiducial Selection . . . . .	108
5.3	Hadronic Recoil . . . . .	108
5.3.1	Algorithm . . . . .	109

5.3.2	Performance . . . . .	110
5.3.3	Limitations . . . . .	113
5.4	Binning of Results . . . . .	114
5.5	Background Estimation . . . . .	115
5.5.1	Backgrounds from $W$ , $Z$ , and top . . . . .	116
5.5.2	QCD in the Muon Channel . . . . .	119
5.5.3	QCD in the Electron Channel . . . . .	124
5.6	Response Matrix . . . . .	127
5.6.1	Definition . . . . .	128
5.6.2	Monte Carlo Response Matrix . . . . .	129
5.6.3	Response Parameterization . . . . .	130
5.6.4	Data Driven Corrections . . . . .	133
5.7	Unfolding . . . . .	138
5.7.1	Smearing . . . . .	138
5.7.2	Bin-by-bin . . . . .	139
5.7.3	Matrix inversion . . . . .	142
	Difficulties with Matrix Inversion . . . . .	142
	Regularization . . . . .	144
5.7.4	Bayesian Unfolding . . . . .	150
5.8	Reconstruction Efficiency Correction . . . . .	153
5.8.1	Efficiency calculation . . . . .	153
5.8.2	Trigger Scale Factors . . . . .	156
	Muon Channel . . . . .	156
	Electron Channel . . . . .	159
5.8.3	Reconstruction Scale Factors . . . . .	160
	Muon Channel . . . . .	160
	Electron Channel . . . . .	162
5.8.4	Resolution Smearing and Scaling . . . . .	162
	Muon Channel . . . . .	163
	Electron Channel . . . . .	164
5.9	Calculation of Uncertainties . . . . .	165
5.9.1	Statistical Formulation . . . . .	167
5.9.2	Background Subtraction . . . . .	169
5.9.3	Response Matrix . . . . .	172
5.9.4	Unfolding . . . . .	176
5.9.5	Efficiency Calculation . . . . .	180
5.9.6	Propagation and Normalization . . . . .	183
5.10	Results . . . . .	186
5.11	Conclusions . . . . .	200

# List of Figures

2.1	The Standard Model particles and their properties [75]. . . . .	4
2.2	Fundamental vertices for electroweak theory. . . . .	5
2.3	Leading order diagrams for production of $W$ and $Z$ bosons at hadron colliders. . . . .	7
2.4	Predicted $W$ transverse momentum spectrum at the LHC from two common Monte Carlo generators. . . . .	8
2.5	Fundamental QCD vertices. . . . .	10
2.6	Example parton distribution functions for the HERA collaboration [48]. The x axis shows $x$ , the fraction of the proton energy held by the parton, and the y axis shows $xf(x)$ , which is the product of $x$ and the probability of selecting a parton with that energy fraction. . . . .	13
2.7	CDF measurement of the $W$ transverse momentum spectrum [26]. . . . .	18
2.8	D0 measurement of the $W$ transverse momentum spectrum [29]. . . . .	19
2.9	Theory-data comparison from D0 measurement of $W$ transverse momentum measurement [29]. . . . .	20
3.1	A diagram of the ATLAS detector, with the various major subdetector systems labelled [1]. . . . .	22
3.2	A diagram of the trajectories of various types of particles in the ATLAS detector [3]. . . . .	23
3.3	Delivered and recorded luminosity during 2010. . . . .	26
3.4	A diagram of the LHC along with its injector chain [8]. . . . .	27
3.5	A diagram of the main LHC bending magnet [1]. . . . .	28
3.6	A diagram of the ATLAS barrel Inner Detector [1]. . . . .	31
3.7	A diagram of the ATLAS endcap Inner Detector [1]. . . . .	32
3.8	Nominal performance of the ATLAS Inner Detector [10]. . . . .	33
3.9	A diagram of the ATLAS Calorimeter [1]. . . . .	37
3.10	Nominal performance of the ATLAS Electromagnetic calorimeter [10]. . . . .	39
3.11	Material prior to entering the ATLAS calorimeter [10]. . . . .	39
3.12	Probability of photon conversion before a radius of 80 and 115 cm [10]. . . . .	40

---

3.13	Nominal performance of the ATLAS Hadronic calorimeter [10]. . . . .	41
3.14	A picture of the accordion structure used in the ATLAS electromagnetic calorimeter [1]. . . . .	42
3.15	A diagram of the ATLAS Muon Spectrometer [1]. . . . .	44
3.16	Nominal standalone performance of the ATLAS muon spectrometer [10]. In the efficiency plots, a good muon is one passing standard quality cuts. . . . .	46
3.17	Factors influencing standalone muon resolution [10]. . . . .	47
3.18	A diagram of a typical ATLAS MDT Chamber [21]. . . . .	49
3.19	Chamber layout of the ATLAS Muon Spectrometer [21]. . . . .	50
3.20	A picture of an assembled ATLAS Muon Spectrometer End-cap Sector, along with support structures [1]. . . . .	51
3.21	A picture of an ATLAS Muon Spectrometer End-cap Wheel [1]. . . .	52
3.22	A diagram of an ATLAS Cathode Strip Chamber detector element [21].	53
3.23	A picture of a test insertion of the ATLAS solenoid into the ATLAS EM Calorimeter [1]. . . . .	57
3.24	A picture the ATLAS Barrel Toroid with support structure [1]. . . .	58
3.25	A picture the ATLAS End-cap Toroid [1]. . . . .	59
3.26	Bending power as a function $\eta$ of the ATLAS toroid magnets [10]. .	60
3.27	Nominal combined performance of the ATLAS muon spectrometer [10]. In the efficiency plot, a good muon is one passing standard quality cuts.	63
3.28	ATLAS trigger rate in comparison with various physical processes at nominal running conditions [10]. . . . .	67
3.29	Expected muon trigger rates at instantaneous luminosity of $10^{31} \text{ cm}^{-2} \text{ s}^{-1}$ [10]. Note that 2010 saw a maximum instantaneous luminosity of $2 \times 10^{32} \text{ cm}^{-2} \text{ s}^{-1}$ , 20 times what is shown here. . . . .	68
3.30	Nominal trigger budget by stream for 2010 running [10]. . . . .	68
4.1	A simple example of the trigger navigation structure. Each grey box represents another step in the trigger algorithm. . . . .	73
5.1	Kinematics from selected events in data and Monte Carlo signal and background samples. Monte Carlo samples are weighted according to the measured luminosity times the theoretical cross section. . . . .	106
5.2	Diagram of the hadronic recoil calculation for $W \rightarrow e\nu$ decays. . . . .	110
5.3	Response matrix showing reconstructed versus true $W p_T$ in $W \rightarrow e\nu$ Monte Carlo for standard (left) and hadronic recoil (right) algorithms.	111
5.4	Bias perpendicular to the $W$ direction in the transverse plane as a function of the angle between the lepton and the $W$ for the standard, uncorrected hadronic recoil, and corrected hadronic recoil algorithms in $W \rightarrow \mu\nu$ Monte Carlo. The amplitude of the oscillation, $A$ , is determined by fitting the bias with a sinusoidal function. . . . .	112

---

5.5	Resolution of the standard and corrected hadronic recoil algorithms as a function of total transverse energy in the event in $W \rightarrow \mu\nu$ Monte Carlo. . . . .	113
5.6	Bin purity from $W \rightarrow \ell\nu$ Monte Carlo . . . . .	116
5.7	Observed muon data with major backgrounds and signal Monte Carlo. All samples except for the QCD sample are from Monte Carlo scaled by the theoretical cross section times the measured luminosity. The QCD sample is obtained using a data driven technique. . . . .	117
5.8	Estimated $W$ , $Z$ , and top backgrounds in the muon channel, separated by sample. . . . .	118
5.9	Total estimated $W$ , $Z$ , and top backgrounds and uncertainties in the muon channel in bins of $W_{pT}$ . Note that an addition 3.4% uncertainty for the luminosity estimate is applied, but not shown here. . . . .	120
5.10	Isolation efficiency from the tag and probe technique using data (black), $Z \rightarrow \mu\mu$ Monte Carlo (blue), and $W \rightarrow \mu\nu$ Monte Carlo (red). . . . .	122
5.11	Isolation cut efficiency in the QCD control region ( $15 < p_T^\mu < 20$ ), calculated as a function of hadronic recoil in QCD Monte Carlo (red), data (black), and electroweak subtracted data (blue). . . . .	123
5.12	Exponential fit of $\epsilon_{QCD}$ in the Monte Carlo signal region. The black points on the fitted curve are the values of $\epsilon_{QCD}$ used to form the correction factor. . . . .	124
5.13	Isolation efficiency extrapolated from control to signal region using Monte Carlo. . . . .	125
5.14	QCD background estimate in the muon channel. Systematic uncertainties are shown in red, and statistical uncertainties are shown in the blue hatched area. . . . .	126
5.15	Monte Carlo based response matrices in the electron and muon channels. . . . .	130
5.16	Bias and resolution fits in $W$ signal Monte Carlo, for the electron channel (red), the muon channel (green), and both channels combined (blue). . . . .	132
5.17	Comparison of the reconstructed simulated sample for each channel (black) with the result of multiplying the fitted response matrix from channel combined Monte Carlo with the true distribution of selected events (red). . . . .	133
5.18	$\sum E_T$ distributions and weights used in $\sum E_T$ reweighting for $W$ Monte Carlo (red), $Z$ Monte Carlo (green), and $Z$ and $W$ data (blue and black). . . . .	135
5.19	$Z$ data bias and resolution in the electron channel. . . . .	136
5.20	The Generic L-Curve. . . . .	149
5.21	Event selection efficiency $\epsilon_W$ , and its uncertainties, as a function of true $W_{pT}$ , in the muon channel. . . . .	154

---

5.22	Event selection efficiency $\epsilon_W$ , and its uncertainties, as a function of true $W p_T$ , in electron channel. . . . .	155
5.23	The efficiency of the muon trigger <code>EF_mu13_MG</code> in data as a function of muon $p_T$ [17]. The scale factor is the ratio of the efficiency in data to the efficiency of <code>EF_mu10_MG</code> in Monte Carlo (not shown.) . . . . .	157
5.24	The efficiency of the muon trigger <code>EF_mu13_MG_tight</code> in data as a function of muon $p_T$ [17]. The scale factor is the ratio of the efficiency in data to the efficiency of <code>EF_mu10_MG</code> in Monte Carlo (not shown.) . . . . .	158
5.25	The trigger scale factor for <code>EF_mu13_MG</code> (left plot) and <code>EF_mu13_MG_tight</code> (right plot) as a function of muon $\eta$ [17]. Red circles are for positive muons and blue triangles are for negative muons. . . . .	158
5.26	Muon reconstruction efficiency and scale factor as a function of inner detector $\eta$ [66]. . . . .	161
5.27	$Z \rightarrow ee$ invariant mass distribution in data (red) and Monte Carlo (blue) before smearing is applied to the Monte Carlo. Events from the barrel are on the left, and those from the endcap are on the right [45].	166
5.28	$Z \rightarrow ee$ invariant mass distribution in data (red) and Monte Carlo (blue) after smearing is applied to the Monte Carlo. Events from the barrel are on the left, and those from the endcap are on the right [45].	166
5.29	Diagonal elements of background uncertainty covariance matrices for the muon channel broken down by sample, and for the total background. The data statistical uncertainty is shown for comparison. . . . .	171
5.30	Diagonal elements of background uncertainty covariance matrices for the electron channel broken down by sample, and for the total background. The data statistical uncertainty is shown for comparison. . . . .	172
5.31	Correlation matrices for the background uncertainty of the muon channel broken down by sample, and for the total background. . . . .	173
5.32	Correlation matrices for the background uncertainty of the electron channel broken down by sample, and for the total background. . . . .	174
5.33	Diagonal elements of the covariance matrix for uncertainties from the response matrix of the muon channel, broken down by source. For all but the fit statistical uncertainty, the maximum difference in any bin is shown as the dotted line and is used as the systematic in all bins. Note that the ALPGEN result is not used in the final systematic. . . . .	177
5.34	Diagonal elements of the covariance matrix for uncertainties from the response matrix of the electron channel, broken down by source. For all but the fit statistical uncertainty, the maximum difference in any bin is shown as the dotted line and is used as the systematic in all bins. Note that the ALPGEN result is not used in the final systematic. . . . .	178
5.35	Correlation matrix for the fit statistical uncertainty for the muon channel. . . . .	179
5.36	Correlation matrix for the fit statistical uncertainty for the electron channel. . . . .	179

---

5.37	Diagonal elements of the covariance matrix of the muon channel for systematic and statistical uncertainties due to unfolding. . . . .	181
5.38	Diagonal elements of the covariance matrix of the electron channel for systematic and statistical uncertainties due to unfolding. . . . .	181
5.39	Correlation matrix for the unfolding statistical uncertainty for the muon channel. . . . .	182
5.40	Correlation matrix for the unfolding statistical uncertainty for the electron channel. . . . .	182
5.41	Muon sample after background subtraction compared with reconstruction level PYTHIA signal Monte Carlo. The deviation is defined as the difference between the data and Monte Carlo divided by the sum in quadrature of their uncertainties. . . . .	187
5.42	Uncertainties after background subtraction for the muon channel. . .	187
5.43	Electron sample after background subtraction compared with reconstruction level PYTHIA signal Monte Carlo. The deviation is defined as the difference between the data and Monte Carlo divided by the sum in quadrature of their uncertainties. . . . .	188
5.44	Uncertainties after background subtraction for the electron channel. .	188
5.45	Muon sample after Bayesian unfolding compared with truth level PYTHIA signal Monte Carlo from events passing event selection. The deviation is defined as the difference between the data and Monte Carlo divided by the sum in quadrature of their uncertainties. . . . .	190
5.46	Diagonal elements of covariance matrix following unfolding for the muon channel. . . . .	190
5.47	Electron sample after Bayesian unfolding compared with truth level PYTHIA signal Monte Carlo from events passing event selection. The deviation is defined as the difference between the data and Monte Carlo divided by the sum in quadrature of their uncertainties. . . . .	191
5.48	Diagonal elements of covariance matrix following unfolding for the electron channel. . . . .	191
5.49	Statistical and systematic correlation matrices following Bayesian unfolding for the muon channel. . . . .	192
5.50	Statistical and systematic correlation matrices following Bayesian unfolding for the electron. . . . .	192
5.51	Muon sample after efficiency correction compared with truth level PYTHIA signal Monte Carlo from events within the fiducial volume. The deviation is defined as the difference between the data and Monte Carlo divided by the sum in quadrature of their uncertainties. . . . .	194
5.52	Diagonal elements of covariance matrix following efficiency correction for the muon channel. . . . .	194

---

5.53	Electron sample after efficiency correction compared with truth level PYTHIA signal Monte Carlo from events within the fiducial volume. The deviation is defined as the difference between the data and Monte Carlo divided by the sum in quadrature of their uncertainties. . . . .	195
5.54	Diagonal elements of covariance matrix following efficiency correction for the electron channel. . . . .	195
5.55	Statistical and systematic correlation matrices following efficiency correction for the muon channel. . . . .	196
5.56	Statistical and systematic correlation matrices following efficiency correction for the electron channel. . . . .	196
5.57	Muon sample after normalization compared with truth level PYTHIA signal Monte Carlo from events within the fiducial volume. The deviation is defined as the difference between the data and Monte Carlo divided by the sum in quadrature of their uncertainties. . . . .	197
5.58	Diagonal elements of covariance matrix following normalization for the muon channel. . . . .	197
5.59	Electron sample after normalization compared with truth level PYTHIA signal Monte Carlo from events within the fiducial volume. The deviation is defined as the difference between the data and Monte Carlo divided by the sum in quadrature of their uncertainties. . . . .	198
5.60	Diagonal elements of covariance matrix following normalization for the electron channel. . . . .	198
5.61	Statistical and systematic correlation matrices following normalization for the muon channel. . . . .	199
5.62	Statistical and systematic correlation matrices following normalization for the electron channel. . . . .	199

# List of Tables

2.1	Measured $W$ and $Z$ production cross sections time branching ratio to leptons for $\sqrt{s} = 1.96$ TeV proton-antiproton collisions at the Tevatron [27, 30].	6
2.2	Measured $W$ and $Z$ production cross sections time branching ratio to leptons for $\sqrt{s} = 7$ TeV proton-proton collisions at the LHC [25, 28].	7
2.3	$W$ boson branching fractions [59].	9
2.4	$Z$ boson branching fractions [59].	9
3.1	Properties of the Large Hadron Collider.	29
3.2	Properties of the ATLAS Inner Detector [24].	30
3.3	Properties of the ATLAS Calorimeter [24].	37
3.4	Properties of the ATLAS Magnet System [24].	56
4.1	Example computing facilities for each tier level at CERN, Brookhaven National Lab (BNL), Harvard, and Boston University (BU).	71
4.2	Run-time customizable options for the TrigNavigationSlimming algorithm.	74
4.3	Physics objects converted from ESD format to ntuple format by the MuonIDNtupleMakers package.	81
5.1	Triggers used in the muon channel analysis as a function of period and run number.	98
5.2	Simulated data samples used in the muon channel analysis. All samples include pileup unless noted.	99
5.3	Simulated data samples used in the electron channel analysis. All samples include pileup except where noted.	100
5.4	Weights used to correct the pileup model used in event simulation. Note that 0 primary vertex events do not pass event selection and thus those weights are not used.	101
5.5	Selection of $W$ candidates for muon channel analysis	102
5.6	Selection of $W$ candidates for electron channel analysis	107

---

5.7	Binning used at the reconstruction and truth levels. . . . .	115
5.8	Trigger efficiency in the electron channel for Monte Carlo and data and for Medium and Tight electrons [44]. . . . .	159
5.9	Electron identification efficiency and scale factor measured using tag and probe [44]. . . . .	162
5.10	Correction factors for muon smearing and scaling from muon resolution studies [16]. . . . .	163
5.11	Sampling and constant terms and their systematic uncertainties in Barrel and Endcap [45]. . . . .	165
5.12	Sources of uncertainty. . . . .	167

# Acknowledgments

There are many people to whom I am deeply indebted:

Masahiro Morii, for first introducing me to particle physics and taking the time to teach me about the field; for always pushing me to do my best, no matter how well or poorly things were going; and for giving me the freedom to learn on my own while making sure I never got lost.

Melissa Franklin, Joao Guimaraes da Costa, and John Huth, for the countless hours of advice, feedback, and comments; for teaching me about the detector; and for always supporting me when times were tough.

My thesis committee members, Gary Feldman and Lisa Randall, for their comments and questions.

Kevin Black, for teaching me how to be a useful member of the group; for helping me grow as a physicist; and for always listening to my complaints.

Tova Holmes, Laura Jeanty, Michael Kagan, Tomo Lazovich, Corrinne Mills, Curt Nehrkorn, and Giovanni Zevi de la Porta for helping me with this analysis; for putting up with my requests, regardless of how reasonable or unreasonable they may have been; and for making physics fun.

Alberto Belloni, Verena Martinez Outschoorn, and Srivas Prasad for their knowledge

about ATLAS and their unwavering willingness to help.

My parents, for helping me find what makes me happy; for their love and support throughout not just graduate school, but my whole life; and for the words of encouragement that every graduate students needs now and then.

My wife, Honor, for everything and more. I could not have done this without her.

# Chapter 1

## Introduction

This thesis describes a measurement of the transverse momentum spectrum of the  $W$  boson from proton-proton collisions at  $\sqrt{s} = 7$  TeV using the ATLAS detector. Chapter 2 begins with a discussion of the theoretical and experimental background that is needed to frame the measurement. In particular, it focuses on the pieces of the Standard Model which are relevant to  $W$  physics as well as previous measurements made at the Tevatron. Chapter 3 provides an overview of the ATLAS detector and the Large Hadron Collider. It also describes some of the nomenclature and terminology that is used in the analysis. Chapter 4 describes some of the software that was used in producing these results. Finally, Chapter 5 describes the full  $W$  transverse momentum analysis.

# Chapter 2

## Background

The  $W$  boson plays an essential role in modern particle physics. The theory of  $W$  boson couplings describes numerous effects from CP violation in neutral meson mixing to the lifetimes of cosmic ray particles, while experimental measurements of  $W$  boson properties have provided crucial insight into physical parameters such as the mass of the Higgs boson. Further, future measurements will use  $W$  or  $W$ -like physics to search for new particles.

This analysis is a measurement of the transverse momentum spectrum of  $W$  bosons from proton-proton collisions at  $\sqrt{s} = 7$  TeV. To frame the motivation and ramifications of this measurement, this section presents theoretical and experimental backgrounds. A brief description of the Standard Model, accompanied by an overview of electroweak physics, with an emphasis on  $W$  physics at hadron colliders, will be presented. Next, a summary of the theory of Quantum Chromodynamics (QCD) will be given. This section will conclude with a description of existing experimental results

related to the transverse momentum spectrum of  $W$  bosons.

## 2.1 The Standard Model

The Standard Model (SM) [43, 60, 49, 61] is the foundation of modern understanding of the behavior of elementary particles. It allows very accurate theoretical predictions of the nature of the most fundamental parts of matter. One can think of it as the answer to all of the how and what type questions that can be asked about the universe at the smallest scales: What holds a nucleus together? How do electrons interact with each other? What is the lifetime of the neutron? It has allowed an unparalleled theoretical understanding of a world very different from the one to which we are accustomed. Because of its importance, much of modern particle physics is dedicated to testing and expanding upon the SM. While this thesis presents results related to only a small subset of the predictions of the SM, it is worthwhile discussing the SM as a whole in order to frame the importance of these measurements.

The SM is a quantum field theory which describes the fundamental particles and their interactions, and in particular describes all of the known forces except for gravity. Particles are divided into two types: fermions, which have half integer spin, and bosons, which have integer spin. Their interactions are described by two basic forces: a  $SU(2) \times U(1)$  gauge group mediated by the  $W$  and  $Z$  bosons as well as the photon, called the electroweak force, and a non-abelian  $SU(3)$  gauge group mediated by the gluon, called the strong force. The particles are further broken down into quarks, which are charged under the strong force, and leptons, which are not. The particles

Three Generations of Matter (Fermions)			
	I	II	III
mass $\rightarrow$	2.4 MeV	1.27 GeV	171.2 GeV
charge $\rightarrow$	$\frac{2}{3}$	$\frac{2}{3}$	$\frac{2}{3}$
spin $\rightarrow$	$\frac{1}{2}$	$\frac{1}{2}$	$\frac{1}{2}$
name $\rightarrow$	u up	c charm	t top
Quarks	d down	s strange	b bottom
	4.8 MeV	104 MeV	4.2 GeV
Leptons	$\frac{-1}{3}$	$\frac{-1}{3}$	$\frac{-1}{3}$
	$\frac{1}{2}$	$\frac{1}{2}$	$\frac{1}{2}$
$\nu_e$ electron neutrino	$<2.2$ eV	$<0.17$ MeV	$<15.5$ MeV
$\nu_\mu$ muon neutrino	0	0	0
$\nu_\tau$ tau neutrino	$\frac{1}{2}$	$\frac{1}{2}$	$\frac{1}{2}$
e electron	0.511 MeV	105.7 MeV	1.777 GeV
$\mu$ muon	$\frac{-1}{2}$	$\frac{-1}{2}$	$\frac{-1}{2}$
$\tau$ tau	$\frac{1}{2}$	$\frac{1}{2}$	$\frac{1}{2}$
Bosons (Forces)			
$Z^0$ weak force	91.2 GeV	0	0
$W^+$ weak force	80.4 GeV	$\pm 1$	1

Figure 2.1: The Standard Model particles and their properties [75].

and their charges, masses, and spins are shown in Figure 2.1.

## 2.2 Electroweak physics

Electroweak theory, first described by Sheldon Glashow, Steven Weinberg, and Abdus Salam in the late 1960s, is a unification of the electromagnetic and weak forces under the gauge group  $SU(2) \times U(1)$  [61]. The gauge group results in four massless gauge bosons, typically termed  $(W^+, W^-, W^0)$  and  $B^0$ , where the  $W$  bosons are the mediators of the  $SU(2)$  group and the  $B$  is the mediator of the  $U(1)$  group. Through

a process known as the Higgs mechanism, whereby a complex doublet develops a non-zero vacuum expectation value, the electroweak symmetry is spontaneously broken and three of the four gauge bosons become massive. The massive bosons are the  $W^+$ ,  $W^-$ , and  $Z$ , while the massless boson is the photon. The fundamental couplings of electroweak theory are shown in Figure 2.2.

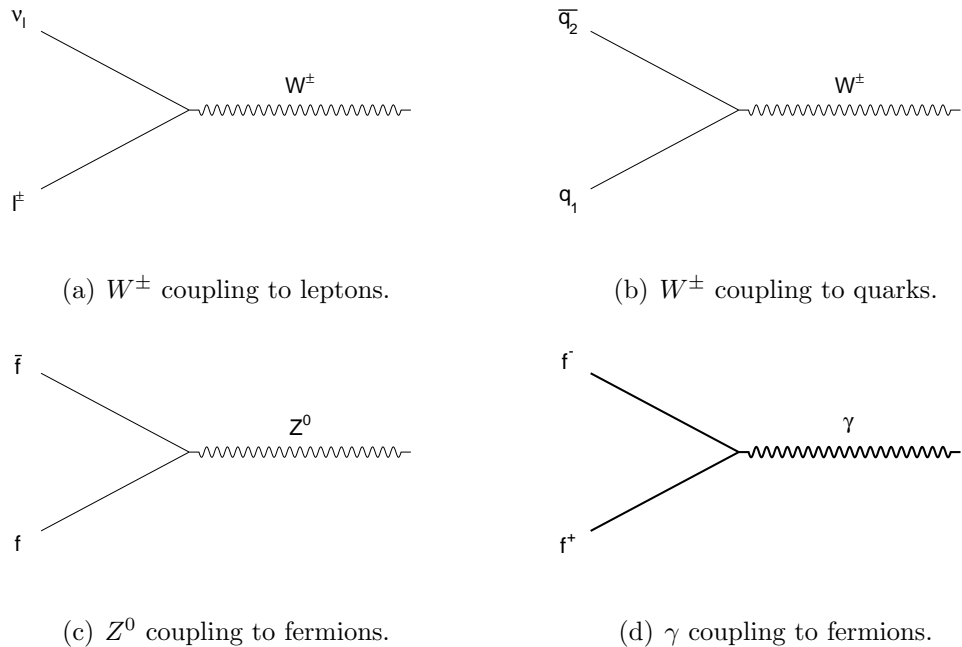


Figure 2.2: Fundamental vertices for electroweak theory.

Electroweak theory has a number of important properties. All charged fermions interact electromagnetically, via interactions with the photons which has a coupling constant such that electromagnetic decays have a characteristic lifetime of roughly  $10^{-16}$ s. All fermions interact weakly, via interactions with the  $Z$  and  $W$  bosons with characteristic decay lifetimes of roughly  $10^{-13}$ s. Particle flavor is conserved in photon and  $Z$  interactions, whereas the  $W$  is capable of mixing up and down

type quarks via couplings described by the Cabibbo-Kobayashi-Maskawa matrix [43, 59], which generally penalizes out of family transitions. Electromagnetic interactions respect parity (P) and charge conjugation (C) symmetries, while weak interactions are maximally P and C violating, and violate the combined symmetry CP as well. The combined symmetry, CPT, where T is time reversal, has never been observed to be broken by any force, and is believed to be generally conserved in all Lorentz invariant quantum field theories.

### 2.2.1 W/Z Production at Hadron Colliders

At hadron colliders,  $W$  and  $Z$  bosons are produced primarily through quark-antiquark annihilation, as shown in Figure 2.3, with production cross sections shown in Tables 2.1 and 2.2. In  $W$  production, the quark and antiquark need be up type and down type (or vice-versa) in order to conserve charge, and the two quarks need not be of the same family, although the production will be Cabibbo suppressed [43] if they are not. In SM  $Z$  production, only quarks of the same type and family are allowed to contribute. This results in slightly different composition of the initial state quarks in the production of  $W$  and  $Z$  bosons. For example, the  $b\bar{b} \rightarrow Z$  production channel is non-negligible at the Large Hadron Collider, while the similar  $b\bar{t} \rightarrow W^-$  or  $t\bar{b} \rightarrow W^+$  is highly suppressed due to the large mass of the top quark.

Experiment	$\sigma_{W \rightarrow \ell\nu}(nb)$	$\sigma_{\gamma^*/Z \rightarrow \ell\ell}(pb)$
CDF	$2.749 \pm 0.173$	$254.9 \pm 16.2$
D $\emptyset$	$2.310 \pm 0.150$	$221 \pm 11$

Table 2.1: Measured  $W$  and  $Z$  production cross sections time branching ratio to leptons for  $\sqrt{s} = 1.96$  TeV proton-antiproton collisions at the Tevatron [27, 30].

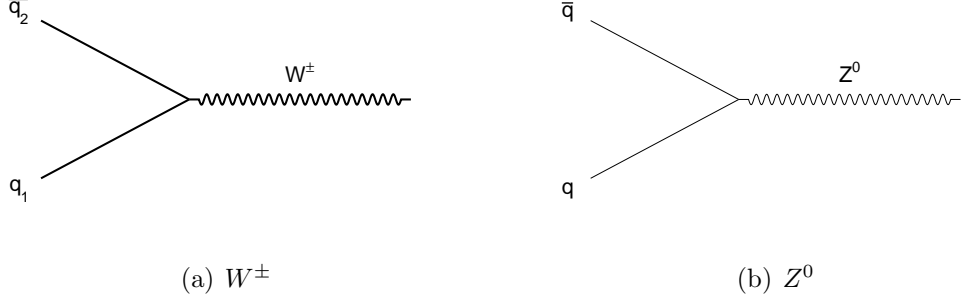


Figure 2.3: Leading order diagrams for production of  $W$  and  $Z$  bosons at hadron colliders.

Experiment	$\sigma_{W \rightarrow \ell\nu}(nb)$	$\sigma_{\gamma^*/Z \rightarrow \ell\ell}(pb)$
ATLAS	$9.96 \pm 1.23$	$820 \pm 119$
CMS	$9.95 \pm 1.13$	$931 \pm 362$

Table 2.2: Measured  $W$  and  $Z$  production cross sections time branching ratio to leptons for  $\sqrt{s} = 7$  TeV proton-proton collisions at the LHC [25, 28].

At leading order, both  $W$  and  $Z$  bosons are produced in hadron colliders with zero transverse momentum, as the initial state is entirely parallel to the beam line. However, at higher order, emission of gluons and other strongly interacting particles from the incident protons produces a boost perpendicular to the beam line. The properties of these emissions are described for low and high transverse momenta in sections 2.3.2 and 2.3.3 respectively. Predictions by two commonly used generators for the  $W$  transverse momentum spectrum at the LHC are shown in Figure 2.4.

## 2.2.2 W/Z Decays

Both  $W$  and  $Z$  bosons decay quickly ( $\sim 10^{-25}$ s) to quarks and leptons, with branching ratios shown in Tables 2.3 and 2.4 [59]. In particular,  $W$  bosons decay to a charged lepton and neutrino roughly 33% of the time and hadrons the remaining 67% of the time, while  $Z$  bosons decay to charged lepton pairs roughly 10% of the

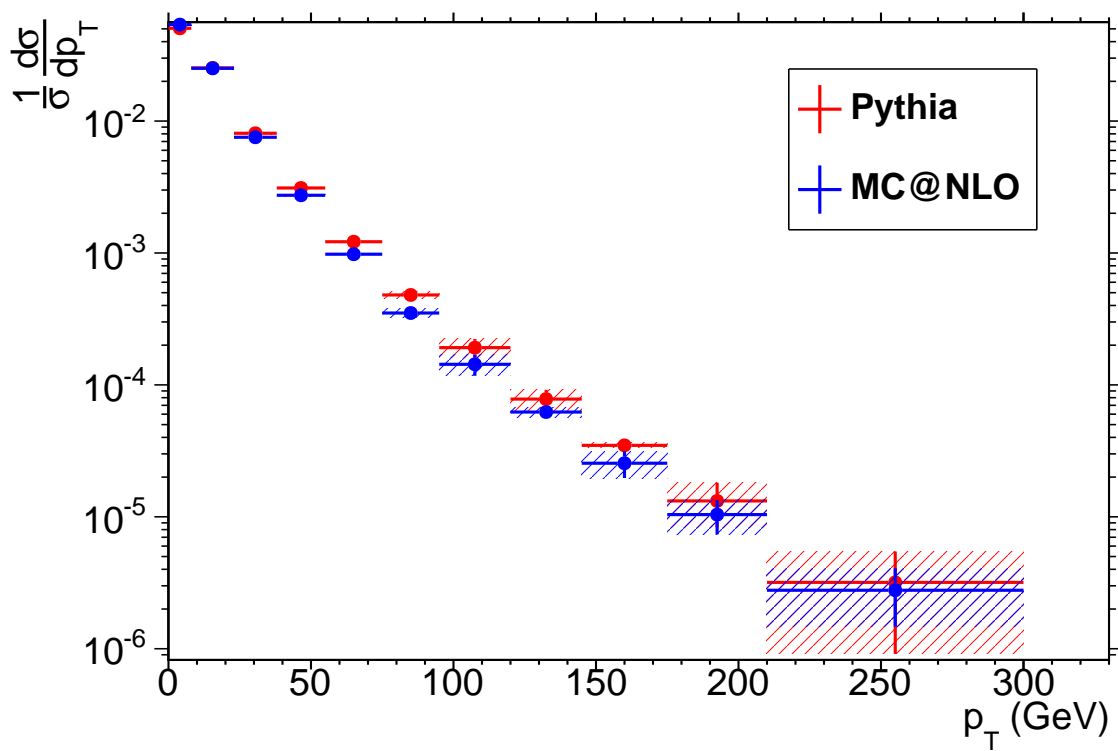


Figure 2.4: Predicted  $W$  transverse momentum spectrum at the LHC from two common Monte Carlo generators.

time, neutrinos roughly 20% of the time, and hadrons the remaining 70% of the time. For both the  $W$  and  $Z$ , the hadronic channel is very difficult to separate from the many orders of magnitude larger dijet background. For the  $Z$ , decays to neutrinos are very difficult to trigger on and reconstruct due to the inability of detectors to observe neutrinos. Thus, although the charged lepton decay channels are only a small fraction of  $W$  and  $Z$  decays, they are typically used for experimental measurements. Specifically, the muon and electron channels are most commonly used as the  $\tau$  often decays hadronically, resulting in similar problems to the direct hadronic decays.

Decay	Branching Fraction (%)
$\ell^\pm\nu$ (per flavor)	$10.80 \pm 0.09$
hadrons	$67.60 \pm 0.27$

Table 2.3:  $W$  boson branching fractions [59].

Decay	Branching Fraction (%)
$\ell^+\ell^-$ (per flavor)	$3.37 \pm 0.0023$
invisible ( any $\nu\nu$ decay )	$20.00 \pm 0.06$
hadrons	$69.01 \pm 0.06$

Table 2.4:  $Z$  boson branching fractions [59].

While the decays of the  $W$  and  $Z$  boson are similar, experimentally measuring their kinematics requires very different approaches. In the case of  $Z \rightarrow \ell\ell$  decays, the charged leptons may be fully reconstructed, and the full 4 vector of the decayed  $Z$  may be calculated. However, in the case of  $W \rightarrow \ell\nu$  decays, the neutrino is lost, and thus the kinematics of the decayed  $W$  may not be directly calculated. Instead, conservation of 4 momentum is used to infer the energy of the neutrino. As will be discussed in

section 2.3.1, even for symmetric beams, in hadron colliders the colliding energy along the beam line is unknown and unbalanced. Instead, the neutrino balances with the momentum of other particles in the event only in the plane perpendicular to the beam line. Thus, one may only calculate the transverse momentum of the  $W$ , and not the component parallel to the beam line.

## 2.3 Quantum Chromodynamics

Quantum Chromodynamics (QCD) [61] describes the interaction of fundamental particles under the strong force, which is a non-abelian  $SU(3)$  gauge group. Both quarks and gluons interact via the strong force (and are thus said to be *colored*), with two fundamental vertices shown in Figure 2.5.

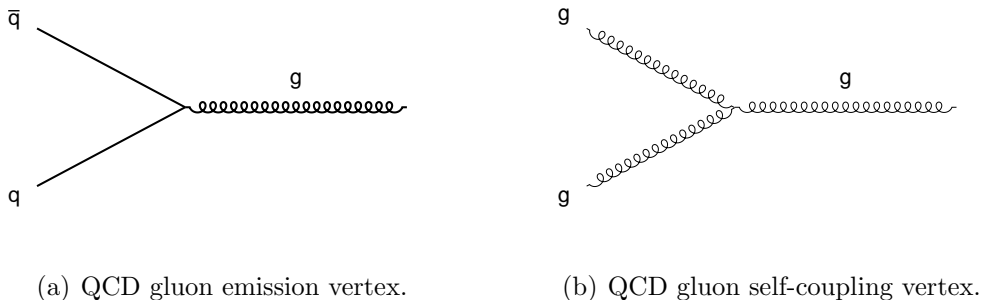


Figure 2.5: Fundamental QCD vertices.

The primary property of QCD that is of interest to  $W$  physics is the so-called *asymptotic freedom*, which refers to the fact that the coupling strength between colored particles decreases with decreasing length scales. In particular, at short distances, or asymptotically large energies, particles become free with respect to the strong force.

Mathematically, this is represented as the running of the coupling constant,  $\alpha_s$ , with interaction energy, as described by:

$$\alpha_s(Q) = \frac{6\pi}{(11n_c - 2n_f) \log(Q/\Lambda_{QCD})} \quad (2.1)$$

where  $Q$  is the energy transfer of the collision,  $n_c = 3$  is the number of color charges,  $n_f = 6$  is the number of quark flavors, and  $\Lambda_{QCD} \sim 100\text{MeV}/c$  is the QCD scale [61].

This running of  $\alpha_s$  results in an ever increasing potential energy as colored particles are separated. In a roughly analogous process to electron-positron pair production in high fields in Quantum Electrodynamics [43], at some point the energy becomes large enough that a quark-antiquark pair is produced and the isolated color charge is neutralized. This phenomenon is known as *confinement* and results in the property of QCD that it is not possible to observe isolated particles which are not neutral with respect to the strong force.

Confinement has a number of important experimental consequences for  $W$  physics. First, it is not possible to collide quarks directly, as it is not possible to produce beams of bare quarks. Instead, at hadron colliders, the beams consist of protons or anti-protons. The consequences of this are discussed in sections 2.3.1 and 2.3.2. Second, collisions involving the emission of a gluon or quark result in a complicated production of particles due to the processes of showering, where quark-antiquark pairs are produced due to confinement, and hadronization, where bare quarks condense into mesons and baryons. The consequences of this are discussed in section 2.3.3.

### 2.3.1 Parton Distribution Functions

Typically, Feynman diagrams for production processes at hadron colliders, such as those for  $W$  and  $Z$  production in Figure 2.3, are written assuming the collision of two quarks. However, as mentioned previously, hadron colliders collide beams of protons or anti-protons as it is not possible to produce beams of bare quarks due to confinement. The discrepancy means that even in symmetric beams, for example 3.5 TeV on 3.5 TeV proton beams as found at the Large Hadron Collider, the collision is asymmetric in two important ways. First, the flavor of the parton (quark or gluon) participating in the collision need not be the same for the two protons or between collisions. Second, because the proton is a composite particle, the energy of the parton is not equivalent to the energy of the proton, and is typically imbalanced even with symmetric beams. Mathematically, these two issues are formulated with the use of parton distribution functions, which describe the probability of extracting a parton of a given flavor with a fraction,  $x$ , of the total proton energy.

PDFs have been measured by a number of collaborations, typically as best fit curves combining measurements from deep inelastic scattering experiments, including CTEQ, HERA, and MSTW [6, 63, 58, 48, 56, 32]. An example PDF from the HERA collaboration is shown in Figure 2.6. Note that PDFs depend on the  $Q^2$ , or energy transfer, of the event, suggesting that the constituents of the proton change with length scale. While there are small differences between the various distributions, the general features are the same. Typically, valence quarks (for protons,  $u$  and  $d$  type quarks) carry roughly a third of the proton energy, while gluons, heavy quarks, and

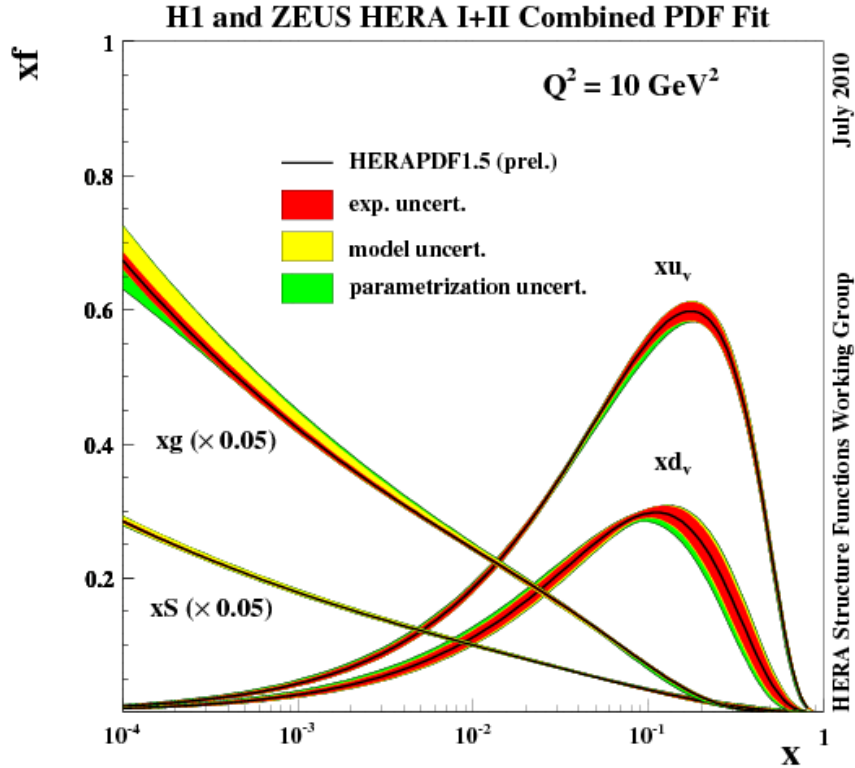


Figure 2.6: Example parton distribution functions for the HERA collaboration [48]. The x axis shows  $x$ , the fraction of the proton energy held by the parton, and the y axis shows  $xf(x)$ , which is the product of  $x$  and the probability of selecting a parton with that energy fraction.

anti-quarks are more likely to have only a small fraction of the proton energy.

While the transverse momentum of the  $W$  boson is not directly affected by the PDF (as to first order they describe only momentum parallel to the beam line), there are a number of indirect effects. Different PDFs have different variances in the distribution of parton energies. In general, larger variances result in collisions that have larger imbalances in colliding energy along the beam axis, which results in larger boosts of the collision frame relative to the lab frame. This results in particles

which are produced closer to the beam line, and thus affects the efficiency for finding particles within the fiducial volume of the detector. Different PDFs also result in slightly different transverse momentum spectra for the decay products of produced  $W$  bosons, which results in slightly different effects from the inherent resolution of the detector.

### 2.3.2 Soft QCD

Because of the running of  $\alpha_S$  with energy, the behavior of gluon emission is very different at high and low energies. Specifically, at high energy,  $\alpha_S$  becomes small, and the behavior of gluon emission becomes *perturbative* - it is possible to sum diagrams of ever increasing number of gluon emissions and result in a finite number. This regime is described in section 2.3.3. However, at low energy,  $\alpha_S$  becomes large with decreasing energy, and it becomes very difficult to calculate the effects of so-called soft QCD.

At low  $W$  transverse momentum, the  $W$  becomes more on shell, producing a divergence in the propagator of the form  $[\alpha_S \log(M_W/p_T)]^n$  for diagrams of order  $n$  in  $\alpha_S$ . This, combined with an increasing  $\alpha_S$ , results in divergences of the form  $[\alpha_S \log(M_W/p_T)]^n$ ,  $\alpha_S^n \log^{n-1}(M_W/p_T)$ , and so on for diagrams of order  $n$  in  $\alpha_S$  [72]. The best known way to approach these divergences is with a technique known as *resummation* [35], whereby an approximation of the leading logarithms of the total sum is calculated via a power series. While this works in the transition region of roughly 30 - 50 GeV, at lower transverse momentum, the divergences become large and the solution breaks down. In this region, the calculation is very difficult, and

is often accomplished via the introduction of a form factor which requires that the calculated cross section go to zero at zero transverse momentum [72].

### 2.3.3 Jet Production

As it is not possible to produce colored particles in the final state to due confinement, the emission of a colored particle (such as a quark or a gluon) during the interaction results in a complicated process by which the emitted particles are turned into color neutral particles like mesons and hadrons. While this is in general very difficult to explicitly model, there are a number of Monte Carlo simulators that implement this process in two steps: showering, in which high energy colored particles radiate gluons, and hadronization, in which color neutral particles are produced. The two most commonly used such simulators are PYTHIA [74] and ALPGEN [55] which approach these processes in a different ways.

As will be discussed in detail later, the transverse momentum of the  $W$  is largely determined by the transverse energy of hadronic activity in the event. Thus correctly simulating hadronic activity is a very important part of modeling the transverse momentum spectrum. PYTHIA is a leading order Monte Carlo, meaning that hard emissions of gluons in  $W$  production are explicitly not included. As this would tend to make the  $W$  transverse momentum spectrum less hard, the showering model of PYTHIA is tuned to match measurements of the  $W$  and  $Z$  transverse momentum spectra from the tevatron [74]. ALPGEN on the other hand, explicitly models  $W$  production associated with the emission of 1 or more hard quarks or gluons. While more physical than the ad-hoc tuning used in PYTHIA there are other problems

associated with this approach. As gluons may be produced during the showering process (ALPGEN does not include showering/hadronization - it is usually interfaced with another package, such as HERWIG [36], to do that), the demarkation between  $n$  and  $n + 1$  jets is not as clear as it would first seem. Typically, processes such as MLM matching [55] are used after showering to separate the produced events into non-overlapping samples and a reweighting procedure is used to combine them.

In addition to PYTHIA and ALPGEN there are a number of other monte carlo packages for simulating hadronic activity in  $W$  events, including RESBOS[2], MCFM[5], FEWZ[57, 41], DYNNLO[7], and MC@NLO[40]. These packages provide either higher order explicit calculation of  $W +$  jet cross sections, differing capabilities for handling of the logarithmic divergences at low transverse momentum or even full showering and hadronization. Because of the sensitivity of the  $W$  transverse momentum spectrum on jet production and model used for showering and hadronization, this measurement provides an important probe of the accuracy of these models.

## 2.4 Previous measurements

The most recent measurements of the  $W$  transverse momentum were performed by the CDF and D $\emptyset$  collaborations at the Tevatron at  $\sqrt{s} = 1.8$  TeV in 1991 and 1998 respectively [26, 29]. Prior to that, measurements were made by the UA1 and UA2 collaborations at the  $Spp\bar{S}$  collider at  $\sqrt{s} \sim 0.5$  TeV in the mid 1980s [33, 34].

The CDF measurement used 2496 candidate  $W \rightarrow e\nu$  events, corresponding to  $4.1 \text{ pb}^{-1}$  of data, and corrected the measured spectrum back to the true distribution using a parameterized bin-by-bin correction. The analysis made use of a Monte Carlo sample that was tuned to match the observed jet and non-clustered energy distributions, and then checked on  $Z \rightarrow ee$  decays by requiring that the calorimeter energy and dilepton energy balance. The Monte Carlo was then used to produce a resolution function that was used to smear an estimate of the truth, and the estimate of the truth was refined until the smeared result matched the truth. The results of the CDF analysis are shown in Figure 2.7.

The D $\emptyset$  measurement used 7132 candidate  $W \rightarrow e\nu$  events, corresponding to  $12.4 \text{ pb}^{-1}$  of data, and compared the observed spectrum with a smeared version of the theoretical prediction. Detector resolution fits from data were used to tune a Monte Carlo simulation, which was then used to produce reconstruction level predictions from theories under study. The reconstruction level predictions were then compared with the observed data. The results of this analysis are shown in Figure 2.8 and Figure 2.9.

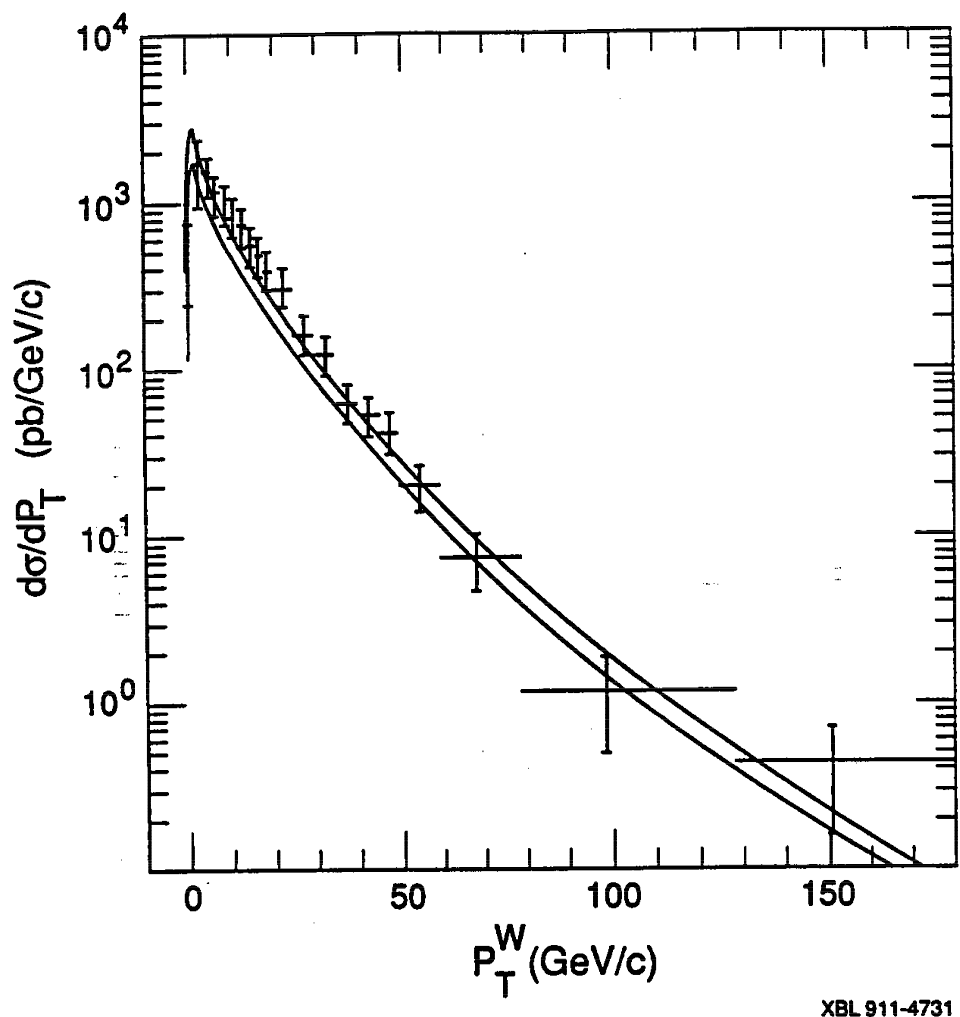


Figure 2.7: CDF measurement of the  $W$  transverse momentum spectrum [26].

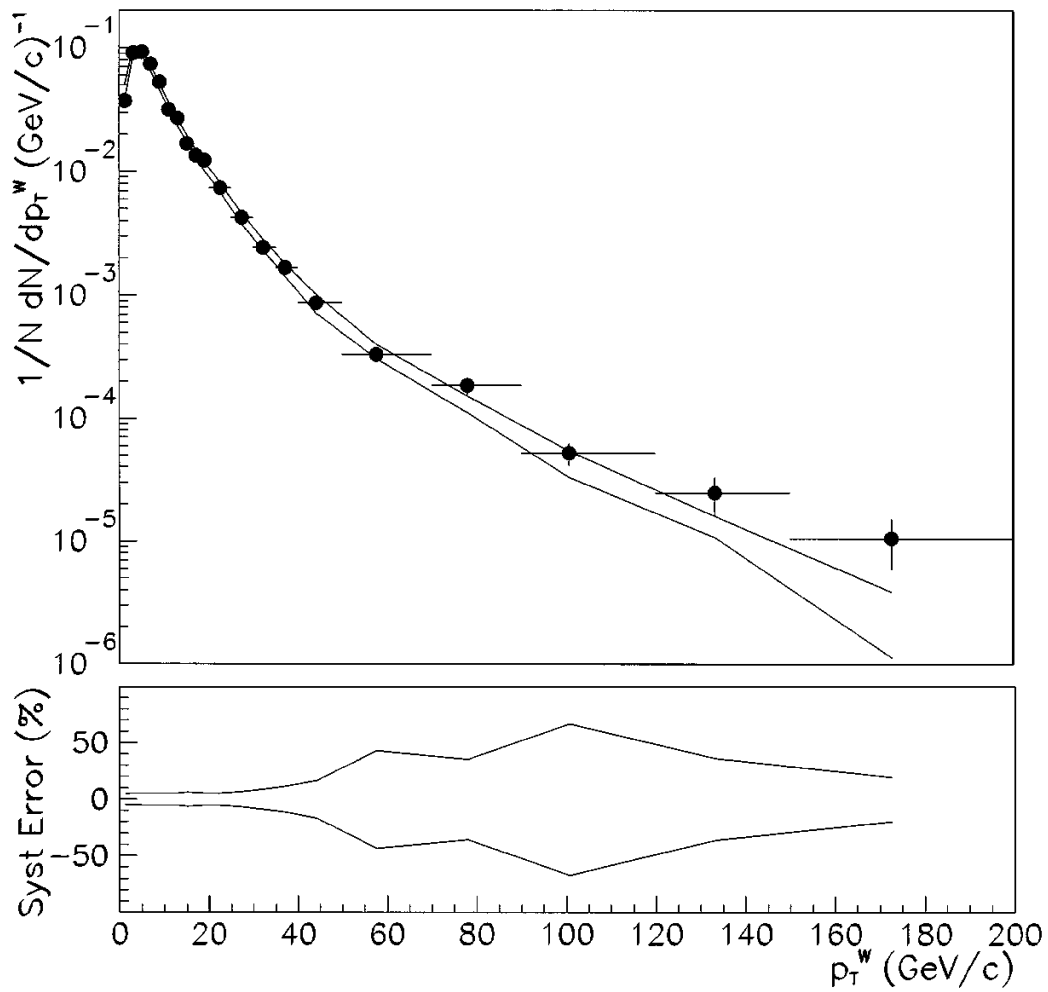


Figure 2.8: D0 measurement of the  $W$  transverse momentum spectrum [29].

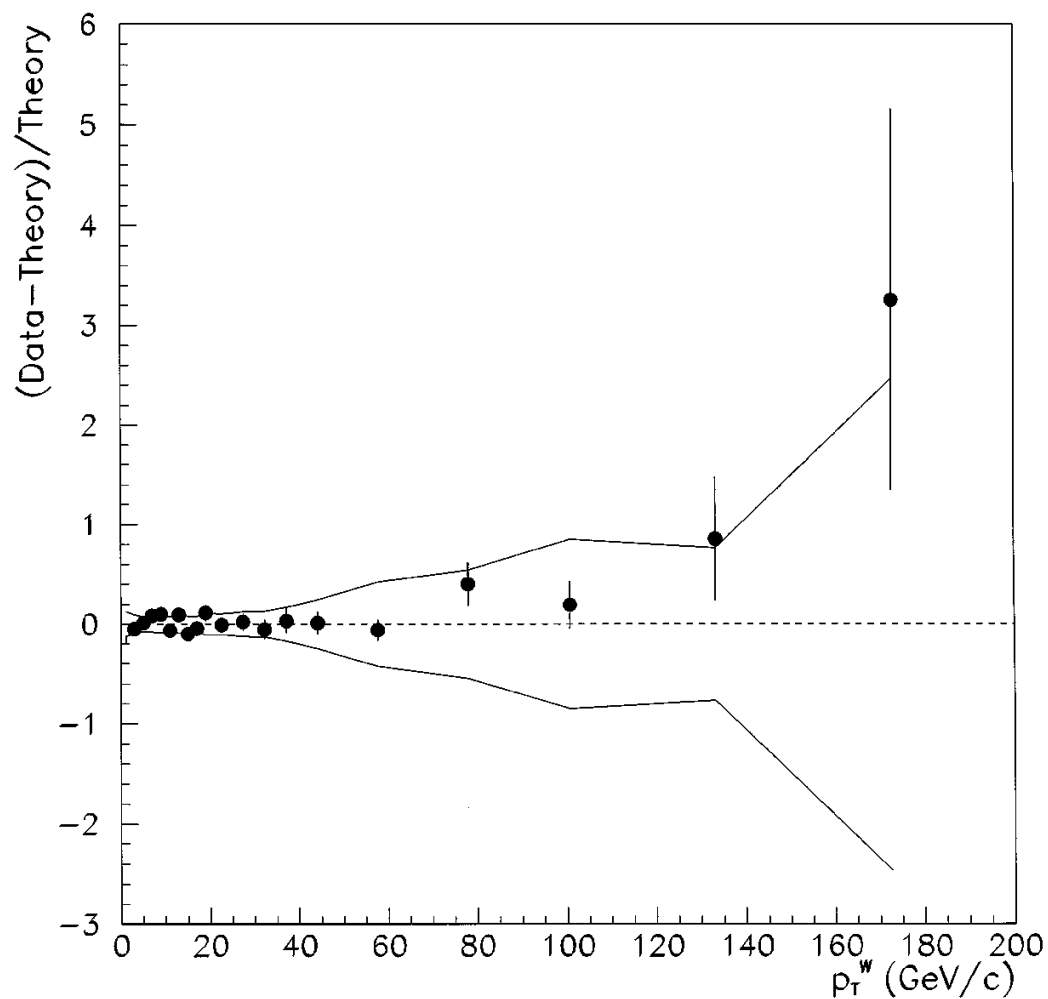


Figure 2.9: Theory-data comparison from D0 measurement of  $W$  transverse momentum measurement [29].

# Chapter 3

## Detector

ATLAS (A Toroidal LHC ApparatuS) is a multipurpose particle detector experiment located at CERN, near Geneva, Switzerland [24, 23]. Proton beams are accelerated by the Large Hadron Collider (LHC) and collided near the center of the detector. Properties of particles produced in collisions are measured by three basic subdetector systems: a cylindrical tracking chamber made of silicon and straw tubes called the Inner Detector; a sampling calorimeter made of lead and steel absorbers, and liquid argon and scintillating tile samplers; and a muon spectrometer made of drift tubes, thin gap, and resistive plate chambers. An overview diagram of the ATLAS detector is shown in Figure 3.1.

Trajectories of various types of particles are show in Figure 3.2. Charged particle track parameters are measured in the inner detector, and a 2 T solenoidal magnetic field is used to provide bending power for momentum measurements. Photon and electron energy is measured in the electromagnetic calorimeter, while baryon and

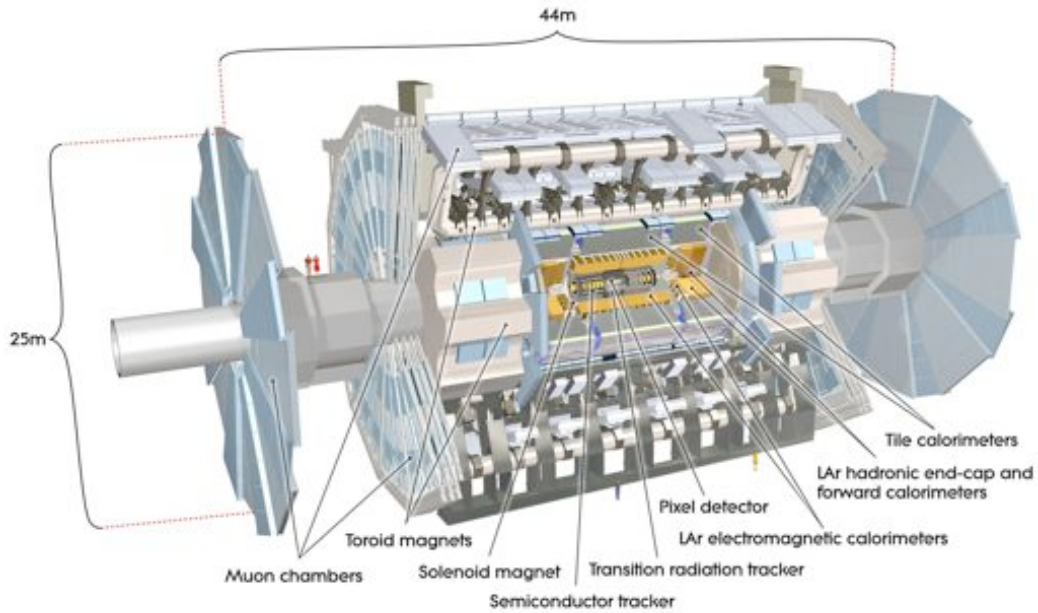


Figure 3.1: A diagram of the ATLAS detector, with the various major subdetector systems labelled [1].

meson energy is measured in the hadronic calorimeter. Muons typically lose only  $\sim 4$  GeV of energy in the calorimeter, and so high transverse momentum muons reach the muon spectrometer at the outside of the detector, where large air core toroids provide bending power for a second momentum measurement. Neutrinos do not interact with the detector and thus can only be inferred from energy balance transverse to the beam line.

### 3.1 Coordinate Systems

The ATLAS coordinate system is defined with the  $z$ -axis parallel to the beam line, the  $x$ -axis horizontal, with positive  $x$  pointing to the center of the LHC ring, and the  $y$ -axis vertical, with positive  $y$  pointing up. Two angles are defined: the azimuthal

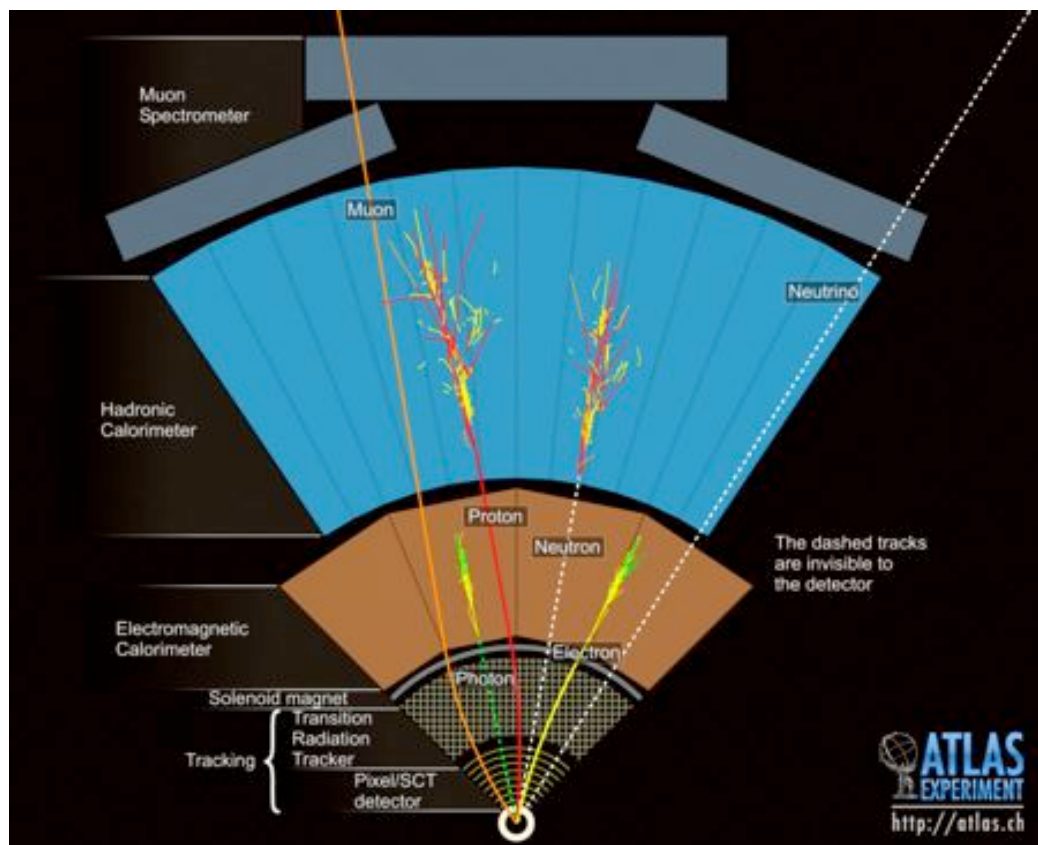


Figure 3.2: A diagram of the trajectories of various types of particles in the ATLAS detector [3].

angle  $\phi$ , which is zero along the positive  $x$  axis and increases towards positive  $y$ , and the polar angle  $\theta$ , which is zero along positive  $z$ , and is  $-\pi$  along negative  $z$ . In hadron colliders, another quantity,  $\eta \equiv -\ln(\tan(\theta/2))$ , is useful as the rate of particle production,  $dN/d\eta$ , is roughly flat over the fiducial volume of the detector. Finally, the quantity  $\Delta R \equiv \sqrt{\Delta\phi^2 + \Delta\eta^2}$  is often used when discussing the angular distance between two objects.

As energy is not balanced in the  $z$  direction, as described in section 2.3.1, it is often useful to refer only to the component of quantities perpendicular to the beam line. For vector quantities, like momentum, this is done by taking the  $x$  and  $y$  components of the vector, and can yield the magnitude of the transverse momentum, denoted  $p_T$ , or the two dimensional vector transverse momentum  $\vec{p}_T$ . In somewhat peculiar notation, the transverse component of scalar quantities, such as the transverse energy,  $E_T$ , is also often used. In this case, the transverse energy is calculated by forming a vector with magnitude given by the energy in a detector element (typically a calorimeter cluster) and direction given by the direction of the detector element. The total transverse energy in the event,  $\sum E_T$ , is calculated by summing the scalar  $E_T$  of each calorimeter cluster (with corrections for muons), while the missing transverse energy  $\cancel{E}_T$  is calculated by taking the magnitude of the vector sum of the  $\vec{E}_T$  of each calorimeter cluster (again corrected for muons). As the name implies, non-zero  $\cancel{E}_T$  is expected to be due to particles that are not measured by the detector, such as neutrinos, although in practice, it can often be due to mis-measurements or imperfect detector calibration.

The trajectories of charged particles are parameterized with 5 parameters:  $1/p_T$ ,  $\phi$ ,  $d_0$ ,  $\cot \theta$ , and  $z_0$ . The momentum of a charged particle is measured via its curvature, which makes  $1/p_T$  a natural parameter, as curvature is proportional to the strength of the bending field divided by the transverse momentum.  $\phi$  is simply the azimuthal angle of the track, and  $\cot \theta$  the cotangent of the polar angle.  $d_0$  is the transverse distance to the beam axis at the point of closest approach. In general, promptly produced particles have a  $d_0 < 130\mu m$ , while particles from long lived particle decays (such as pions and kaons) have a measured  $d_0$  greater than 1 mm. Finally,  $z_0$  is the distance from the origin along the  $z$ -axis at the point of closest approach of the track. In general, the spread of the collision area in  $z$  results in collision  $z_0$ 's of up to 10 cm relative to the origin, and so  $z_0$  is commonly measured relative to the  $z$  position of reconstructed primary vertices.

## 3.2 The Large Hadron Collider

The Large Hadron Collider (LHC) is a proton-proton and heavy ion collider located near Geneva, Switzerland [39]. It is designed with a center of mass energy of 14 TeV and an instantaneous luminosity of  $10^{34} \text{ cm}^{-2}\text{s}^{-1}$  for proton-proton collisions, and 2.8 TeV per nucleon with an instantaneous luminosity of  $10^{27} \text{ cm}^{-2}\text{s}^{-1}$  for lead-lead collisions. In 2010, it achieved proton-proton collisions with a center of mass energy of 7 TeV, a peak instantaneous luminosity of  $\sim 2 \times 10^{32} \text{ cm}^{-2}\text{s}^{-1}$ , and a total integrated luminosity of  $48.1 \text{ pb}^{-1}$ . The delivered and recorded integrated luminosity over the course of 2010 is shown in Figure 3.3.

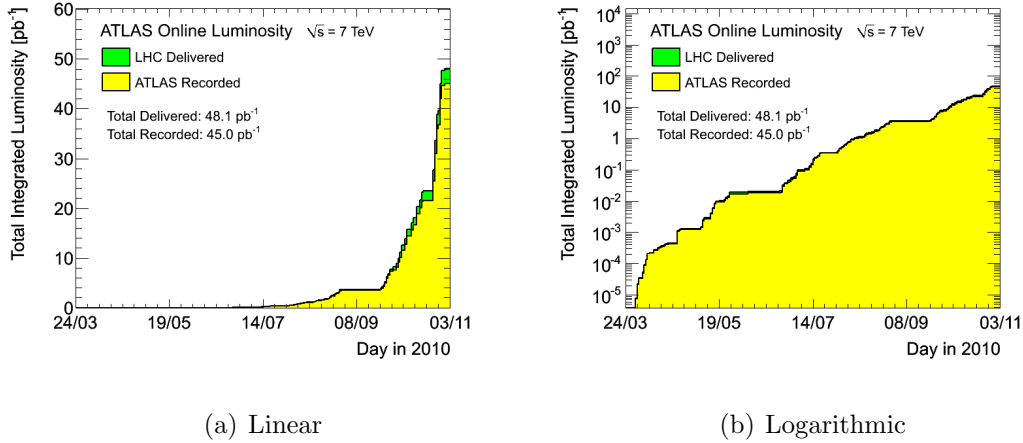


Figure 3.3: Delivered and recorded luminosity during 2010.

The general layout of the LHC, along with its injector chain, is shown in Figure 3.4. Protons are produced at an energy of 50 MeV from the LINAC accelerator system, and then routed to Proton Synchrotron Booster (PSB), where they are accelerated to 1.4 GeV. From there, they are accelerated by the Proton Synchrotron (PS) to 25 GeV, and by the Super Proton Synchrotron (SPS) to 450 GeV, after which they are injected into the LHC. All of the injector accelerators were built prior to the construction of the LHC and underwent extensive upgrades to handle the needed luminosity and bunch spacing requirements of the LHC.

The LHC magnet system is based upon superconducting NbTi Rutherford cables operating at a nominal field over 8 T and cooled to less than 2 K by superfluid helium. The layout of the main dipole bending magnet is shown in Figure 3.5. To fit in the existing LEP tunnel, the dipole magnets were built with both beam pipes inside the same cryostat, wrapped in superconducting coils. The design used provides magnetic fields in the opposite direction in each beam pipe in order to correctly bend the

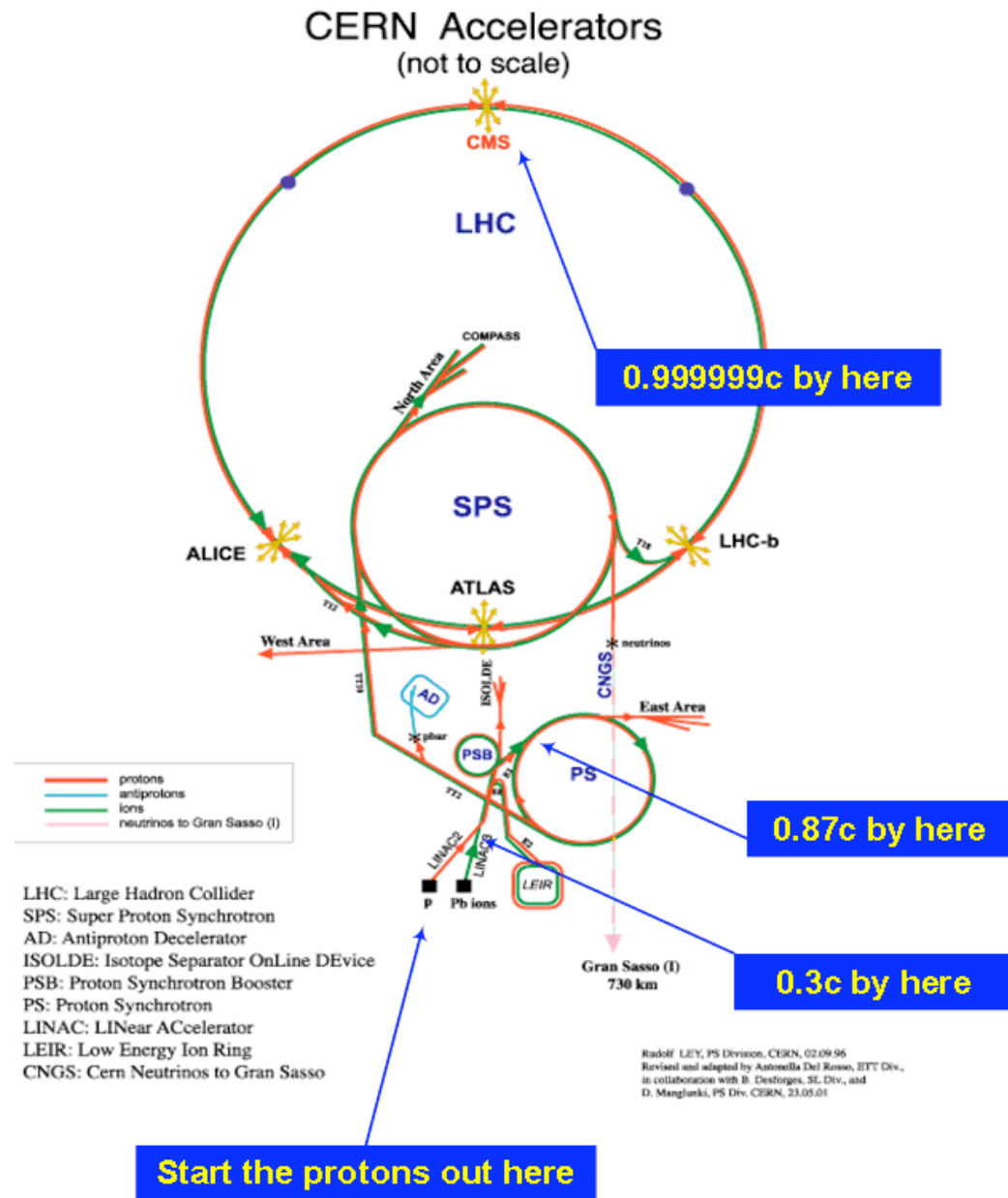


Figure 3.4: A diagram of the LHC along with its injector chain [8].

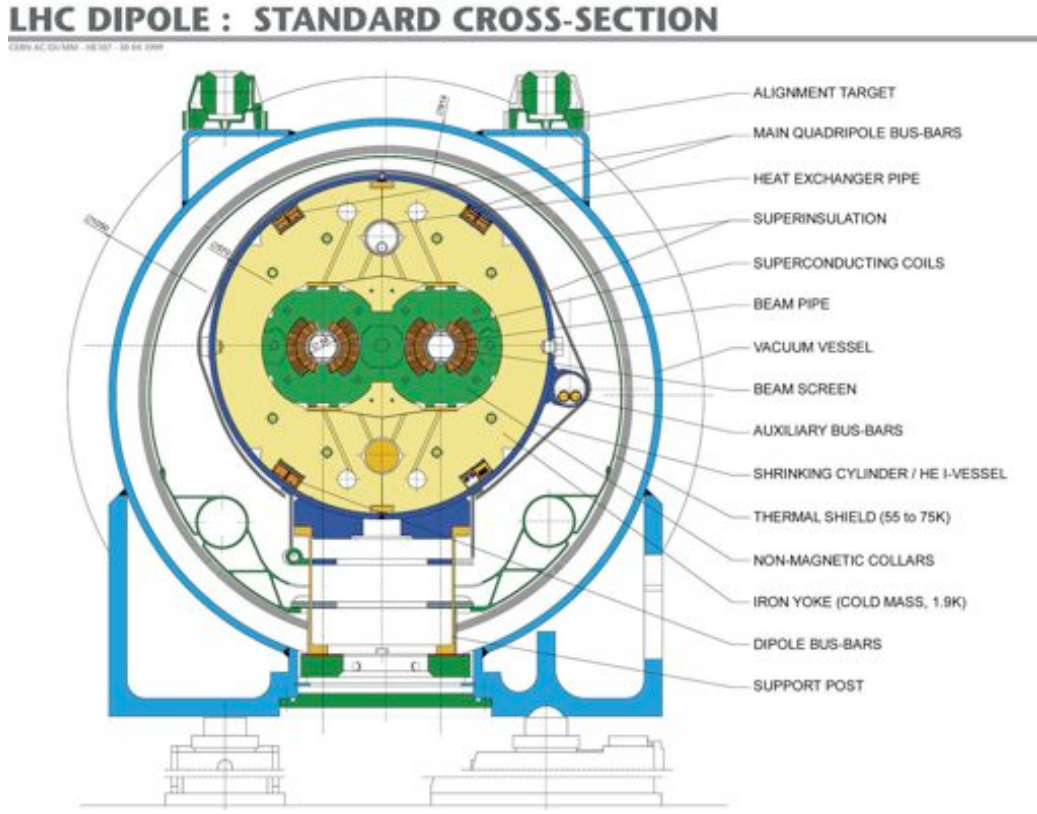


Figure 3.5: A diagram of the main LHC bending magnet [1].

counter rotating beams. In addition to the 14 m long 1,232 such bending magnets in the LHC, there are over 3,000 smaller superconducting and normal conducting magnets for beam corrections, focusing, and insertions in collisions. In particular, a number of strong focusing magnets are used to squeeze the proton bunches prior to collisions in order to maximize the instantaneous luminosity.

The general parameters of the LHC beams are shown in Table 3.1. Protons are injected into the LHC in *bunches*, which is  $\sim 10^{11}$  protons squeezed into a single RF bucket approximately 4 ns long. In order to increase the number of bunches in the beam, and therefore the instantaneous luminosity, bunches are typically injected into

Property	Nominal Value	Peak 2010 Value
Ring Circumference [ km ]	26.695	26.695
Energy per Beam [ TeV ]	7	3.5
Instantaneous Luminosity [cm <sup>-2</sup> s <sup>-1</sup> ]	10 <sup>34</sup>	2 × 10 <sup>32</sup>
Bunches per beam	2808	368
Bunch spacing [ ns ]	25	75
Bunch length [ ns ]	4	4
Protons per bunch	1.15 × 10 <sup>11</sup>	1.15 × 10 <sup>11</sup>
Beam spot size (x) [ $\mu\text{m}$ ]	16.7	44.8
Beam spot size (y) [ $\mu\text{m}$ ]	16.7	44.8
Beam spot size (z) [ cm ]	7.55	7.55
$\beta^*$ [m]	0.55	2
Luminosity per bunch [cm <sup>-2</sup> ]	4 × 10 <sup>26</sup>	5 × 10 <sup>25</sup>

Table 3.1: Properties of the Large Hadron Collider.

the LHC as *bunch trains*, which are a series of bunches nominally separated by 25 ns (75 ns in 2010). Bunch trains are produced by a multiple splitting procedure in the PS, whereby high intensity bunches from the PSB are split twelve ways forming a bunch pattern of 72 bunches followed by 12 empty buckets [39]. The bunch structure of the LHC results in two important consequences for physics, termed *in time* and *out of time* pileup respectively. In in time pileup, the fact that bunches consist of many protons results in multiple collisions per bunch crossing - roughly four at peak 2010 luminosity. In out of time pileup, the fact that bunch trains are used with a bunch spacing of 75 ns means that multiple bunch crossings occur while the detectors are still responding to the first collision. In both cases, the extra collisions are unlikely to contain high  $p_T$  objects, but can result in extra energy and particle multiplicity in the event.

Sub detector	Location	Resolution ( $\mu m$ )	Channels ( $10^6$ )	$\eta$ coverage
Pixel	B-layer	$R\phi = 12, z = 66$	16	$\pm 2.5$
	2 barrel layers	$R\phi = 12, z = 66$	81	$\pm 1.7$
	5 endcap disks (per side)	$R\phi = 12, R = 77$	43	$1.7 - 2.5$
SCT	4 barrel layers	$R\phi = 16, z = 580$	3.2	$\pm 1.4$
	9 Endcap wheels (per side)	$z\phi = 16, R = 580$	3.0	$1.4 - 2.5$
TRT	Barrel	170 (per hit)	0.1	$\pm 0.7$
	9 Endcap	170 (per hit)	0.32	$0.7 - 2.5$

Table 3.2: Properties of the ATLAS Inner Detector [24].

### 3.3 Inner Detector

Tracking of charged particles in ATLAS is provided by the Inner Detector (ID), which is a 1.2 m cylindrical tracking chamber consisting of three subdetectors. Closest to the beampipe, typically providing three space-point measurements, is a very high-granular and high-precision semiconductor based tracker called the Pixel Detector. Outside of the Pixel Detector is the Semiconductor Tracker (SCT), which typically provides eight space-point measurements. Finally, providing on average 36 space-point measurements is the Transition Radiation Tracker (TRT), which uses straw tubes to provide both position information and particle identification. The general parameters of the ID are shown in Table 3.2, and schematic views are shown in Figures 3.6 and 3.7.

The nominal performance of the ID is shown in Figure 3.8. At  $p_T$  less than roughly 15 GeV, resolution is dominated by multiple scattering in the detector material, while above 15 GeV,  $d_0$  and  $z \times \sin(\theta)$  resolution become very good, approaching the

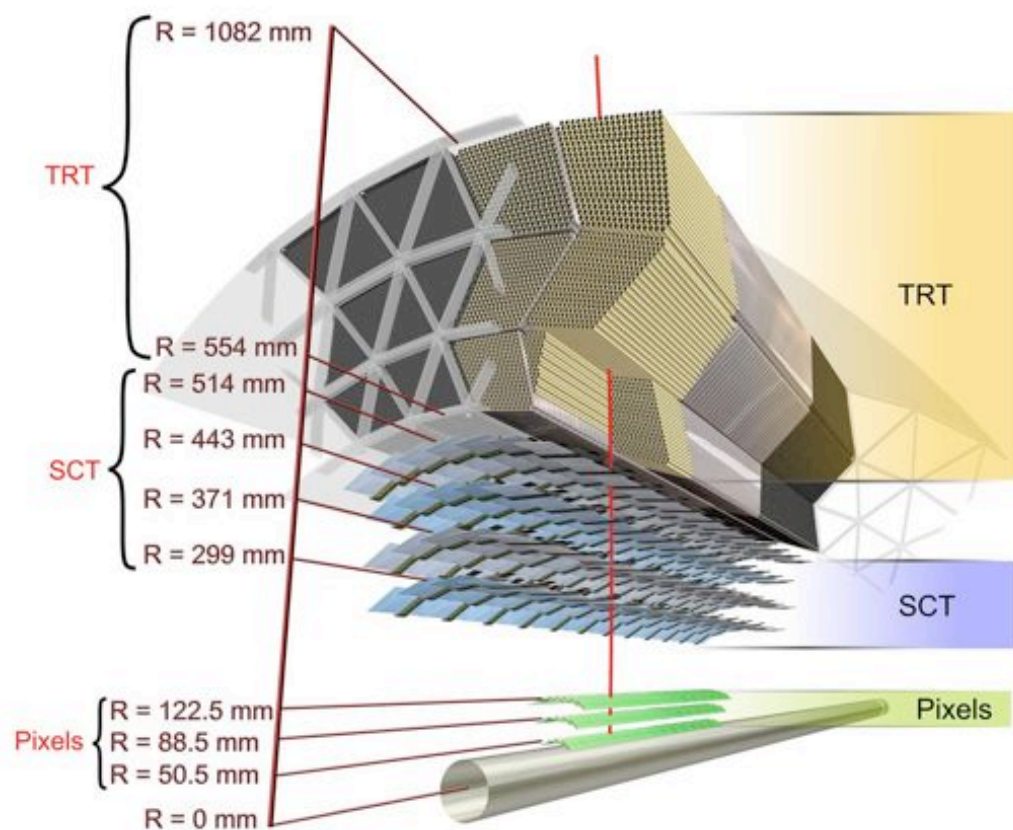


Figure 3.6: A diagram of the ATLAS barrel Inner Detector [1].

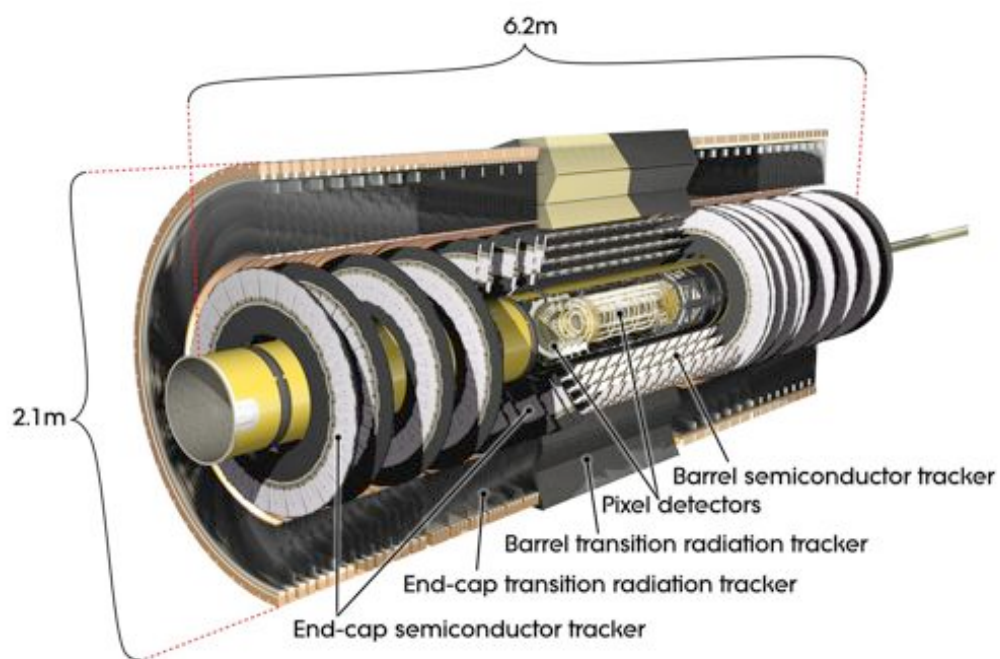


Figure 3.7: A diagram of the ATLAS endcap Inner Detector [1].

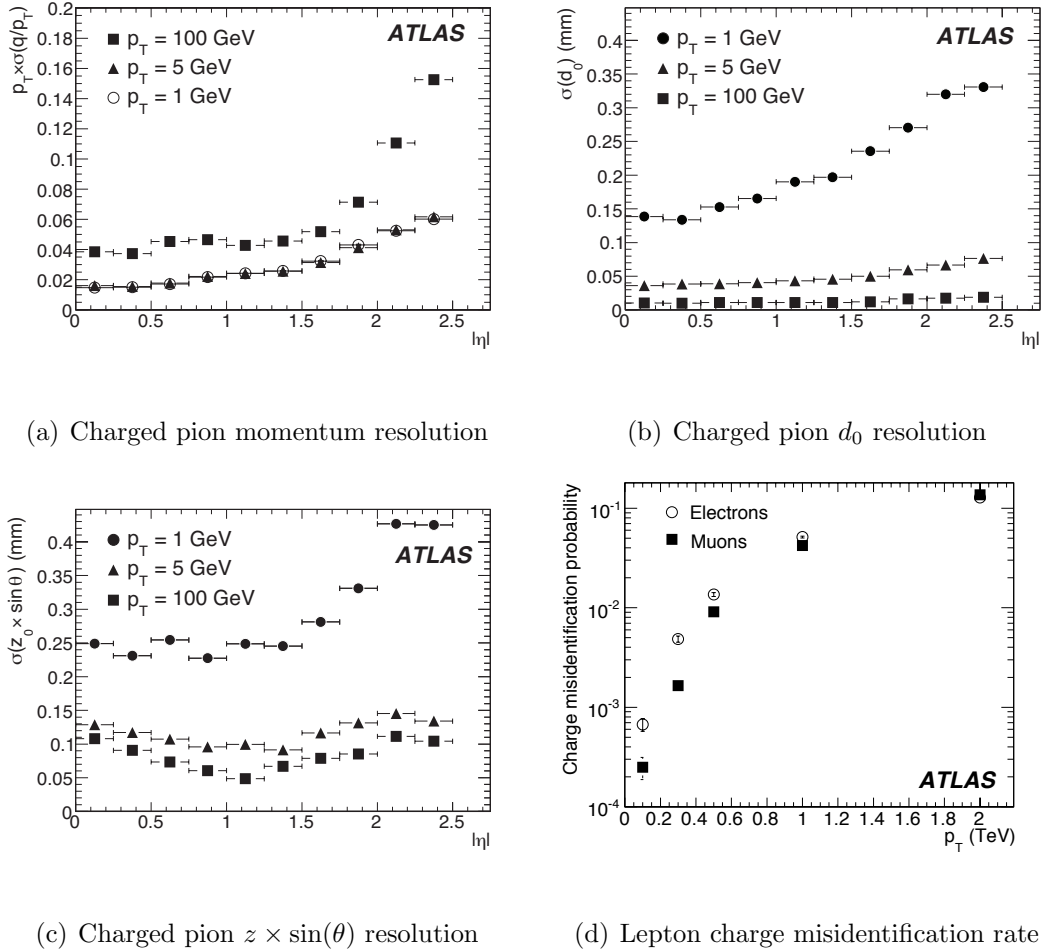


Figure 3.8: Nominal performance of the ATLAS Inner Detector [10].

100 $\mu$ m level and better. Charged particle momentum measurements are performed by determining the bending radius due to the 2 T solenoidal field. Above roughly 15 GeV, the momentum resolution is dominated by the ability to resolve the sagitta of the particle, which depends on the largely TRT hit resolution. At 100 GeV, the momentum resolution is better than 5% over the majority of the detector. At very high energies (above roughly 1 TeV), charge misidentification becomes very problematic, with a charge mis-measurement rate approaching 5%.

### 3.3.1 Pixel Detector

The Pixel Detector is designed to provide very high resolution measurements very near the beampipe in order to allow vertexing of displaced decays such as those from  $B$  hadrons despite the very high particle multiplicity of LHC collisions. It is broken into three modules: a removable single layer at 5 cm from the center of the beam pipe called the B-layer; a pair of barrel layers at radii of 9 and 12 cm respectively; and an end cap module consisting of five layers between 11 and 20 cm.

Each detector element is roughly  $50 \mu\text{m}$  in  $R\phi$  and  $300 \mu\text{m}$  in  $z$ , which provides very high resolution as well as helps avoid detector saturation in the very high flux environments so close to the ATLAS collision point. 61,440 elements are formed into a 62.4 mm long by 21.4 mm wide pixel module, which is read out and buffered by 16 readout chips. Each layer is then formed by tiling pixel elements, resulting in a final sub detector system with 140 million detector elements and roughly 1.7% of a radiation length per layer.

### 3.3.2 Semiconductor Tracker

The Semiconductor Tracker (SCT) is designed to provide 8 precision measurements of particle trajectory, which are useful in determining of the particle vertex and trajectory. In order to avoid the high cost, in dollars, material, and readout channels, of the Pixel Detector, the SCT consists of silicon microstrip detectors bonded in small angle stereo to provide measurement in the long ( $R$  or  $z$ ) dimension. The SCT is split into two modules: a barrel module which provided four space point measurements,

and an endcap with nine wheels.

768 readout strips with an  $80 \mu\text{m}$  pitch are arranged in a  $6.36 \times 6.40 \text{ cm}^2$  detector element. Two detector elements are bonded together to form a collection of 12.8 cm long strips. Two such 12.8 cm long strips are then glued together, one on top of each other, with a 40 mrad angle between them, and the readout electronics are fitted to the combination. A barrel layer is formed by placing the merged elements such that the precision measurement is in  $R\phi$  and the coarse measurement is in  $z$ . Similarly, an endcap wheel is formed with the precision measurement in  $z\phi$  and the coarse measurement in  $R$ . The resulting SCT sub detector has 6.2 million readout channels, with a resolution in of  $16 \mu\text{m}$  in the precision direction and  $500 \mu\text{m}$  in the coarse direction. As will be discussed in section 3.6, the bending due to the magnetic field in the ID is only in  $\phi$ , and thus the coarse measurement is not needed for momentum measurements.

### 3.3.3 Transition Radiation Tracker

The Transition Radiation Tracker (TRT) provides approximately 36 measurements of particle trajectories in the bending direction as well as electron identification capability with modest cost in terms of dollars, readout channels, and material, by using long, thin straw tubes. Each straw tube has an inner diameter of 4 mm, a  $30 \mu\text{m}$  diameter gold-plated W-Re wire held at high voltage, and is filled with a mixture of 70% Xenon, 20%  $\text{CO}_2$ , and 10%  $\text{CF}_4$  gas. To enhance mechanical and electrical properties, the tubes are wrapped with Kapton film and reinforced with aluminum and carbon fiber. Charged particles incident on the tubes ionize the gas mixture and

the produced electrons drift in the electric field of the wire. A measurement of the drift time is converted to drift radius via a calibrated function called the RT relation, and the drift radius is used in pattern finding. To aid in particle identification, a radiator is inserted between the tubes which causes the emission of transition radiation photons by high  $\beta$  particles (i.e., electrons and positrons). The amount of charge deposited in the straw tube is then used to separate high threshold hits, which include transition radiation, from low threshold hits, which do not.

The complete TRT consists of a barrel and two end-cap modules. The barrel contains roughly 50,000 straw tubes, split at the center to reduce occupancy and stretched axially from  $z = -72$  cm to  $z = +72$  cm. Each end-cap consists of 18 wheels of radial straw tubes of varying length to produce full coverage to  $|\eta| = 2.5$ . The per hit resolution of each straw tube is roughly  $170\ \mu\text{m}$ , which gives a combined measurement of better than  $50\ \mu\text{m}$  in the bending direction of the ID magnet system. As there is no segmentation along the length of the wire, there is no information about the particle trajectory in the direction perpendicular to the bending direction.

## 3.4 Calorimeter

The ATLAS calorimeter is composed of a lead/liquid argon electromagnetic (EM) calorimeter extending to  $|\eta| = 3.2$  surrounded by an iron/scintillating tile and copper/tungsten/liquid argon hadronic calorimeter extending to  $|\eta| = 4.9$ . A diagram of the ATLAS calorimeter is shown in Figure 3.9 and the general properties are shown in Table 3.3.

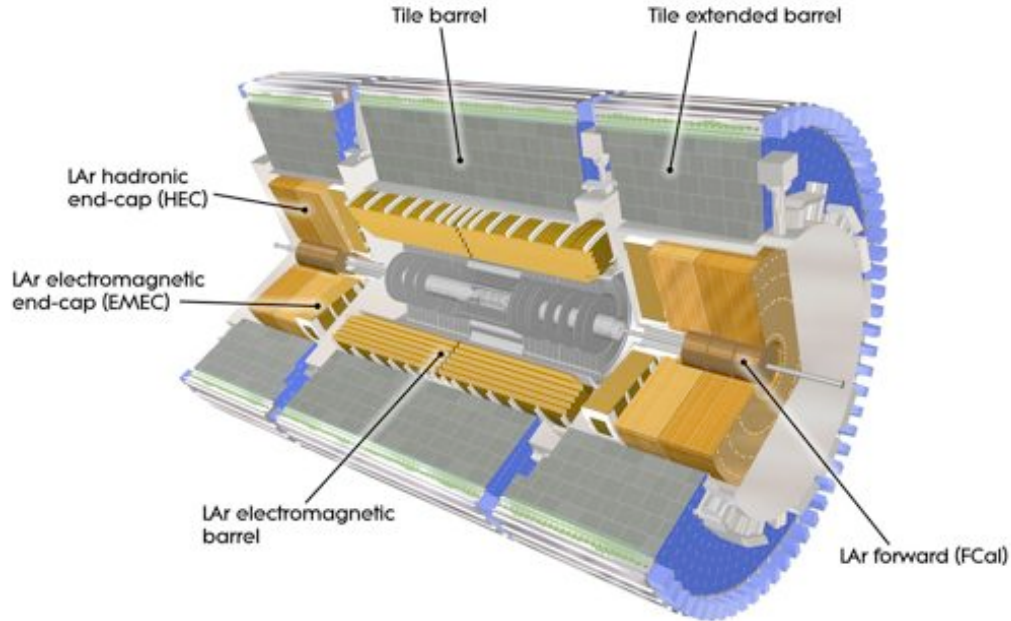


Figure 3.9: A diagram of the ATLAS Calorimeter [1].

Name	Coverage	Layers	Granularity ( $\Delta\eta \times \Delta\phi$ )
EM Barrel Layer 1	$ \eta  < 1.475$	1	$0.003 \times 0.1$
EM Barrel Layer 2	$ \eta  < 1.475$	1	$0.025 \times 0.025$
EM Barrel Layer 3	$ \eta  < 1.475$	1	$0.05 \times 0.025$
EM Endcap Layer 1	$1.375 <  \eta  < 3.2$	1	$\sim 0.004 \times 0.1$
EM Endcap Layer 2	$1.375 <  \eta  < 3.2$	1	$\sim 0.025 \times 0.025$
EM Endcap Layer 3	$1.5 <  \eta  < 2.5$	1	$0.05 \times 0.025$
Presampler	$ \eta  < 1.8$	1	$0.025 \times 0.1$
Hadronic Tile Layers 1, 2	$ \eta  < 1.7$	2	$0.1 \times 0.1$
Hadronic Tile Layer 3	$ \eta  < 1.7$	1	$0.2 \times 0.1$
Hadronic LAr endcap	$1.5 <  \eta  < 2.5$	4	$0.1 \times 0.1$
Hadronic LAr forward	$2.5 <  \eta  < 3.2$	4	$0.2 \times 0.2$
FCAL	$3.1 <  \eta  < 4.9$	3	$\sim 0.2 \times 0.2$

Table 3.3: Properties of the ATLAS Calorimeter [24].

The nominal performance of the ATLAS EM calorimeter is shown in Figure 3.10. The very high segmentation in the inner layer of the EM calorimeter allows measurement of  $\eta$  and  $\phi$  to better than 5 mrad over most of the fiducial volume. It is worth noting that there is slightly worse performance in  $\phi$  due to larger segmentation, as well as the tendency of clusters to be smeared in the solenoid bending direction due to the emission of bremsstrahlung. A major challenge in precision measurements of electron and photon energy resolution is the large amount of material before the calorimeter, shown in Figure 3.11, which results in a high probability of photon conversion, shown in Figure 3.12. Despite this, the EM calorimeter provides a photon energy resolution nearing 2% at 100 GeV with excellent linearity. Studies to determine the resolution from data using  $Z \rightarrow ee$  decays will be presented as part of this analysis. Finally, it is worth noting the dramatically decreased performance in almost all measures in the crack region near  $|\eta| = 1.4$ . For most analyses, including the electron channel of this analysis, objects from the crack region are specifically excluded due to the poor performance.

The nominal performance of the hadronic calorimeter is shown in Figure 3.13. The hadronic calorimeter provides good jet response up to jet energies beyond 1 TeV. Importantly for this analysis, the  $\cancel{E}_T$  resolution is roughly 8 GeV in most electroweak events, with a direction resolution better than 0.1 radians when there is at least 80 GeV of  $\cancel{E}_T$ . The  $\cancel{E}_T$  performance in electroweak events will be measured using data driven techniques as part of this analysis.

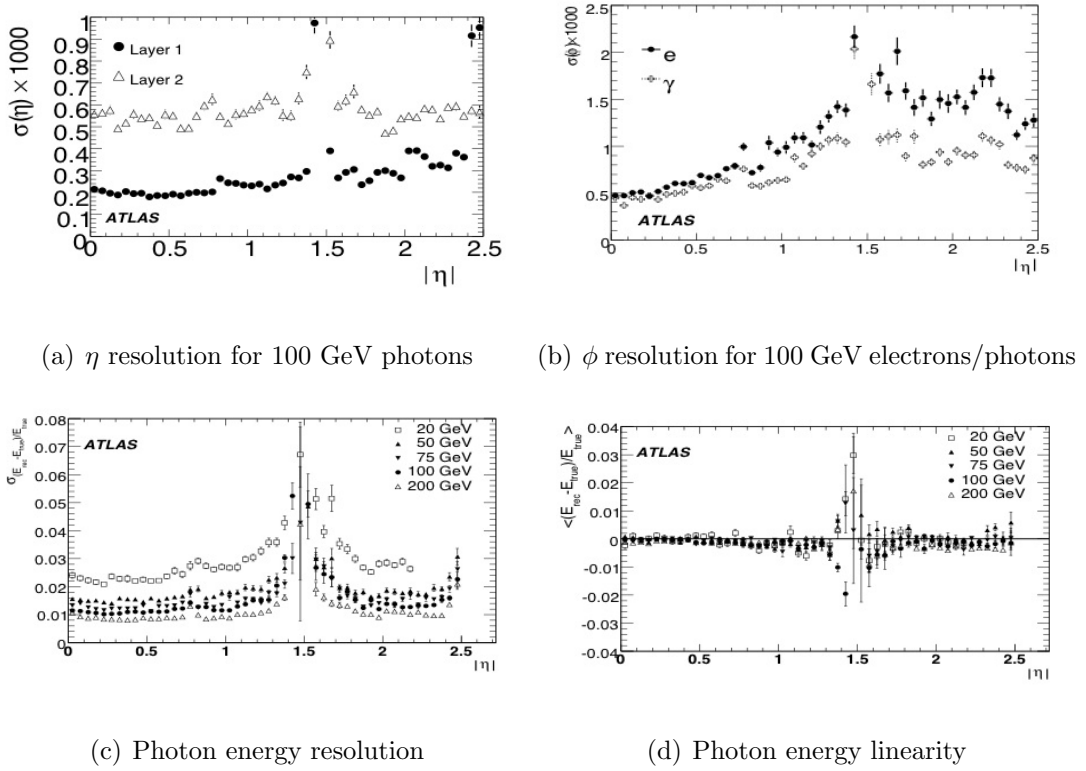


Figure 3.10: Nominal performance of the ATLAS Electromagnetic calorimeter [10].

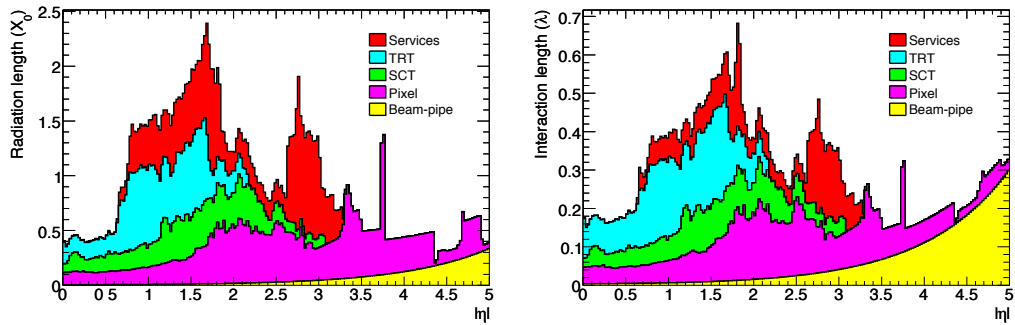


Figure 3.11: Material prior to entering the ATLAS calorimeter [10].

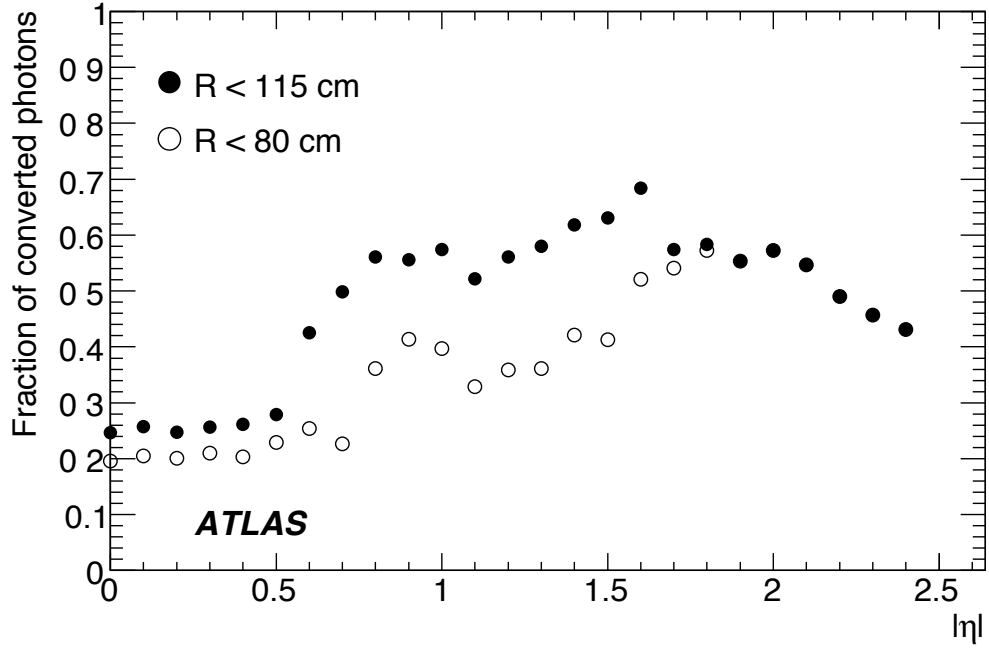


Figure 3.12: Probability of photon conversion before a radius of 80 and 115 cm [10].

### 3.4.1 Electromagnetic Calorimeter

The electromagnetic (EM) calorimeter consists of two distinct modules: the barrel, with coverage up to  $|\eta| = 1.475$ , and the end-cap, with coverage over  $1.375 < |\eta| < 3.2$ . The barrel is broken down further into two identical half barrels with a space of 6 mm at  $z = 0$  and each end-cap is broken into two wheels, with an outer wheel covering  $1.375 < |\eta| < 2.5$  and an inner wheel covering  $2.5 < |\eta| < 3.2$ .

The EM calorimeter is a liquid argon calorimeter with Kapton electrodes and lead absorber plates in an accordion shape as shown in Figure 3.14, which allows fully symmetric  $\phi$  coverage without an azimuthal cracks. Incident charged particles produce electromagnetic showers in the lead, which cause ionization in the liquid argon,

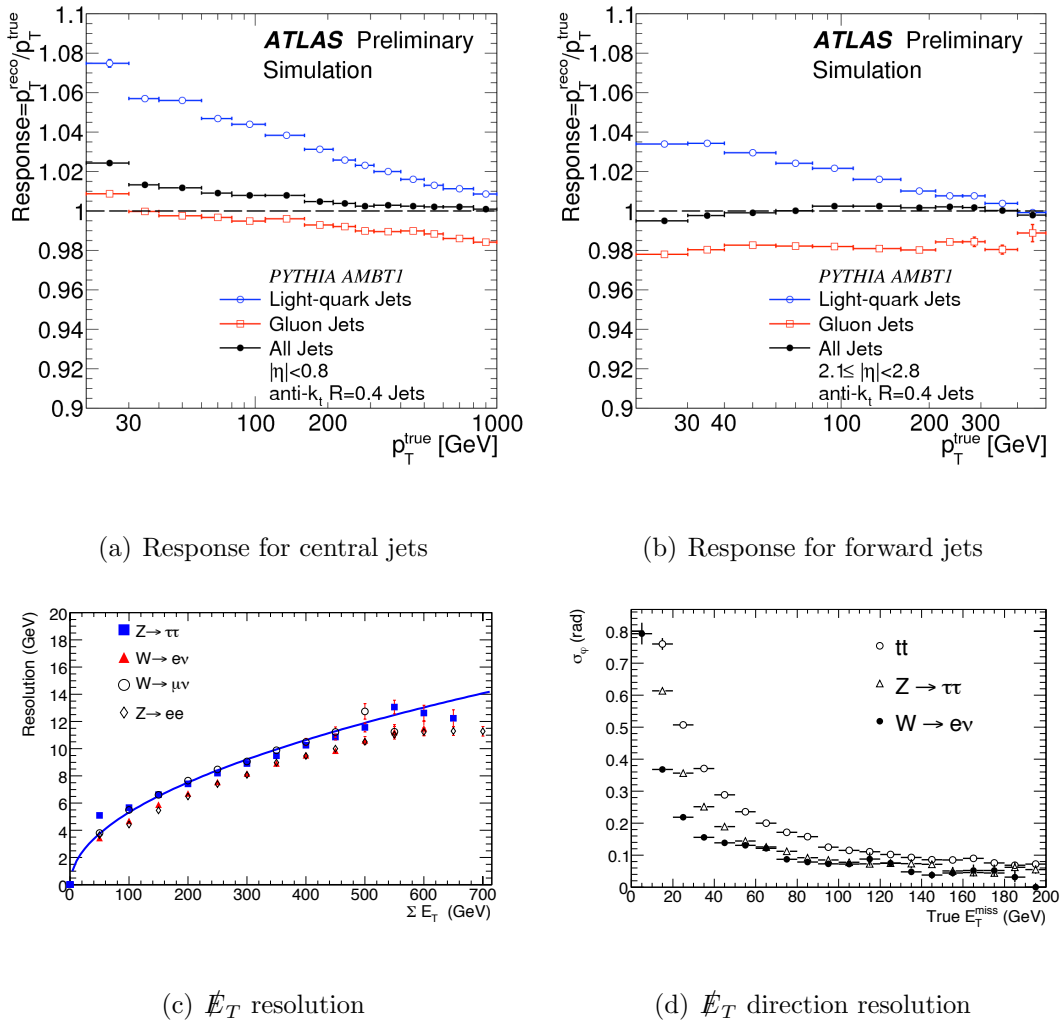


Figure 3.13: Nominal performance of the ATLAS Hadronic calorimeter [10].



Figure 3.14: A picture of the accordion structure used in the ATLAS electromagnetic calorimeter [1].

which in turn produces an electrical signal in the Kapton electrodes, and results in a measurement of the deposited energy. The total thickness of the EM calorimeter is  $> 24$  radiation lengths over the entire coverage.

To provide precision shower shape, direction, and particle identification, the EM calorimeter is segmented longitudinally into 3 layers, and in  $\eta$  and  $\phi$  with a granularity of roughly  $0.05 \times 0.05$ , which depends on  $\eta$  and  $\phi$ . The resulting number of channels is  $\sim 190,000$ . Due to the considerable amount of material in the ID (roughly 2 radiation lengths), it is necessary to correct for photon and electron energy loss and showering prior to the calorimeter. To account for this, a presampler, which consists of a finely segmented active liquid argon layer, is placed before the entrance to the EM calorimeter.

### 3.4.2 Hadronic Calorimeter

The ATLAS hadronic calorimeter is a sampling calorimeter that uses three technologies to handle the increasing particle flux rates with increasing  $|\eta|$ . In the barrel, for  $|\eta| < 1.7$ , iron is used as the absorber, while scintillating tiles are used as the active material. This region is further subdivided into two regions, the barrel ( $|\eta| < 1.0$ ) and the extended barrel ( $0.8 < |\eta| < 1.7$ ) in order to allow access for services and cables. In the endcap, between  $|\eta| = 1.5$  and  $|\eta| = 3.2$ , copper plates are used as the absorber, while liquid argon is used as the active material, as it has much better performance than the scintillating tiles in the face of high occupancy.

In the very high particle flux of the forward region up to  $|\eta| = 4.9$ , a hybrid copper/tungsten system is used. A metal matrix filled with concentric rods and tubes made of the absorbing material is filled with liquid argon and a high voltage is applied to the rods. In all cases, incident particles interact with the absorber material, producing a hadronic shower in the active material that is read as either scintillation or particle ionization by the readout electronics.

In order to reduce punch through to the muon system and provide a precise measurement of the energy of the very high energy jets produced at the LHC, the ATLAS hadronic calorimeter is 10 interaction lengths or larger over its entire coverage. Granularities of  $(0.1 - 0.2) \times (0.1 - 0.2)$  combined with between 3 and 4 longitudinal sampling layers provide sufficient resolution for measuring showering development and location while limiting readout complexity and cost.

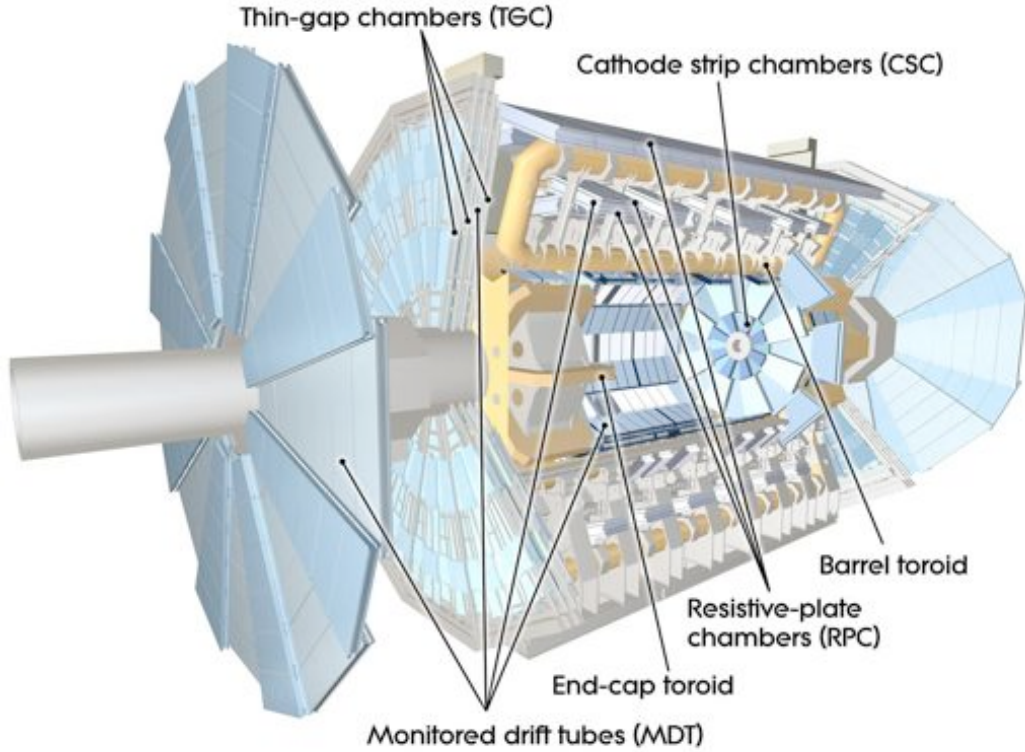


Figure 3.15: A diagram of the ATLAS Muon Spectrometer [1].

### 3.5 Muon Spectrometer

The ATLAS Muon Spectrometer provides particle tracking up to  $|\eta| = 2.7$  and triggering up to  $|\eta| = 2.4$ . Precision measurements in the magnetic bending direction are made by gas drift tubes, called Monitored Drift Tubes (MDT), while second coordinate information and triggering are provided by Resistive Plate Chambers (RPC) in the barrel and Thin Gap Chambers (TGC) in the endcap. In the inner most layer of the forward region ( $2.0 < |\eta| < 2.7$ ), Cathode Strip Chambers (CSC) are used to handle the very high particle multiplicity. A diagram of the ATLAS Muon Spectrometer is shown in Figure 3.15.

The nominal performance of the Muon Spectrometer is shown in Figure 3.16. The muon spectrometer provides stand alone tracking efficiency of over 90% for muons above 10 GeV, with a resolution of roughly 4% up to 150 GeV. The factors that go into the momentum resolution are shown in Figure 3.17. Below 10 GeV, many muons do not make it through the calorimeter (where they lose, on average, 4 GeV) or are bent out of the fiducial volume of the detector by the 4 T field from the toroidal magnets. Between 10 GeV and 20 GeV, the resolution is dominated by energy loss in the calorimeter and other material. Between 20 GeV and roughly 200 GeV, the resolution is dominated by multiple scattering. Finally, very high  $p_T$  muon resolution is dominated by hit resolution, which is primarily due to misalignments. At nominal alignment, the expected resolution of the muon spectrometer is 10% at 1 TeV. A measurement from data of the muon resolution using  $Z \rightarrow \mu\mu$  decays is presented as part of this analysis. Finally, it is also worth noting the structure in  $\eta$ . Near  $|\eta| = 0$ , performance is reduced by a gap in the muon spectrometer for services. In the transition region near  $|\eta| = 1.3$ , performance is reduced due to the spacing between the endcap and barrel, as well as poor bending power in the region between the endcap and barrel toroids.

### 3.5.1 Monitored Drift Tubes

As will be discussed in section 3.6, the bending direction in the Muon Spectrometer is in  $\eta$ , which makes a very precise measurement of the particle trajectory in  $\eta$  crucial to measuring muon momentum at high  $p_T$ . Monitored Drift Tubes (MDT) are used over almost all of the coverage to perform this measurement. Each tube is made of

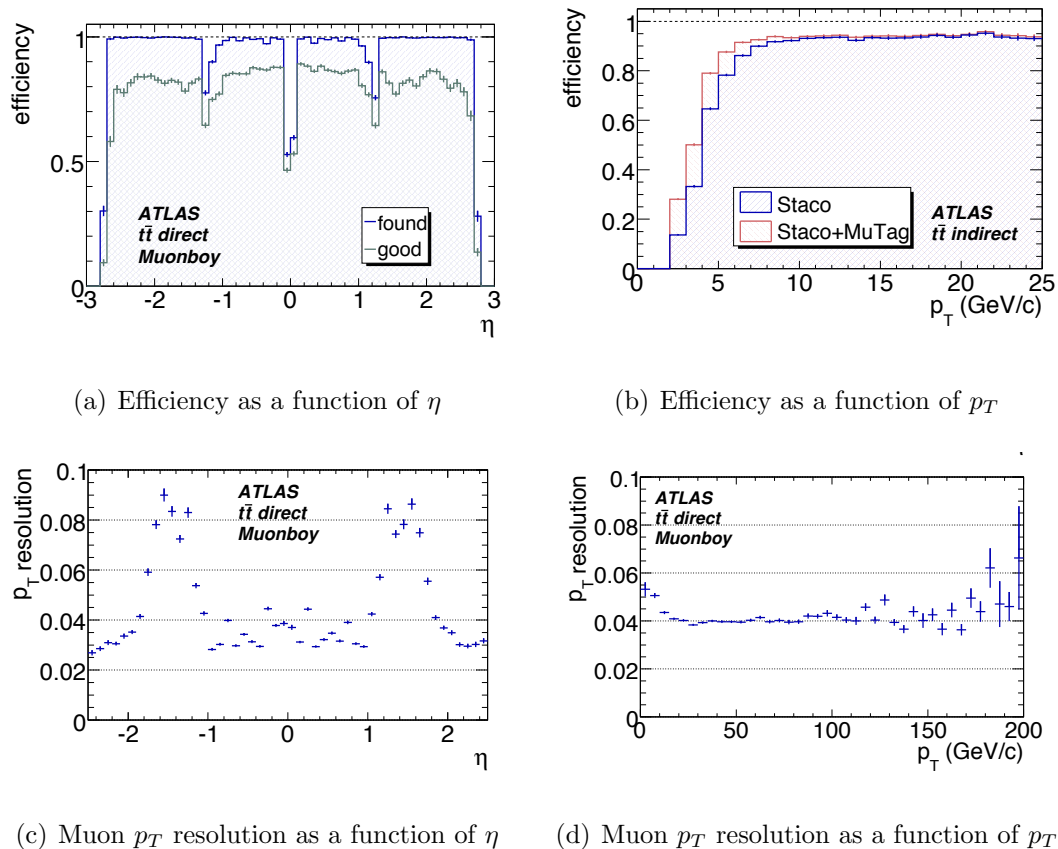


Figure 3.16: Nominal standalone performance of the ATLAS muon spectrometer [10]. In the efficiency plots, a good muon is one passing standard quality cuts.

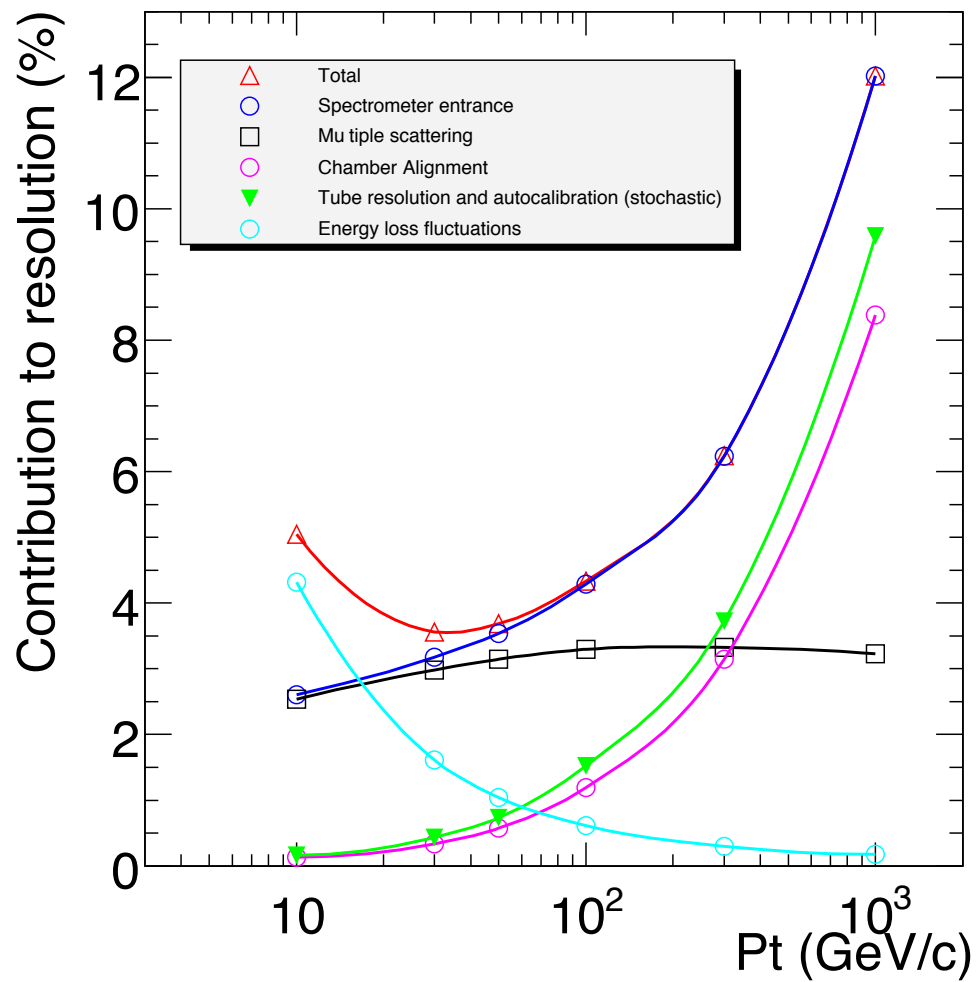


Figure 3.17: Factors influencing standalone muon resolution [10].

aluminum with a diameter of 30 mm, a wall thickness of 400  $\mu\text{m}$ , and a variable length from 70 cm to 6.3 m depending on the location. At the center of each tube a wire of 50  $\mu\text{m}$  W-Re is run and held at a nominal voltage of 3 kV. The tubes are filled with a constantly circulated gas mixture of 93% Argon and 7% CO<sub>2</sub> held at 3 bar absolute pressure, which yields a nominal maximum drift time of 700 ns. Charged particles incident on a tube ionize the gas mixture, and the electrons are driven by the charged wire. The readout electronics are used to measure the total deposited charge as well as the time of the leading pulse. The charge information is used to suppress noise, while the timing information is converted to a drift radius based upon calibrated RT relations, providing a single hit resolution of  $\sim 80 \mu\text{m}$ . As there is no information along the length of the wire, second coordinate information is added during pattern matching using information from the trigger chambers described in the next sections.

Individual tubes are constructed into chambers, an example of which is shown in Figure 3.18. Each chamber consists of a support structure surrounded on both top and bottom by three or four layers of tubes depending on the location. Tubes within neighboring layers are staggered by half a tube in order to reduce ambiguity in pattern matching. Optical alignment is used within the support structure of a single chamber in order to monitor for deformations and between chambers using sensors and patterns mounted to the surface of chambers in order to monitor inter-chamber alignment. The ultimate alignment goal is 30  $\mu\text{m}$  within a projective tower of chambers.

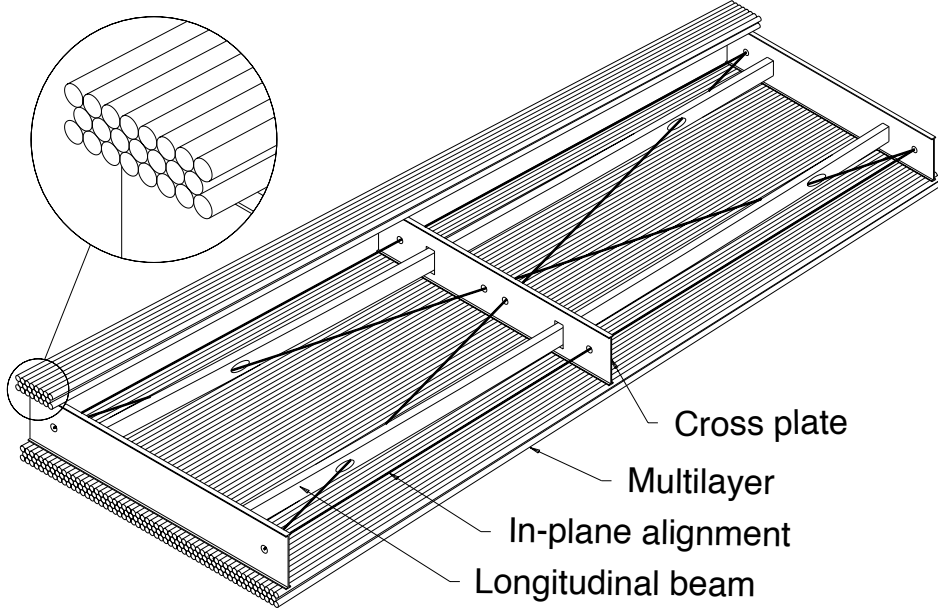
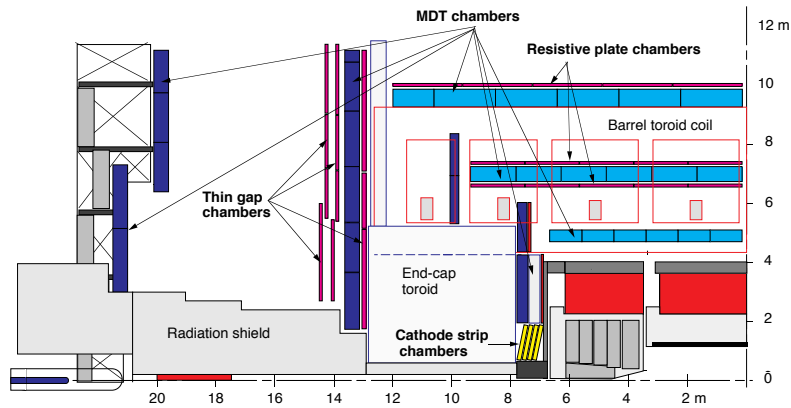


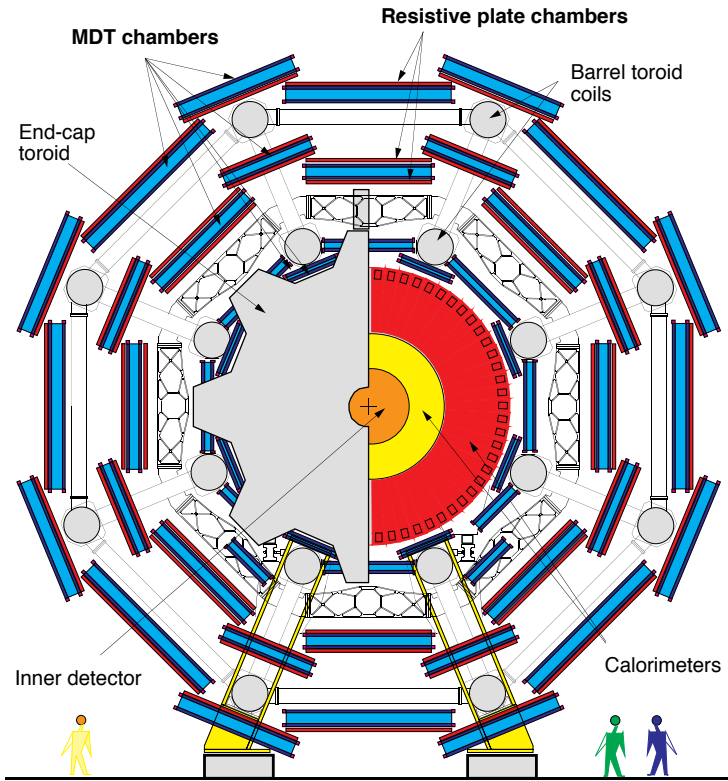
Figure 3.18: A diagram of a typical ATLAS MDT Chamber [21].

Chambers are then formed into the barrel and endcap muon spectrometers, according to the pattern shown in Figure 3.19. In the barrel ( $|\eta| < 1.0$ ), chambers are arranged in three layers at fixed  $R$  values of roughly 5 m, 7.5 m, and 10 m. As shown in Figure 3.19(b), there is slight overlap between adjacent chambers in the same layer, which provides full coverage in  $\phi$  except for some small regions at the bottom of the detector which are used for support structure. In addition, there is a small gap at  $\eta = 0$  for services and cables.

In the end-cap from  $|\eta| = 1$  to  $|\eta| = 2.7$ , chambers are arranged into a wedge shape called a sector, shown in Figure 3.20, and sectors are formed into a wheel, shown in Figure 3.21. Four wheels per side are placed at roughly  $z = 7$ m, 10m, 14m, and 22m, and are concentric with the beam axis, as shown in Figure 3.19(a). Note that in the



(a) Side View



(b) Transverse View

Figure 3.19: Chamber layout of the ATLAS Muon Spectrometer [21].



Figure 3.20: A picture of an assembled ATLAS Muon Spectrometer End-cap Sector, along with support structures [1].

inner most wheel, for  $|\eta| > 2.0$ , the MDTs are replaced with CSCs, which will be described in the section 3.5.2.

### 3.5.2 Cathode Strip Chambers

In the inner layer of the far forward region ( $2.0 < |\eta| < 2.7$ ), the large particle flux results in occupancy levels of MDT chambers that are untenable. Instead, in this region, Cathode Strip Chambers are used, which provide both precision and second coordinate information. The detector element of a CSC resembles a multiwire proportional chambers and is shown in Figure 3.22. Cathode strips with a readout pitch of 5.08 mm are located 2.54 mm from a series of anode wires with 2.54 mm pitch. The wires are held at high voltage and the gap filled with a mixture of 30% Ar,



Figure 3.21: A picture of an ATLAS Muon Spectrometer End-cap Wheel [1].

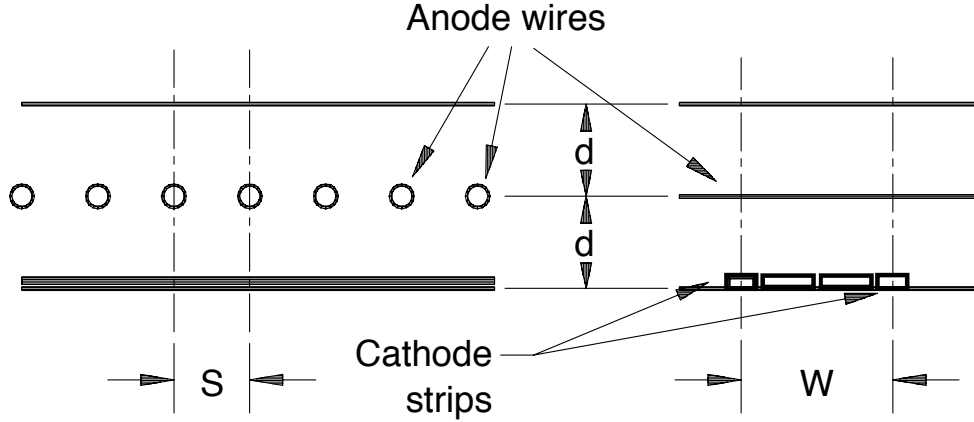


Figure 3.22: A diagram of an ATLAS Cathode Strip Chamber detector element [21].

50% CO<sub>2</sub>, and 20% CF<sub>4</sub>. Incident charged particles induce ionization which causes an avalanche to form on the anode wires and a charge to be induced on the cathode stripe readout. Charge is spread between neighboring strips, and interpolation allows a hit resolution of roughly 60  $\mu\text{m}$ . Short drift distances result in drift times of approximately 30 ns with a resolution of roughly 7 ns.

The CSCs replace the MDTs in the high  $\eta$  region of the inner MDT wheel. Two orthogonal layers are placed back to back in order to provide second coordinate information. As the geometry of the CSCs is such that they give best resolution when the incident particle is normal to the detector plane, the CSC layers are tilted with respect to the vertical, as shown in Figure 3.19(a).

### 3.5.3 Resistive Plate Chambers

Resistive plate chambers (RPC) are used to provide triggering and second coordinate information in the barrel ( $|\eta| < 1.0$ ). An RPC detector element consists of a pair of 2 mm resistive parallel bakelite plates forming a 2 mm gap which is filled with a mixture of tetrafluoroethane ( $C_2H_2F_4$ ) and  $SF_6$ . A strong electric field (typically 4.5 kV/mm) is applied which causes primary ionization electrons to produce an avalanche, which in turn produces a signal in the readout electronics. A detector element typically provides space-time resolutions of 1 cm  $\times$  1 ns.

Individual RPC strips are built into chambers with 2 pairs of overlapping layers of  $\eta$  strips (those parallel to the MDTs) and  $\phi$  strips (those perpendicular to the MDTs). Three layers of RPC chambers are then sandwiched against the MDT chambers are shown in Figure 3.19(b). In particular, RPC chambers are placed on the inner and outer faces of the middle barrel MDT layers, along with a third layer attached the the outer MDT barrel layer.

### 3.5.4 Thin Gap Chambers

Thin Gap Chambers (TGC) are used to provide triggering and second coordinate information in the end-cap ( $1.0 < |\eta| < 2.4$ ). The TGCs are designed as a multiwire proportional chamber with a wire-to-wire distance larger than the wire to cathode distance. A pair of graphite cathodes are spaced 2.8 mm apart with a series of 50  $\mu m$  wires run at a spacing of 1.8 mm down the middle of the gap. The wires are held at a voltage of approximately 3 kV, and the gap filled with a mixture of 55%  $CO_2$  and

45% n-pentane ( $n\text{-C}_5\text{H}_{12}$ ). Incident particles produce ionization in the gap which is drifted by the electric field of the anode wire. The small drift distance yields a very fast response, while segmentation of the cathode readout perpendicular to the wire configuration allows the second coordinate to be measured.

TGC chambers consist of multiple layers of detector elements layered with a separating honeycomb structure. As with the MDTs, chambers are built into sectors and then wheels which are attached flush against the MDT wheels as shown in figure 3.19(a). The inner layer consists of a single doublet of detector elements and is used only for second coordinate measurements. The middle layer consists of a triplet and two doublets which provide both triggering and second coordinate information during pattern matching.

## 3.6 Magnet System

The ATLAS magnet system is based around a solenoid providing bending power for the ID and three air core toroids providing bending power for the Muon Spectrometer. The solenoid system provides a central field of 2 T with a peak field of 2.6T, while the toroids provide a 3.9 T peak field in the barrel and a 4.1 T peak field in the end-cap. The resulting bending power as characterized by  $\int B d\ell$  is 2 to 6 Tm in the barrel and 4 to 8 Tm in the end-cap. A list of the properties of the magnet system is shown in Table 3.4.

Property	Solenoid	Barrel Toroid	End-cap Toroid
Inner diameter [ m ]	2.44	9.44	1.65
Outer diameter [ m ]	2.63	20.1	10.67
Length [ m ]	5.3	25.3	5
Total Weight [ tons ]	5.7	830	239
Number of coils	1	8	8
Turns per coil	1173	120	116
Current [ kA ]	7.6	20.5	20
Stored Energy [ MJ ]	38	1080	206
Peak Field [ T ]	2.6	3.9	4.1

Table 3.4: Properties of the ATLAS Magnet System [24].

### 3.6.1 Solenoid

The central solenoid is made of 1173 turns of Al/Cu/NbTi superconducting cable running between the ID and the EM Calorimeter. This generates a very strong and uniform field parallel to the  $z$  axis, which results in bending of charged particles in the  $\phi$  direction. It is cooled by a flowing helium at 4.5 K through tubes welded onto the windings. As the resolution of the calorimeter is heavily dependent on the amount of material between it and the interaction point, extreme effort has been made to minimize the amount of material in the solenoid. In particular, the LAr calorimeter and solenoid share a single vacuum vessel while the coil itself is designed to be as thin as possible. A picture of a test insertion of the solenoid into its resting place inside the EM calorimeter is shown in Figure 3.23.

### 3.6.2 Toroids

The toroids are designed to provide sufficient bending power for the ATLAS muon spectrometer to measure the momentum of a 1 TeV muon to 10%. Despite the high



Figure 3.23: A picture of a test insertion of the ATLAS solenoid into the ATLAS EM Calorimeter [1].

precision of the ATLAS MDTs, the required bending is of the order of a few  $T \cdot m$ . For lower  $p_T$  measurements, however, it is desirable to reduce the amount of material in the muon spectrometer, so as to reduce the effects of multiple scattering. The result is a set of air core toroids that provide a strong magnetic field over a large bending volume.

There are three air core toroid magnets in the ATLAS magnet system which provide bending power for the muon spectrometer: a single barrel toroid and two end-cap toroids. All three toroids consist of eight coils assembled symmetrically around the beam axis. This configuration produces a magnetic field in  $\phi$  and therefore bending in  $\eta$ . A picture of the barrel toroid is shown in Figure 3.24, and a picture of the end-cap toroid is shown in Figure 3.25. The bending power as a function  $\eta$  is shown

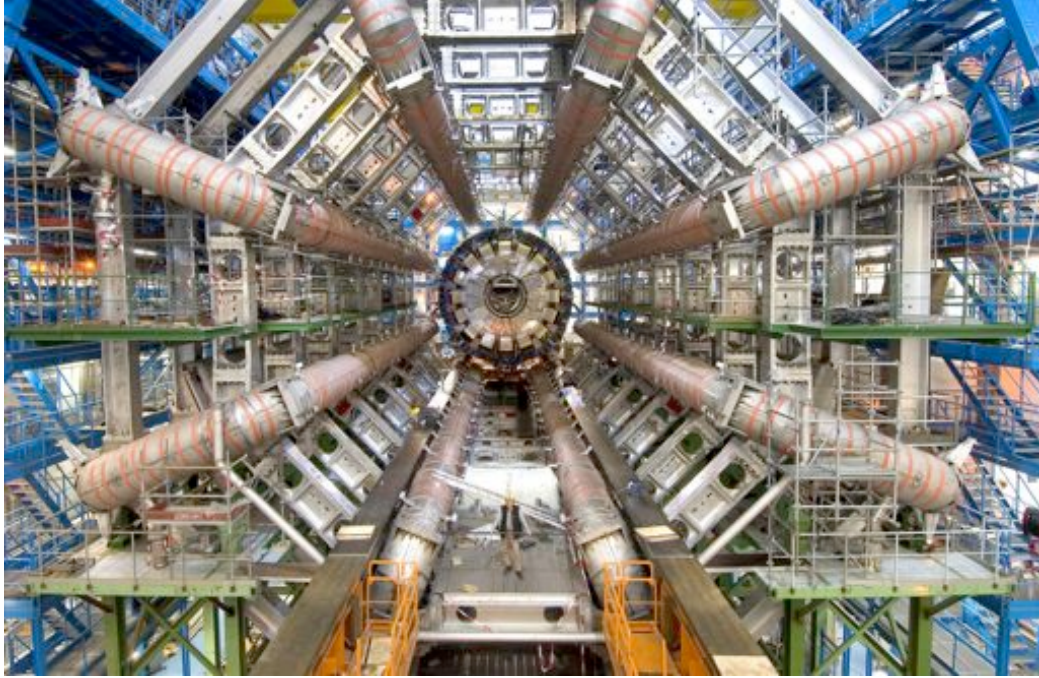


Figure 3.24: A picture the ATLAS Barrel Toroid with support structure [1].

in Figure 3.26.

The barrel toroid encloses the middle layer of the barrel MDTs, as shown in Figure 3.19(b), while the end-cap toroid is located between the inner and middle MDT end-cap layers, as shown in Figure 3.19(a). Thus, in the barrel bending occurs over the range between the inner and outer layers, while bending in the end-cap only occurs between the inner and middle layers. In the transition region between the barrel and end-cap ( roughly  $|\eta| = 1.0$  to  $|\eta| = 1.4$  ) the field becomes a very complicated superposition of the fields due to the end-cap and barrel toroids. In particular, the bending power,  $\int B d\ell$ , becomes small or even negative in some regions of the transition region. To somewhat reduce this effect, the coils of the end-cap toroid are rotated at  $22^\circ$  relative to the coils of the barrel toroid.



Figure 3.25: A picture the ATLAS End-cap Toroid [1].

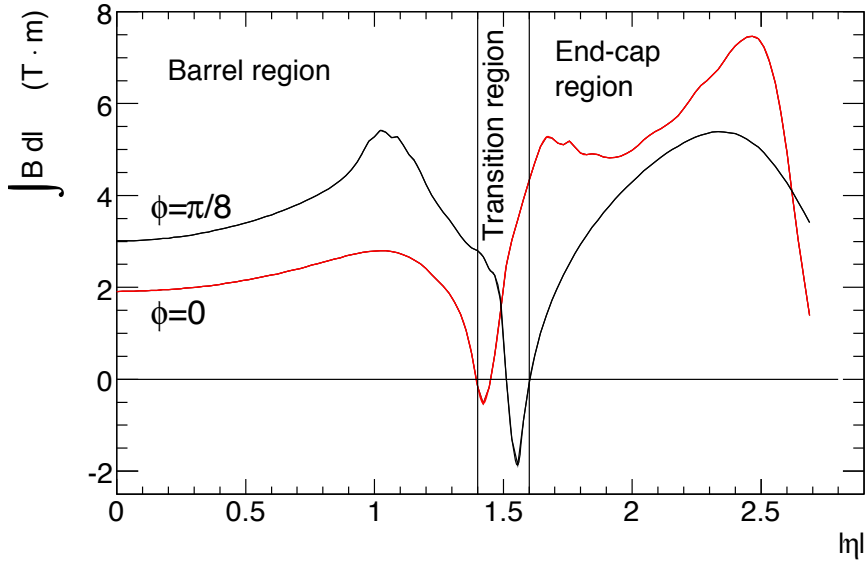


Figure 3.26: Bending power as a function  $\eta$  of the ATLAS toroid magnets [10].

### 3.7 Combined Muon Tracking

The design of the ATLAS detector provides particularly good measurements of muon properties due to the ability to perform muon tracking in both the inner detector and the muon spectrometer. Muons are identified by matching inner detector tracks to calorimeter clusters matching the properties of minimum ionizing particles (calorimeter tagged muons), by matching inner detector tracks to segments in a single chamber of the muon spectrometer (segment tagged muons), or by matching inner detector tracks to tracks in the muon spectrometer (combined muons). Calorimeter tagged muons are useful for muons in the very low  $p_T$  range ( $< 5$  GeV) which do not always make it through the calorimeter. Segment tagged muons are useful in the low  $p_T$  range ( $< 10$  GeV), where muons tend to make it through the calorimeter but can be swept out of the spectrometer acceptance due to the magnetic field. They are also

useful for recovering efficiency in regions where services or support structures block the inclusion of all three layers of the muon spectrometer. Finally, combined muons provide the best resolution with the lowest fake rate and thus are the best choice when tagged muons are not necessary. As this analysis uses high  $p_T$ , high quality muons, only combined muons are used.

Combined muons can be formed in a number of different ways. When an inner detector track and a muon spectrometer track are matched, the entire track may be refit using the hits of both sub-tracks. Alternatively the track parameters of the combined track may be determined by performing a  $\chi^2$  minimization using the inner detector and muon spectrometer tracks as inputs, thus forming combined parameters which are a weighted sum of the sub tracks. While ATLAS uses both pattern recognition techniques, due to technical issues with the implementation of the first technique, this analysis uses only the second technique.

Measuring the muon momentum and track parameters twice using both the inner detector and the muon spectrometer has a number of beneficial properties. First, by comparing the two sub track properties, it was possible to perform calibration and resolution measurements using only cosmic rays. Second, each sub-detector has peak performance in different  $p_T$  regimes, which greatly improves the resolution of the combined track. At relatively low  $p_T$  (less than roughly 40 GeV), the momentum measurement of the muon is dominated by multiple scattering and energy loss due to material. As the inner detector has much less material in front of it than the muon spectrometer, it provides the best resolution measurement in this range. However,

at higher  $p_T$ , the dominant uncertainty comes from the measurement of the muon curvature. As the muon spectrometer air core toroids have very large bending power due to the large field and bending distance, and the MDT's have very good resolution, the muon spectrometer provides the best resolution measurement at high  $p_T$ .

The performance of combined muons is shown in Figure 3.27. Combined tracking alleviates some of the problems seen in standalone tracking, shown in Figure 3.16. Although there is still a noticeable efficiency drop in the crack region near  $|\eta| = 0$  and the transition region near  $|\eta| = 1.4$ , the resolution in the those regions is much better. Further, the performance at low  $p_T$  is much improved due to the inclusion of the inner detector.

## 3.8 Trigger

The ATLAS trigger is designed around a three tiered real time event filtering system that reduces the event rate from the nominal collision rate of 40 MHz to a write to tape rate of roughly 200 Hz. The first tier, called level 1, is implemented as hardware pattern matching, which gives it very fast computation speed and low latency. The second tier, called level 2, consists of a dedicated cluster of commodity computers running simplified versions of the tracking and pattern matching algorithms used in reconstruction on subsets of the total detector data for the event. The final tier, called the event filter, is run on a larger cluster of commodity computers and is responsible for running reconstruction on the full event in order to provide a final acceptance or rejection of the event.

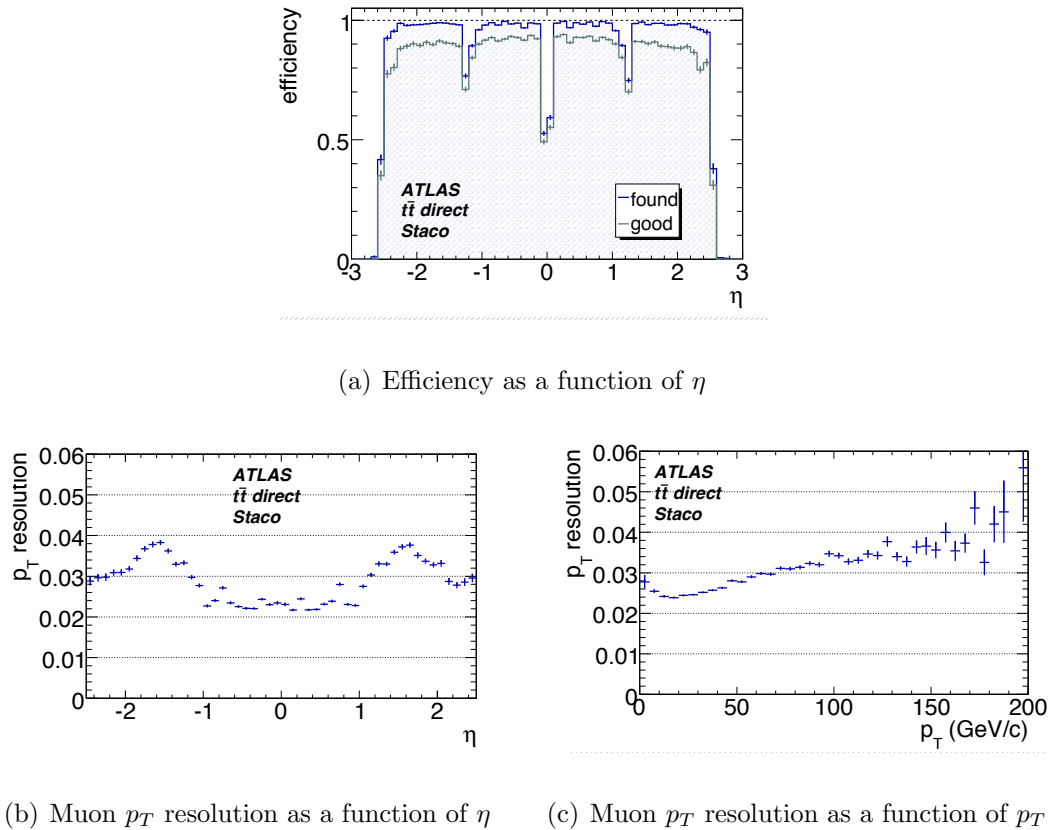


Figure 3.27: Nominal combined performance of the ATLAS muon spectrometer [10]. In the efficiency plot, a good muon is one passing standard quality cuts.

### 3.8.1 Level 1 Trigger

The level 1 trigger is responsible for reducing the nominal collision rate of 40 MHz to a front end electronics readout rate limited accept rate of 75 kHz with a latency of less than  $2.5\ \mu\text{s}$ . It does this by performing hardware pattern matching with a subset of the available detector data. High transverse momentum muons are identified using RPCs in the barrel and TGCs in the end-caps. Hits within a projective road in  $\eta$  and  $\phi$  are compared with pre-computed patterns to determine the muon  $p_T$  threshold. In the calorimeter, energy and trajectories are determined by a sliding window algorithm which reduces the granularity of the detector. As with the muons, the results are used to form thresholds passed by the objects. The total energy and missing energy are computed by summing over the calorimeter towers.

In addition to identifying events of interest, the level 1 trigger also determines the bunch crossing as well as Regions of Interests (RoIs), where there is activity that caused a trigger to be passed, which are crucial for the level 2 trigger. During the level 1 accept latency, the readout of the detector is buffered in pipeline memories on the front end readout electronics. As the total amount of information is very large (roughly  $10^7$  channels per 25 ns of buffering time), it is crucial that the level 1 latency be kept as low as possible.

### 3.8.2 Level 2 Trigger

Once an event is selected by the level 1 trigger, the detector data is moved from the front end pipelines to roughly 1700 read out buffers (ROBs), which store the data

during the level 2 latency. The level 1 trigger then indicates to the level 2 trigger the RoIs in the event, and the level 2 reads out the data from the ROBs for those regions. This readout strategy dramatically decreases the amount of data that must be moved and processed by the level 2.

The level 2 trigger is then responsible for reducing the event rate from the level 1 accept rate of 75 kHz to a level 2 accept rate of roughly 1 kHz. The level 2 trigger operates with the full granularity of the detector, but only on the ROI's identified by the level 1 trigger. In both muon and calorimeter triggers, this results in a much sharper  $p_T$  measurement, yielding a steeper trigger turn on curve. For muons, the level 2 trigger achieves this by adding measurements of the muon  $p_T$  from the MDTs as well as from the ID. For electrons, hadrons, and taus, performance is gained by using the full granularity of the calorimeter combined with track matching from the ID. Minor refinements can be made to photons, jets, and energy sum triggers by using the full calorimeter resolution as well as more sophisticated calibrations.

### 3.8.3 Event Filter

Following a level 2 accept, the full event data is moved from the ROBs to the final trigger stage, called the Event Filter (EF), in a process known as event building. The EF uses the full detector information and runs offline reconstruction algorithms in order to reduce the final accept rate to roughly 200 Hz. Events accepted by the EF are then recorded for offline processing and made part of the ATLAS data set.

### 3.8.4 Trigger Menu and Performance

The trigger rate compared with cross sections for common physics processes at nominal running conditions is shown in Figure 3.28. At nominal conditions, even  $W$  and  $Z$  events must be prescaled in order to accommodate the very high rate of production. During 2010, production rates were much lower due to the lower center of mass energy and the factor of 50 lower instantaneous luminosity. The rate of muon triggers expected at instantaneous luminosity of  $10^{31} \text{ cm}^{-2} \text{ s}^{-1}$  (20 times lower than what was achieved in 2010) is shown in Figure 3.29. To accommodate the trigger budget by stream, shown in Figure 3.30, the main muon physics trigger for 2010 required a threshold of 13 GeV, which yields a rate of roughly 20 Hz. Trigger performance, in both the muon and electron channels, was measured in data using  $Z \rightarrow \ell\ell$  decays and will be presented as part of this analysis.

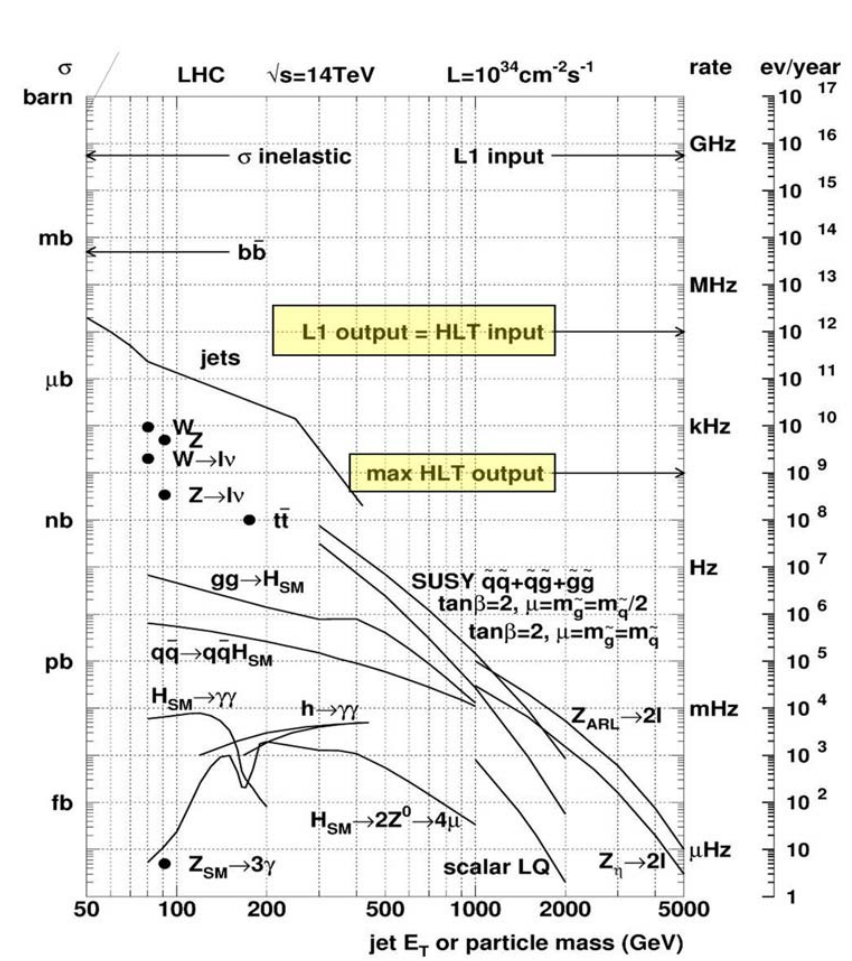


Figure 3.28: ATLAS trigger rate in comparison with various physical processes at nominal running conditions [10].

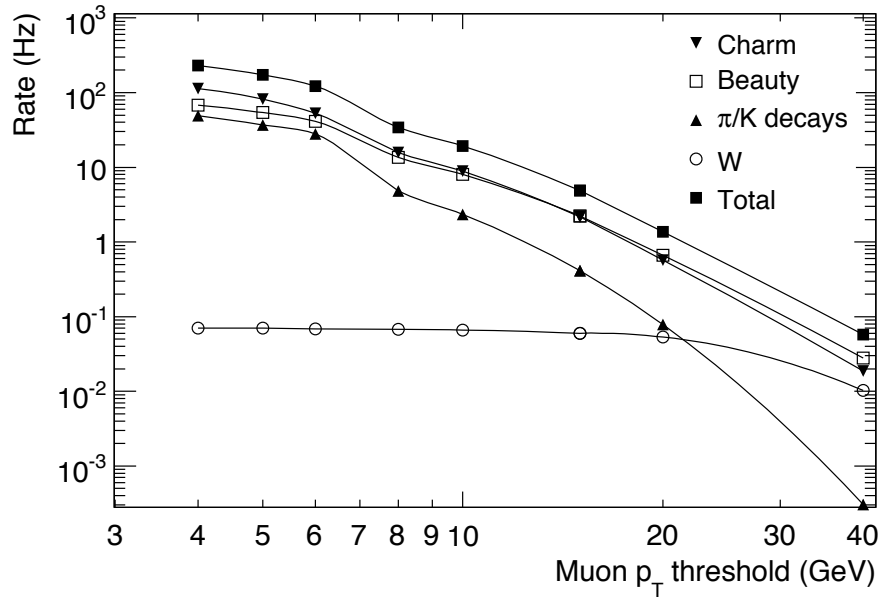


Figure 3.29: Expected muon trigger rates at instantaneous luminosity of  $10^{31} \text{ cm}^{-2} \text{ s}^{-1}$  [10]. Note that 2010 saw a maximum instantaneous luminosity of  $2 \times 10^{32} \text{ cm}^{-2} \text{ s}^{-1}$ , 20 times what is shown here.

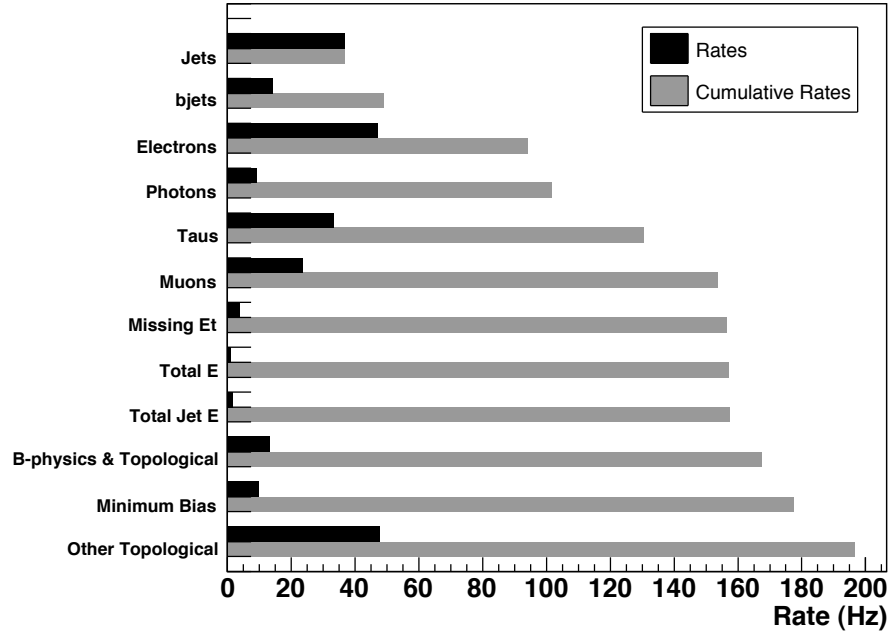


Figure 3.30: Nominal trigger budget by stream for 2010 running [10].

# Chapter 4

## Software

ATLAS employs a complex and sophisticated software framework in order to record, reconstruct, and analyze data. In general, offline software is divided into *production*, which is typically run and maintained centrally, either on the grid or at the CERN computing facility, and *analysis*, which is typically run and maintained by individual users or groups on their local computing facilities. In section 4.1, a brief overview of the ATLAS computing model is given. In sections 4.2 and 4.3 four software packages related to trigger, performance, and analysis are highlighted. Note that these sections contain implementation details that are not essential to a general understanding of the analysis.

### 4.1 ATLAS Computing Model

The ATLAS computing model [22] describes the development of the software and hardware required to efficiently reconstruct and distribute data recorded by the AT-

LAS detector. The software consists of all so-called *offline* software which is run after the data has been read out of the detector and recorded to disk, as opposed to the software which runs the trigger system and is run in real time (and so called *online*). The hardware consists of a distributed tiered system involving computing resources at institutes and universities around the world, which is tied together by a cloud computing system known as the LHC Computing Grid (LCG) [62].

Data read out from the detector is subject to a number of additional processing steps, each of which produces derived datasets with a different format and information content. Events selected by the Event Filter, described in section 3.8, are recorded in the RAW format, which consists simply of the byte-stream style output of the subdetectors without an object oriented representation, and is roughly 2 MB/event. Reconstruction, which uses pattern matching algorithms to convert energy depositions and hits to particle trajectories, is then run on the RAW data and produces Event Summary Data (ESD) and Analysis Object Data (AOD) data files. The ESD format is roughly 500 kB/event, and consists of all needed information for physics analysis (such as basic object information), as well as more in depth information about detector hits and energy depositions needed for calibration and performance measurements. The AOD format is roughly 100 kB/event and contains basic information needed for physics analysis. Typically analysis or analysis group specific ntuples are produced of varying size and detail from the ESDs and AODs for final processing.

To provide the facilities for processing, storing, and distributing ATLAS data, a tiered cloud based system known as the grid is used. ATLAS computing resources are

located at institutional and university facilities around the world, and each facility is assigned to a tier based upon available resources. The ATLAS experiment has a single Tier 0 site, located at CERN, which is responsible for storing and distributing the RAW data read out from the detector, as well as performing first pass reconstruction. For each region (typically a continent or large country), a Tier 1 facility is responsible for storing the derived ESD and AOD datasets and providing computing resources for reprocessing of the RAW data and analysis of the hosted data. Tier 2 facilities are generally more specialized facilities that offer region specific computing and storage needs for things such as simulation, calibration, and analysis. Finally, Tier 3 facilities are usually dedicated the analysis needs of a given university or institution. An example facility for each tier is shown in Table 4.1.

Facility Type	Location	Approximate Storage	Approximate CPU
Tier 0	CERN	4 PB disk / 9 PB tape	14k cores
Tier 1	BNL	5 PB disk / 3 PB tape	12k cores
Tier 2	Harvard/BU	500 TB disk	2,200 cores
Tier 3	Harvard	130 TB disk	300 cores

Table 4.1: Example computing facilities for each tier level at CERN, Brookhaven National Lab (BNL), Harvard, and Boston University (BU).

## 4.2 Production Software

In ATLAS, production software refers to software that is run and maintained centrally (either at the Tier 0 or on the grid) in order to satisfy certain requirements of the collaboration, and includes software for doing reconstruction, data preparation and validation, and simulation. This section highlights three pieces of production software: `TrigNavigationSlimming`, which is used to reduce the trigger information for derived

dataset production; `TriggerObjectMatching`, which is used to associate offline and online objects for analysis and derived dataset production; and `MuonIDNtupleMakers`, which produces derived datasets for muon performance studies.

### 4.2.1 Trigger Navigation Slimming

During reconstruction, the full information about the state of the trigger is recorded in a tree structure called the trigger navigation. A simple example of the trigger navigation is shown in Figure 4.1. For each event, a tree is built with a node whose daughters correspond to each Region of Interest found at level 1 (see section 3.8). The daughter of each node, then, represents the seeded algorithms for that RoI. For example, the muon trigger might start with an algorithm that builds a track in the inner detector. If a track is found with sufficient  $p_T$  and quality within the RoI, that algorithm will seed another algorithm that searches for a muon track in the muon spectrometer, and assuming that is successful, another algorithm which combines them. In this way, each node of the tree represents a trigger algorithm that was run at some stage of the trigger. Further, each node contains information about the result of the algorithm and the full properties of the reconstructed object.

While this information is very useful for everything from trigger debugging and validation to analysis, it is also very costly to store. On average, the trigger navigation information is roughly 10 kB/event, and can be much larger for complicated events. Compared with the design size of 100kB/event for AODs, this is simply too large to store for analysis. Further, much of the information is not necessary at every step: intermediate nodes, for example, might be unnecessary for calculating the trigger

efficiency of a given object. The `TrigNavigationSlimming` algorithm [68] is designed to remove trigger elements and features from the navigation structure during derived dataset production in order to reduce size and remove corrupted elements from the data file.

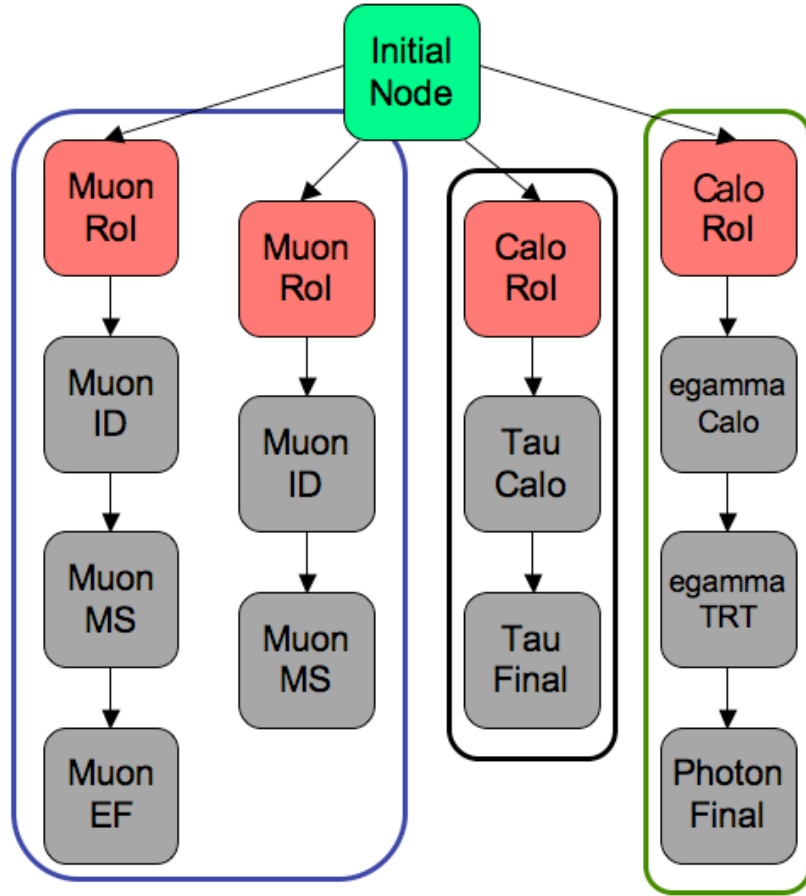


Figure 4.1: A simple example of the trigger navigation structure. Each grey box represents another step in the trigger algorithm.

A high degree of flexibility and customization is crucial to the trigger navigation slimming package in order to allow it to be used for a variety of derived datasets. This

list of possible options is provided in Table 4.2. Trigger algorithms to be saved or removed can be specified in a number of ways. Streams include the output of specific subdetector triggers, such as the muon or calorimeter streams. Groups refer to similar physics based triggers, such as the group of all single muon triggers. Chains refer to a complete trigger, such as mu15, which is the 15 GeV muon trigger. Features refer to the objects created by trigger algorithms that store the reconstructed trigger object properties, such as trigger electron. Nodes can additionally be specified for removal based upon their location within in the tree (if they are terminal or not), whether the chain they belong to passed or failed, or by the RoI which seeded them.

Option Name	Description
PrintTree	Prints navigation structure for debugging
Squeeze	Remove all nodes which are not initial, RoI, or terminal
ProtectChains	Do not remove final nodes of subchains
RemoveFeatureless	Remove nodes which did not build trigger objects
RemoveGhosts	Remove nodes which were placed in the ghost state
RemoveFailedChains	Remove nodes from chains which were not passed
WriteTree	Write the slimmed navigation structure to the output file
ProtectOtherStreams	Only remove explicitly listed streams
StreamInclusionList	Remove streams not belonging to this list
StreamExclusionList	Remove streams on this list
GroupInclusionList	Remove groups not belonging to this list
GroupExclusionList	Remove groups on this list
ChainInclusionList	Remove chains not on this list
ChainExclusionList	Remove chains on this list
FeatureInclusionList	Remove features not on this list
FeatureExclusionList	Remove features on this list
BranchInclusionList	Remove RoI's not on this list
BranchExclusionList	Remove RoI's on this list

Table 4.2: Run-time customizable options for the TrigNavigationSlimming algorithm.

The most challenging aspect of slimming the navigation is the proper propagation of information. For example, imagine a chain consisting of an inner detector tracking algorithm, a muon tracking algorithm, and a combined tracking algorithm. When slimming the first two, it is necessary to propagate the feature links to the reconstructed trigger object properties from the first two nodes to the combined node in order to avoid corrupting the output of the trigger algorithm. Further, many analysis tools, such as `TriggerObjectMatching` discussed in section 4.2.2, expect the terminal node of each chain to not be removed, regardless of its state. The option ”ProtectChains” was offered to ensure the usabilities of these tools on derived datasets.

As with all production software, it is of upmost importance that the `TrigNavigationSlimming` algorithm run smoothly and correctly over the very large amount of data processed by the production system. A nightly testing suite was built to test the package for run time problems and corrupted output. Each night, the slimming software is automatically run on a nominal dataset with the most up to date build of the production software and the run time output scanned for errors and other problems. The slimmed navigation structure is then queried and the answers compared with answers to queries from the non-slimmed navigation structure.

#### 4.2.2 Trigger Object Matching

Association of offline and online objects is important both for analysis, where analyzers are interested in determining trigger efficiencies and avoiding overlaps, and performance, where trigger experts are interested in debugging and validating the

trigger system. In the case of analysis, users typically want to know which physics object caused the event to be recorded. For example, in  $t\bar{t}$  events, there might be many high  $p_T$  leptons, and so it might be necessary to know if the event was triggered by an electron or a muon, or even which electron or muon. In the case of performance measurements, it is often necessary to compare the properties of objects as measured by the trigger and reconstruction system. As the trigger system is constrained by time, memory, and limited access to detector information, and the reconstruction is not, a comparison of the two provides valuable feedback as to the performance of the trigger software.

In practice, associating offline and online objects can be very tricky. First, there are a number of technical challenges related to retrieving and comparing two pieces of information stored in very different ways. Second, there are often detector related effects that are important when associating objects. For example, associating muons between offline and online might be done based upon their track parameters or upon the physical hits associated with their tracks in the two systems. Finally, the system must be implemented in a way that is flexible (in that the definition of association may be arbitrarily redefined), efficient, and easy to use. The `TriggerObjectMatching` code [69] is used both directly by analyzers and during the production of derived datasets.

## Object Retrieval

The first step to offline/online object association to retrieve the objects from the trigger navigation (described in section 4.2.1). The mechanism for retrieving trigger

objects from the navigation is provided by a separate tool called the `TrigDecisionTool`, and unfortunately is not the same for all types of trigger objects. In particular, there are three distinct ways for trigger objects to be retrieved from the navigation. In the simplest case, directly attached classes, it is possible to request the objects directly from the `TrigDecisionTool`. In the second case, container attached classes, it is necessary to request a container of the class requested. For example, if one wishes to access objects of type `TrigMuonEF`, it is necessary to request objects of type `TrigMuonEFCContainer` and flatten the resulting container. Finally, objects from the level 1 trigger are stored in a different structure that is accessed through the objects they seed.

To present a unified interface to the user regardless of the type of object, `TriggerObjectMatching` utilizes compile time resolution with trait classes. Consider, for example, if requests to the matching framework were passed directly to the `TrigDecisionTool`. Directly attached classes would work, but if, for example, the user requested associated objects of type `TrigMuonEF`, the request call to the `TrigDecisionTool` would fail as the correct call is for objects of type `TrigMuonEFCContainer`. Similarly, calls for level 1 objects would also fail. Instead, a trait class is kept for all trigger objects. Consider the following code:

```
struct DirectAttached {};  
  
struct ContainerAttached {};  
  
struct AncestorAttached {};  
  
template<typename T>
```

```
struct ClassTraits {  
    typedef DirectAttached type;  
};
```

By default, `ClassTraits<T>::type` evaluates to `DirectAttached` for all classes `T`. It is then possible to specialize the `ClassTraits` struct for container attached and level 1 objects. For example:

```
template<>  
struct ClassTraits<TrigMuonEF> {  
    typedef ContainerAttached type;  
};
```

will result in the resolution of `ClassTraits<TrigMuonEF>::type` to `ContainerAttached`. A similar approach is used for level 1 objects.

Once the trait classes are built, a `retrieveObjects` function may be written with the attachment type as an argument, and the correct procedure (directly retrieving, flattening, etc.) may be implemented for each type using function overloading. Note that because typedefs and function overloading are evaluated at compile time, it is possible to present a unified interface to the users of `TriggerObjectMatching` for all trigger types, even if the direct retrieval function for the type requested are not implemented by `TrigDecisionTool`. This is a powerful feature that completely insulates the user from the inner workings of the `TrigDecisionTool` and the trigger navigation.

## Distance Definition

Once the required trigger objects are retrieved, it is necessary to determine which trigger objects are associated with which reconstruction objects. To do this association, the user is allowed to specify a generic class that evaluates the distance between objects. This class can be generic to multiple objects, or can be specific to only the pair of objects under study. Because a class is supplied, the distance definition can depend on any properties of the two objects, and even on external tools such as detector conditions, alignment parameters, and other objects in the event.

By default, if no distance class is specified by the user, association is done based upon  $\Delta R = \sqrt{\Delta\eta^2 + \Delta\phi^2}$  of the two objects. However, even this calculation is not as simple as it would seem. For example, for muon trigger objects, the muon parameters are measured with respect to different points in the detector for different trigger algorithms, and thus must be compared to different parameters of the offline object based upon the trigger algorithm being used. Similar, electron  $\eta$  and  $\phi$  are best determined by the track parameters in some algorithms and best by the cluster parameters in others. To determine the appropriate way to calculate the default  $\eta$  and  $\phi$  of a trigger object, compile time resolution and class traits are used as in object retrieval. This is again a powerful technique which means that objects can be associated even if nothing analogous to  $\eta$  and  $\phi$  exists, so long as a relevant distance class is defined.

### 4.2.3 Muon ID Ntuple Makers

In the fall of 2009, the first collisions at the Large Hadron Collider led to a need for a quick ability to process and analyze collision data for the first time. While a number of ntuple formats were being developed, only a small handful were usable on the first data. Muon ID Ntuple Makers [67] was developed starting in mid 2009 and then continuing throughout 2010 as a lightweight and easy to run package for producing ntuples from ATLAS collision data for early muon based analysis and official performance measurements of the Muon Combined Performance (MCP) group. Called MCP ntuples, the data format was focused on very detailed and low level information about reconstructed muons and the muon trigger system.

The heart of the package is the `NtupleMakerBase` class, which is responsible for managing writing output variables to disk. For each physics object, an ntuple dumper was produced, which converted relevant quantities from ESD datasets into ntuple variables. The available dumpers are listed in Table 4.3. Basic generic information about the events including how they were reconstructed, which run and luminosity block they are from, and the name of the file run over is dumped for each event. Basic information is dumped for calorimeter clusters, electrons and photons, jets, missing energy, and displaced and primary vertices. Detailed information is dumped for muons, inner detector tracks, muon hits and segments, muon trigger, and, in simulated events, the truth record. This trade off between space and detail level allows the ntuples to be used for performance and basic muon analyses without overloading the computing and storage resources of ATLAS. The current ntuples are roughly 100kB/event for

2010 collision data, with a size that depends heavily on beam conditions.

Physics Object	Information
Event Info	Software version, filename, and event numbers
Calorimeter Clusters	position, energy, shower shapes
Electron/Photon	4 momentum, particle id, shower shapes
Jets	4 momentum, tagging weights, shower shapes
Missing Energy	x and y missing energy, and total energy
Muons	track parameters, hit and quality information
Muon RoI	parameters, trigger flags, and detector information
Muon Segments and Tags	position, direction, quality, and detector information
Muon Hits	position, timing, charge, drift radius, and detector
Inner Detector Tracks	track parameters, hit and quality information
Trigger	Trigger flags, collision timing and quality
Primary Vertex	position and associated track information
Displaced Vertex	position and associated track information
Truth (MC only)	full truth record for all particles

Table 4.3: Physics objects converted from ESD format to ntuple format by the MuonIDNtupleMakers package.

Ntuples are currently produced for the MCP group as part of central production, or may be produced by individual users on the grid. Auto configuration is used so that the ntuple makers correctly identify when they are running on AODs or ESDs, and when they are running on collision data, cosmic ray data, or Monte Carlo, and adjust their output accordingly.

### 4.3 ROOT Reader Framework

This section describes a physics analysis framework based around ROOT [71] that was designed and implemented at Harvard between 2008 and 2011 [67]. It attempts to address three main problems encountered by modern particle physics analysis. First,

too often the physics code is directly tied to the data format being used. While this is unavoidable to some degree, too much of a break down of the ideas of encapsulation result in code that is very difficult to maintain and use when there are even minor changes in data format, much less the major changes that occurred in ATLAS in 2008 - 2011. This framework insulates physics code from the data format, making analysis code directly transferable between a number supported formats. Second, it is often difficult for analyzers to share code in a way that ensures reproducibility and reusability. This framework encourages object oriented modular design which greatly increases the ability to share code. Finally, there are a number of techniques and tools, such as slimming, skimming, and batch processing, which are often implemented in ways that make them difficult to use together. This framework implements these tools and others in a consistent and easy to use way.

The reader framework is broken into three distinct areas: Objects, which describe physics objects like electrons, muons, and missing energy; Readers, which are standalone plugins that build objects assuming a given data format; and Analysis, which maintains the event loop and executes user code. The following sections describe each of these parts in detail.

### 4.3.1 Objects

Objects serve as a layer of abstraction between physics analysis and data format. For an analyzer, exactly how a muon is stored on disk is immaterial. Rather, the only thing that is important is what information is available about each muon, and how that information can be used to select events and perform analysis.

In the reader framework, all analysis operations are done on objects, and these objects are independent of the data format. As different data sets can have different information about each object, this means it is possible for some objects to not be fully defined. For example, in format A, there may be information about the number of MDT hits a muon track contains, while that information may be lacking in format B. In both cases, the muon object is the same, but only in the first is MDT hit information available. In general, every physics object has an associated object in the reader framework. Examples include everything from muons to missing transverse energy to muon raw hits.

This strategy has a number of benefits. First, code that is written in one format may be run with no changes at all on a different format. In practice, as most data formats store roughly the same information, simply with different names and in different ways, there is no difference to the physics analysis. This dramatically decreases turn around time when updating analyses. Second, this approach promotes object oriented analysis, which greatly improves code readability and reusability. For example, a great deal of code in particle physics is written over large lists of vectors loaded from a ROOT file. The names of these vectors are often difficult to decipher, and there is no inherent grouping between them. In the reader framework, all of the relevant information is packaged into a single object which may be passed around with ease, and parameter values are accessed with simple function calls. Finally, operations on lists of objects (which are incredibly common in particle physics) are made much simpler and easier to understand.

Another benefit of using objects is that their life cycle can be strictly controlled. In other words, it is possible to control exactly when objects can be created and when objects can be destroyed. The creation of objects is limited to the readers, which will be described in the next section, and it is not possible to change the parameters of objects once they are created. This ensures that objects are created in a consistent fashion and cannot be corrupted. The destruction of objects is controlled automatically by a custom memory manager that is used in the framework. In particular, all objects are automatically destroyed at the end of each event, with no input from the analyzer. This removes the possibility of memory leaks, which otherwise are a very common source of problems in C++ physics analysis code.

Memory management is achieved automatically through a custom memory manager class called `MemManager`. `MemManager` keeps a linked list of memory allocated from the heap to use when allocating objects. For all objects in the framework, `operator new` is overloaded to request memory from `MemManager`. At the end of each event, the framework analysis code sends a clear request to `MemManager`, which in turn destroys the objects created in that event and clears their memory from its internal buffer for future use. This protects against improper or missing deletes, resulting in a corrupted pointer or a memory leak, and provides a small performance improvement. In the very rare case that an object is required to live beyond the current event, it is possible to request memory directly from the heap, which results in an object with a standard C++ life cycle.

### 4.3.2 Readers

Readers are standalone classes that read an input format and produce objects for use by analysis code. Typically, users interact with them via build object calls which return a vector of the object in question. For example, `buildMuons()` returns `std::vector<Muon*>`. In general, these build functions handle all of the complexity of converting the information from on disk to in memory, and the user code need only specify a few simple parameters like what reconstruction algorithm should be read or whether, in the case of simulated data, the values should be smeared to better match those observed in data.

There are three distinct phases in the lifecycle of a reader class. When the framework has been initialized and the data format being read has been determined, all readers are sent a `readBranches()` call, in which they declare which on disk variables should be read and where the resulting information should reside in memory. This step is very format specific, as it requires in depth knowledge of the available information and naming schemes. The next step is the build phase, which occurs when analysis code issues a build object call. At this point, the memory identified in the `readBranches()` call has been successfully filled, and those values are used to construct the object. Note that objects are built only on demand, which dramatically improves performance. Finally, at the end of each event, all readers are sent an `update()` message, which can be used to clear caches and prepare for the next event.

An extra layer of abstraction was added between the readers and the I/O libraries provided by ROOT in the form of two classes: `ReaderBase` and `VectorReader`. Re-

quests to read variables in `readBranches()` are passed through `ReaderBase`, which validates the variable names. When requested variables are not found, the `ReaderBase` provides default values in memory and logs the misread. Such a mechanism was found to be absolutely essential in order to allow code to run without crashing despite small, inconsequential changes to unused variables. `VectorReader` provides a convenient way for grouping variables that should be run together. When a variable is requested, it may be assigned to a group. Variables in the same group are read back as a block, and error checking and corruption detection is performed automatically in order to ensure the self consistency of these variables.

In general, differing format support is provided by passing along the `readBranches()` and `build` object calls to separate functions for each format. `ReaderBase` provides an interface to the file handling objects, described in the next section, to determine the type of format being read. For example, in the `readBranches()` function of the `MuonReader`, there are `readBranch` style functions for each format, and the correct function is chosen based upon the `ReaderBase` format interface. Currently, four major formats are supported, which cover the most commonly used formats for most ATLAS Standard Model analyses ( $t\bar{t}$  is the major exception), as well as exotics analyses involving  $W$  or  $Z$  like particles, and the official formats used for muon performance measurements. It is also worth noting that the protections offered by `ReaderBase` mean that current readers can be run on slimmed and skimmed datasets (discussed in section 4.3.5) with no changes.

There are a number of performance considerations that have been taken into account in the framework. The most performance critical aspect of the framework is the code in `VectorReader`, as this is called at least once for every variable of every object built (in practice, there are more than 10,000 calls per event to the accessor functions). To maximize performance, the `VectorReader` is built as a hashed key-value database, utilizing a fully in memory self balancing, red-black tree. Additional improvement is gained through the extensive use of caching. All built objects are cached until the end of the event, which means that subsequent calls to a build object style function in a single event are essentially free. This caching dramatically improves performance.

### 4.3.3 Analysis

`AnalysisBase` provides an interface between analysis code, called `UserAnalysis` in this section, and the readers, drives the event loop, and does basic file handling. All `UserAnalysis` algorithms in this framework inherit from `AnalysisBase`, which in turn uses multiple inheritance to inherit from all of the readers, giving `UserAnalysis` direct access to the build object functions.

The event loop of `AnalysisBase` has four distinct phases. During configuration, `UserAnalysis` sets the basic properties of the analysis, such as the number of events to run over, the input files, and the print level. Configuration is typically done in a standalone run script, and the remaining phases are begun by calling `run()` on `UserAnalysis`.

Once `run()` is called, initialization begins, during which three things happen. First, `AnalysisBase` opens the first specified input file and checks the input format. Second, a `readBranches()` message is sent to all of the readers. Finally, `UserAnalysis` is sent an `initialize` message, which can be used to do whatever pre-event setup need be done.

In order to determine the input format, `AnalysisBase` opens the input file and checks the naming convention of the storage tree in the file. In some cases, this information alone is enough to identify the format. If it is not, the trees are searched for the existence of certain key variables. Many formats have distinct tagging variables (such as the format name and version) specifically for this kind of auto-configuration. For others, a set of distinctive and unlikely to change variables are chosen.

Once initialization is complete, the events are looped over. For each event, three things happen. First, `AnalysisBase` sends a message to the ROOT I/O libraries to load the information for that event from disk into memory, as specified by the reader `readBranches()` calls. Next, a `processEvent` message is sent to `UserAnalysis`, in response to which `UserAnalysis` does whatever processing it need on the event, such as filling histograms or recording data. Finally, an `update` message is sent to each the readers, causing them to clear their cache and prepare for a new event.

Once all the events have been read (or the event limit is reached), `AnalysisBase` enters its final stage. `UserAnalysis` is sent a `finalize` message, allowing it to perform aggregate computation or write results to a file, and the framework is prepared for job completion.

#### 4.3.4 Batch Support

Particle physics analysis is a perfect candidate for parallel processing as each event may be processed in any order, and is fundamentally separate from every other event. In particular, massive gains in throughput may be gained by breaking a large job into many small pieces, running each piece on a different CPU, and then combining the output. The reader framework provides native support for batch processing based on the MapReduce algorithm [42]. Note that this support is only provided for clusters running Load Sharing Facility (LSF) as their batch controller.

When a job is submitted, `AnalysisBase` determines the job properties by communicating with the LSF daemon. If the job is being run interactively, then no changes are made. If the job is being run in batch mode, the input file list is adjusted according to the the job index and total number of jobs so that the input files are split evenly among all jobs. The job splitting procedure is done without input from the user, so that code may be run completely unmodified in interactive or in batch modes. Additionally, for debugging purposes, it is possible to mimic a job configuration when running interactively, which greatly improves the ability to correct problems in batch processing.

Writing to output files is more complicated in parallel processing than when running interactively because multiple access at the same time to the same output file will corrupt the results. To handle this, the reader framework includes the `FileHandler` class, which allows analysis code to write objects (such as histograms or canvases) to files in a batch safe way. Jobs which are writing a file write a locking file, typically

a short text file specifying which files they are currently using. When `FileHandler` attempts to write to a file, it first checks for the existence of a lock file. An atomic non-overwriting write is used to attempt to create a lock file, and if no lock file exists, it creates a lock file, and updates the output file to contain the object being written. When it finishes writing, it removes the lock file. In the case that a lock file already exists, there are two possible actions based upon the write mode. If the write mode is forced, `FileHandler` will halt execution and wait until the lock is removed. If the write mode is unforced, `FileHandler` will continue with execution, and check back periodically to see if the lock is free. The result is a single, merged output file with the combined output of all jobs.

#### 4.3.5 Skimming and Slimming

Particle physics analysis makes use of many data reduction techniques in order to reduce the time it takes to perform analysis. The reader framework provides two basic types of data reduction: skimming, in which specific events of interest are filtered out into a new dataset, and slimming, in which only certain variables in the dataset are written to the output. Both of these are highly integrated into the analysis framework, and may use any of the other features mentioned, including, most importantly, batch support, without any changes.

`AnalysisBase` provides an easy to use interface for skimming datasets. In the `initialize()` function of analysis code, a skimming job registers a skim with `AnalysisBase`, providing a name, an output file, and optional parameters about how often to flush the results to disk. In the `processEvent()` function, the skimming

job simply calls `acceptEvent()` and provides the name of the skim passed in order to include the event in the output. The framework then handles the writing of the output files and the batch interface. Note that it is possible to create many skims in a single job.

To produce slimmed datasets, the user must provide a class which describes which variables should be included. It is possible to include existing variables as well as produce new variables. The latter feature is very useful when producing summary quantities that are calculated from many otherwise unneeded inputs. As with skimming, the user need only setup the slimming during `initialize()` and fill it during `processEvent()`, and includes simple batch support. In the 2010 analyses, aggressive slimming and skimming produced datasets that were ten to one hundred thousand times faster to run over than the originals.

#### 4.3.6 Cut Flows

Most physics analyses consist of a sequential list of cuts that are applied to objects in the event. It is common to produce plots of the properties of events passing each cut in the list and a table of the total number of events at each stage. The reader framework provides an optional component called `CutFlow` in order to make these tasks easier and less error prone.

The basic unit of the `CutFlow` framework is the `Cut`. A `Cut` describes a single step in the analysis. For example, there might be a step which requires at least one muon passing certain quality requirements, or a step requiring a trigger be passed. The

reader framework provides a library of highly configurable `Cut` classes that represent the most commonly used analysis steps, including object quality requirements, trigger requirements, detector status requirements, and object combinations (such as the formation of a  $Z$  boson from two leptons).

A `CutFlow` object is then a list of `Cut` objects along with their configuration for a specific analysis. Each analysis has its own `CutFlow` object, and some complicated analyses with many chains have more than one. The `CutFlow` framework provides a number of useful convenience functions. First, analysis code may find out whether an individual event passed any or all of the cuts. Second, analysis code may retrieve the objects which caused an event to pass or fail an individual cut. Finally, a number of useful summary statistics and plots are produced automatically and written out at the end of the job.

This strategy offers a number of very useful benefits. Code development is much faster, as many common tasks are done automatically and there is a high degree of reusability. Many analysis can be done simply by configuring a set of existing cuts from the library. However, even more important is that this design promotes code that tends to have fewer bugs. Multiple different analyses use each cut object, which means each cut object is highly validated. Additionally, the design leads to code that is simpler to read and separates tasks more clearly, which makes it easier to catch problems. Lastly, code is developed around the analysis goals, rather than around the underlying data format or framework, which results in code that better reflects physics rather than C++.

# Chapter 5

## $Wp_T$

This chapter describes the measurement of the  $W$  transverse momentum spectrum in the decay channels  $W \rightarrow \mu\nu$  and  $W \rightarrow e\nu$  and is adapted from the internal ATLAS note describing the analysis [13]. In general, this chapter focuses more on the muon channel than the electron channel, and provides more detail than the internal note where appropriate.

There are three distinct regimes in which this spectrum is measured. After event selection and background subtraction, there is an estimate of  $Wp_T$  spectrum at the *reconstruction* level which includes the effects of both detector resolution and event selection efficiency. Using a technique known as *unfolding*, the reconstruction level spectrum is corrected for detector resolution resulting in a  $Wp_T$  spectrum at the *truth selected* level. This regime has been corrected for detector resolution, but still contains event selection effects. Finally, the truth selected spectrum is corrected to the *truth fiducial* level which is the  $Wp_T$  spectrum for  $W$  decays within the fiducial volume of

the detector. Note that there is no correction back to the total  $Wp_T$  spectrum as such an extrapolation is based entirely off of Monte Carlo, and thus includes a large degree of theoretical uncertainty.

Events are selected by looking for a high  $p_T$  isolated lepton along with large missing transverse energy. There are two general types of backgrounds that mimic this signal. The first, called QCD backgrounds, comes from the production of two or more (typically heavy flavor) jets in which a lepton is produced from particle decay or a jet is misidentified as a lepton and mismeasurement of the jet energy results in missing transverse energy. While the vast majority of such events are rejected by the event selection requirements, the very high jet production cross section at the LHC results in a non-negligible jet background. As this is poorly modeled in simulation, the size and shape of the QCD background is extracted from data. The second is from true sources of high  $p_T$  isolated leptons and includes  $W$  decays to  $\tau$ 's,  $Z \rightarrow \ell\ell$  decays where a lepton is lost,  $t\bar{t}$  semileptonic and dileptonic decays, and leptonic single top decays. This type of background is typically better modeled in simulation, and so is extracted from Monte Carlo that has been corrected to better match observed data.

Due to the presence of the undetected neutrino in the decay of the  $W$ , the  $Wp_T$  must be inferred from momentum balance in the event. The simplest way to do this is to take the missing transverse energy as the  $p_T$  of the neutrino and sum this with the  $p_T$  of the reconstructed lepton. However, this is an undesirable solution because it explicitly depends on the flavor of the lepton (as different corrections are applied for electron and muon to the  $\cancel{E}_T$ ) and thus makes the combination of the channels more

difficult. Instead, this analysis takes advantage of the fact that the  $W$  must balance in the transverse plane with the hadronic activity in the event. In particular, the sum of all of the calorimeter energy depositions (corrected for the lepton depositions) in the event gives a picture of the  $W$  transverse momentum, known as the *hadronic recoil*, that is independent of lepton flavor.

Correcting from the reconstruction level to the truth selected level involves correctly accounting for the smearing of the spectrum due to detector resolution. This analysis unfolds the measured  $Wp_T$  spectrum by solving the equation

$$\mathbf{x} = \mathbf{A}\mathbf{y} \quad (5.1)$$

where  $\mathbf{x}$  is the measured spectrum,  $\mathbf{y}$  is the true distribution, and  $\mathbf{A}$  is the *response matrix*, which describes how true  $Wp_T$  is mapped to reconstructed  $Wp_T$ . Correctly modeling the detector response with an accurate  $\mathbf{A}$  is a central goal of the measurement and is done with  $Z \rightarrow \ell\ell$  data events. Correction factors are extracted from the resolution difference in  $Z$  decays in data and Monte Carlo, and these factors are used to correct  $W$  Monte Carlo and produce a data driven response matrix. The resulting response matrix is used to extract the truth selected  $Wp_T$  spectrum using an iterative unfolding algorithm called Bayesian unfolding, and the unfolded spectrum is then corrected to the truth fiducial level using correction factors derived from Monte Carlo.

## 5.1 Data and Simulation Samples

This analysis is based on approximately  $30\text{ pb}^{-1}$  of data collected from September 25th to October 29th, 2010 and corresponds to approximately 105k  $W$  candidates in the electron channel and 125k in the muon channel. This is only approximately 90% of the total data recorded by ATLAS in 2010 with good detector and beam conditions. The unused portion of the data came from before September 25th and was dropped in order to maintain stable trigger and reconstruction conditions throughout the analysis.

In addition, this analysis used a number of simulated samples in order to perform background subtraction, efficiency corrections, and build a map of the detector response. Wherever possible, the simulated samples were corrected to better match observed data with event reweighting based upon the number of reconstructed vertices and lepton momentum smearing and scaling. This section describes the requirements placed upon the collected data, the simulated samples that were used, and the Monte Carlo corrections that were applied.

### 5.1.1 Data Quality and Luminosity

All data used in this analysis is required to pass requirements on beam and detector conditions as specified by a Good Runs List (GRL) [18]. Both the electron and muon channels require stable beams with  $\sqrt{s} = 7\text{ TeV}$  and good working conditions for the trigger, calorimeter, muon spectrometer, inner detector, and luminosity monitors. There is a small difference in the requirements for the muon and electron channels, in

that the muon channel requires additional offline quality checks to be passed for the muon chambers, and each channel requires that their respective trigger is working.

The integrated luminosity is measured using van der Meer scans to be  $32.6\text{ pb}^{-1}$  for the electron channel and  $30.2\text{ pb}^{-1}$  for the muon channel with an uncertainty of 3.4% [11]. The exclusion of the early data results in a loss of roughly  $3.8\text{ pb}^{-1}$  per channel. The data was processed using `AtlasProduction` release 15.6.13.2 and analyzed from D3PDs produced by Standard Model  $W/Z$  group production.

### 5.1.2 Trigger Requirements

Electron channel events are required to pass the `EF_e15_medium` trigger, which is an Event Filter 15 GeV calorimeter based electron trigger. This trigger is not available in the Monte Carlo, and so the `L1_EM14` trigger (a 14 GeV calorimeter based Level 1 trigger) is used instead and the trigger efficiency is scaled according to the measured data efficiency over the Monte Carlo efficiency (see section 5.8.2).

The lowest unprescaled single muon trigger was rapidly changing as the instantaneous luminosity of the LHC ramped up over 2010. While dropping the early data helped reduce this complexity tremendously, there were still two distinct muon triggers used for this analysis, shown in Table 5.1. For the first half of the data, the `EF_mu13_MG` trigger was used. This is an Event Filter trigger based upon the MuGirl algorithm using extrapolated ID tracks matched to hits in the muon spectrometer. It is seeded by `L1_MU0`, which requires a coincidence in the muon trigger chambers, but does not place an explicit  $p_T$  threshold, and requires an Event Filter  $p_T$  of at least 13

---

Period	Trigger	Int. Lumi [ $pb^{-1}$ ]
G2 - I1(up to run 167576)	EF_mu13_MG	15.2
I1 (from run 167607) - I2	EF_mu13_MG_tight	15.0

Table 5.1: Triggers used in the muon channel analysis as a function of period and run number.

GeV. For the remainder of the data, `EF_mu13_MG` was prescaled, and so the slightly tighter `EF_mu13_MG_tight` was used. This is very similar to `EF_mu13_MG`, except that is it seeded by the level 1 trigger `L1_MU10` instead, which requires a 10 GeV  $p_T$  threshold at level 1. These algorithms are very loose in their matching criteria, and independent of the offline reconstruction algorithm. Neither of these triggers were available in Monte Carlo, and so the `EF_mu10_MG` trigger was used, and scaled with the ratio of the measured trigger efficiencies in data and Monte Carlo (see section 5.8.2).

### 5.1.3 Simulation Samples

The simulated samples used in this analysis are shown in Tables 5.2 and 5.3 for the muon and electron samples respectively. In most cases, simulated samples include multiple interactions per collisions, called pileup, in order to more correctly model the energy distributions in data events. The number of reconstructed vertices is used to weight the Monte Carlo to the number of interactions observed in data, as described in section 5.1.4.

Signal Monte Carlo was used in the production of the data driven response matrix, to calculate the efficiency corrections, and to estimate systematic uncertainties.  $Z \rightarrow \mu\mu$  Monte Carlo was used in the production of the data driven response matrix,

and, along with  $W \rightarrow \tau\nu$ ,  $Z \rightarrow \tau\tau$ ,  $t\bar{t}$ , and single top Monte Carlo, to estimate the electroweak background. Finally, heavy flavor and multijet Monte Carlo (called QCD) was used as part of extrapolation of isolation efficiencies of QCD events from the control to signal regions in the QCD background estimate.

The  $W p_T$  spectrum at the truth fiducial level is compared with predictions from PYTHIA [74] which has been tuned to the  $W$  and  $Z$   $p_T$  spectrums observed at the Tevatron. For estimations of systematics, a sample produced with ALPGEN [55] and a sample produced by PYTHIA but reweighted to match the  $W p_T$  spectrum produced by RESBOS [2] are used.

Process	Generator	Cross-section (nb)	$N_{evt}(\times 10^6)$
$W \rightarrow \mu\nu$	PYTHIA	10.46	7.7
$W \rightarrow \mu\nu$	ALPGEN+ HERWIG	10.46	1.8
$Z \rightarrow \mu\mu$	PYTHIA	0.989	0.3
$W \rightarrow \tau\nu$	PYTHIA	10.46	0.1
$Z \rightarrow \tau\tau$	PYTHIA	0.989	0.1
$t\bar{t}$ (without pileup)	MC@NLO	0.165	0.2
single top (without pileup)	MC@NLO	0.00712	0.02
J0 ( $8 < p_T^{jet} < 17$ GeV )	PYTHIA	$9.86 \times 10^6$	0.4
J1 ( $17 < p_T^{jet} < 35$ GeV )	PYTHIA	$6.78 \times 10^5$	0.4
J2 ( $35 < p_T^{jet} < 70$ GeV )	PYTHIA	$4.10 \times 10^4$	0.4
J3 ( $70 < p_T^{jet} < 140$ GeV )	PYTHIA	$2.20 \times 10^3$	0.4
J4 ( $140 < p_T^{jet} < 280$ GeV )	PYTHIA	87.7	0.4
J5 ( $280 < p_T^{jet} < 560$ GeV )	PYTHIA	2.35	0.4

Table 5.2: Simulated data samples used in the muon channel analysis. All samples include pileup unless noted.

---

Process	Generator	Cross-section (nb)	$N_{evt}(\times 10^6)$
$W \rightarrow e\nu$	PYTHIA	10.46	7.0
$Z \rightarrow ee$	PYTHIA	0.989	1.0
$W \rightarrow \tau\nu$ (without pileup)	PYTHIA	10.46	0.15
$Z \rightarrow \tau\tau$	PYTHIA	0.989	0.10
$t\bar{t}$ (without pileup)	MC@NLO	0.165	1.0
“JF17”	PYTHIA	$1.15 \times 10^6$	10.

Table 5.3: Simulated data samples used in the electron channel analysis. All samples include pileup except where noted.

### 5.1.4 Monte Carlo Corrections

The Monte Carlo modeling of detector conditions is corrected to match the observed data in three basic ways. First, the Monte Carlo is corrected to the number of reconstructed primary vertices observed in data. This serves to better model the actual pileup in the LHC and therefore improve the agreement between Monte Carlo and data in modeling the energy in the calorimeter. To perform this correction, both channels measured the number of reconstructed primary vertices with at least 3 tracks in events passing the GRL requirements, trigger requirement, and which had at least one high  $p_T$  lepton. The lepton requirement was  $E_T > 18$  GeV and passing Robust Medium [20] requirements in the electron analysis, and a combined muon with at least 20 GeV in the muon analysis. In order to suppress cosmic rays, the muon analysis additionally required that all primary vertices be within 20 cm of the nominal interaction point to be counted. As an identical procedure was used to generate pileup in all simulated samples, a single set of weights as a function of reconstructed vertices was calculated for each channel, and is shown in Table 5.4.

Vertices	0	1	2	3	4	5	6	7	8	9	10
Muon Weight	1	1.48	1.10	0.89	0.77	0.72	0.70	0.70	0.79	0.92	0.87
Electron Weight	1	1.48	1.11	0.89	0.77	0.71	0.69	0.67	0.77	0.83	1.10

Table 5.4: Weights used to correct the pileup model used in event simulation. Note that 0 primary vertex events do not pass event selection and thus those weights are not used.

In general the reconstruction and trigger efficiencies are not perfectly modeled in the Monte Carlo. Differences in efficiency between data and simulation as a function of  $Wp_T$  can affect the shape of the efficiency corrected spectrum, and thus must be accounted for. Data efficiencies were measured using  $Z$  decays and used to correct the Monte Carlo as described in more detail in section 5.8.

Finally, correct modeling of the lepton resolution plays an important role in building the data driven response matrix which is used to unfold the reconstructed  $Wp_T$  spectrum. Studies were performed to measure the lepton resolution and scale using the  $Z$  mass constraint and the results were used to correct the simulation. This is described in more detail in section 5.8.

## 5.2 Event Selection

Selected events are required to have one high quality, high  $p_T$  lepton with transverse energy or momentum greater than 20 GeV, missing transverse energy greater than 25 GeV, and a transverse  $W$  mass of at least 40 GeV. This section describes the details of this selection for each channel, with a focus on the muon selection. The requirements are generally the same as used in other ATLAS  $W$  and  $Z$  analyses and are based off of detailed studies done for first  $W$  measurements [14, 19, 12].

Collision-like Event	
Trigger	<code>EF_mu13_MG</code> or <code>EF_mu13_MG_tight</code>
Jet Cleaning	Cleaning Cuts (see [47] )
Primary Vertex	At least one PV with $N_{trk} \geq 3$ and $ z_0  < 200$ mm
High $p_T$ muon	
Muon Preselection	Combined Staco Muon $p_T > 15$ GeV, $ \eta  < 2.4$
Muon Quality	$p_T^{MS} > 10$ GeV $ (p_T^{MS} - p_T^{ID})/p_T^{ID}  < 0.5$ $N_{pix} \geq 1$ , $N_{SCT} \geq 6$ $N_{TRT} = N_{TRT}^{hits} + N_{TRT}^{outliers}$ if $ \eta  < 1.9$ , then require $N_{TRT}^{hits} > 5$ and $N_{TRT}^{outliers}/N_{TRT} < 0.9$ if $ \eta  \geq 1.9$ and $N_{TRT}^{hits} > 5$ , then require $N_{TRT}^{outliers}/N_{TRT} < 0.9$
Muon PV matching	$ z_0^\mu - z_0^{vtx}  < 10$ mm
$W \rightarrow \mu\nu$	
Tight Kinematics	$p_T^\mu > 20$ GeV
Muon isolation	$(\sum p_T \text{ (cone 0.4)}) / p_T^\mu < 0.2$
Missing $E_T$	$E_T^{miss} > 25$ GeV
Transverse Mass	$M_T > 40$ GeV

Table 5.5: Selection of  $W$  candidates for muon channel analysis

### 5.2.1 Muon Event Selection

Selection of muon candidates is divided into three stages: collision like event requirements, high  $p_T$  muon selection, and  $W$  selection. These cuts are summarized in Table 5.5.

Events are first required to pass the lowest unprescaled single muon trigger as described in section 5.1.2. In order to prevent the inclusion of events containing large noise spikes in the calorimeter, jet cleaning cuts are applied on the quality, timing, and energy distribution of jets in the event, as described in more detail in [47]. Finally, a primary vertex with at least 3 associated tracks within 20 cm of the nominal origin of

the detector in  $z$  is required. This serves to reject cosmic rays, which would otherwise mimic  $W \rightarrow \mu\nu$  decays if one leg of the muon was lost, while maintaining higher than 99.9 % efficiency on signal events [14].

The selection of high quality, high  $p_T$  muons used in this analysis is based on detailed studies done by the Muon Combined Performance group and matches the selection used by other late 2010  $W$  and  $Z$  analyses [15, 19, 14, 12]. For completeness, the rational behind this selection will be discussed in detail here.

Only combined muons - those with matching inner detector and muon spectrometer tracks - are used as they provide the best momentum resolution with the lowest fake rate. In particular, they are very effective at rejecting muons from pion and kaon decays in flight. Muons are restricted to  $|\eta| < 2.4$  in order to be within the fiducial volume of the muon trigger. A preselected sample of events with muons with  $p_T > 15$  GeV is used to perform data/simulation comparisons and as a high statistics control region for the QCD background estimation.

High quality muons are selected through a series of cuts on the quality of the individual inner detector and muon spectrometer tracks. First, the muon spectrometer track is required to have a  $p_T$  of at least half the  $p_T$  of the inner detector track, with a minimum cutoff of 10 GeV. This largely serves to reject muons from decays of the form  $\pi^\pm \rightarrow \mu^\pm \nu$  or  $K^\pm \rightarrow \mu^\pm \nu$ , as the momentum of the muon and the meson will be very different due to the emission of a neutrino.

The inner detector track is also required to have the expected number of hits in the pixel, semiconductor, and transition radiation trackers. The number of outliers is another important variable, and represents the number of TRT hits which do not match well to the track during pattern matching. For non-prompt muons (such as those from heavy flavor and pion decays), there is often a kink or a missing segment near the interaction point, and these cuts serve to reject these muons.

The muon is also required to have a point of closest approach to the beamline within 10 mm of a selected primary vertex in the  $z$  axis. This cut serves to reject cosmic ray muons that are produced in time with a high energy collision. Without this cut, high  $p_T$  cosmic rays in which the top or bottom half of the tracks are lost would be reconstructed as  $W$  candidates.

Finally,  $W$  candidates are selected by placing requirements on the muon isolation, the  $\cancel{E}_T$  of the event, and the transverse mass of the  $W$ . Muons from  $W$  and  $Z$  decays are typically produced far away from any hadronic depositions in the calorimeter, whereas muons from heavy flavor decays (like  $b$  jets) tend to be produced close to hadronic activity. To remove these background muons, the  $p_T$ 's of all the tracks within  $\Delta R < 0.4$  of the muon are summed, and the result is required to be less than 20 % of the muon  $p_T$ . The  $\cancel{E}_T$  in the event is calculated by taking negative of the sum over the calibrated calorimeter clusters and the momentum of reconstructed muons (accounting for energy depositions in calorimeter by the muon). To select events with a high  $p_T$  neutrino, the magnitude of  $\cancel{E}_T$  is required to be at least 25 GeV. Finally, the transverse mass is calculated as:

$$m_T^2 = 2p_T \cancel{E}_T (1 - \cos(\phi_\mu - \phi_\nu)) \quad (5.2)$$

where  $p_T$  is the transverse momentum of the selected muon,  $\phi_\mu$  is the muon azimuthal angle, and  $\phi_\nu$  is the azimuthal angle of the missing transverse energy. The transverse mass is used as the existence of the neutrino makes the calculation of the full mass of the  $W$  impossible.

General kinematic quantities for the selected data as well as the signal and background Monte Carlo samples are shown in Figure 5.1. The Monte Carlo samples are weighted according to the measured luminosity and the theoretical cross-section. Note that for the full background subtraction, described in section 5.5, data driven estimates are used for the multijet background (called QCD here). Using this selection, 124,797  $W$  candidates are selected in the dataset used for the analysis.

### 5.2.2 Electron Event Selection

Selection of electron candidates is divided into three sections: collision like event requirements, high  $E_T$  electron selection, and  $W$  selection. These requirements are summarized in Table 5.6.

Collision like event requirements begin with the trigger requirement described in section 5.1.2. Events with large spikes in calorimeter energy likely due to noise are removed in order to prevent bias to high  $\cancel{E}_T$  with Jet Cleaning and OTX Cleaning cuts described in [47] and [46] respectively. Finally, the event is required to have a reconstructed primary vertex with at least three tracks. Unlike the muon selection,

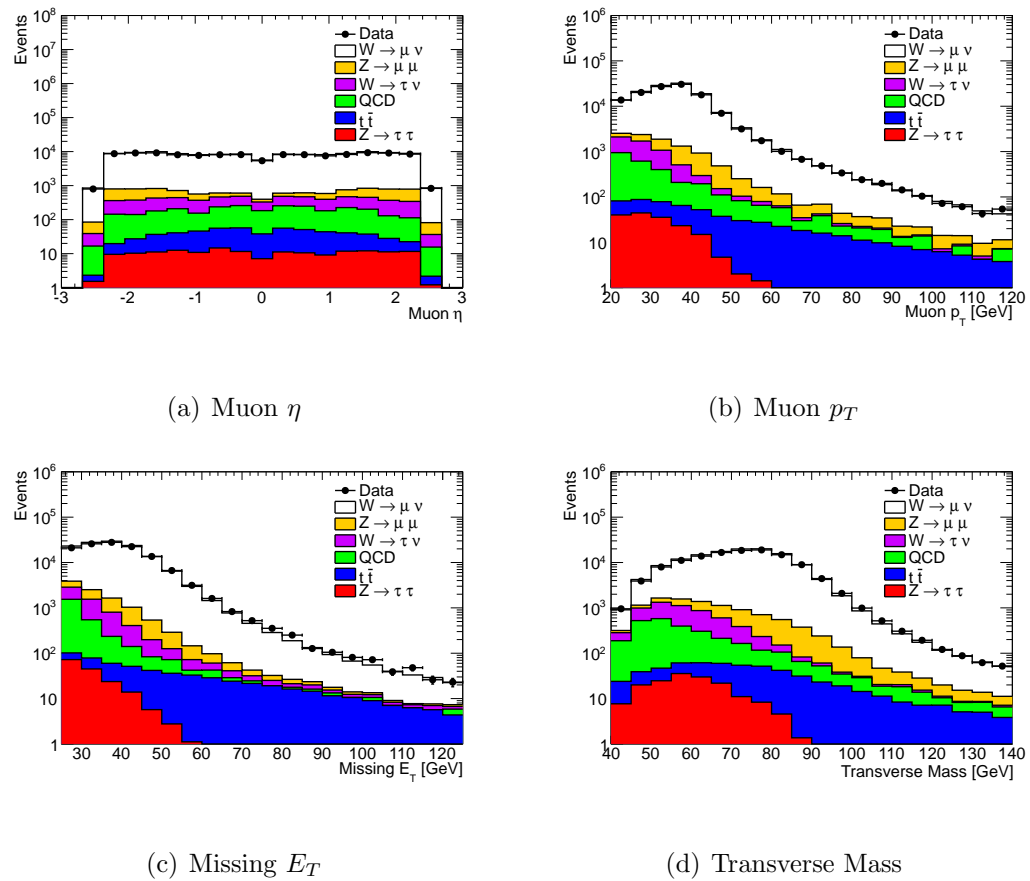


Figure 5.1: Kinematics from selected events in data and Monte Carlo signal and background samples. Monte Carlo samples are weighted according to the measured luminosity times the theoretical cross section.

Collision-like Event	
Trigger	<code>EF_e15_medium</code>
Jet Cleaning	Cleaning Cuts (see [47] )
OTX Cleaning	Object Quality Checks (see [46])
Primary Vertex	At least one PV with $N_{\text{trk}} \geq 3$
High $E_T$ electron	
Electron Kinematics	$E_T > 20$ GeV $ \eta_e  < 1.37$ or $1.52 <  \eta_e  < 2.47$
Electron Quality	Robust Tight [20]
$W$	
Missing $E_T$	$\cancel{E}_T > 25$ GeV
Transverse Mass	$M_T > 40$ GeV

Table 5.6: Selection of  $W$  candidates for electron channel analysis

no explicit cut is made on the  $z$  position of the primary vertex relative to the nominal collision point.

The electron object selection has been studied in great detail during the first  $W$  analyses and more information can be found in [20] and [9]. This analysis uses a selection consistent with other late 2010  $W$  analyses, such as the charge asymmetry analysis [14]. Electrons are required to pass the Robust Tight [20] cuts, which require a high quality shower consistent with an electron and a good track match in direction and  $E/p$ . They are also required to have  $E_T > 20$  GeV and  $|\eta|$  within the fiducial acceptance of the electromagnetic calorimeter.

Events are then checked to be kinematically consistent with the decay of a  $W$  boson into an electron and neutrino. A  $\cancel{E}_T > 25$  GeV cut is applied as a proxy for selection of the neutrino and to reduce the effect of QCD background. Finally, a transverse mass cut on the  $\cancel{E}_T$  and selected electron combination is applied. There are a total

of 104,904  $W \rightarrow e\nu$  candidates selected from the data sample used in this analysis.

### 5.2.3 Fiducial Selection

The  $Wp_T$  spectrum is corrected back to the fiducial volume rather than the total truth level as this limits theoretical uncertainties when doing the efficiency correction. The fiducial requirements are defined at the truth level as  $p_T^\ell > 20$  GeV,  $|\eta_\ell| < 2.4$ ,  $p_T^\nu > 25$  GeV, and  $m_T^W$ , calculated with the neutrino instead of the missing energy, greater than 40 GeV. These requirements are similar to the event selection requirements described previously.

## 5.3 Hadronic Recoil

Due to the existence of the neutrino, which is not measured by the detector, it is not possible to reconstruct the  $Wp_T$  directly. Instead, the transverse momentum of the neutrino can be inferred by the energy imbalance in the transverse plane, and then summed with the selected lepton  $p_T$  to generate the  $Wp_T$ . However, this approach misses an important point: the transverse momentum of the  $W$  can be directly calculated by summing the energy and momenta of all particles in the event other than the  $W$  decay products. In particular, the  $Wp_T$  can be measured without reference to the lepton  $p_T$  by summing the energy depositions in the calorimeter. This technique, known as hadronic recoil [31], is very powerful because it is lepton flavor independent, and thus allows the detector response in the muon and electron channels to be combined directly.

The hadronic recoil algorithm forms the vector sum of all calorimeter cluster momenta except for those in a cone around the selected lepton. As it is likely for the lepton, especially in the case of electrons, to deposit energy in the calorimeter, clusters within a small cone of the lepton are removed. In general there will be depositions unrelated to the lepton near the lepton and these will be removed. To account for this bias, clusters are selected from a cone taken from a similar detector region, but far from the lepton, in the same event, and rotated into the lepton cone. This section describes this algorithm in more detail.

### 5.3.1 Algorithm

The uncorrected hadronic recoil is defined as:

$$\vec{R}_{uncorr} = \sum_{\Delta R > \Delta R_{min}} \vec{p}_{T,clus}, \quad (5.3)$$

where  $\Delta R$  is the distance between the cluster and the closest selected lepton,  $\Delta R_{min}$  is a parameter of the algorithm, and the sum is taken over the momentum of the calorimeter clusters in the transverse plane.

For each selected lepton, a sampling cone axis is picked by randomly rotating the lepton axis in  $\phi$  outside an allowed spacing from the lepton and the recoil. That is,  $\eta_{cone} = \eta_{lepton}$  and  $\phi_{cone}$  is chosen randomly such that  $\Delta\phi(cone, lepton) > \Delta\phi_{lepton}$  and  $\Delta\phi(cone, recoil) > \Delta\phi_{recoil}$ , where  $\Delta\phi_{lepton}$  and  $\Delta\phi_{recoil}$  are parameters of the algorithm. The correction factor is then defined as:

$$\vec{R}_{cone} = \sum_{\Delta R_{cone} < \Delta R_{min}} \vec{p}_{T,clus}. \quad (5.4)$$

That is, the sum of the clusters within the cone around the new, randomly selected axis. The correction factor,  $\vec{R}_{cone}$ , is then rotated in  $\phi$  by  $\Delta\phi(lepton, cone)$ , the angle in  $\phi$  between the lepton and cone axis, and the corrected recoil is taken as the sum of the uncorrected and cone recoils:

$$\vec{R}_{corr} = \vec{R}_{uncorr} + \vec{R}_{cone} \quad (5.5)$$

A diagram of this algorithm in the electron channel is shown in Figure 5.2.

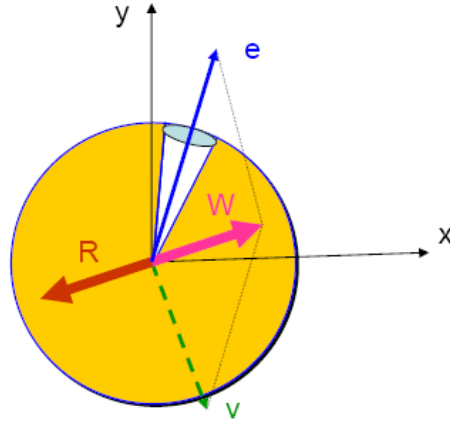


Figure 5.2: Diagram of the hadronic recoil calculation for  $W \rightarrow e\nu$  decays.

### 5.3.2 Performance

The performance of this algorithm is characterized by the bias and resolution parallel to the true recoil and perpendicular to the true recoil. These projections are

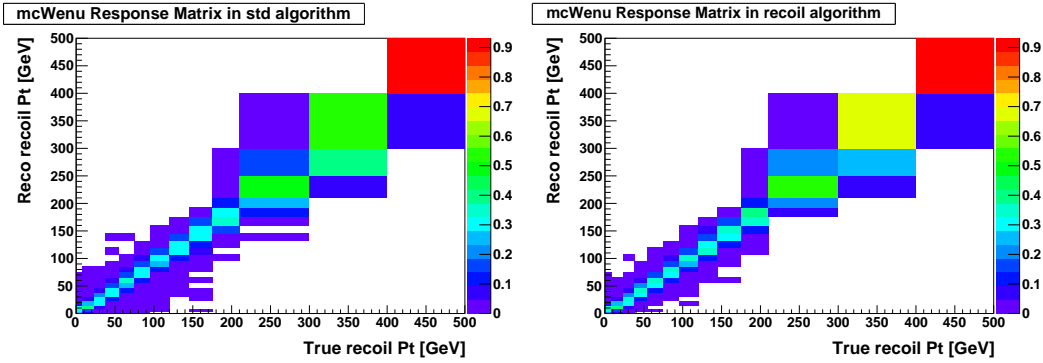


Figure 5.3: Response matrix showing reconstructed versus true  $Wp_T$  in  $W \rightarrow e\nu$  Monte Carlo for standard (left) and hadronic recoil (right) algorithms.

defined by the equations:

$$p_{\parallel}^{reco}(W) = R_{\parallel} = p_T^{\vec{r}eco} \cdot \vec{u} , \quad p_{\perp}^{reco}(W) = R_{\perp} = p_T^{\vec{r}eco} \cdot \vec{v} \quad (5.6)$$

where  $\vec{u}$  and  $\vec{v}$  are unit vectors parallel and perpendicular to the truth  $Wp_T$  respectively. At the truth level, one has  $p_{\parallel}^{true} = p_T^{true}$  and  $p_{\perp}^{true} = 0$ . These quantities are of interest because the behavior of the parallel and perpendicular components can be quite different. In particular, the perpendicular component probes only the resolution, while the parallel component can probe the bias as well.

Performance was measured relative to the standard calculation which uses missing energy to infer the  $p_T$  of the neutrino, and in each case the hadronic recoil algorithm performed as well or better than the standard algorithm. Figure 5.3 shows the relationship between reconstructed and true  $Wp_T$  for both the hadronic recoil and standard algorithms. In particular, there are fewer off diagonal elements using hadronic recoil, which makes unfolding from the reconstruction level to the truth selected level much easier.

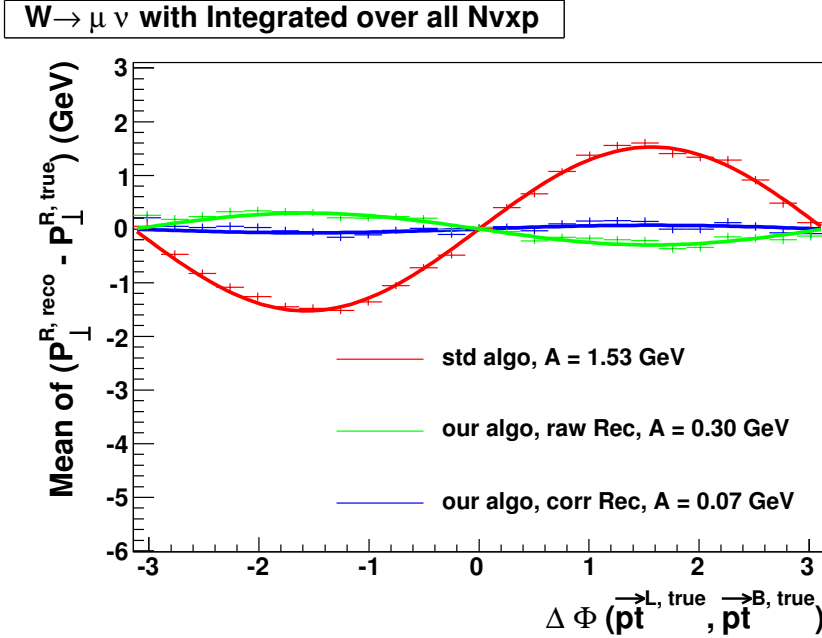


Figure 5.4: Bias perpendicular to the  $W$  direction in the transverse plane as a function of the angle between the lepton and the  $W$  for the standard, uncorrected hadronic recoil, and corrected hadronic recoil algorithms in  $W \rightarrow \mu\nu$  Monte Carlo. The amplitude of the oscillation,  $A$ , is determined by fitting the bias with a sinusoidal function.

The effect of bias due to leptonic energy deposition was measured by examining the bias perpendicular to the true  $W p_T$  as a function of the angle between the  $W$  and the lepton. In particular, when the lepton and the  $W$  are aligned, this bias should be 0, while it should be maximal when they are perpendicular. The resulting bias is shown in Figure 5.4 for the muon channel. In the standard algorithm, the magnitude of the bias is roughly 1.5 GeV, while with the uncorrected hadronic recoil algorithm, the bias is reduced to roughly three hundred MeV. Applying the fully correctly hadronic recoil algorithm removes this bias completely. There is a corresponding improvement in resolution as a function total  $E_T$  in the event, which is shown in Figure 5.5.

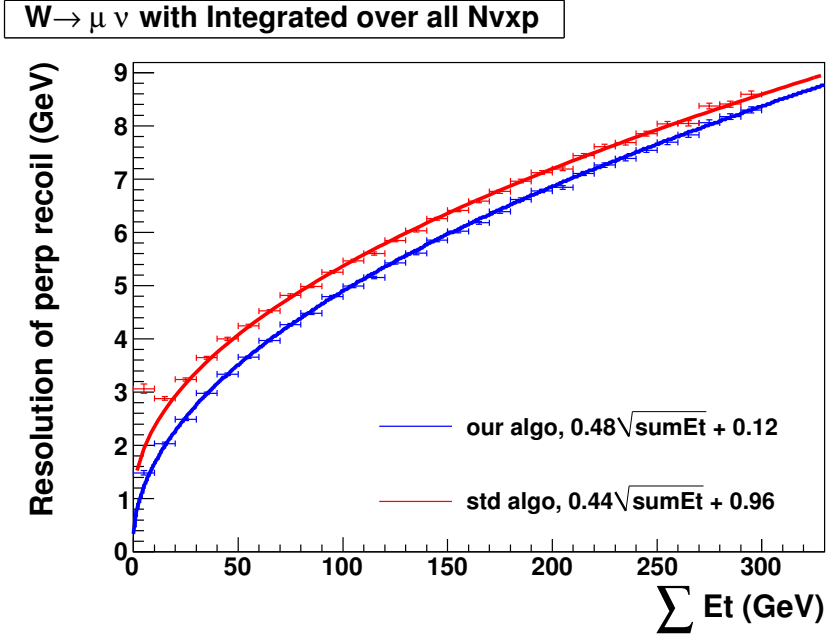


Figure 5.5: Resolution of the standard and corrected hadronic recoil algorithms as a function of total transverse energy in the event in  $W \rightarrow \mu \nu$  Monte Carlo.

### 5.3.3 Limitations

The main limitation of this technique is that it implicitly assumes that the selected leptons are well isolated. If they are not, then the correction technique performs very poorly, as it replaces a region around the lepton, which contains a lot of calorimeter activity, with a region from the detector specifically picked to have no hard calorimeter activity. This often results in an imbalance in the hadronic recoil, which increases the magnitude of the reconstructed  $Wp_T$ .

This is not a problem for signal leptons which are highly isolated. However, for data driven background estimates, particularly those for QCD backgrounds, it is common to look at background rich low  $\cancel{E}_T$  control regions. In cases such as this,

the approach used is to select events using  $\cancel{E}_T$ , but calculate the background effective  $Wp_T$  spectrum using the hadronic recoil.

## 5.4 Binning of Results

Binning plays an important role in this analysis due to the bin-to-bin correlations that are introduced when unfolding and when normalizing. Smearing due to detector resolution pushes events from a given true  $Wp_T$  bin into the surrounding reconstruction level  $Wp_T$  bins, and so the unfolding process tends to correlate neighboring bins. The final result is normalized in order to provide a shape that is independent of luminosity. In this case, as the  $Wp_T$  spectrum is rapidly falling, the normalization is heavily dependent on the contents of the first few bins. In particular, fluctuations in the first bin results in fluctuations in the later bins due to the change in number of observed events. This results in global correlations between the first few bins and all of the remaining bins. The relative size of bins plays an important role in determining the degree of this correlation.

At low  $p_T$ , the binning decision is driven by the resolution of the detector. In particular, there is an inherent resolution of approximately 6 GeV. As the measured  $Wp_T$  is actually the sum in quadrature of two pieces (recoil in  $x$  and recoil in  $y$ ), both of which are subject to this resolution, there is a Jacobian peak in the reconstructed  $Wp_T$  spectrum that is due solely to detector effects and contains no physics information. Even further, it can be shown that below approximately 8 GeV, very differing shapes in true  $Wp_T$  result in very similar shapes in reconstructed  $Wp_T$  due to this

resolution effect. Thus, unfolding with true bins with width less than 8 GeV results in very large correlation and systematic errors, and is avoided in this analysis.

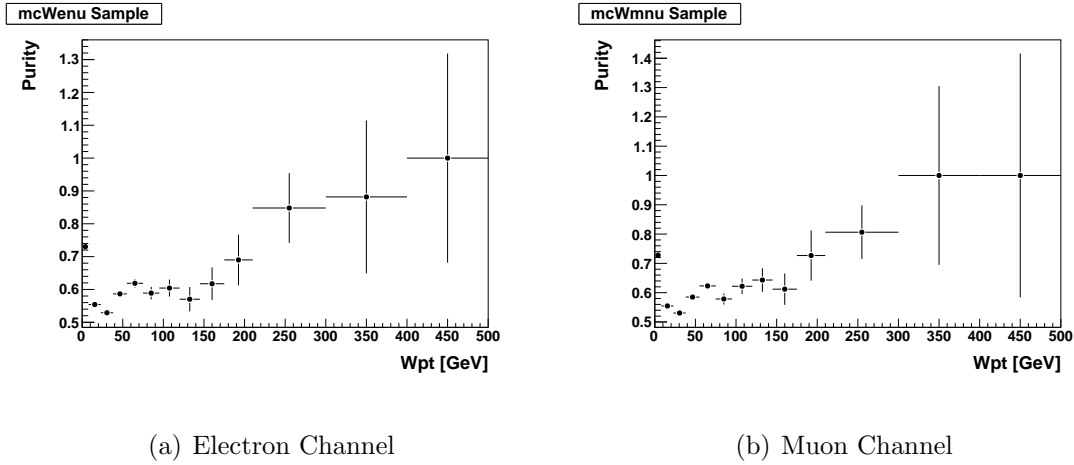
The final binning was a compromise between minimizing correlations and uncertainties and maximizing physics content. As will be discussed later, the unfolding algorithms are able to improve their accuracy through the use of finer binning at the reconstruction level than the truth level, and so that strategy was used. The reconstruction and truth level binnings are shown in Table 5.7, and the resulting purities are shown in Figure 5.6. Note that while the binning extends to 500 GeV, results are only shown up to 300 GeV. This is done in order to avoid edge effects due to migration outside of the response matrix range during the unfolding process.

Level	Binning [ GeV ]
Reconstruction	0, 4, 8, 15, 23, 30, 38, 46, 55, 65, 75, 85, 95, 107, 120, 132, 145, 160, 175, 192, 210, 250, 300, 400, 500
Truth	0, 8, 23, 38, 55, 75, 95, 120, 145, 175, 210, 300, 400, 500

Table 5.7: Binning used at the reconstruction and truth levels.

## 5.5 Background Estimation

The background contamination in the  $W$  sample is estimated using data driven techniques for QCD backgrounds and from Monte Carlo simulation for  $W$ ,  $Z$ , and top backgrounds. In both cases, backgrounds are estimated in bins of  $Wp_T$  as calculated using the hadronic recoil algorithm.  $W$ ,  $Z$ , and top backgrounds are estimated by applying the  $W$  event selection to corresponding Monte Carlo samples, and then scaling the number of events by the theoretical cross section times the luminosity.

Figure 5.6: Bin purity from  $W \rightarrow \ell\nu$  Monte Carlo

QCD backgrounds are estimated in both channels in roughly the same way. The low  $\cancel{E}_T$  region is used to form a control sample, which is then extrapolated to the signal region using Monte Carlo that has been corrected to the data. Cosmic ray contamination in the muon channel has been estimated to be less than one event, and is therefore ignored [14]. The observed muon data is shown with the major backgrounds identified in Figure 5.7.

### 5.5.1 Backgrounds from $W$ , $Z$ , and top

$W$ ,  $Z$ , and top have very similar properties in both the electron and muon channels and make up roughly 6% of the total selected sample. In particular, the largest backgrounds, which are considered here, are from  $W \rightarrow \tau\nu$ , in which the  $\tau$  decays to a lepton of interest,  $Z \rightarrow \ell\ell$ , where a lepton is lost,  $Z \rightarrow \tau\tau$ , and  $t\bar{t}$ . Additionally, there is a very small background from single top production (decaying to a  $\tau$  or the lepton under study).

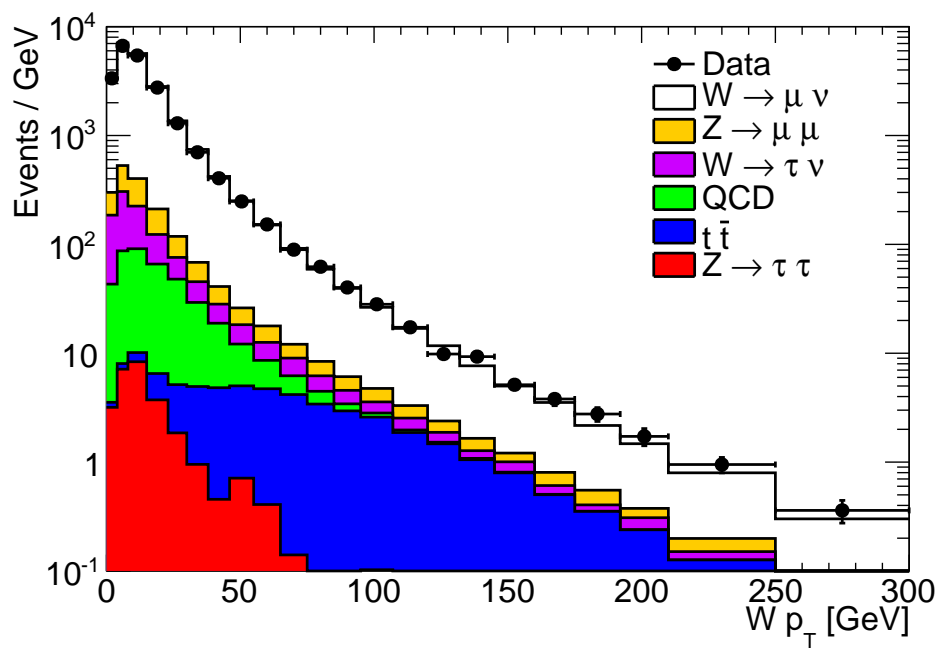


Figure 5.7: Observed muon data with major backgrounds and signal Monte Carlo. All samples except for the QCD sample are from Monte Carlo scaled by the theoretical cross section times the measured luminosity. The QCD sample is obtained using a data driven technique.

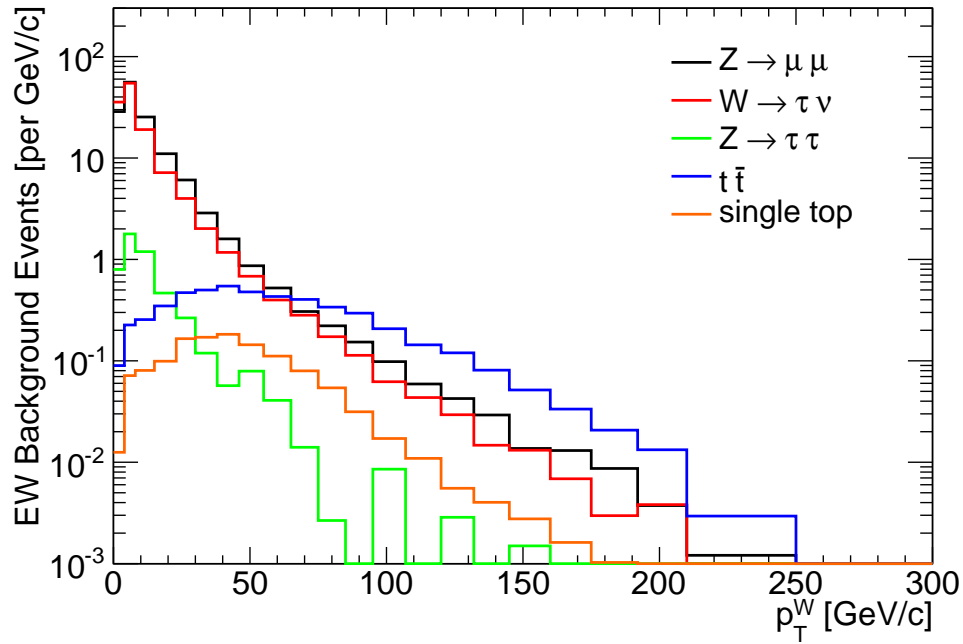


Figure 5.8: Estimated  $W$ ,  $Z$ , and top backgrounds in the muon channel, separated by sample.

The shapes of these backgrounds are estimated by applying the event selection described in section 5.2 to Monte Carlo samples which have been corrected as described in section 5.1.4. The total number of background events is determined by scaling each sample according to its theoretical cross section multiplied by the measured luminosity. The separate contributions from each sample in the muon channel are shown in Figure 5.8. The resulting number of total  $W$ ,  $Z$ , and top background events per bin is shown in Figure 5.9 for the muon channel.

Systematic uncertainties on the electroweak background estimate include uncertainties on the scale factors used to correct the trigger and reconstruction efficiencies, a very conservative 3% uncertainty due to variation of selection efficiency on the

PDF set used (see [18]), an uncertainty introduced by muon resolution smearing and scaling corrections, and finally an uncertainty on the theoretical prediction of the sample of cross section. The trigger and reconstruction efficiency scale factor uncertainties are computed as described in sections 5.8.2 and 5.8.3. The smearing and scaling uncertainty is taken, very conservatively, to be 100% of the difference between the background estimate with and without the correction applied. The cross section uncertainties for the  $W$  and  $Z$  backgrounds are taken to be 5% and completely correlated. The single top cross section uncertainty is taken as 10% and correlated with the  $t\bar{t}$  cross section uncertainty, which is taken to be 6%. Finally, the overall estimate is assigned a 3.4% uncertainty due scaling by the measured luminosity. The resulting uncertainties, broken down by source, are shown in Figure 5.9 for the muon channel.

### 5.5.2 QCD in the Muon Channel

The QCD background in the muon channel is estimated using a data driven technique called the *matrix method* [14, 19] which uses the QCD rich non-isolated muon sample as a control region. The standard muon event selection is performed, with the isolation requirement reversed, and then the resulting events are scaled by isolation efficiencies as a function of hadronic recoil measured in data.

For each bin,  $i$ , in hadronic recoil, let  $N_{isol}^i$  and  $N_{loose}^i$  be the number of events passing the isolated selection and the number of events passing selection with no isolation respectively. Further, let  $\epsilon_{QCD}^i$  and  $\epsilon_{non-QCD}^i$  be the efficiency of events in the  $i$ -th bin to pass the isolation cut for QCD and non-QCD ( $W$ ,  $Z$ , top) events respectively. The two counts  $N_{isol}$  and  $N_{loose}$  may be written as:

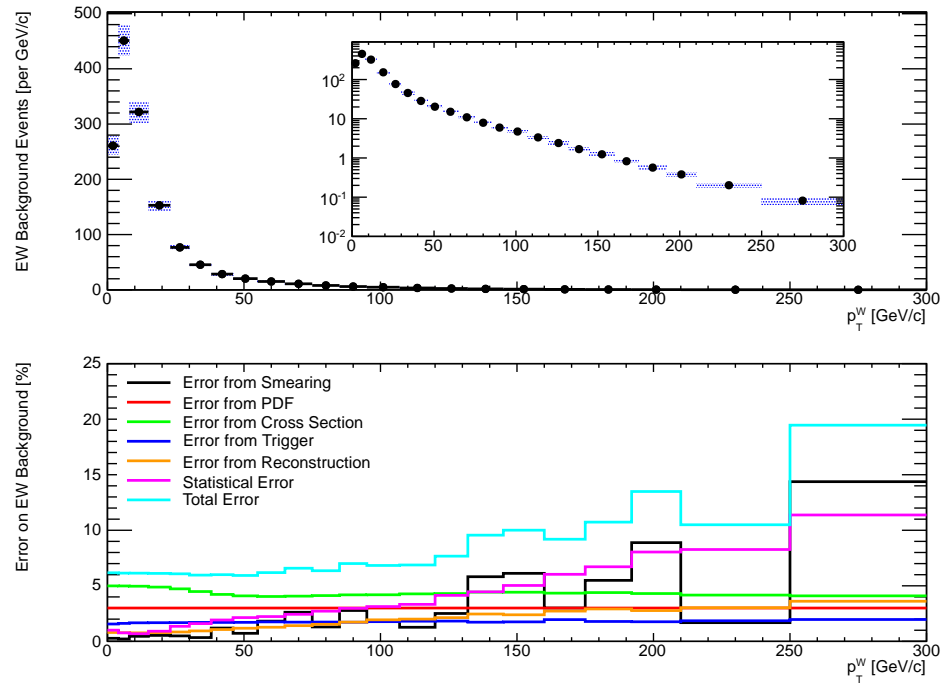


Figure 5.9: Total estimated  $W$ ,  $Z$ , and top backgrounds and uncertainties in the muon channel in bins of  $Wp_T$ . Note that an addition 3.4% uncertainty for the luminosity estimate is applied, but not shown here.

$$\begin{aligned} N_{\text{loose}}^i &= N_{\text{non-QCD}}^i + N_{\text{QCD}}^i \\ N_{\text{isol}}^i &= \epsilon_{\text{non-QCD}}^i N_{\text{non-QCD}}^i + \epsilon_{\text{QCD}}^i N_{\text{QCD}}^i \end{aligned} \quad (5.7)$$

where  $N_{\text{QCD}}^i$  and  $N_{\text{non-QCD}}^i$  are the number of events in the  $i$ -th bin of hadronic recoil from QCD and non-QCD sources respectively. These equations may be solved for  $N_{\text{QCD}}^i$  yeilding:

$$N_{\text{QCD}}^i = \frac{N_{\text{loose}} \epsilon_{\text{non-QCD}}^i - N_{\text{isol}}^i}{\epsilon_{\text{non-QCD}}^i - \epsilon_{\text{QCD}}^i} \quad (5.8)$$

The expected number of QCD background events in the  $i$ -th bin is then given by:

$$N_{\text{QCD}}^i \epsilon_{\text{QCD}} = \epsilon_{\text{QCD}} \left( \frac{N_{\text{loose}} \epsilon_{\text{non-QCD}}^i - N_{\text{isol}}^i}{\epsilon_{\text{non-QCD}}^i - \epsilon_{\text{QCD}}^i} \right) \quad (5.9)$$

Error propagation yields that the statistical uncertainty of the estimate is given by:

$$\frac{\delta N_{\text{QCD}}^i}{N_{\text{QCD}}^i} = \frac{1}{\sqrt{N_{\text{loose}}^i}} \oplus \left( \frac{\delta \epsilon_{\text{nonQCD}}^i}{\epsilon_{\text{nonQCD}}^i - \alpha_i} - \frac{\delta \epsilon_{\text{nonQCD}}^i}{\epsilon_{\text{nonQCD}}^i - \epsilon_{\text{QCD}}^i} \right) \oplus \frac{\delta \alpha_i}{\epsilon_{\text{nonQCD}}^i} \oplus \frac{\delta \epsilon_{\text{QCD}}^i}{\epsilon_{\text{nonQCD}}^i - \epsilon_{\text{QCD}}^i} \quad (5.10)$$

where  $\alpha_i = N_{\text{isol}}^i / N_{\text{loose}}^i$  is the total isolation efficiency of the sample.

$N_{\text{isol}}$  and  $N_{\text{loose}}$  can be counted directly by applying the muon event selection. The additional parameters that must be measured in bins of hadronic recoil are  $\epsilon_{\text{nonQCD}}$  and  $\epsilon_{\text{QCD}}$ . As  $W$  and  $Z$  muons behave very similarly (and are assumed to be the same in this procedure), it is possible to use tag and probe [19], described in detail in section 5.8.2, to determine  $\epsilon_{\text{nonQCD}}$  from data. The resulting values for  $\epsilon_{\text{nonQCD}}$  in

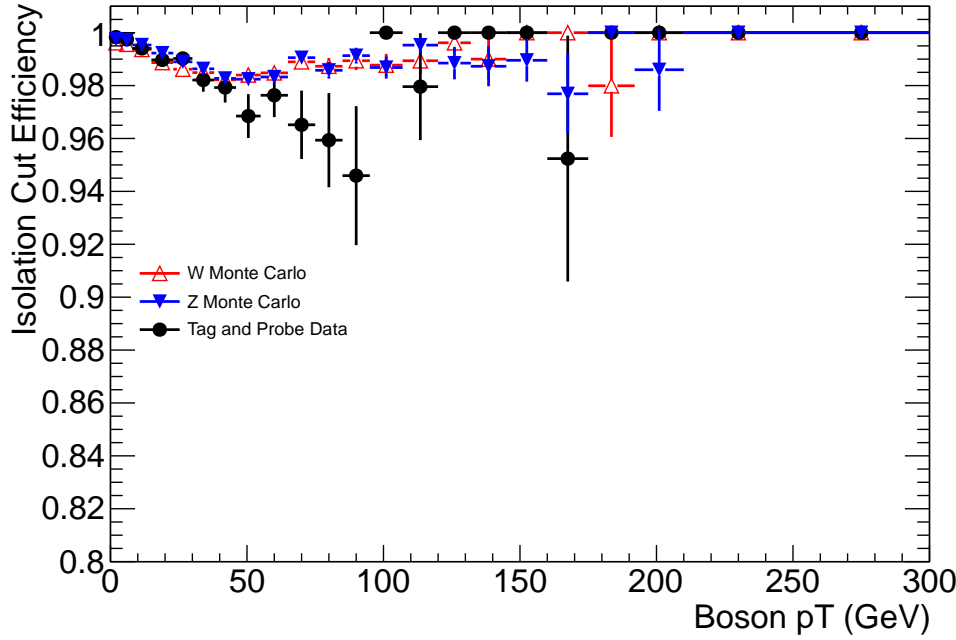


Figure 5.10: Isolation efficiency from the tag and probe technique using data (black),  $Z \rightarrow \mu\mu$  Monte Carlo (blue), and  $W \rightarrow \mu\nu$  Monte Carlo (red).

data and Monte Carlo are shown in Figure 5.10.  $\delta\epsilon_{nonQCD}$  is taken to be the statistical errors from this technique and propagated according to equation 5.10.

$\epsilon_{QCD}$  is measured in data using a control region and extrapolated with Monte Carlo to the signal region. The control region consists of all events passing preselection as described in Table 5.5. In particular, events are required to pass trigger, GRL, jet cleaning, and primary vertex requirements, and are further required to have a combined muon with  $p_T$  at least 15 GeV and no more than 20 GeV. There are no  $\cancel{E}_T$  cuts made as these are heavily correlated with hadronic recoil. This region is dominated by QCD events, with a small percentage of  $W$ ,  $Z$ , and top backgrounds, which are removed using Monte Carlo.  $\epsilon_{QCD}$  is then calculated as a function of

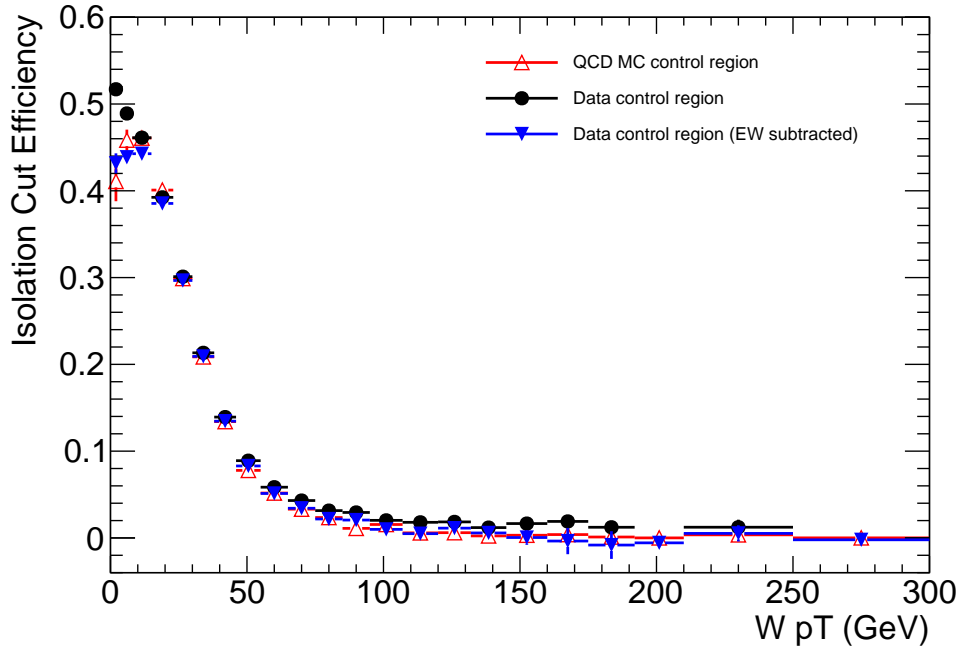


Figure 5.11: Isolation cut efficiency in the QCD control region ( $15 < p_T^\mu < 20$ ), calculated as a function of hadronic recoil in QCD Monte Carlo (red), data (black), and electroweak subtracted data (blue).

hadronic recoil using events in this region. The results are shown in Figure 5.11. Uncertainties on  $\epsilon_{QCD}$  include both statistical uncertainties as well as uncertainties on the electroweak background component.

The estimate of  $\epsilon_{QCD}$  is extrapolated from the control region to the signal region using Monte Carlo. For each bin in hadronic recoil,  $\epsilon_{QCD}$  is calculated in both the signal and control regions, and the data driven estimate is corrected by the difference of the two. Conservatively, a systematic uncertainty equal to this correction is added to the QCD background estimate. To reduce the large statistical uncertainty in the measurement of  $\epsilon_{QCD}$  in the Monte Carlo signal region, the Monte Carlo value of

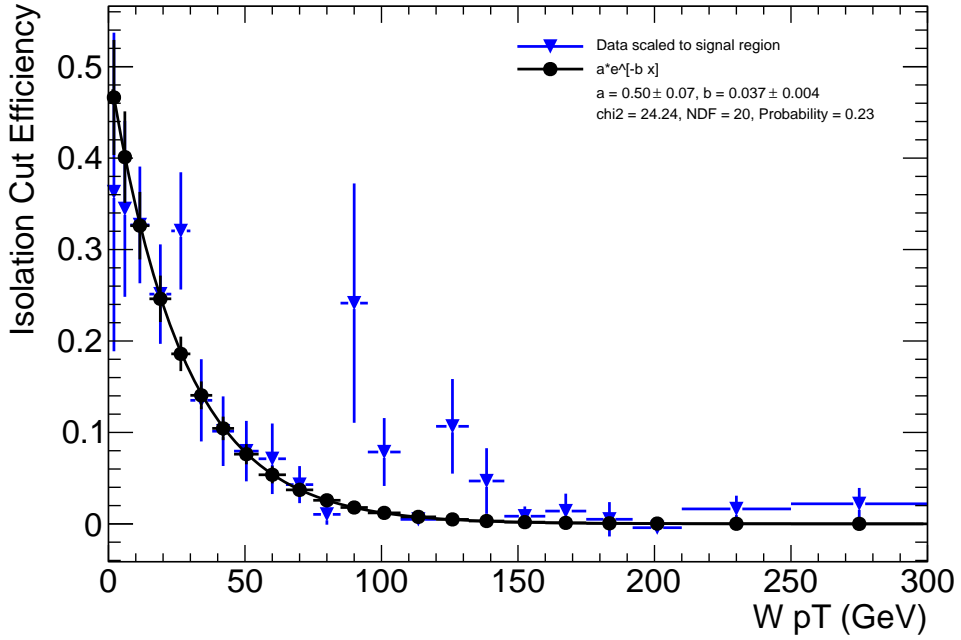


Figure 5.12: Exponential fit of  $\epsilon_{QCD}$  in the Monte Carlo signal region. The black points on the fitted curve are the values of  $\epsilon_{QCD}$  used to form the correction factor.

$\epsilon_{QCD}$  was fit with an exponentially falling distribution and the results of the fit were used to evaluate the correction factor. Note that this was not necessary for  $\epsilon_{QCD}$  in the Monte Carlo control region. The results of this fit are shown in Figure 5.12, and the resulting corrected  $\epsilon_{QCD}$  is shown in Figure 5.13. The final QCD background estimate, with associated uncertainties, is shown in Figure 5.14.

### 5.5.3 QCD in the Electron Channel

$W$  candidates passing all electron selection requirements except for the  $\cancel{E}_T$  requirement are used to produce a spectrum of  $\cancel{E}_T$  that is fit with templates for QCD and  $W$ ,  $Z$ , and top samples. A binned maximum likelihood fit is performed in bins of

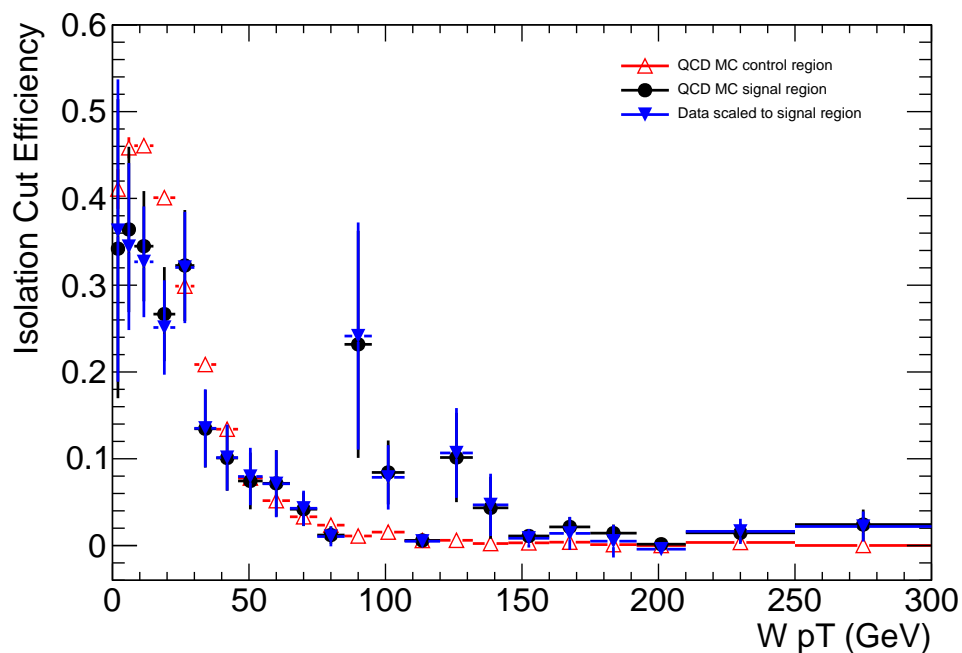


Figure 5.13: Isolation efficiency extrapolated from control to signal region using Monte Carlo.

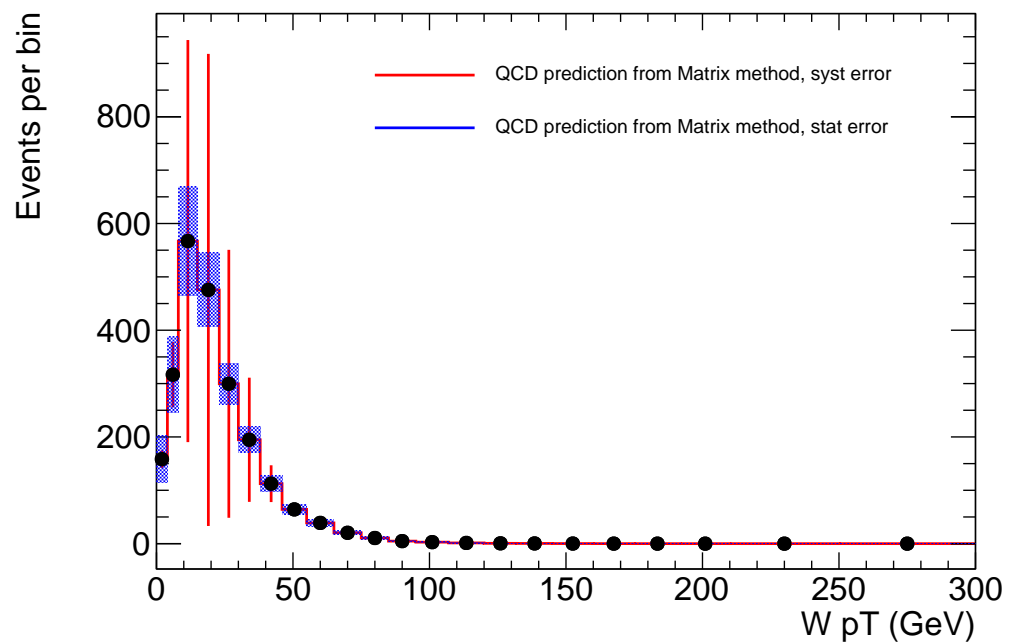


Figure 5.14: QCD background estimate in the muon channel. Systematic uncertainties are shown in red, and statistical uncertainties are shown in the blue hatched area.

$Wp_T$  using  $\cancel{E}_T$  as the discriminating variable in order to estimate the size and shape of the QCD background.

The signal and  $W$ ,  $Z$ , and  $t\bar{t}$  background templates in  $\cancel{E}_T$  are taken from Monte Carlo samples. The event selection without the  $\cancel{E}_T$  cut is applied along with corrections described in section 5.1.4 to produce a template for each sample. An overall template is then formed by calculating the weighted sum of the individual samples with weights according to the sample theoretical production cross section. The only errors on the templates which are considered are Monte Carlo statistical errors.

The QCD background template is derived using a data driven method. Events are selected for a control region by reversing the quality cuts used to reject QCD electrons. In particular, the electron must pass the normal requirements but fail requirements related to the shower shape, the number of high threshold TRT hits, or must fail isolation requirements. The modified selection was tested on QCD dijet Monte Carlo in order to confirm that it did not bias the  $\cancel{E}_T$  distribution used to form the template. Systematic uncertainties on the QCD template were formed by taking the difference in the templates when varying the various quality selection cuts.

## 5.6 Response Matrix

The response matrix defines the relationship between measured values and true values, and good modeling of the response matrix is crucial to correctly determining the  $W$  transverse momentum spectrum. This section describes the response matrix

in general, as well as the formulation used in this analysis to incorporate data driven estimations of the calorimeter resolution and bias. The eventual goal of this formulation is to invert the response matrix to determine the truth  $Wp_T$  distribution, using a process known as unfolding, which is described in section 5.7.

### 5.6.1 Definition

Consider a binned measurement of some variable, such as the  $p_T$  of the  $W$ . There is an underlying true distribution,  $\mathbf{t}$ , which is described by the values,  $t_i$ , in each bin. There is also a measured distribution,  $\mathbf{m}$ , which is different from the true distribution  $\mathbf{t}$  due to the resolution of the detector. Each event that makes up the true distribution is measured with some value, which means that each measured bin,  $m_i$ , may be written as a weighted sum over the elements of  $\mathbf{t}$ :

$$m_i = \sum_j \alpha_{ij} t_j \quad (5.11)$$

where the weights,  $\alpha_{ij}$ , describe the probability of an event in true bin  $j$  being reconstructed in measured bin  $i$ . As this is simply matrix multiplication, this relationship may be written more compactly as:

$$\mathbf{m} = \mathbf{A}\mathbf{t} \quad (5.12)$$

where  $\mathbf{A}$  is the matrix of the weights  $\alpha_{ij}$  and is known as the response matrix.

There are a number of important properties of the response matrix. First, the degree to which  $\mathbf{A}$  is diagonal describes the resolution and bias of the detector. That

is, for a detector with zero bias and infinitely good resolution, the measured value for each event is identical to the true value, and  $\mathbf{A}$  is equal to the identity matrix. Second,  $\mathbf{A}$  need not be square, as the number of measured and true bins need not be identical. In particular, this analysis uses roughly twice as many reconstruction bins as true bins, as this provides more information during the unfolding process. Finally, it is assumed that every event that makes up the true distribution  $\mathbf{t}$  also has some associated measured value. In reality, the event selection is less than 100%, and so some events within the fiducial volume are not reconstructed. Thus,  $\mathbf{A}$  describes the relationship between the true and measured values of selected events, and inverting this matrix results in a distribution at the truth selected level, which must be further corrected to the truth fiducial level via efficiency corrections.

### 5.6.2 Monte Carlo Response Matrix

The simplest response matrix is made using pure signal Monte Carlo. For each selected event, the true and reconstructed  $Wp_T$  values are used to fill  $\mathbf{A}$ . This is shown for muon and electron channels in Figure 5.15.

This response matrix has a number of advantages. First, it is very easy to formulate, as all of the necessary information is already available. Second, it can be filled with very high statistics, as it is very easy to produce more Monte Carlo if it is needed. However, it does not necessarily correctly represent the actual performance of the ATLAS calorimeter. In particular, as the response of the calorimeter is crucial to a correct measurement of the true  $Wp_T$ , any differences between simulation and data performance will bias the measurement. Thus, this analysis uses a more complicated

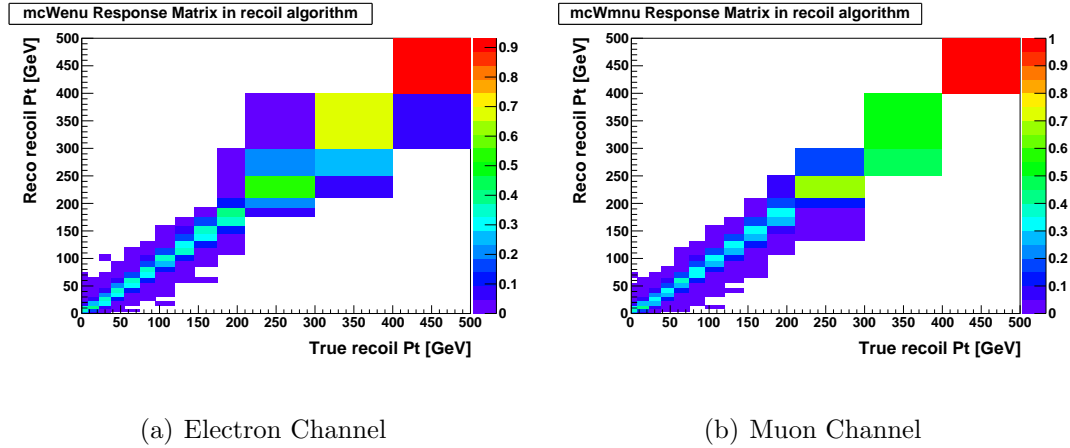


Figure 5.15: Monte Carlo based response matrices in the electron and muon channels.

response matrix formulation that allows the direct inclusion of data driven corrections.

### 5.6.3 Response Parameterization

To a very good approximation, the resolution and bias of the hadronic recoil can be parameterized as a function of the total transverse energy in the event,  $\sum E_T$  (taken as a scalar sum), and the true  $p_T$  of the  $W$ ,  $p_T^{true}$ . In particular, because of the formulation of the hadronic recoil, there is no need to include the lepton kinematics in the parameterization.

As defined in equation 5.6, the measured  $p_T$  is broken into components  $p_{\parallel}$  and  $p_{\perp}$ , which are parallel and perpendicular to the true  $p_T$  of the  $W$  respectively. For a given  $\sum E_T$  and  $p_T^{true}$ , both components are distributed according to a Gaussian distribution to very good approximation. The Gaussian distribution is parameterized according to three parameters:  $b(p_T^{true})$ , the bias as a function of  $p_T^{true}$ ;  $\sigma_{\parallel}(\sum E_T)$ , the parallel resolution as a function of  $\sum E_T$ ; and  $\sigma_{\perp}(\sum E_T)$ , the perpendicular resolution as a

function of  $\sum E_T$ . Mathematically, this can be written as:

$$p_{\parallel}(p_T^{true}, \sum E_T) \sim p_T^{true} + G(b(p_T^{true}), \sigma(\sum E_T)^2); \quad (5.13)$$

$$p_{\perp}(p_T^{true}, \sum E_T) \sim 0 + G(0, \sigma(\sum E_T)^2). \quad (5.14)$$

where  $G(\mu, \sigma^2)$  denotes a Gaussian distribution with mean  $\mu$  and variance  $\sigma^2$ .

Fits to the parameters  $b(p_T^{true})$ ,  $\sigma_{\parallel}(\sum E_T)$ , and  $\sigma_{\perp}(\sum E_T)$  in signal Monte Carlo are shown in Figure 5.16. From the parameterizations, the response matrix is made using signal Monte Carlo. For each event in the signal Monte Carlo passing event selection, the  $p_{\parallel}$  and  $p_{\perp}$  are computed using the simulated  $p_T^{true}$  and  $\sum E_T$ . The resulting values are used to compute a smeared  $p_T$  via the formula:

$$p_T = \sqrt{p_{\parallel}^2 + p_{\perp}^2} \quad (5.15)$$

and the true and smeared  $p_T$  are used to fill the response matrix. In order to maximize statistical power, this random sampling is repeated 10 times for each Monte Carlo event.

To check the quality of the fitting procedure, the reconstruction level values from the simulation are compared with the result of multiplying the response matrix obtained via fitting with the true distribution of selected events. The result of this comparison is displayed in Figure 5.17. A systematic uncertainty due to the parameterization is calculated by comparing the results of unfolding with the parameterized and Monte Carlo response matrices, and is discussed in more detail in section 5.9.

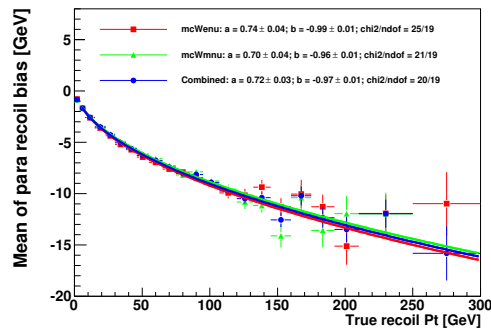
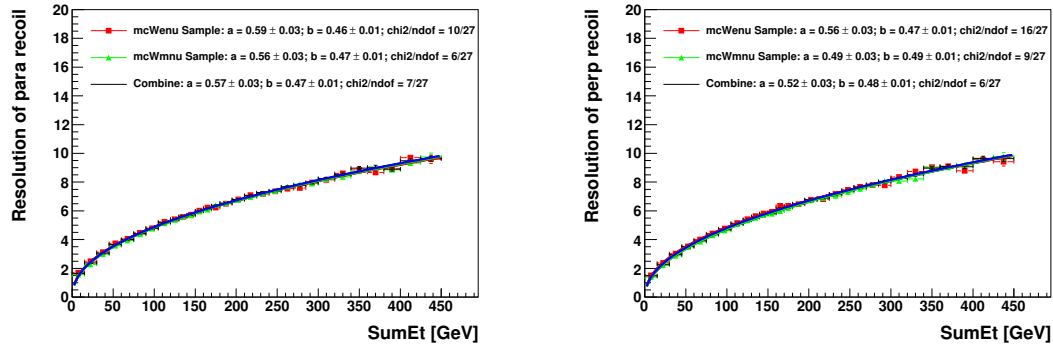
(a)  $b(p_T^{true})$ (b)  $\sigma_{\parallel}(\sum E_T)$ (c)  $\sigma_{\perp}(\sum E_T)$ 

Figure 5.16: Bias and resolution fits in  $W$  signal Monte Carlo, for the electron channel (red), the muon channel (green), and both channels combined (blue).

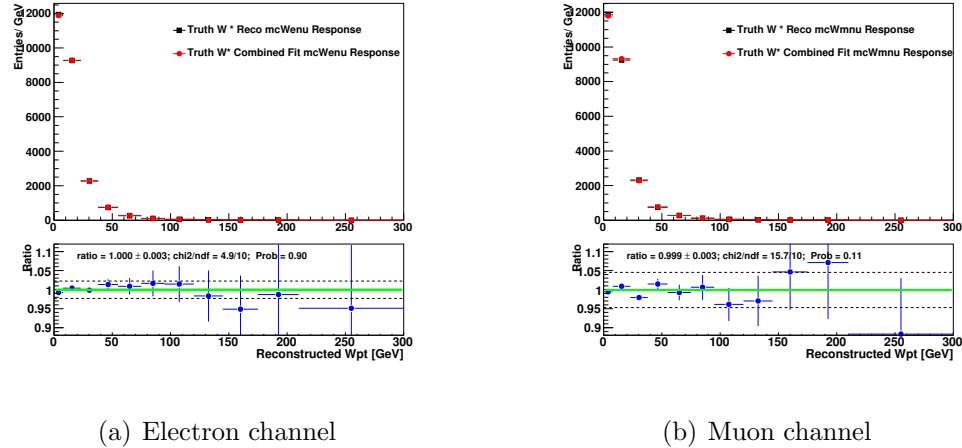


Figure 5.17: Comparison of the reconstructed simulated sample for each channel (black) with the result of multiplying the fitted response matrix from channel combined Monte Carlo with the true distribution of selected events (red).

#### 5.6.4 Data Driven Corrections

The parameterization described in the previous section is used because it allows a straightforward framework for including corrections from data.  $Z \rightarrow \ell\ell$  decays behave very similarly to  $W \rightarrow \ell\nu$  decays except that it is possible to directly measure the  $Z$   $p_T$  by combining the momentum of the two selected leptons. As the lepton resolution is much better than the calorimeter resolution, comparisons between the  $Z$  dilepton  $p_T$  and  $Z$  hadronic recoil  $p_T$  provide an important probe of the calorimeter performance.

$Z$  events are selected using the same selection as the  $W$  selection described in section 5.2 except that the  $\cancel{E}_T$  and transverse mass requirements are replaced with a requirement of two oppositely charged leptons with a combined mass between 66 GeV and 116 GeV. In these events, the fitting procedure is repeated, except that the

dilepton  $p_T$  is used in place of  $p_T^{true}$ , which is not accessible in data. The bias and resolution from  $W$  Monte Carlo is corrected with the difference between the bias and resolution in  $Z$  data and Monte Carlo according to the formulas:

$$b_W^{cor} = b_W^{MC} + (b_Z^{data} - b_Z^{MC}), \quad (5.16)$$

$$\sigma_W^{cor} = \sigma_W^{MC} + (\sigma_Z^{data} - \sigma_Z^{MC}) \quad (5.17)$$

A number of assumptions are made in using these corrections. First, it is assumed that the properties of  $Z$  and  $W$  events are very similar. While this is in general true, to improve the agreement,  $Z$  data and Monte Carlo, as well as  $W$  Monte Carlo events are reweighted to match the  $\sum E_T$  distribution observed in  $W$  data. The distributions used for this reweighting are shown in Figure 5.18. The difference between the  $\sum E_T$  weighted and unweighted fits is very small, and the full difference is taken as a systematic for this technique.

It is also assumed that the difference between  $Z$  data and  $Z$  Monte Carlo is due entirely to calorimeter resolution. In particular, as the  $Z$  events are measured with respect to the dilepton  $p_T$  rather than the true boson  $p_T$ , differences in the data and Monte Carlo lepton resolution will be counted here. To account for this, the Monte Carlo lepton momentum measurement is smeared and scaled according to detailed measurements using the  $Z$  mass constraint in data (as described in section 5.8.4). These corrections are very small compared to the calorimeter resolution differences, and thus the full difference between applying and not applying them is taken as a systematic uncertainty.

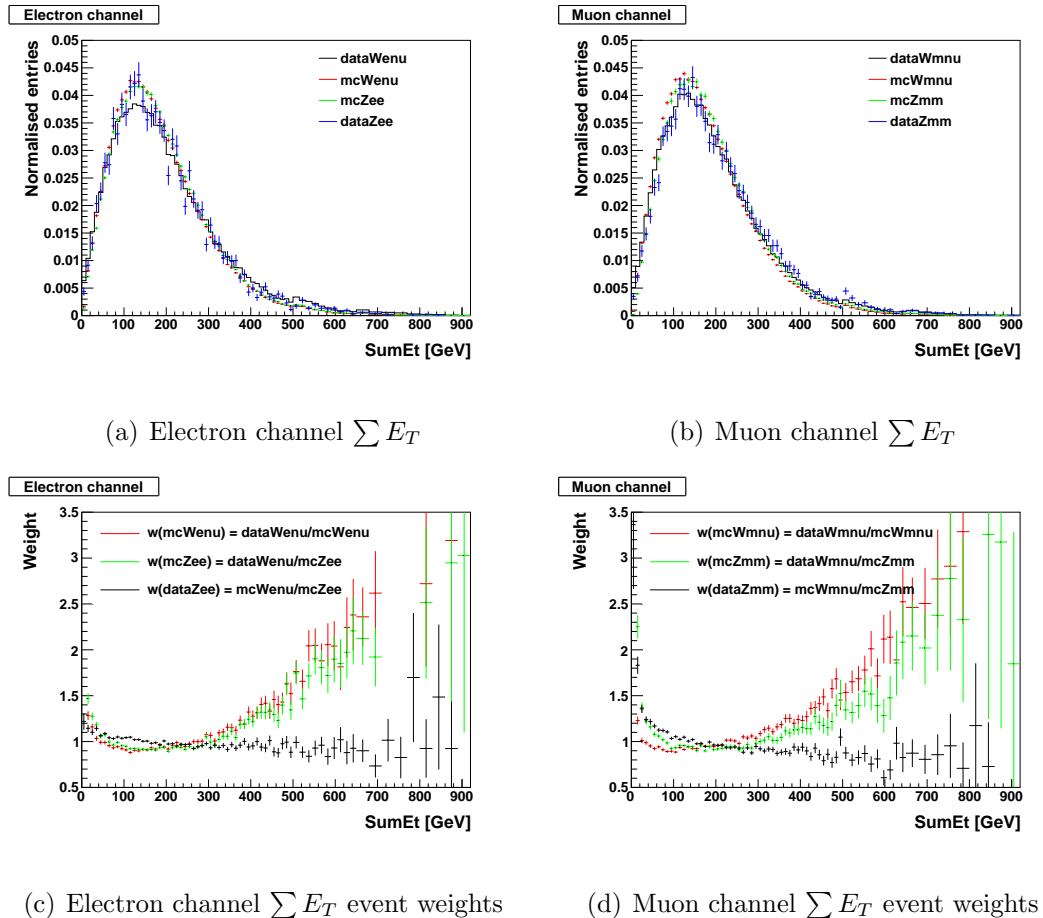
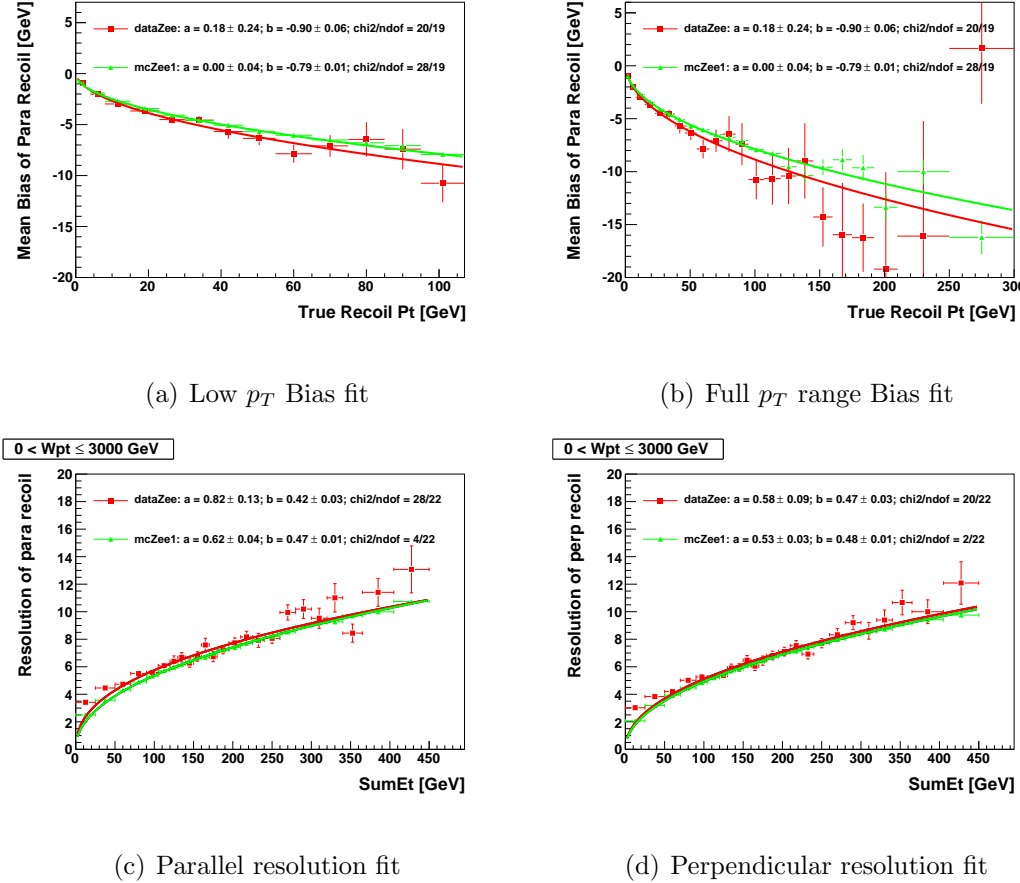


Figure 5.18:  $\sum E_T$  distributions and weights used in  $\sum E_T$  reweighting for  $W$  Monte Carlo (red),  $Z$  Monte Carlo (green), and  $Z$  and  $W$  data (blue and black).

Figure 5.19:  $Z$  data bias and resolution in the electron channel.

The resulting fits are shown for the electron channels in Figures 5.19. As described previously,  $W$  signal Monte Carlo is then smeared using the fit results. For each event in the  $W$  signal Monte Carlo passing event selection, the true  $Wp_T$  and  $\sum E_T$  in the event are converted to a smeared  $p_{\parallel}$  and  $p_{\perp}$  using the formulas in equation 5.14, and the reconstructed  $p_T$  is taken to be the sum in quadrature of  $p_{\parallel}$  and  $p_{\perp}$ . A response matrix is then built with the resulting values of  $p_T^{true}$  and the smeared  $p_T$ .

The use of Monte Carlo in filling the data driven response matrix results in a small dependence on the Monte Carlo true  $Wp_T$  distribution. In particular, while the overall shape of the true  $Wp_T$  does not affect the response matrix, the distribution of  $Wp_T$  within a given bin does. For an extreme example, consider a response matrix made with two true bins with edges at 0, 50, and 100 GeV, and four reconstruction bins with edges at 0, 25, 50, 75, and 100 GeV. Further imagine the response of the detector is perfect, in the sense that  $b$  and  $\sigma$  are both identically zero. The response matrix contains 8 elements:  $\alpha_{ij}$  for  $i = 1, 2, 3, 4$  and  $j = 1, 2$ . To preserve the number of events, for any truth bin  $j$ ,  $\sum_i \alpha_{ij}$  must be 1 - in other words, the matrix must be column normalized. Thus, changes in the number of events in truth bins 1 and 2 do not affect the produced matrix. However, if the underlying truth distribution tends to put events in the low region of each truth bin, events in the response matrix will migrate from bins  $\alpha_{21}$  and  $\alpha_{42}$  will migrate to bins  $\alpha_{11}$  and  $\alpha_{32}$  and the response matrix will change. Thus, the distribution of true  $Wp_T$  within bins does matter when filling a response matrix. To account for this, a systematic uncertainty is calculated by finding the difference between unfolded results using the nominal response matrix, and one filled with a true distribution reweighted to match the distribution from RESBOS.

A final source of uncertainty in this procedure is the limited statistics of the  $Z$  sample. During the fitting procedure, the covariance matrix of the fit parameters are extracted, and, using a large number of pseudoexperiments, the variations of the resulting response matrices due to sample statistics are examined, and a systematic calculated. A full discussion of the systematic uncertainty calculations is given in

section 5.9.

## 5.7 Unfolding

A central part of the  $Wp_T$  measurement is the correction from the reconstruction level  $p_T$  spectrum to the truth level by accounting for detector effects. In the formulation introduced in the previous section, this is done by solving the equation:

$$\mathbf{m} = \mathbf{A}\mathbf{t} \quad (5.18)$$

where  $\mathbf{m}$  is the binned measured distribution,  $\mathbf{t}$  is the binned true distribution, and  $\mathbf{A}$  is the response matrix describing the mapping of  $p_T^{true}$  to  $p_T^{reco}$ . This process, called *unfolding*, is difficult for a number of reasons, including imperfect knowledge of  $\mathbf{m}$  and  $\mathbf{A}$ , the introduction of large bin-to-bin correlations in the solution for  $\mathbf{t}$ , and inherent bias in the solution. This section describes these challenges, as well as a number of techniques to overcome them. A full description of the statistical background of unfolding and other similar inverse problems is available in [4, 51, 54, 38, 52].

### 5.7.1 Smearing

As with most things in life, the easiest unfolding technique is simply not to unfold at all. That is, in many cases the goal of the analysis is test a theory, and in those cases, it is possible to apply the response matrix to the theory rather than attempt to unfold the measured values. The theory and measurement are then compared at the reconstruction level, where a  $\chi^2$  or other difference test may be employed to validate

the theory.

This strategy has a number of desirable properties. Matrix multiplication is computationally much simpler than matrix inversion, and avoids essentially all of the pitfalls that will be discussed in the remainder of the section. However, there are a few limitations to this technique. First, while it is easy to test existing theories, it is hard for theorists to test future theories with the results, as the folding procedure is very dependent on detector specifics. This may be somewhat alleviated by publishing the response matrix as part of the result, but even that is subject to correctly matching conditions in terms of pileup and  $\sum E_T$ . Second, it is not possible to use results from smearing as an input to models that require a truth distribution. For example, it is difficult to tune Monte Carlo distributions to match experimental data without the truth spectrum. It is possible to iteratively solve for the best truth spectrum that folds into the observed data, but that pseudo-unfolding technique has all of the drawbacks and few of the positives of the unfolding techniques to be discussed. Finally, with smearing, it is very difficult to combine channel results as they have different event selection efficiency shaping effects. For these reasons, smearing is not used in this analysis.

### 5.7.2 Bin-by-bin

The simplest and most commonly used unfolding technique presented here is known as bin-by-bin unfolding. For each bin in the measured spectrum,  $\mathbf{m}$ , a correction factor,  $c_i$ , is calculated from a control sample (typically from Monte Carlo simulation) that describes the ratio of the measured to true spectra in that bin. For example,

given a simulated sample of measured  $\mathbf{m}^{\text{sim}}$  and true  $\mathbf{t}^{\text{sim}}$ , the correction factors are simply:

$$c_i = m_i^{\text{sim}} / t_i^{\text{sim}} \quad (5.19)$$

For a measured data sample  $\mathbf{m}^{\text{data}}$ , the final unfolded result is given by:

$$t_i^{\text{data}} = m_i^{\text{data}} / c_i = \frac{m_i^{\text{data}} t_i^{\text{sim}}}{m_i^{\text{sim}}} \quad (5.20)$$

This technique has a number of advantages. It is very conceptually simple, avoids complicated error calculations and bin-to-bin correlations, and requires little computation. However, it has a number of disadvantages as well. Most importantly, as the name implies, all of the corrections are within a single bin - there are no explicit bin-to-bin migration corrections. Thus, when bin purities are low, the unfolded result is highly biased to the control sample used to produce the  $c_i$  correction factors.

As an example of this bias, consider a dataset with two bins in the true and measured spectra, and a perfectly modeled response matrix with a large degree of bin to bin migration:

$$\mathbf{A} = \begin{pmatrix} a_{11}a_{12} \\ a_{21}a_{22} \end{pmatrix} \quad (5.21)$$

In this simple case, the matrix can be inverted analytically, yielding a solution for the unfolded first bin of:

$$t_1^{data} = \frac{1}{a_{11}a_{22} - a_{12}a_{21}} (a_{22}m_1^{data} - a_{12}m_2^{data}) \quad (5.22)$$

Compare this with the result from bin-by-bin unfolding using a Monte Carlo control sample. Assuming the Monte Carlo correctly models the response matrix, the measured spectrum as a function of the true spectrum is given by:

$$m_1^{sim} = a_{11}t_1^{sim} + a_{12}t_2^{sim} \quad (5.23)$$

$$m_2^{sim} = a_{21}t_1^{sim} + a_{22}t_2^{sim} \quad (5.24)$$

Applying the correction factor  $c_i = m_i^{sim}/t_i^{sim}$  to the observed data yields a bin-by-bin unfolded result for the first bin of:

$$t_1^{data} = \frac{m_1^{data}t_1^{sim}}{m_1^{sim}} = m_1^{data} \left( \frac{t_1^{sim}}{a_{11}t_1^{sim} + a_{12}t_2^{sim}} \right) \quad (5.25)$$

Compare equations 5.22 and 5.25. The analytic result is a linear combination of observed data, weighted by appropriate factors from the response matrix. The bin-by-bin unfolded result, however, is the observed data multiplied by a factor that depends on the truth distribution of the Monte Carlo sample used to produce the correction factors. For large bin-to-bin migrations (which means  $a_{12}$  far from zero), variations of the truth distribution of the Monte Carlo will result in variations in the unfolded value. The larger the migration, the larger this bias.

As it is expected that bin-to-bin migration will play an important role in this analysis, bin-by-bin unfolding is not used.

### 5.7.3 Matrix inversion

In the case where bin to bin migration effects are larger, it is tempting to solve equation 5.18 by simply inverting the response matrix,  $A$ , yielding:

$$\mathbf{t} = \mathbf{A}^{-1} \mathbf{m} \quad (5.26)$$

This approach, known as matrix inversion, has a number of benefits. It is conceptually simple and takes advantage of the large amount of work that has gone into efficiently inverting even large matrices. However, this technique is plagued by a number of problems. In particular, statistical fluctuations result in large oscillations in the unfolded spectrum due to the correlations between bins. To combat these fluctuations, a technique known as *regularization* is used. The specifics of the regularization parameters and techniques are very analysis specific and can result in large bias in the final result. This section describes the underlying issues with matrix inversion, and the techniques used to address them.

#### Difficulties with Matrix Inversion

Consider the same example used in section 5.7.2, with a 2x2 response matrix  $\mathbf{A}$  with elements  $a_{ij}$ . As before, the inverted solution for the first bin is given by:

$$t_1^{data} = \frac{1}{a_{11}a_{22} - a_{12}a_{21}} (a_{22}m_1^{data} - a_{12}m_2^{data}) \quad (5.27)$$

Assuming that both bins have the same purity,  $b$ , this can be rewritten as:

$$t_1^{data} = \frac{1}{2b - 1} (bm_1^{data} - (1 - b)m_2^{data}) \quad (5.28)$$

As  $b$  decreases towards 50%, the coefficients of  $m_1$  and  $m_2$  increase dramatically. For example, at  $b = 60\%$ ,  $t_1 = 3m_1 - 2m_2$ . At  $b = 55\%$ ,  $t_1 = 5.5m_1 - 4.5m_2$ . At  $b = 51\%$ ,  $t_1 = 25.5m_1 - 24.5m_2$ . In general, as the purity decreases, the unfolded solution becomes a difference between the two measured bins with larger and larger coefficients. As the measured bins are typically poisson distributed, these large coefficients greatly amplify otherwise insignificant statistical fluctuations.

A more general example of this amplification of statistical uncertainty due to bin purity can be seen in an example from [4]. Consider a symmetric response matrix  $\mathbf{A}$  (symmetry is not needed in general, but it makes the linear algebra a bit cleaner). As  $\mathbf{A}$  is symmetric, it may be decomposed as:

$$\mathbf{A} = \mathbf{U}\mathbf{D}\mathbf{U}^T \quad (5.29)$$

where  $\mathbf{U}$  is some orthogonal matrix and  $\mathbf{D}$  is a diagonal matrix with entries equal to the eigenvalues of  $\mathbf{A}$ . Applying this transformation to equation 5.18 yields

$$\mathbf{U}^T \mathbf{m} = \mathbf{D} \mathbf{U}^T \mathbf{t} \quad (5.30)$$

which is simply a rotated version of equation 5.18 as  $\mathbf{U}$  is orthogonal. This can be seen by writing  $\mathbf{m}' = \mathbf{U}^T \mathbf{m}$  and  $\mathbf{t}' = \mathbf{U}^T \mathbf{t}$ , yielding

$$\mathbf{m}' = \mathbf{D} \mathbf{t}' \quad (5.31)$$

Now, however, the response matrix  $\mathbf{D}$  is diagonal, and so can be directly inverted yielding:

$$\mathbf{t}' = \mathbf{D}^{-1} \mathbf{m}' \rightarrow t'_i = \sum_j \frac{m'_j}{\lambda_j} \mathbf{u}_j \quad (5.32)$$

where  $\lambda_j$  is the  $j$ -th eigenvalue of the original response matrix  $\mathbf{A}$ . The true value is given by a sum of terms like  $m/\lambda$ , where  $m$  is poisson distributed, and  $\lambda$  becomes small when bin purities decrease. As with the  $2 \times 2$  case, this division results in statistical fluctuations that are highly amplified.

## Regularization

It is clear that in order to reduce the amplification of small statistical fluctuations, it is necessary to damp the effect of small eigenvalues that occur when bin purities decrease. A common approach to this is to expand simple matrix inversion to so called *regularized matrix inversion*, where bias is intentionally injected into the solution in order to decrease oscillations. In particular, this analysis examined a technique known as Tikhonov regularization [73, 50], which will be described here. These techniques are particularly appealing because they are already supported in ROOT, via the TUnfold and TUnfoldSys classes [64, 65].

The fundamental idea behind regularization is that injecting a small amount of bias can dramatically reduce oscillations and improve the quality of the solution. Mathematically, this can be stated as a  $\chi^2$  minimization problem:

$$\chi^2 = (\mathbf{A}\mathbf{t} - \mathbf{m})^T \mathbf{V}_m^{-1} (\mathbf{A}\mathbf{t} - \mathbf{m}) + \tau^2 (\mathbf{L}\mathbf{t})^T (\mathbf{L}\mathbf{t}) \quad (5.33)$$

where  $\mathbf{V}_m$  is the covariance matrix of the data,  $\tau$  is the *regularization parameter*, and  $\mathbf{L}$  is a matrix describing the *regularization condition*.

Equation 5.33 describes the minimization of two components: the first term represents the difference between the measured value and the folded truth value, as used in the iterative smearing described in section 5.7.1; the second term describes a penalty applied by the regularization condition, which is commonly taken to be the difference in size between neighboring bins, and will be discussed in more detail shortly. The regularization parameter,  $\tau$ , determines how much the solution should depend on the goodness of the inversion, and how much should depend on the regularization condition. In particular, for  $\tau = 0$ , this is equivalent to simple matrix inversion with zero bias, and for infinite  $\tau$ , this is equivalent to maximal bias, as the measured value will be ignored completely.

This formulation has a number of advantages. First, it allows the inclusion of non-square response matrices, which cannot be accommodated by simple matrix inversion. In particular, including more measured bins than truth bins adds additional information to the problem and can improve unfolding results [4].

Second, this formulation may be solved analytically by differentiating  $\chi^2$  with respect to  $\mathbf{t}$ :

$$\frac{d\chi^2}{d\mathbf{t}} = 0 \quad (5.34)$$

$$\rightarrow 0 = \mathbf{A}^T \mathbf{V}_m^{-1} (\mathbf{A}\mathbf{t} - \mathbf{m}) + (\mathbf{A}\mathbf{t} - \mathbf{m})^T \mathbf{V}_m^{-1} \mathbf{A} + \tau^2 \mathbf{L}^T (\mathbf{L}\mathbf{t}) + \tau^2 (\mathbf{L}\mathbf{t})^T \mathbf{L} \quad (5.35)$$

$$\rightarrow \mathbf{A}^T \mathbf{V}_m^{-1} \mathbf{m} = (\mathbf{A}^T \mathbf{V}_m^{-1} \mathbf{A} + \tau^2 \mathbf{L}^T \mathbf{L}) \mathbf{t} \quad (5.36)$$

$$\rightarrow \mathbf{t} = (\mathbf{A}^T \mathbf{V}_m^{-1} \mathbf{A} + \tau^2 \mathbf{L}^T \mathbf{L})^{-1} \mathbf{A}^T \mathbf{V}_m^{-1} \mathbf{m} \quad (5.37)$$

The analytic solution allows equation 5.33 to be solved many times very quickly when doing parameter optimization, as will be discussed shortly.

Third, this formulation allows bias to be injected in order to reduce the impact of oscillations due to statistical fluctuations. Consider an example presented in [53], in which, for simplicity,  $\mathbf{L}$  is taken to be the identity matrix. From equation 5.36, this yields:

$$\mathbf{A}^T \mathbf{V}_m^{-1} \mathbf{m} = (\mathbf{A}^T \mathbf{V}_m^{-1} \mathbf{A} + \tau^2 \mathbf{1}) \mathbf{t} \quad (5.38)$$

As with equation 5.30, it is possible to decompose  $\mathbf{A}^T \mathbf{V}_m^{-1} \mathbf{A}$  into  $\mathbf{U} \Lambda \mathbf{U}^T$  where  $\mathbf{U}$  is an orthogonal matrix of eigenvectors, and  $\Lambda$  is the matrix of eigenvalues. Letting  $\mathbf{z} = \mathbf{A}^T \mathbf{V}_m^{-1} \mathbf{m}$  yields:

$$(\Lambda + \tau^2 \mathbf{1}) \mathbf{U}^T \mathbf{t} = \mathbf{U}^T \mathbf{z} \quad (5.39)$$

With  $\mathbf{b} = \mathbf{U}^T \mathbf{x}$  and  $\mathbf{c} = \mathbf{U}^T \mathbf{z}$  as before, this yields:

$$(\Lambda + \tau^2 \mathbf{1}) \mathbf{b} = \mathbf{c} \quad (5.40)$$

which may be solved (as  $\Lambda$  is the diagonal matrix of eigenvalues) as:

$$b_i = \frac{c_i}{\lambda_i + \tau^2} \quad (5.41)$$

or, back in the original coordinates:

$$\mathbf{t} = \sum_j \frac{c_j}{\lambda_j + \tau^2} \mathbf{u}_j \quad (5.42)$$

This may be compared with the unregularized solution in equation 5.32. They are equivalent, except that  $\lambda_j \rightarrow \lambda_j + \tau^2$  in the denominator. The problem of statistical fluctuations being amplified by small eigenvalues is fixed by the insertion of the  $\tau^2$  parameter. Thus, by injecting a small bias in the solution, the oscillations are largely prevented. The art of regularized unfolding is finding the correct selection of the amount and type of bias to inject, which corresponds to picking correct values for  $\tau$  and for the regularization condition matrix,  $\mathbf{L}$ .

There are a number of common regularization conditions, including size, derivative, and curvature. These are described by matrices in the following way:

$$\mathbf{L}_{size} = \begin{pmatrix} 1 & 0 & 0 & \cdots & 0 \\ 0 & 1 & 0 & \cdots & 0 \\ \vdots & \vdots & \vdots & \ddots & \vdots \\ 0 & 0 & 0 & \cdots & 1 \end{pmatrix} \quad \mathbf{L}_{derivative} = \begin{pmatrix} 1 & 0 & 0 & \cdots & 0 & 0 \\ -1 & 1 & 0 & \cdots & 0 & 0 \\ 0 & -1 & 1 & \cdots & 0 & 0 \\ \vdots & \vdots & \vdots & \ddots & \vdots & \vdots \\ 0 & 0 & 0 & \cdots & -1 & 1 \end{pmatrix}$$

$$\mathbf{L}_{curvature} = \begin{pmatrix} 1 & 1 & 0 & 0 & \cdots & 0 & 0 & 0 \\ 1 & -2 & 1 & 0 & \cdots & 0 & 0 & 0 \\ 0 & 1 & -2 & 1 & \cdots & 0 & 0 & 0 \\ \vdots & \vdots & \vdots & \vdots & \ddots & \vdots & \vdots & \vdots \\ 0 & 0 & 0 & 0 & \cdots & 1 & -2 & 1 \\ 0 & 0 & 0 & 0 & \cdots & 0 & 1 & 1 \end{pmatrix}$$

The regularization condition term of equation 5.33 is  $\tau^2 (\mathbf{L}\mathbf{t})^T (\mathbf{L}\mathbf{t})$ . In the case of  $\mathbf{L}_{size}$ , truth distributions which have large entries are penalized. In the case of  $\mathbf{L}_{derivative}$ , truth distributions with large differences between neighboring bins are penalized. Finally, in the case of  $\mathbf{L}_{curvature}$ , truth distributions with large differences between the average of the two closest neighboring bins are penalized. This analysis examined all three regularization conditions, and found that none were suitable. Size based regularization prefers solutions that are flat, which works poorly for the rapidly changing  $W p_T$  distribution. Curvature and derivative based unfolding can have large edge effects due to their reliance on neighboring bins. This was unacceptable in this analysis given the importance of the first bin near zero  $Wp_T$ .

The final piece of regularized unfolding is the selection of  $\tau$ . Several algorithms have been developed to optimize the value of  $\tau$  [4, 51, 37] and the *L-Curve* [50] algorithm will be presented here. The L-Curve algorithm is based upon balancing the two terms of the  $\chi^2$  equation so that the solution is neither under- or over-regulated. Consider the plot of the two terms of the  $\chi^2$  equation parameterized by  $\tau$  shown in Figure 5.20. Ideally, plots of these two terms have an L shape with three regions. On the left of the plot is a vertical region, where changing  $\tau$  does not change the residual, but does change the amount of regularization. This is the under-regularized region. On the right hand side of the plot, there is a horizontal region where changing  $\tau$  does not change the regularization, but does increase the residual. This is the over-regularized region, where there is too much bias in the solution. Between the two there is a kink, which has minimum regularization and residual. The L-Curve algorithm picks this value of  $\tau$  by selecting the point at which the curvature is maximized.

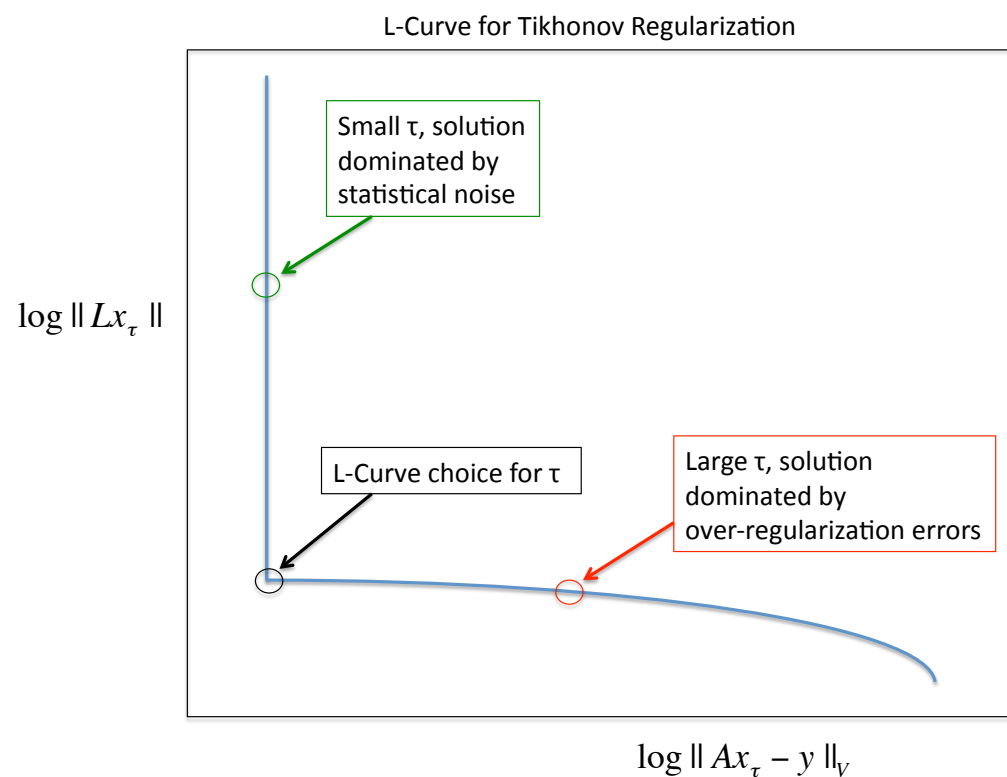


Figure 5.20: The Generic L-Curve.

While there are many advantages to this technique, there are also a number of disadvantages which resulted in the choice not to use this technique for the final result of this analysis. First, the regularization conditions typically penalize large curvature or size changes in neighboring bins in order to damp oscillations. In this analysis, the distribution is rapidly falling, with a quickly rising peak in the first bins. Many times the  $\chi^2$  optimization penalized this expected feature which resulted in large ( $\sim 10\%$ ) biases in the first bins of the final result. Second, the L-Curve technique requires solving the  $\chi^2$  equation many, many times in order to generate the curve, which is very computationally expensive. As the uncertainty propagation framework for this analysis described in section 5.9 is based heavily upon the use of toy Monte Carlo and pseudoexperiments, the added computational burden of this technique made things considerably more difficult. Finally, the L-Curve algorithm has difficulties optimizing  $\tau$  when the L-Curve lacks a region of large curvature, which was observed in this analysis. Because the L-Curves were found to be smooth, the error on the optimal  $\tau$  was large, resulting in large overall error.

#### 5.7.4 Bayesian Unfolding

The unfolding technique used for the final result in this analysis is an algorithm called *Bayesian unfolding*. Bayesian unfolding is an iterative approach which repeatedly solves Bayes theorem using the previous solution as the prior and the response matrix as the description of the probability of observed data given the true distribution. A brief description of the pertinent points of the algorithm are given here, with a more detailed description in [38].

Bayesian unfolding attempts to determine the probability distribution of true events given the observed data and the response matrix :

$$P(\mathbf{t} \mid \mathbf{m}, \mathbf{A}, I) \quad (5.43)$$

where, as before,  $\mathbf{t}$  is the true distribution,  $\mathbf{m}$  is the measured distribution,  $\mathbf{A}$  is the response matrix, and the new variable,  $I$ , is the underlying assumptions of the analysis, which are usually left as implicit.

The probability distribution in equation 5.43 is determined by using Bayes Theorem:

$$P(\mathbf{t} \mid \mathbf{m}, \mathbf{A}, I) \propto P(\mathbf{m} \mid \mathbf{t}, \mathbf{A}, I) \cdot P(\mathbf{t} \mid I) \quad (5.44)$$

where the term on the right is the likelihood of the observed data multiplied by the prior on the underlying truth distribution.

A clear problem with this approach is that the unfolded value will be strongly influenced by the underlying prior distribution. In particular, if a Monte Carlo model is used to produce a prior, as is typically the case, the unfolded values will be biased towards the Monte Carlo, which was the reason for the rejection of the bin-by-bin approach. Further, this method can suffer from similar problems as seen in the matrix inversion approach: namely, oscillations due to amplified statistical errors. To solve both of these problems, Bayesian unfolding uses an iterative smoothing approach which allows the number of iterations to be used as a regularization parameter.

The first iteration uses the Monte Carlo truth distribution as the prior. For subsequent iterations, the result from the previous iteration is used as the prior. The more iterations that are run, the less the bias from the Monte Carlo truth distribution becomes. However, at the same time, as the bias decreases, the statistical uncertainty increases, as statistical fluctuations are amplified due to the positive feedback nature of the system. Thus, the number of iterations serves to balance the strength of the bias with the size of the oscillations, exactly as the regularization parameter did in the regularized matrix inversion technique. In general, the number of iterations taken is small (less than 5), as otherwise the statistical errors become very large.

There are a number of advantages of this technique. As with the other techniques discussed, it is implemented in the RooUnfold package, which makes using it in ROOT very simple. Second, it contains only one parameter, the number of iterations, which is easily understood, and because good solutions occupy a relatively small phase space in this parameter, it is easy to search and optimize over it. Third, the algorithm is very fast, which makes uncertainty calculations via toy Monte Carlo and pseudoexperiments, as described in section 5.9, computationally feasible. Finally, the prior distribution does not negatively impact the ability of the algorithm to correctly unfold the rapidly falling distribution at low  $Wp_T$ , like was observed in the  $\chi^2$  based regularized matrix unfolding. For these reasons, with the stability in the rapidly falling region of the distribution being most important, this analysis uses Bayesian unfolding for its final result.

## 5.8 Reconstruction Efficiency Correction

As the response matrix only accounts for smearing of events that have been reconstructed, following unfolding it is necessary to correct the  $Wp_T$  spectrum for event selection efficiency. Using Monte Carlo corrected to match the efficiency observed in data, the event selection efficiency,  $\epsilon_W$ , is calculated as a function of true  $Wp_T$ .  $\epsilon_W$  is then used to correct the  $Wp_T$  spectrum from the truth selected level to the truth fiducial level. This section contains how these corrections and their systematics uncertainties are calculated.

### 5.8.1 Efficiency calculation

The event selection efficiency  $\epsilon_W$  is calculated according to:

$$\epsilon_W^i = \frac{\sum_{\substack{\text{events} \in i \\ \text{events}}} w_{reco}}{\sum_{\substack{\text{events} \in i \\ \text{events}}} w_{true}} \quad (5.45)$$

where  $\epsilon_W^i$  is the efficiency in the  $i$ -th bin in true  $Wp_T$ ,  $w_{true}$  is the pileup vertex weight, described in section 5.1.4, times the generator weight (which is simply 1 for the PYTHIA signal sample used) and  $w_{reco}$  is  $w_{true}$  times the trigger and reconstruction scale factors, which are the ratio of the efficiency in data to that of Monte Carlo, measured in bins of  $p_T$  and  $\eta$  of the lepton. These scale factors are described in more detail in the next sections. For each bin in  $Wp_T$ ,  $\epsilon_W^i$  is given by the ratio of the sum over all events in that true  $Wp_T$  bin and which are reconstructed to the sum over all events in that bin in true  $Wp_T$  that fall within the fiducial volume. Note that because of detector resolution effects, this is not a true efficiency, in the sense that

it is possible for events that do not appear in the fiducial volume (and thus are not in the denominator) to appear in the numerator. In particular, because of lepton resolution, it is not uncommon for leptons which fall slightly below the fiducial  $p_T$  or  $E_T$  cut of 20 GeV at the truth level to be selected as passing the reconstruction requirements. The resulting efficiencies in the muon and electron channel are shown in Figures 5.21 and 5.22 respectively.

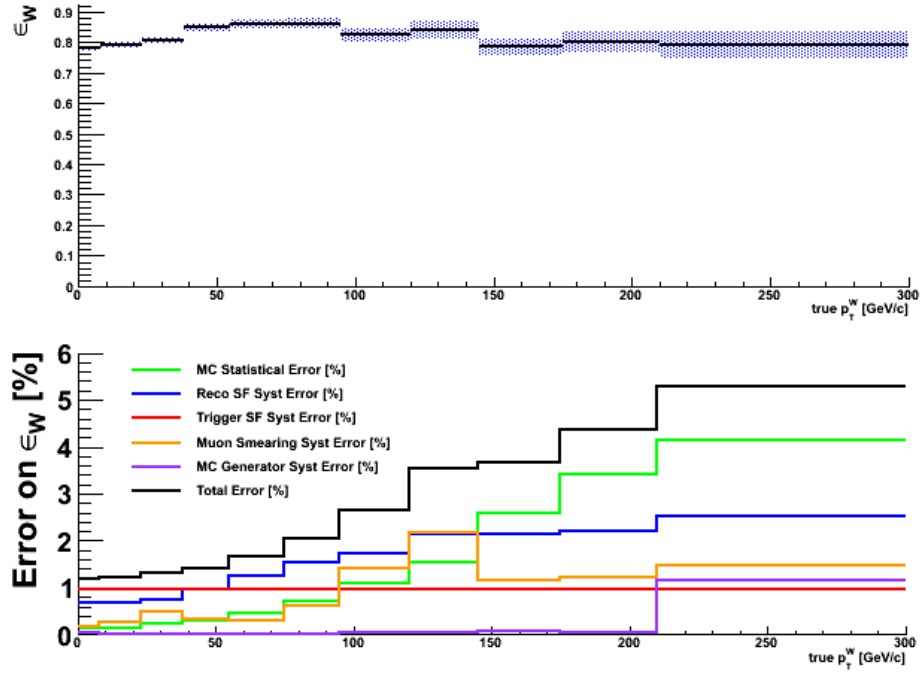


Figure 5.21: Event selection efficiency  $\epsilon_W$ , and its uncertainties, as a function of true  $W p_T$ , in the muon channel.

Several sources of uncertainty are considered for the correction factor. First, uncertainties on the trigger and reconstruction scale factors are propagated to the weight  $w_{reco}$  using a method described in section 5.8.2. Second, uncertainties on the efficiency of the analysis cuts due to detector resolution are estimated by turning the smearing

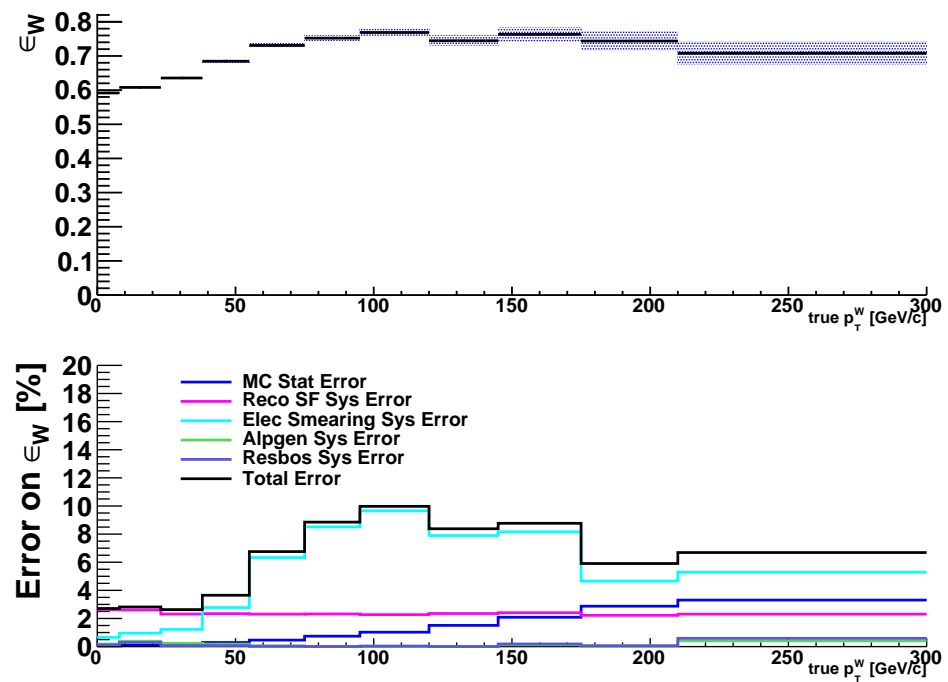


Figure 5.22: Event selection efficiency  $\epsilon_W$ , and its uncertainties, as a function of true  $W p_T$ , in electron channel.

and scaling described in section 5.8.4 off, comparing with the nominal result, and taking the full difference as a systematic uncertainty. Third, the uncertainty due to the choice of Monte Carlo generator is determined by rerunning the  $\epsilon_W$  calculation with a PYTHIA signal sample reweighted to match the  $W p_T$  spectrum from ALPGEN plus Herwig/Jimmy. The generator uncertainty is taken as the full difference between the ALPGEN result and the nominal result. Finally, a statistical uncertainty is assigned from the number of simulated events in the signal Monte Carlo. The individual uncertainties and the total uncertainty is shown in Figure 5.21 for the muon channel and Figure 5.22 for the electron channel.

### 5.8.2 Trigger Scale Factors

The trigger scale factor is the ratio of the trigger efficiency measured in data to that measured in Monte Carlo, and is used to correct the Monte Carlo so that it more correctly describes the observed data. It is measured relative to reconstructed leptons, and so can depend on the selection used.

#### Muon Channel

The muon trigger efficiency was measured using the so-called *tag and probe* technique, which uses the  $Z$  mass constraint to select a very pure sample of isolated, high  $p_T$  muons. The details of this analysis are described elsewhere [17], but a brief summary is given here.

Events were selected according to the Collision-like requirements described in section 5.2.1, and were required to have two oppositely charged muons passing the high

$p_T$  muon requirements, with an combined invariant mass within 15 GeV of the nominal  $Z$  mass, and differences in  $d_0$  and  $z_0$  of less than 2 mm. As the events are selected using the trigger under study, trigger matching (described in detail in section 4.2.2) is used. A muon is called a tag if it matches to a passed trigger object from the event filter chain under study. The other muon is then called a probe, and the trigger efficiency is taken to be the fraction of probe muons which then match to a passing trigger object from the event filter chain under study. Note that if both muons pass the trigger, then both will count as a tag and a probe. The result of this efficiency measurement for `EF_mu13_MG` and `EF_mu13_MG_tight` are shown in Figures 5.23 and 5.24. As two triggers are used, the final scale factor is taken to be the luminosity weighted average of the individual trigger scale factors. Trigger scale factors are shown as a function of muon  $\eta$  in Figure 5.25, and are calculated as a function of both  $\eta$  and  $p_T$  for the analysis.

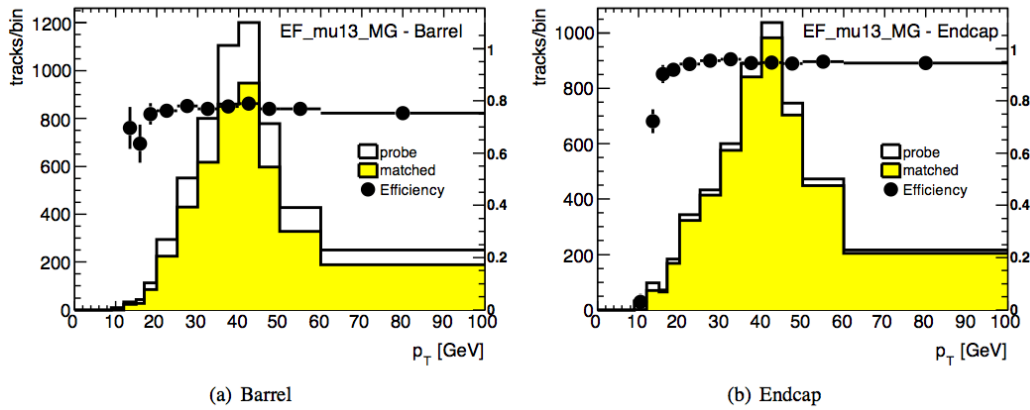


Figure 5.23: The efficiency of the muon trigger `EF_mu13_MG` in data as a function of muon  $p_T$  [17]. The scale factor is the ratio of the efficiency in data to the efficiency of `EF_mu10_MG` in Monte Carlo (not shown.).

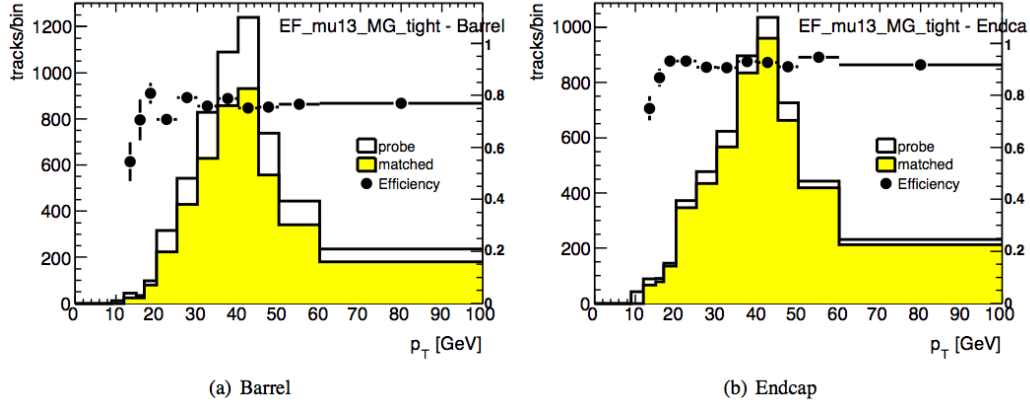


Figure 5.24: The efficiency of the muon trigger `EF_mu13_MG_tight` in data as a function of muon  $p_T$  [17]. The scale factor is the ratio of the efficiency in data to the efficiency of `EF_mu10_MG` in Monte Carlo (not shown.)

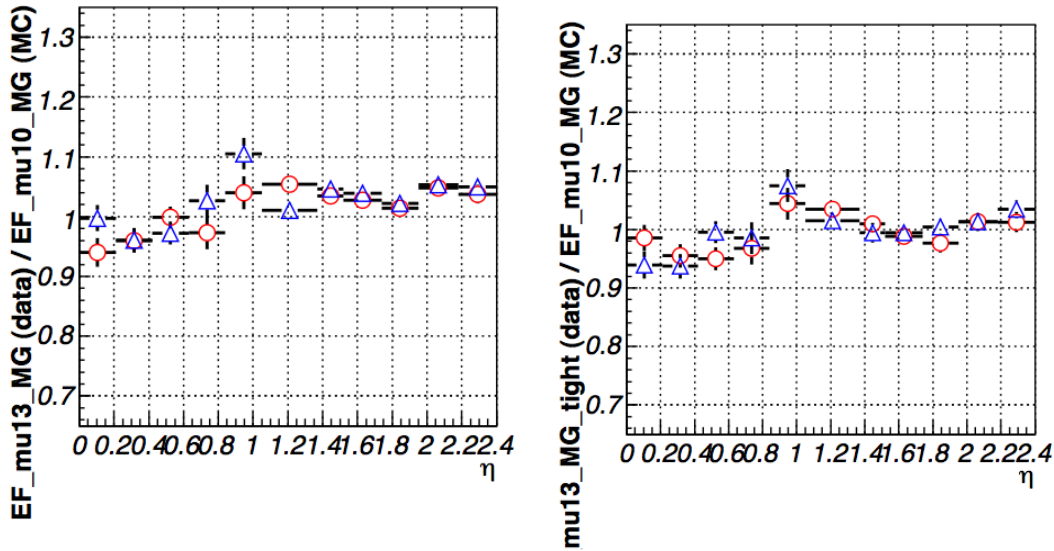


Figure 5.25: The trigger scale factor for `EF_mu13_MG` (left plot) and `EF_mu13_MG_tight` (right plot) as a function of muon  $\eta$  [17]. Red circles are for positive muons and blue triangles are for negative muons.

The uncertainties on the trigger scale factor in the muon channel are described in detail in [17] and include statistical uncertainties, as well as systematic uncertainties that are evaluated by changing the muon selection requirements and the  $Z$  candidate selection. The scale factor and uncertainties are expressed as functions of muon kinematics and must be propagated in order to express them as a function of true  $Wp_T$ . To correctly calculate the resulting correlated errors, the following formula is used:

$$\frac{\sigma_{\epsilon_W}^2}{\epsilon_W^2} = \frac{\left(\sum_{i,j} \sigma_{t_{ij}} w_{true_{ij}}\right)^2}{\left(\sum_{i,j} t_{ij} w_{true_{ij}}\right)^2} \quad (5.46)$$

where  $i$  and  $j$  are indices running over bins of reconstructed muon  $p_T$  and  $\eta$ ,  $\sigma_{t_{ij}}$  is the uncertainty on the trigger scale factor in one bin of  $p_T$  and  $\eta$ ,  $t_{ij}$  is the trigger scale factor, and  $w_{true_{ij}}$  is the vertex weight of events falling in the  $i$ -th,  $j$ -th bin.

## Electron Channel

The electron trigger efficiency is very close to one and was measured in data relative to reconstructed Medium and Tight electrons using  $Z$  tag and probe [44]. In both selections the data and Monte Carlo efficiencies are consistent within statistical error, as shown in table 5.8, and so no trigger scale factor is applied to the electron channel.

	Offline Medium	Offline Tight
Data	$98.67 \pm 0.10$	$99.03 \pm 0.09$
MC	$99.235 \pm 0.006$	$99.538 \pm 0.005$
Scale Factor	$0.9943 \pm 0.0010$	$0.9950 \pm 0.0009$

Table 5.8: Trigger efficiency in the electron channel for Monte Carlo and data and for Medium and Tight electrons [44].

### 5.8.3 Reconstruction Scale Factors

The reconstruction scale factor is the ratio of the measured reconstruction efficiency in data and in Monte Carlo and is used to correct the Monte Carlo to more correctly model the observed data. In general, this represents inefficiencies in the quality cuts used in selecting high  $p_T$  leptons. For muons, this is largely mismeasurements in the transition region of the muon spectrometer, and for the electrons, this is largely due to problems in electron identification.

#### Muon Channel

The measurement of the muon reconstruction scale factor is also made using the tag and probe technique, which is described in detail in [66]. Events are selected according to the Collision-like requirements described in section 5.2.1. In selected events, tags and probes are then formed. A tag is a muon passing all the high  $p_T$  muon requirements in section 5.2.1, while a probe is an inner detector track passing all the of ID quality,  $p_T$ , and  $|\eta|$  requirements. An event is selected if a tag and probe combination is found with  $\Delta d_0$  and  $\Delta z_0$  less than 2 mm,  $\Delta\phi > 2$ , and a combined mass within 10 GeV of the nominal  $Z$  mass. The muon reconstruction efficiency is then taken to be the fraction of probe tracks matching to a combined muon and is calculated as a function of inner detector track  $\eta$ , as shown in Figure 5.26.

The uncertainty on the reconstruction scale factor is dominated by systematic uncertainty, of which the main component is background contamination. This uncertainty is propagated to  $\epsilon_W$  using equation 5.46 in a similar way to the trigger scale factor. The two relative scale factor uncertainties are summed in quadrature.

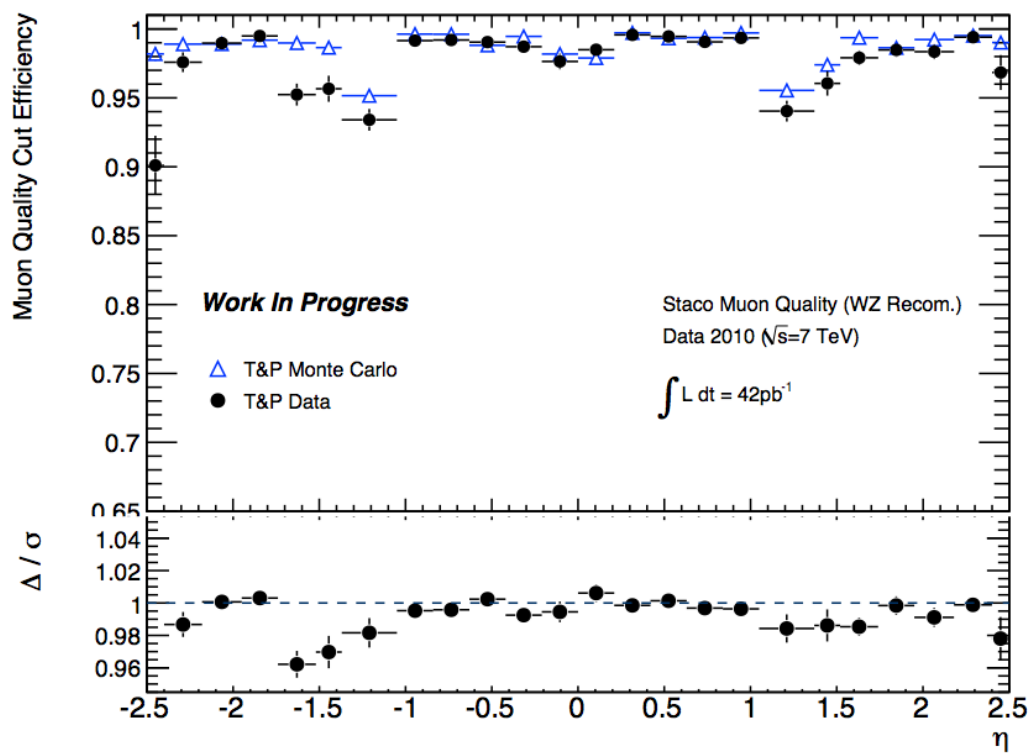


Figure 5.26: Muon reconstruction efficiency and scale factor as a function of inner detector  $\eta$  [66].

## Electron Channel

The electron identification efficiency was measured similarly using  $Z$  tag and probe [44]. The resulting scale factors as well as their uncertainties are shown in table 5.9. The propagation of these uncertainties to  $\epsilon_W$  was done similarly to the muon channel using equation 5.46.

Eta bin	$[-2.47, -2.01]$	$[-2.01, -1.52]$	$[-1.37, -0.8]$	$[-0.8, 0]$
SF tight	$0.925 \pm 0.034$	$0.995 \pm 0.024$	$1.006 \pm 0.021$	$0.982 \pm 0.018$
Eta bin	$[0, 0.8]$	$[0.8, 1.37]$	$[1.52, 2.01]$	$[2.01, 2.47]$
SF tight	$0.987 \pm 0.018$	$1.033 \pm 0.025$	$1.028 \pm 0.045$	$0.936 \pm 0.034$

Table 5.9: Electron identification efficiency and scale factor measured using tag and probe [44].

### 5.8.4 Resolution Smearing and Scaling

The lepton momentum resolution plays two important roles in this analysis. First, it affects the selection efficiency. In particular, for some values of  $Wp_T$ , the lepton  $p_T$  requirement can be in the region of rapidly rising  $p_T$  spectrum. In these cases, the efficiency increases with worsening resolution. Second, it affects the measurement of the data driven response matrix, as differences between the Monte Carlo and data lepton resolutions can be interpreted as differences in calorimeter resolution. To correctly account for this, both the electron  $E_T$  and muon  $p_T$  in Monte Carlo are smeared and scaled using values determined from data driven techniques using the  $Z$  mass constraint.

## Muon Channel

Differences between the muon momentum resolution in the data and in Monte Carlo are largely driven by misalignment, which is typically heavily dependent on the region of the detector that the muon passed through. The dimuon mass peak of the observed  $Z$  data was fit using templates built from Monte Carlo and a  $\chi^2$  minimization was performed on the smearing and scaling parameters in order to maximize the agreement. The full details of the analysis are described in [16].

Muon scaling is performed according to the equation:

$$p_T \rightarrow p_T(1 + C) \quad (5.47)$$

for the  $|\eta|$  dependent scaling factors shown in table 5.10.

Correction	$ \eta  < 1.05$	$ \eta  < 1.7$	$ \eta  < 2.0$	$ \eta  < 2.5$
$C$	-0.00066	-0.0011	0.012	0.0049
$\Delta p_2^{ID}$	0.000403	0.000913	0.001273	0.002667
$\Delta p_1^{MS}$	0.02619	0.067	0.0377	0.0407
$\Delta p_2^{MS}$	0.00018	0.00018	0.00018	0.0005

Table 5.10: Correction factors for muon smearing and scaling from muon resolution studies [16].

Muon momentum smearing is performed separately on the inner detector and muon spectrometer tracks of the muon, and then the correction to the combined  $p_T$  is taken as a weighted sum of the corrections to the parts. The muon spectrometer  $p_T$  is smeared according to:

$$p_T(MS) \rightarrow p_T(MS) \times (1 \oplus f(0, 1) \times \Delta p_1^{MS} \oplus f(0, 1) \times \Delta p_2^{MS} \times p_T) \quad (5.48)$$

where  $f(0, 1)$  is a normally distribution random number, and  $p_i^{MS}$  is an  $|\eta|$  dependent correction factor shown in table 5.10.

The inner detector  $p_T$  is smeared according to:

$$p_T(ID) \rightarrow p_T(ID) \times (1 \oplus f(0, 1) \times \Delta p_2^{ID} \times p_T) (|\eta| < 1.9) \quad (5.49)$$

and

$$p_T(ID) \rightarrow p_T(ID) \times (1 \oplus f(0, 1) \times \Delta p_2^{ID} \times p_T / \tan^2 \theta) (|\eta| > 1.9) \quad (5.50)$$

where  $p_2^{ID}$  is an  $|\eta|$  dependent correction factor shown in table 5.10.

The combined muon  $p_T$  is then corrected by:

$$p_T(CB) \rightarrow p_T(CB) \times \left[ 1 + \frac{\Delta p_T^{MS} / \sigma(MS) \oplus \Delta p_T(ID) / \sigma(ID)}{1 / \sigma(MS) \oplus 1 / \sigma(ID)} \right] \quad (5.51)$$

where  $\Delta p_T$  is the smearing correction for either the muon spectrometer or inner detector measurement, and  $\sigma$  is the expected resolution of the detector for that  $p_T$ . This mirrors the measurement of combined muon  $p_T$  normally done by the tracking software.

## Electron Channel

As with the muon channel, detailed studies of  $Z$  decays in data have shown that there are disagreements between the electron  $E_T$  resolution in data and in Monte

Carlo. The details of these studies are shown in [45]. The electron energy is corrected according to the equation:

$$E \rightarrow E + f(0, 1) \sqrt{\left(S \cdot (1 + \Delta S) \cdot \sqrt{E}\right)^2 + (C \cdot (1 + \Delta C) \cdot E)^2 - \left(S \cdot \sqrt{E}\right)^2 - (C \cdot E)^2} \quad (5.52)$$

where  $f(0, 1)$  is a normally distributed random number, as before,  $S$  and  $C$  are the correction factors given in table 5.11, and  $\Delta S$  and  $\Delta C$  are their respective uncertainties.

Eta bin	[0.0, 1.4]	[1.4, 2.5]
S	$0.1 \pm 0.2$	$0.1 \pm 0.2$
C	$0.007 \pm 1.0$	$0.007 \pm 4.0$

Table 5.11: Sampling and constant terms and their systematic uncertainties in Barrel and Endcap [45].

The quality of the smearing is assessed by comparing the Monte Carlo and data  $Z$  peaks. Prior to smearing, the prediction is shown in Figure 5.27, and after smearing in 5.28.

## 5.9 Calculation of Uncertainties

Unfolding and normalization introduce non-negligible correlations between bins in the final result. Because of this, the uncertainty propagation framework in this analysis is based around the production and propagation of covariance matrices. The uncertainties on the background estimation described in section 5.5 are converted to covariance matrices after unfolding using pseudo-experiments. The uncertainties

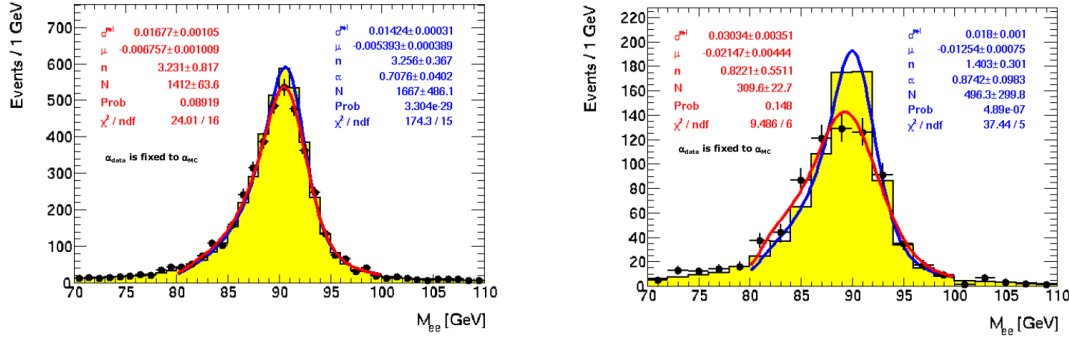


Figure 5.27:  $Z \rightarrow ee$  invariant mass distribution in data (red) and Monte Carlo (blue) before smearing is applied to the Monte Carlo. Events from the barrel are on the left, and those from the endcap are on the right [45].

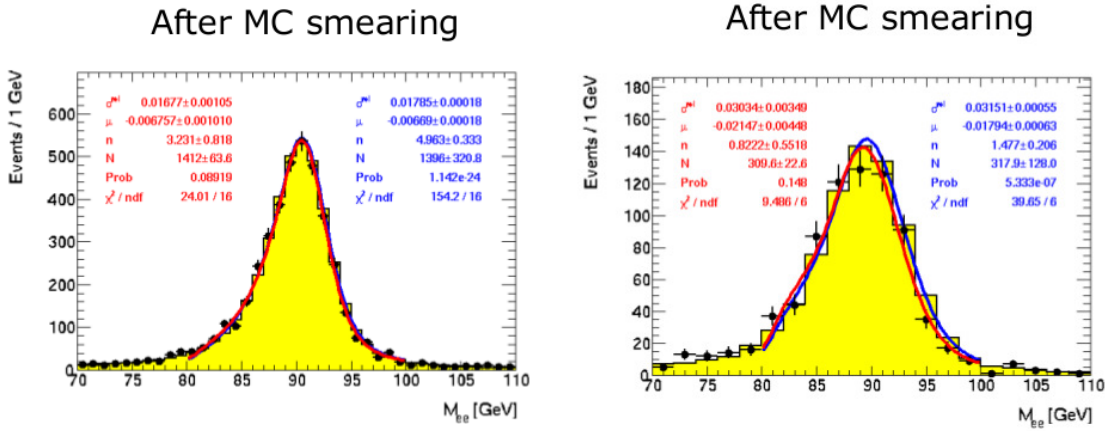


Figure 5.28:  $Z \rightarrow ee$  invariant mass distribution in data (red) and Monte Carlo (blue) after smearing is applied to the Monte Carlo. Events from the barrel are on the left, and those from the endcap are on the right [45].

on the response matrix and those due to bias of the unfolding algorithm are also reported as covariance matrices and combined with the background covariance matrices. Finally, the uncertainties on the efficiency correction described in section 5.8 are combined, and the final, normalized result is presented with a covariance matrix for both the statistical and systematic uncertainties. The statistical uncertainty of the result is also determined using pseudo-experiments, as the unfolding introduces non-trivial statistical correlations. This section describes the details of the calculation of the covariance matrices, which are listed in Table 5.12, and their propagation to the final answer.

Source	Covariance Name	Evaluation Method
QCD Bkg Subtraction	$V_{QCD}$	Pseudoexperiments
WZ Bkg Subtraction	$V_{WZ}$	Pseudoexperiments
top Bkg Subtraction	$V_{t\bar{t}}$	Pseudoexperiments
$\sum E_T$ reweighting	$V_{sumet}$	On/Off comparison
Lepton resolution and scale	$V_{smearing}$	On/Off comparison
Generator dependence	$V_{truth}$	Comparison with RESBOS
Fit parameterization	$V_{fit}$	Comparison with Generated
Fit statistics	$V_{fitstats}$	Pseudoexperiments
Unfolding Bias	$V_{bias}$	Closure Test
Unfolding Statistical Errors	$V_{stat}^{unfolding}$	Pseudoexperiments
Efficiency correction	$V_{eff}$	Analytic Propagation

Table 5.12: Sources of uncertainty.

### 5.9.1 Statistical Formulation

A number of uncertainty calculations in this analysis use pseudo-experiments, in which either the response matrix or the background estimate is fluctuated and a covariance matrix is produced. The statistical formulation of this process is described

here.

Consider a histogram,  $\mathbf{x}$ , with  $n$  bins, whose elements are  $\mathbf{x} = x_1, \dots, x_n$ . For each pseudo-experiment, a new histogram,  $\mathbf{x}^j$ , with elements  $\mathbf{x}^j = x_1^j, \dots, x_n^j$  is produced.

Three quantities are built from this set of  $p$  measurements.

First, the average histogram,  $\mathbf{E}$  is defined by

$$E_i = \frac{1}{p} \sum_j x_i^j \quad (5.53)$$

Next, the covariance matrix  $\mathbf{V}$  is defined by

$$V_{ij} = \frac{1}{(p-1)} \sum_k [(x_i^k - E_i)(x_j^k - E_j)] \quad (5.54)$$

The covariance matrix has a number of nice properties. In particular, the diagonal elements are the square of the standard deviation of that bin. Ignoring correlations between bins, then, one may plot the square root of the diagonals to represent the uncertainty. This also means that for uncorrelated uncertainties, summing in quadrature is equivalent to adding covariance matrices. However, because the covariance matrices include the absolute variance of each bin, and there are large variations in the number of entries per bin in this analysis, it is difficult to visualize uncertainties using covariance matrices. For example, if the first bin has 10,000 events with an uncertainty of 1%, while the last bin has 10 entries with an uncertainty of 10%, the diagonal element of the covariance matrix for the first bin will be roughly 10,000 times larger than that for the last bin.

To allow easier visualization, a third quantity, the correlation matrix,  $\rho$ , is also calculated:

$$\rho_{ij} = \frac{V_{ij}}{\sqrt{V_{ii}V_{jj}}} \quad (5.55)$$

The correlation matrix has the nice property that the diagonals are, by construction, 1, and the off diagonals are between  $-1$  and  $1$ . Entries which have correlations near 1 tend to vary up and down together, while those with correlations near  $-1$  tend to vary oppositely, and entries with correlations near 0 tend to be independent.

### 5.9.2 Background Subtraction

The background uncertainties described in section 5.5 are converted to a covariance matrix in a two step process. First, the background estimations are varied within their uncertainties over 1000 trials. Next, the data is background subtracted using the estimated background for each trial, and unfolded. The resulting covariance matrix formed from the unfolded results of the pseudoexperiments is used as the uncertainty for the background subtraction.

The backgrounds are broken into three groups:  $W/Z$  style backgrounds ( $W \rightarrow \tau\nu$ ,  $Z \rightarrow \ell\ell$ , and  $Z \rightarrow \tau\tau$ ), top style backgrounds ( $t\bar{t}$  and single top), and the QCD background. The uncertainties are broken into two types: shape uncertainties, which are considered 100% uncorrelated bin-to-bin, and scale uncertainties, which are considered 100% correlated bin-to-bin. For the  $W/Z$  and top backgrounds, the shape uncertainties are taken to be the statistical uncertainty, the PDF uncertainty, and the

scale factor uncertainties, while the scale uncertainty is taken to be the cross section uncertainty. For the QCD, the total uncertainty is taken as a shape uncertainty.

For each pseudo-experimental trial of the background variations, the background estimate is produced as follows. First, a luminosity is picked according to a gaussian distribution centered around the nominal value with a width of 3.4%. The  $W/Z$  and top backgrounds are scaled according to this luminosity, while the QCD is left unchanged. Next, for the  $W/Z$  and top backgrounds, a scale value is picked from a gaussian distribution centered around one, with a width given by the scale uncertainty, and the background group is scaled by that amount. Note that this technique accounts for the fact that the cross section uncertainties on the  $W/Z$  and top style backgrounds are correlated within the group, but not correlated to each other. Finally, for each background group, the estimate is changed bin by bin according to the shape uncertainty. In order to allow visualization of the uncertainty due to each source, each trial actually produces four background estimates: one where only the  $W/Z$  backgrounds are varied, one where only the top backgrounds are varied, one where only the QCD is varied, and one where all three are varied simultaneously. As there are small correlations between the samples (due mainly to the luminosity appearing in both  $W/Z$  and top backgrounds), only the final estimate, where all three groups are varied, is used in the final analysis.

The pseudo-experiment variations of the backgrounds then are translated into covariance matrices. For each trial, the estimated background for that variation is subtracted from the observed data, and the result is unfolded using the nominal response

matrix. The uncertainty covariance matrices for the background subtraction, which are termed  $V_{WZ}$ ,  $V_{t\bar{t}}$ ,  $V_{QCD}$ , and  $V_{BKG}$  are calculated over the pseudo-experiments according to equation 5.54. The resulting diagonals of the covariance matrix, for each background varied separately, along with all three varied at once, is shown for the muon channel in Figure 5.29 and for the electron channel in Figure 5.30, while the correlation matrices are shown in Figures 5.31 and 5.32 respectively.

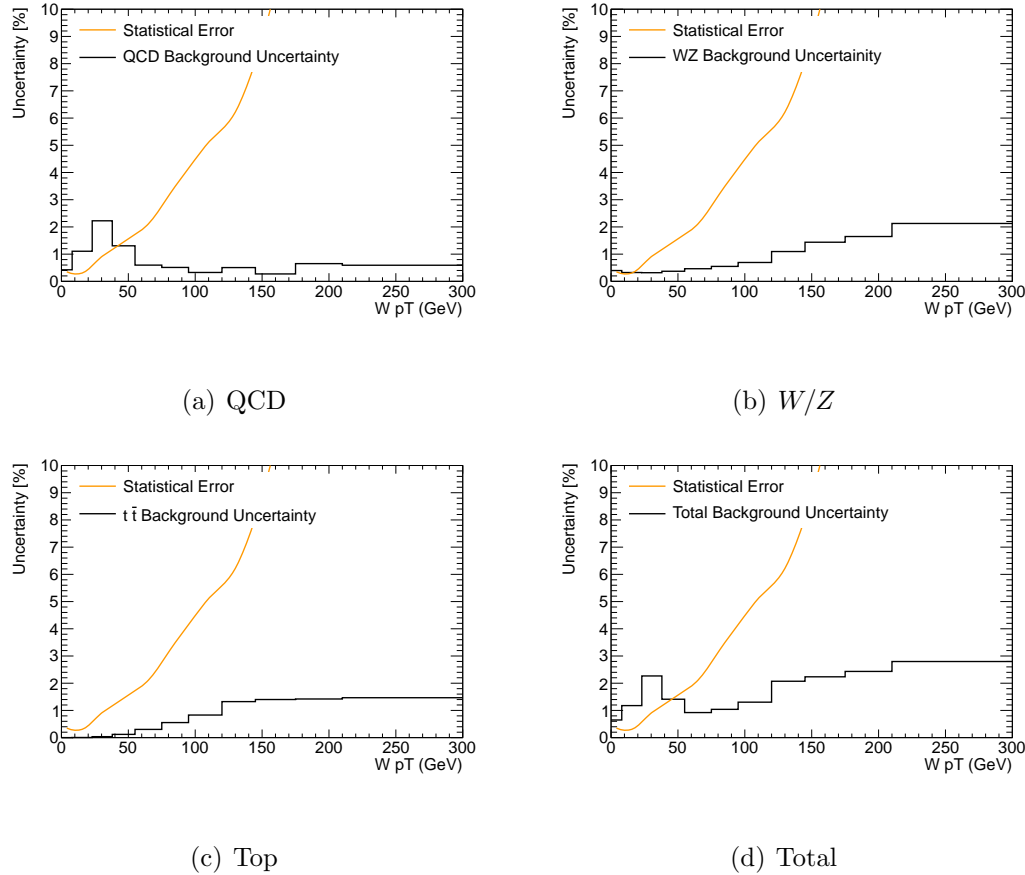


Figure 5.29: Diagonal elements of background uncertainty covariance matrices for the muon channel broken down by sample, and for the total background. The data statistical uncertainty is shown for comparison.

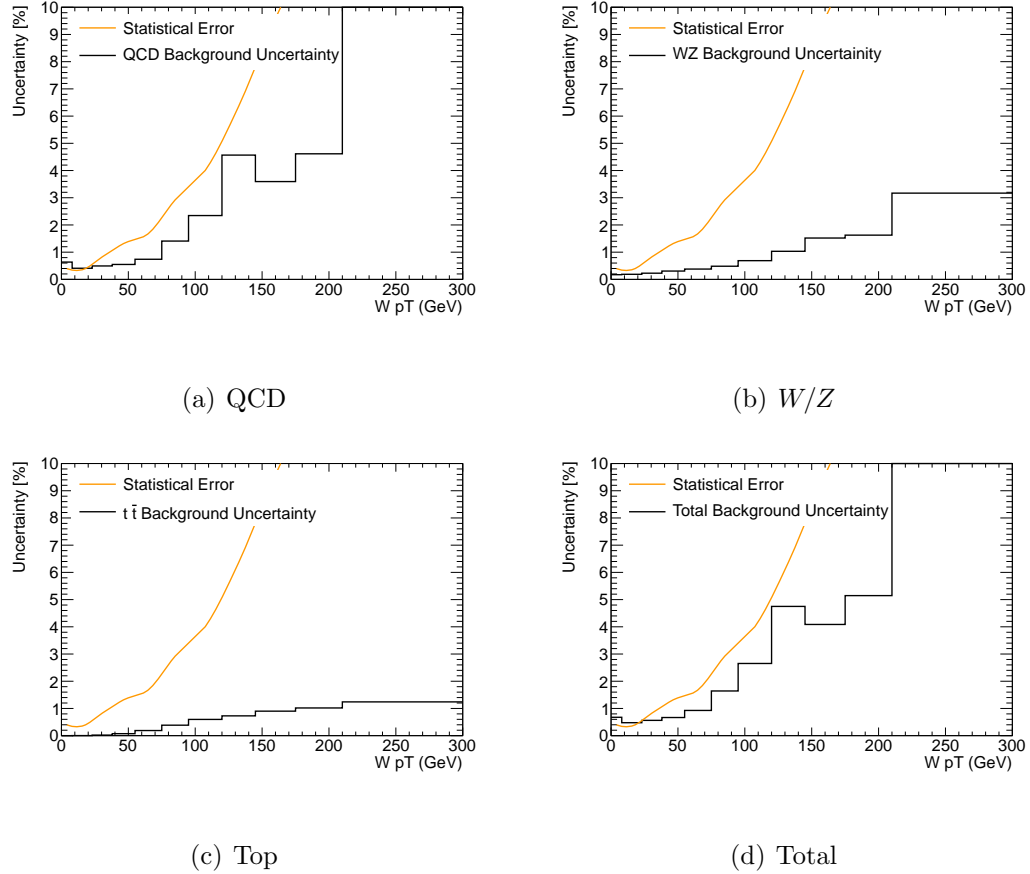


Figure 5.30: Diagonal elements of background uncertainty covariance matrices for the electron channel broken down by sample, and for the total background. The data statistical uncertainty is shown for comparison.

### 5.9.3 Response Matrix

There are two types of uncertainties on the response matrix which are considered here. The first type is due to fluctuations in the formulation of the response due to the limited statistics of the data and Monte Carlo samples. Covariance matrices for these types of uncertainties are calculated by sampling from the fitting functions described in section 5.6, producing many copies of the response matrix varied within error, and then unfolding. This process is repeated for 100 trials. The second type is

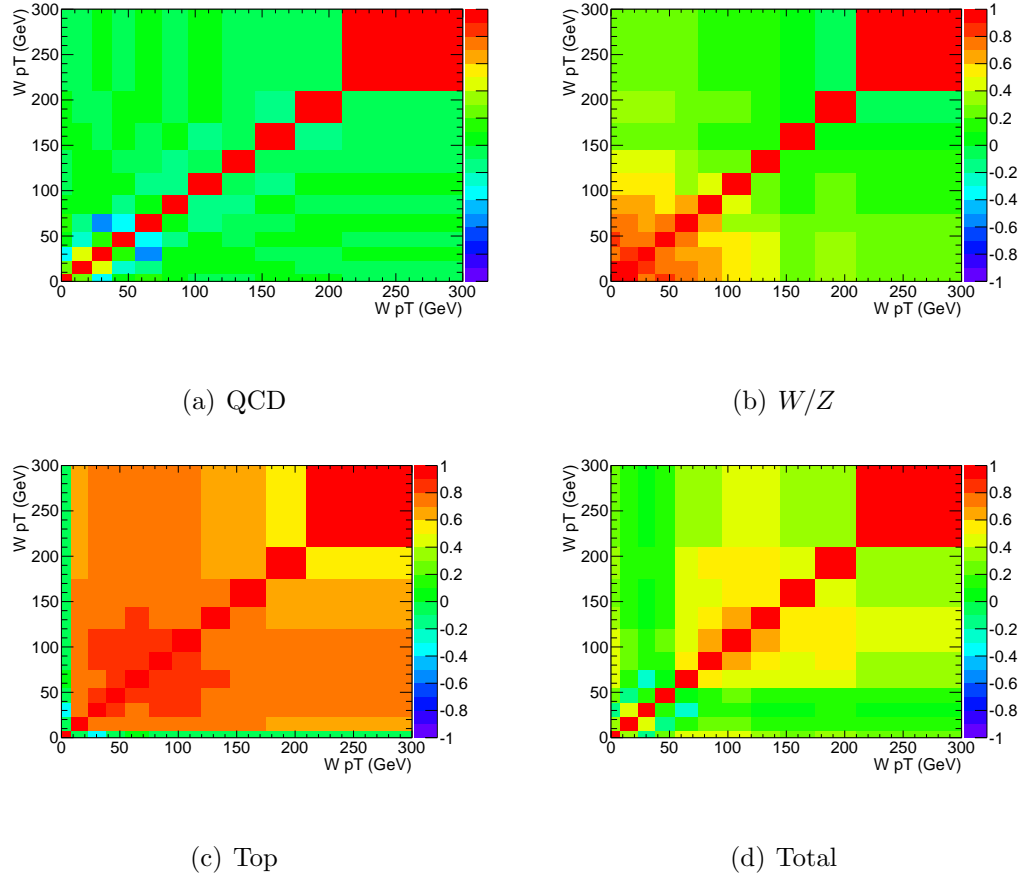


Figure 5.31: Correlation matrices for the background uncertainty of the muon channel broken down by sample, and for the total background.

due to uncertainties in the formulation of the response matrix from the reweighting procedure described in section 5.6. Covariance matrices for these types are produced by folding the sample with the nominal response matrix, and then unfolding with the response matrix under study. As each contribution is independent, the resulting covariance matrix for the uncertainty of the response matrix is taken as the sum of the covariance matrices produced in these studies.

Fluctuations in the fitting results of the response matrix formulation are propagated to the systematic covariance matrix by performing pseudo-experiments in which the

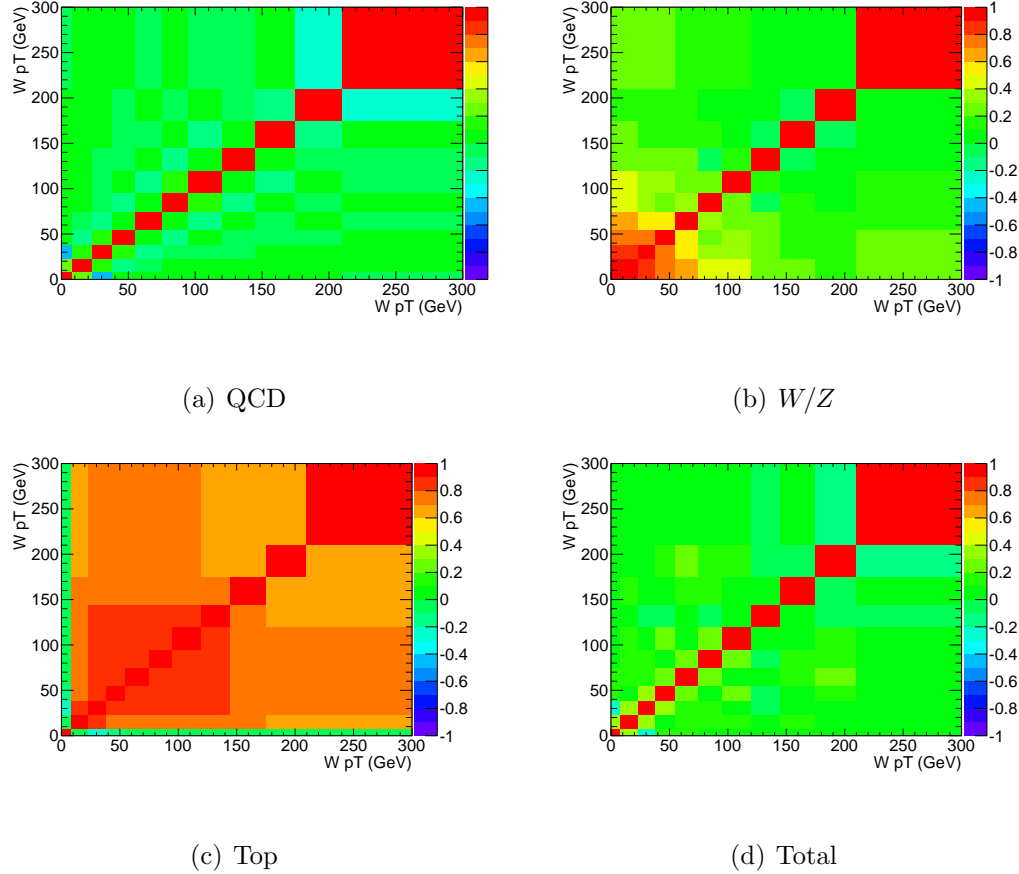


Figure 5.32: Correlation matrices for the background uncertainty of the electron channel broken down by sample, and for the total background.

fit parameters are varied within their allowed errors. First, the nominal fits are performed on the  $Z$  data, the  $W$  Monte Carlo, and the  $Z$  Monte Carlo, and the parameter errors and covariances are recorded. For each pseudo-experiment, the fit parameters for all three data samples are sampled from the fit errors using Cholesky decomposition (see [70] for the ROOT implementation used in this analysis) in order to correctly account for the correlations between the fit parameters. The filling of the response matrix described in section 5.6 is then repeated with the sampled fit parameters, and a new response matrix is produced. The background subtracted data is then

unfolded with each produced response matrix, and the systematic covariance matrix, called  $V_{fitstat}$  is produced from the trials according to the formulation described in section 5.9.1.

Systematic uncertainties for the reweighting and fitting procedure described in section 5.6 are produced by comparing the results of unfolding signal Monte Carlo with the various weightings removed with the nominal unfolding. Four types of systematics are considered.

While PYTHIA is used to form the nominal response matrix, it is necessary to determine the effects of the underlying truth distribution used to sample the fitted response matrix. To determine this, the signal Monte Carlo is unfolded with the data driven response matrix sampled using PYTHIA Monte Carlo and another sampled using PYTHIA Monte Carlo that has been reweighted to match the  $Wp_T$  spectrum produced by the RESBOS generator. For comparison, a similar procedure is done with the  $Wp_T$  spectrum produced by the ALPGEN generator, but this is not used as the ALPGEN predictions are highly inconsistent with the reconstruction level  $Wp_T$  spectrum.

Similarly, the effects of  $\sum E_T$  reweighting and lepton resolution smearing and scaling are probed by comparing the results of unfolding the signal Monte Carlo with  $\sum E_T$  reweighting and lepton momentum smearing turned off with the results of unfolding with the nominal response matrix. Finally, the effects of the fitting procedure itself are considered by comparing the results of unfolding with a response matrix built by fitting the signal Monte Carlo with a response matrix built by simply filling

the matrix with the truth and reconstructed values of the Monte Carlo.

In all cases, the maximum difference in any bin is conservatively taken as the systematic for all bins, and a diagonal covariance matrix is built for each source using those values. This results in four systematic covariance matrices, termed  $V_{sumet}$ ,  $V_{smearing}$ ,  $V_{truth}$ , and  $V_{fit}$ . The diagonal elements of these covariance matrices are shown for the muon channel in Figure 5.9.3 and for the electron channel in Figure 5.9.3, while the correlation matrix for the fit statistical uncertainty is shown in Figures 5.35 and 5.36 respectively.

#### 5.9.4 Unfolding

Two sources of unfolding uncertainty are considered in this analysis. First, the unfolding algorithm tends to enlarge the statistical errors on the sample, as well as produce correlations between bins. This statistical uncertainty is calculated by poisson fluctuating the Monte Carlo 100 times and comparing with the nominal truth distribution. Second, there is a small but non-negligible systematic uncertainty due to inherent bias in the unfolding algorithm. This is calculated by folding and then unfolding the same sample with the nominal response matrix.

To calculate the statistical uncertainty following unfolding, which is used as the final statistical uncertainty for the result, pseudo-experiments involving poisson fluctuating the Monte Carlo are used. For each trial, the reconstructed signal Monte Carlo is scaled to the number of events observed in data after background subtraction, and each bin value is sampled according to a poisson distribution with parameter

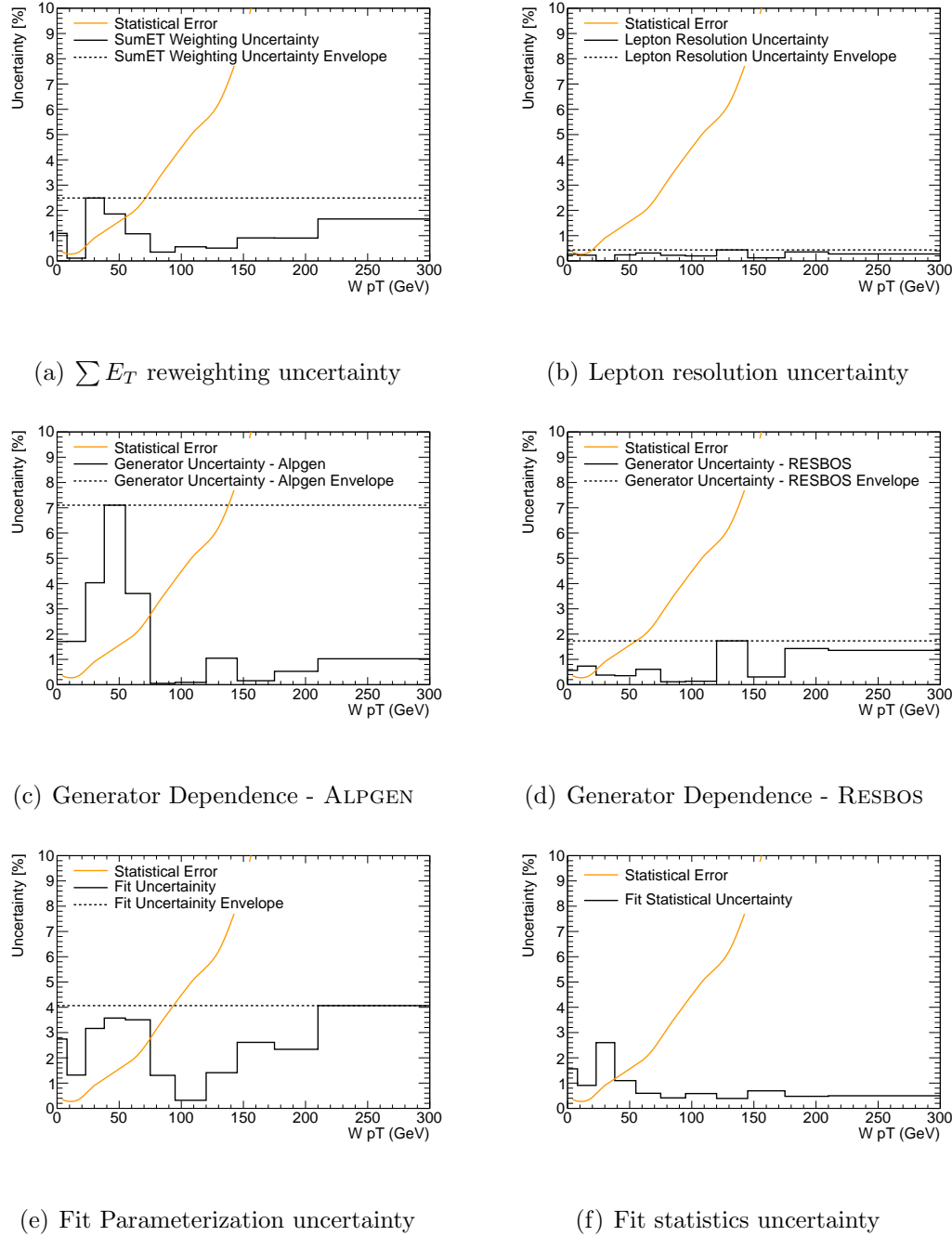


Figure 5.33: Diagonal elements of the covariance matrix for uncertainties from the response matrix of the muon channel, broken down by source. For all but the fit statistical uncertainty, the maximum difference in any bin is shown as the dotted line and is used as the systematic in all bins. Note that the ALPGEN result is not used in the final systematic.

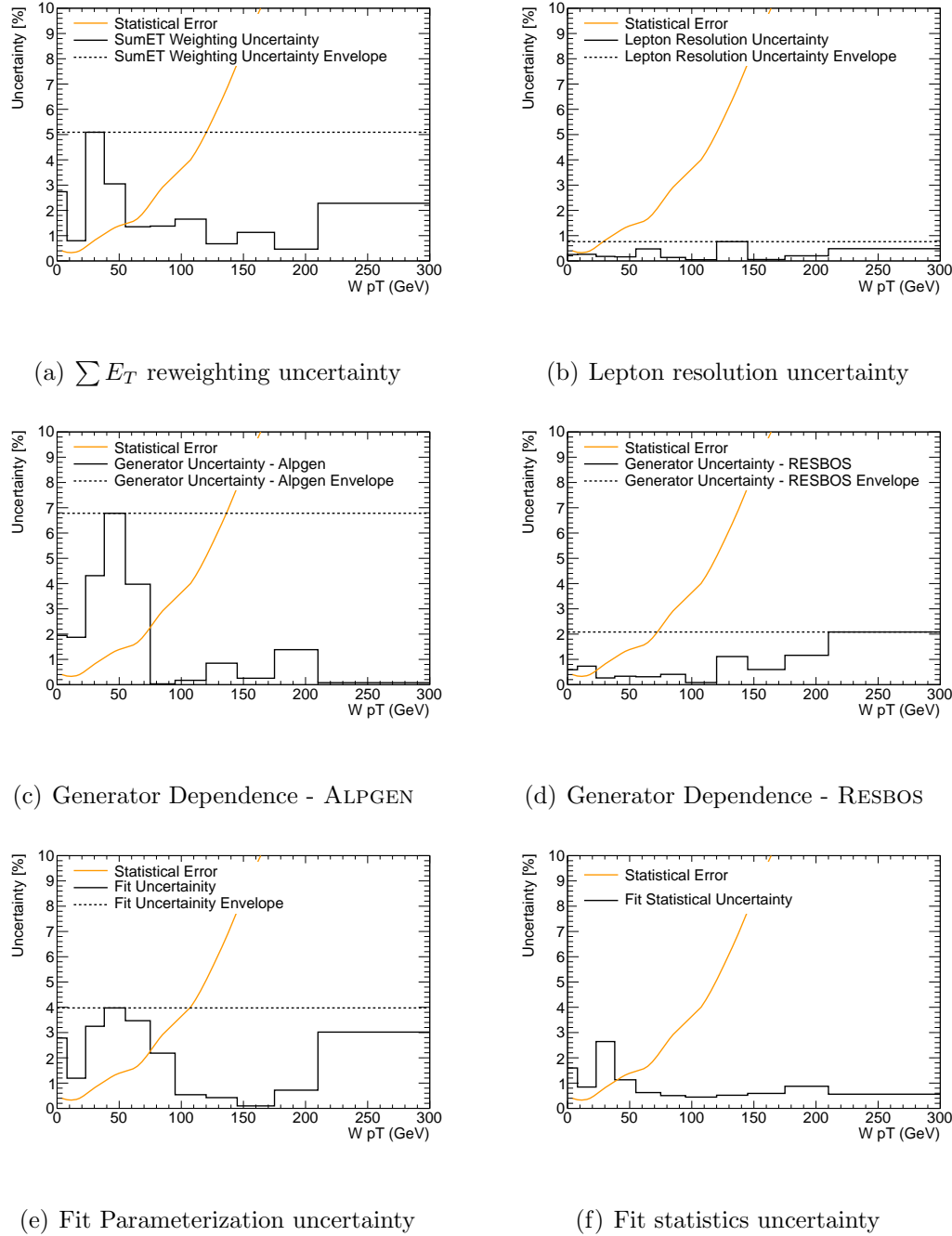


Figure 5.34: Diagonal elements of the covariance matrix for uncertainties from the response matrix of the electron channel, broken down by source. For all but the fit statistical uncertainty, the maximum difference in any bin is shown as the dotted line and is used as the systematic in all bins. Note that the ALPGEN result is not used in the final systematic.

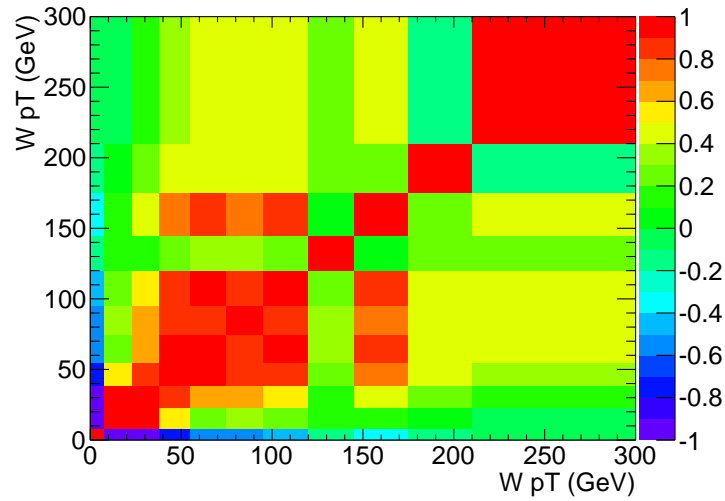


Figure 5.35: Correlation matrix for the fit statistical uncertainty for the muon channel.

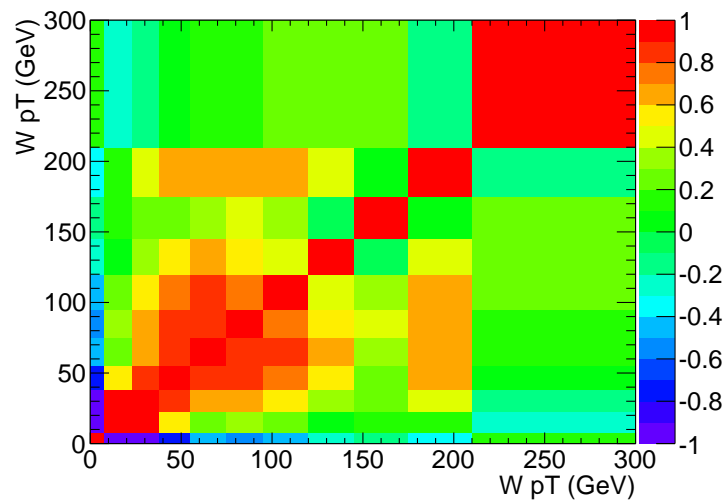


Figure 5.36: Correlation matrix for the fit statistical uncertainty for the electron channel.

equal to the number of entries in the bin after scaling. The fluctuated reconstruction level Monte Carlo is then unfolded using the nominal response matrix, and the answer is compared with the unfluctuated Monte Carlo truth distribution for selected events. The resulting difference is used to fill the covariance matrix for the statistical uncertainty after unfolding, termed  $V_{stat}^{unfolding}$ .

The other source of uncertainty in the unfolding process is the bias of the algorithm. This is understood by dividing the Monte Carlo into two samples: a sample for building the response matrix, and a sample for evaluating the systematic. The reconstructed Monte Carlo distribution of the second sample is then unfolded using a response matrix built from filling the truth and reconstruction values from the first sample. The result is then compared with the truth distribution in the second sample for selected events, and the full bin-by-bin difference is taken as the systematic uncertainties. A diagonal covariance matrix,  $V_{bias}$ , is built using these uncertainties. The diagonal elements of the unfolding statistical and systematic covariance matrices are shown for the muon channel in Figure 5.37 and for the electron channel in Figure 5.38, while the correlation matrices for the unfolding statistical uncertainty are shown in Figures 5.39 and 5.40 respectively.

### 5.9.5 Efficiency Calculation

The efficiency correction uncertainties are typically small compared with other uncertainties, and the efficiency corrections themselves are relatively flat. Thus, we consider uncertainties on the efficiency to be bin-by-bin uncorrelated, and use a diagonal covariance matrix to represent its uncertainties.

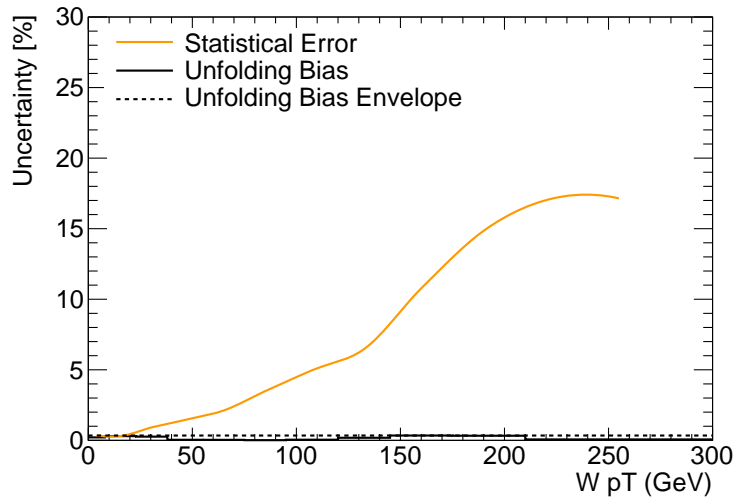


Figure 5.37: Diagonal elements of the covariance matrix of the muon channel for systematic and statistical uncertainties due to unfolding.

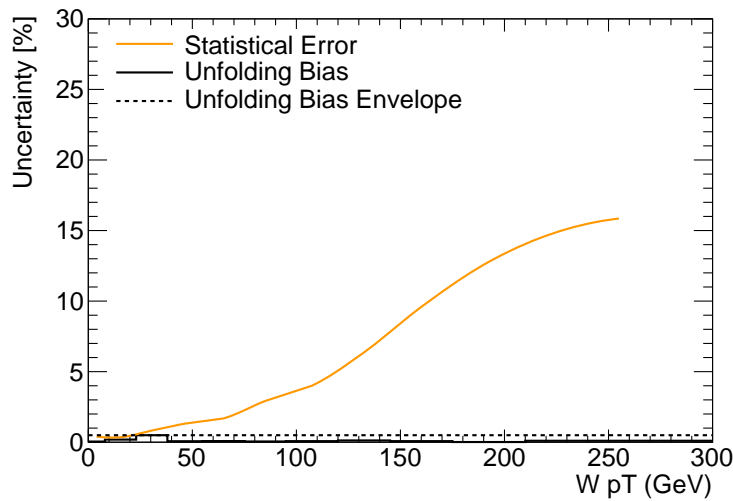


Figure 5.38: Diagonal elements of the covariance matrix of the electron channel for systematic and statistical uncertainties due to unfolding.

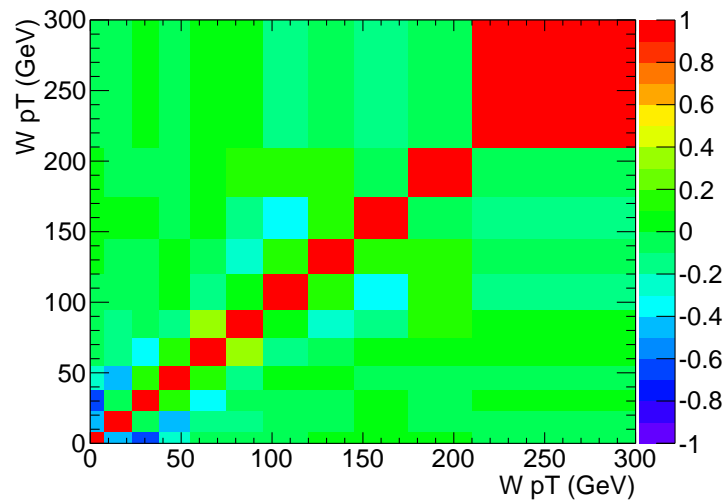


Figure 5.39: Correlation matrix for the unfolding statistical uncertainty for the muon channel.

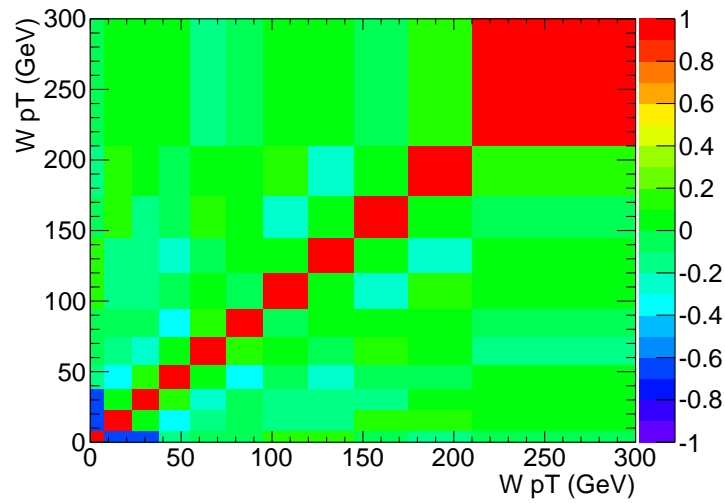


Figure 5.40: Correlation matrix for the unfolding statistical uncertainty for the electron channel.

### 5.9.6 Propagation and Normalization

In general, the propagation of uncertainties which are not correlated among each other is accomplished via simple addition of the covariance matrices. However, for more complicated operations like unfolding and efficiency correction, the propagation of the matrices becomes more complicated. The precise steps used to propagate the statistical and systematic uncertainties are described here.

The observed data is initially assigned a systematic covariance matrix of all zeroes, and a diagonal statistical covariance matrix with entries equal to the number of entries in each bin of the data. After background subtraction, the statistical covariance matrix is unchanged, while the systematic covariance matrix is taken to be a diagonal covariance matrix with the simple errors described in section 5.5. These uncertainties are used only for visualizing the results at this stage, and then are removed for the unfolding step. Following unfolding, the covariance matrices described in the proceeding section are used. The statistical covariance matrix of the data is taken from the results of the process described in section 5.9.4, while the systematic covariance matrix is taken to be the sum of the covariance matrices described in sections 5.9.2, 5.9.3, and 5.9.4.

Mathematically, the uncertainties after unfolding are given by:

$$V_{stat} = V_{stat}^{unfolding}$$

where  $V_{stat}$  is the statistical covariance matrix of the data, and  $V_{stat}^{unfolding}$  is the statistical covariance due to unfolding that is determined using pseudo-experiments as

described in section 5.9.4 and

$$V_{syst} = V_{BKG} + V_{bias} + V_{sumet} + V_{smearing} + V_{truth} + V_{fit} + V_{fitstat}$$

where  $V_{syst}$  is the systematic covariance matrix of the data,  $V_{BKG}$  is the covariance matrix of background uncertainties,  $V_{bias}$  is the covariance matrix of the unfolding bias, and  $V_{sumet}$ ,  $V_{smearing}$ ,  $V_{truth}$ ,  $V_{fit}$ ,  $V_{fitstat}$  are the various response matrix covariance matrices.

The efficiency correction step requires a division, which results in an amplification of the covariance matrix. To simplify this calculation, as discussed, the covariance matrix for the efficiency correction is assumed to be diagonal. The statistical covariance matrix is updated as follows:

$$V_{stat}^{i,j} \rightarrow \frac{V_{stat}^{i,j}}{\epsilon_i \epsilon_j} \quad (5.56)$$

where  $V_{stat}^{i,j}$  is the  $ij$ -th entry of the data statistical covariance matrix and  $\epsilon_i$  is the value of the efficiency correction in the  $i$ -th bin. Similarly, the systematic covariance matrix is updated by:

$$V_{syst}^{i,j} \rightarrow \frac{V_{syst}^{i,j}}{\epsilon_i \epsilon_j}, i \neq j \quad (5.57)$$

$$V_{syst}^{i,i} \rightarrow \frac{x_i^2}{\epsilon_i^2} \left( \frac{V_{syst}^{i,i}}{x_i^2} + \frac{\sigma_i^2}{\epsilon_i^2} \right) \quad (5.58)$$

where  $x_i$  is the unfolded measurement (before efficiency correction) in the  $i$ -th bin, and  $\sigma_i$  is the uncertainty on the  $i$ -th bin of the efficiency correction.

Following efficiency correction, the last step is normalization. Typically, scaling by a number simply multiplies the covariance matrix by that number squared. However, in the case of normalization, the operation itself introduces correlations between bins. For example, in a two binned histogram, fluctuations up in the first bin result in smaller results for the second bin after normalization. To account for this effect, the following normalization procedure is used in this analysis:

Consider a histogram with bins  $x_1, \dots, x_n$ , and a covariance matrix  $\mathbf{V}$ . The transformation  $\mathbf{x} \rightarrow \mathbf{y}$  transforms the covariance matrix by:

$$\mathbf{V} \rightarrow \mathbf{A} \mathbf{V} \mathbf{A}^T \quad (5.59)$$

where  $A_{ij} = \left[ \frac{\delta y_i}{\delta x_j} \right]$ . Let  $N = \sum_i x_i$  be the total number of events and  $N_i = N - x_i$  be the sum of events not in the  $i$ -th bin. Then, the normalization transformation is

$$x_i \rightarrow \frac{x_i}{N_i + x_i} \quad (5.60)$$

which yields

$$A_{ii} = \frac{N_i}{N^2} \quad (5.61)$$

$$A_{ij} = \frac{-x_i}{N^2}, i \neq j \quad (5.62)$$

Both the final statistical and systematic covariance matrices are transformed according to equation 5.59 using the above values.

## 5.10 Results

Following event selection, described in sections 5.2, the  $Wp_T$  spectrum is background subtracted using the background estimation described in section 5.5. The results of this are shown in Figure 5.41 for the muon channel, and Figure 5.43 for the electron channel, with the uncertainties shown in Figures 5.42 and 5.44. The background subtracted spectra are compared with reconstruction level PYTHIA signal Monte Carlo.

The uncertainty on the background subtracted spectrum in the muon channel is dominated by statistical uncertainties beyond 50 GeV. Below 50 GeV, there is a roughly flat 1% uncertainty due to the  $W$  and  $Z$  backgrounds, with an additional 2% uncertainty due to the QCD estimate. At higher  $p_T$ , the QCD becomes negligible, but the uncertainty due to the top background estimation becomes more important. Comparison between the observed data and the Monte Carlo reveals a large difference at very low  $p_T$ , where the data is far below the Monte Carlo. This is due to the fact that the resolution in data is worse than in the Monte Carlo, and the data driven response matrix has not yet been used to correct for this effect. The electron channel displays similar behavior.

The observed spectrum is then unfolded using iterative Bayesian unfolding, described in section 5.7.4, using 3 iterations, and the channel combined data driven response matrix described in section 5.6. The uncertainties are calculated according to the methods described in section 5.9. The results of the unfolding, compared with the truth level distribution of events passing event selection from PYTHIA Monte Carlo

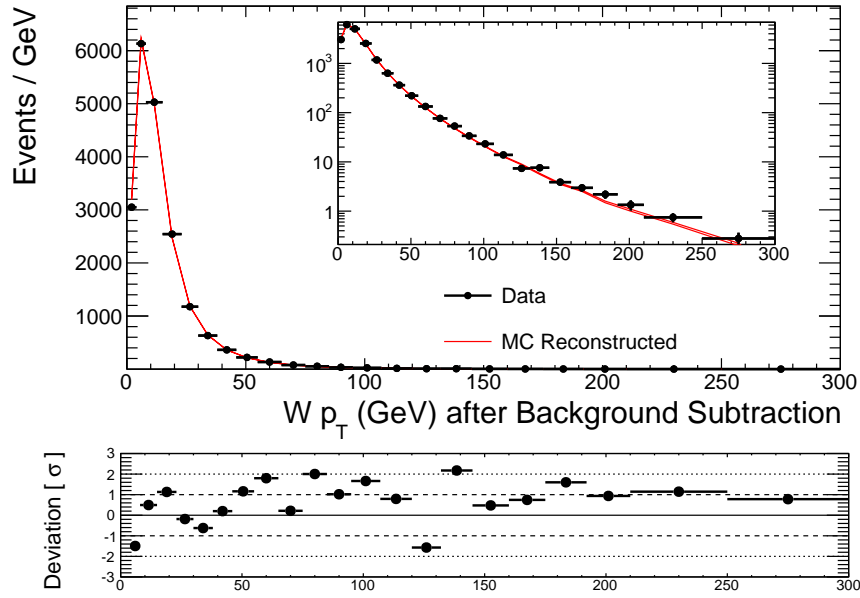


Figure 5.41: Muon sample after background subtraction compared with reconstruction level PYTHIA signal Monte Carlo. The deviation is defined as the difference between the data and Monte Carlo divided by the sum in quadrature of their uncertainties.

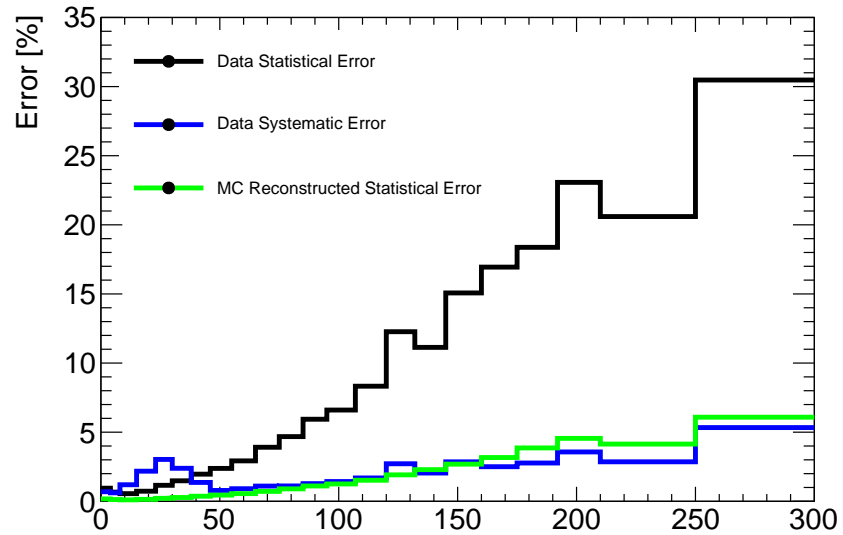


Figure 5.42: Uncertainties after background subtraction for the muon channel.

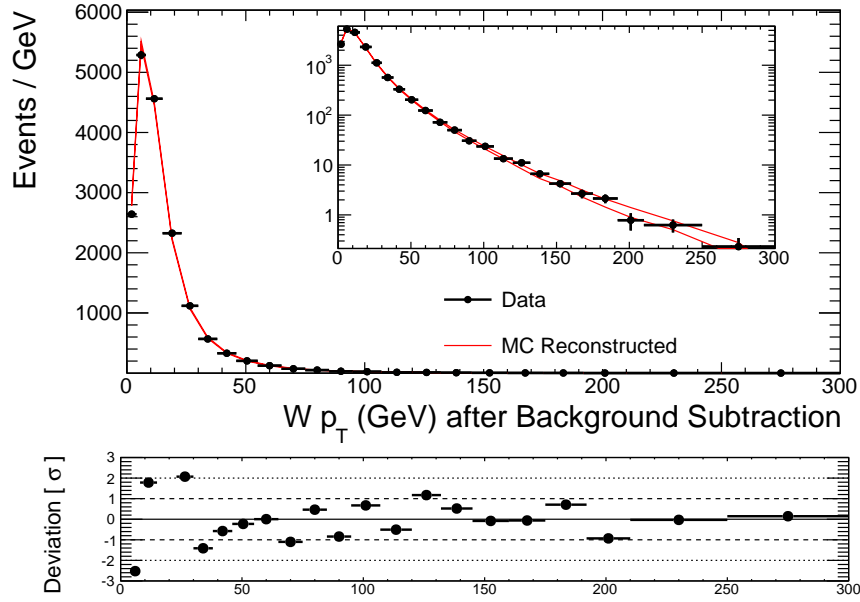


Figure 5.43: Electron sample after background subtraction compared with reconstruction level PYTHIA signal Monte Carlo. The deviation is defined as the difference between the data and Monte Carlo divided by the sum in quadrature of their uncertainties.

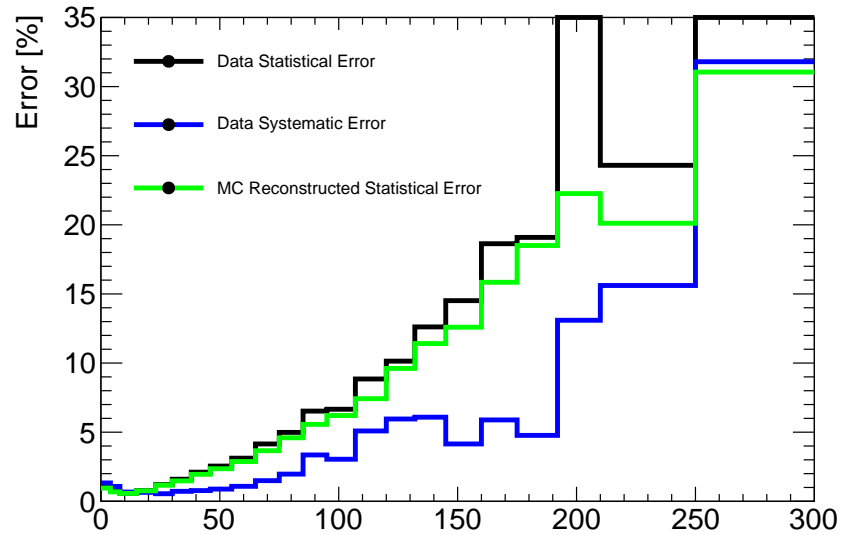


Figure 5.44: Uncertainties after background subtraction for the electron channel.

are shown in Figure 5.45 for the muon channel and in Figure 5.47 for the electron channel. The associated statistical and systematic correlation matrices are shown in Figures 5.49 and 5.50 respectively, and the diagonal elements of the covariance matrices are shown in Figures 5.46 and 5.48.

Following unfolding, the deviation between Monte Carlo and data is no longer present, as the data driven corrections to the response matrix have been applied to correct the differences in resolution. The muon channel systematic uncertainty is roughly flat in  $p_T$  at 5 %, with a small increase near 30 GeV due to uncertainty in the QCD background estimate. The dominant component of the systematic uncertainty is due to the fit parameterization. As wider bins are used at truth level than at reconstruction level, the statistical uncertainty has gone down and is only dominant above 100 GeV. The electron results are similar, with a higher overall systematic uncertainty due to larger uncertainties in the background estimations.

The unfolded spectrum is then corrected to the fiducial volume via a Monte Carlo based efficiency correction described in section 5.8. The results of this correction are shown in Figure 5.51 for the muon channel and Figure 5.53 for the electron channel and are compared with the truth level distribution of events in the PYTHIA signal Monte Carlo that fall within the fiducial volume. The statistical and systematic correlation matrices are shown in Figures 5.55 and 5.56, with the diagonal elements shown in Figures 5.52 and 5.54.

The results after efficiency correction are very similar to those after unfolding. There is a slight increase in the systematic uncertainty for the muon channel above 100

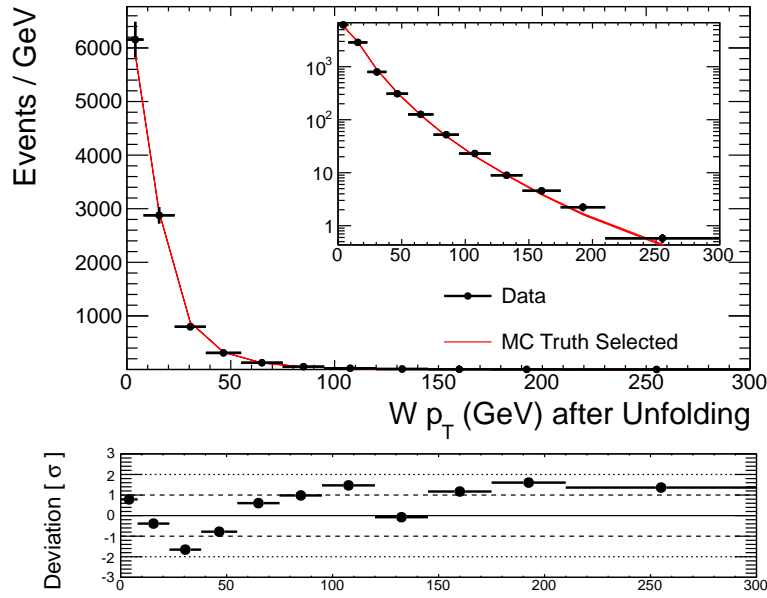


Figure 5.45: Muon sample after Bayesian unfolding compared with truth level PYTHIA signal Monte Carlo from events passing event selection. The deviation is defined as the difference between the data and Monte Carlo divided by the sum in quadrature of their uncertainties.

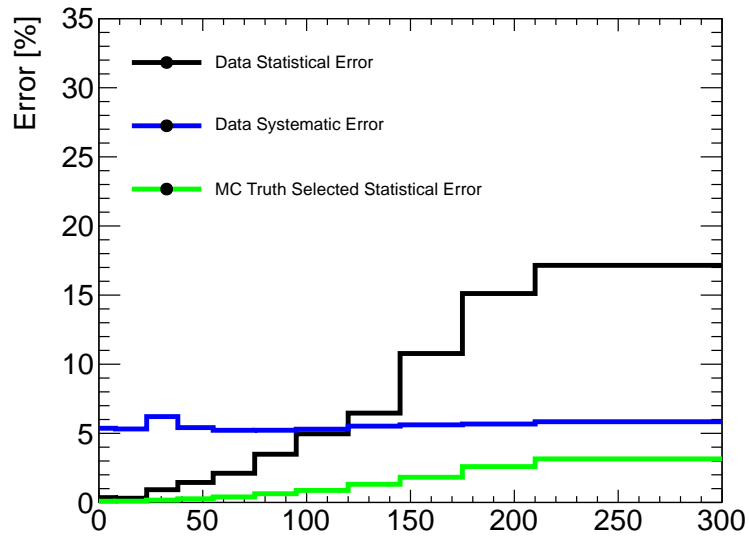


Figure 5.46: Diagonal elements of covariance matrix following unfolding for the muon channel.

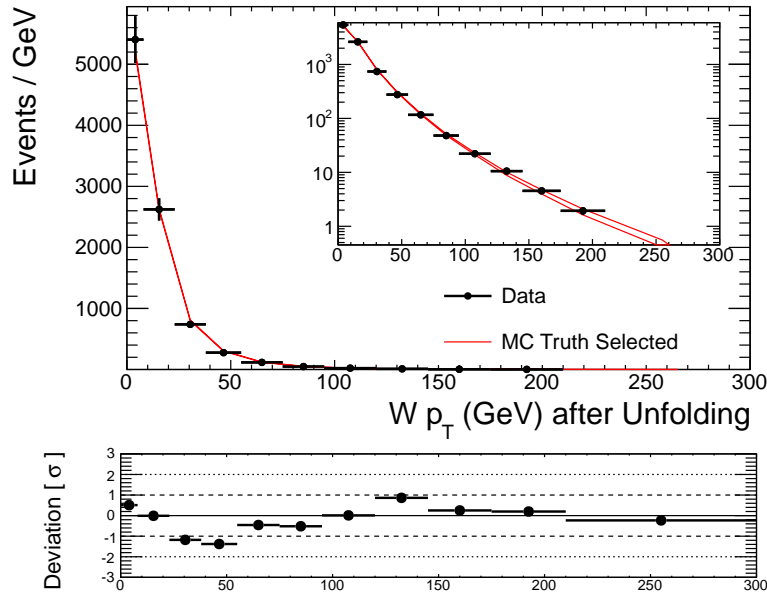


Figure 5.47: Electron sample after Bayesian unfolding compared with truth level PYTHIA signal Monte Carlo from events passing event selection. The deviation is defined as the difference between the data and Monte Carlo divided by the sum in quadrature of their uncertainties.

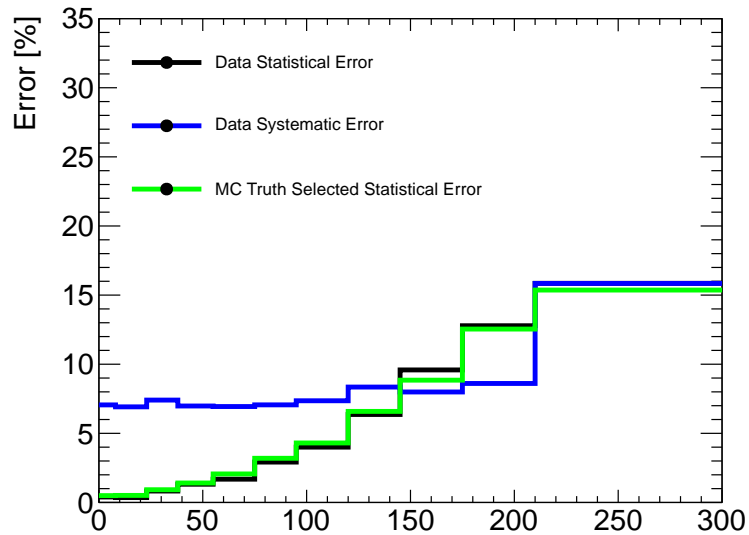


Figure 5.48: Diagonal elements of covariance matrix following unfolding for the electron channel.

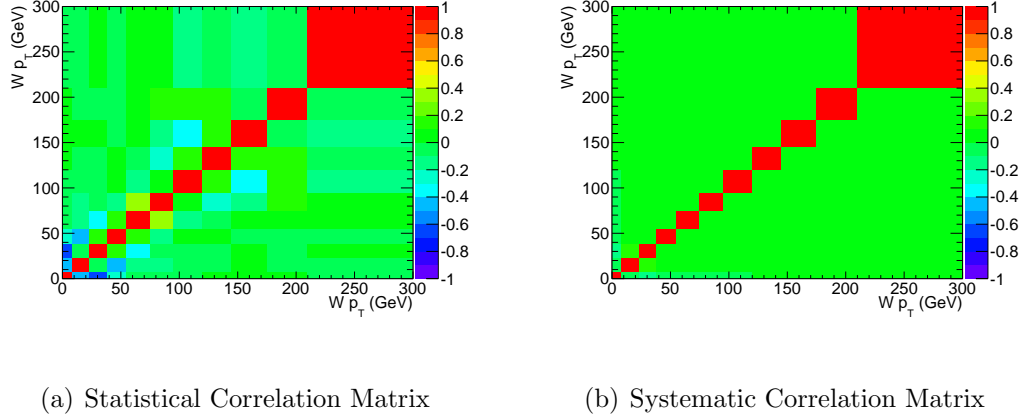


Figure 5.49: Statistical and systematic correlation matrices following Bayesian unfolding for the muon channel.

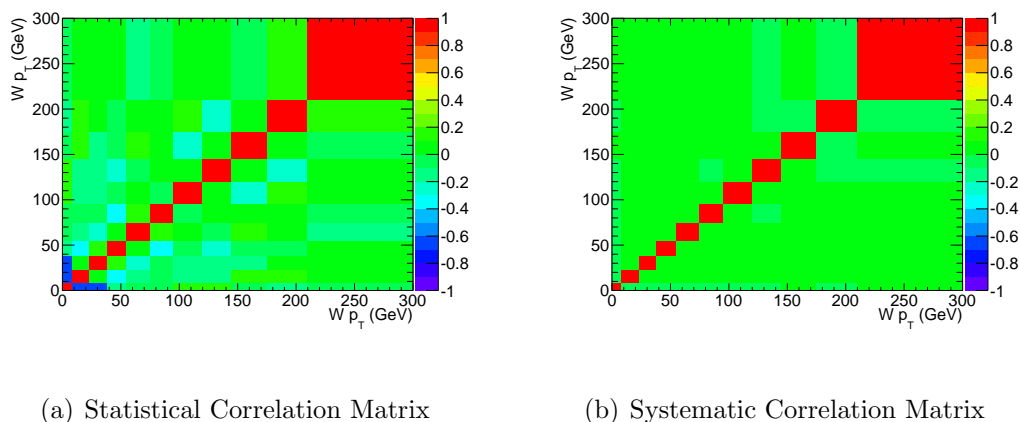


Figure 5.50: Statistical and systematic correlation matrices following Bayesian unfolding for the electron.

GeV due to differences between Monte Carlo models of the event selection efficiency. The electron channel has a significantly larger uncertainty on the estimate of the efficiency due to poorer Monte Carlo statistics and differences between the lepton energy resolution in Monte Carlo and data.

The final step is to normalize the distribution. This is done according to the procedure described in section 5.9.6. The results of the normalization are shown in Figure 5.57 for the muon channel and Figure 5.59 for the electron channel. The final statistical and systematic correlation matrices are shown in Figures 5.61 and 5.62, with diagonal elements of the covariance matrices shown in Figures 5.58 and 5.60.

The final results show good agreement between the observed data and the Monte Carlo predictions, as well as between the two channels. The normalization process decreases the systematic uncertainty slightly at low  $p_T$  (as those bins tend contain most of the events), while increasing the systematic uncertainty at higher  $p_T$ . The muon channel result is dominated by statistical uncertainty beyond 150 GeV. Below that, it is dominated by systematic uncertainties, which are primarily due to the parameterization scheme used in deriving the data driven response matrix and, at lower  $p_T$ , the estimate of the QCD background. The electron channel result is systematically limited across the entire  $p_T$  range, and is dominated by the estimate of the selection efficiency and the QCD background. Strong anti-correlations between bins can be seen, especially in the region below 50 GeV.

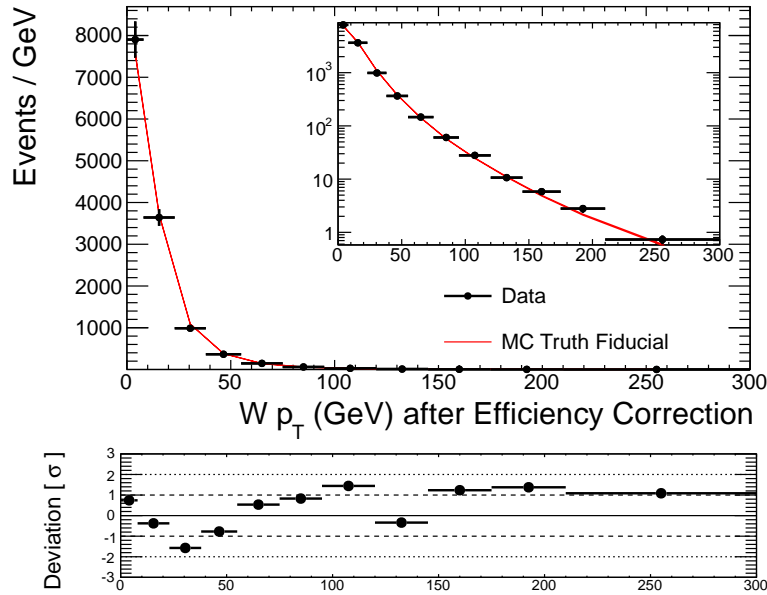


Figure 5.51: Muon sample after efficiency correction compared with truth level PYTHIA signal Monte Carlo from events within the fiducial volume. The deviation is defined as the difference between the data and Monte Carlo divided by the sum in quadrature of their uncertainties.

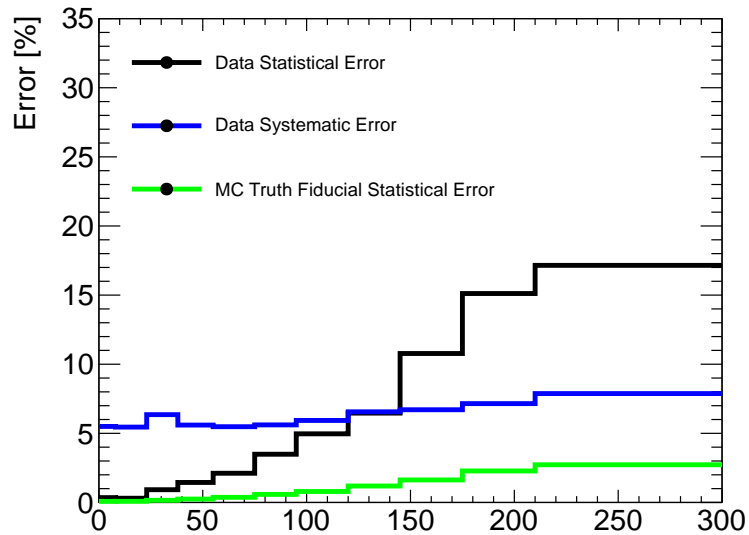


Figure 5.52: Diagonal elements of covariance matrix following efficiency correction for the muon channel.

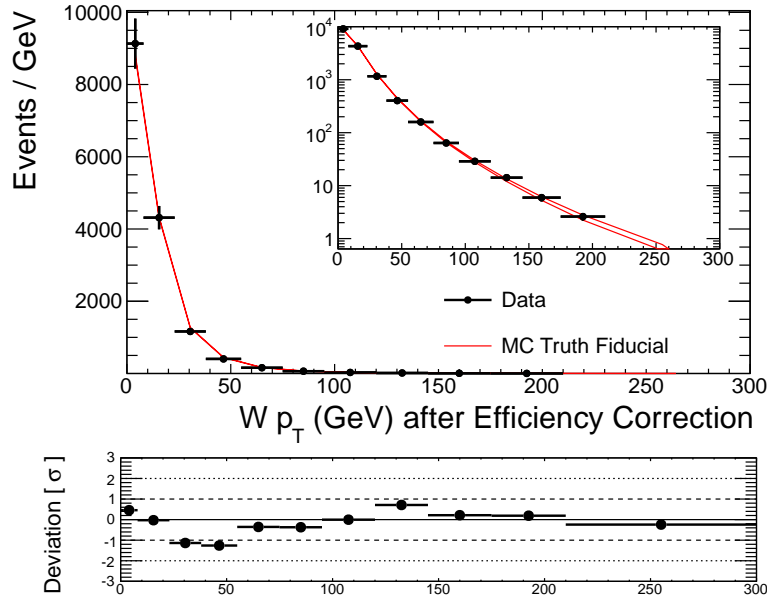


Figure 5.53: Electron sample after efficiency correction compared with truth level PYTHIA signal Monte Carlo from events within the fiducial volume. The deviation is defined as the difference between the data and Monte Carlo divided by the sum in quadrature of their uncertainties.

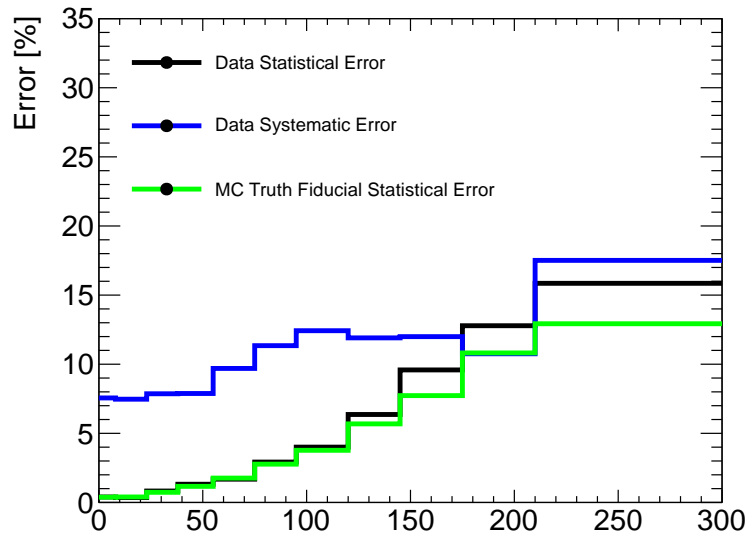


Figure 5.54: Diagonal elements of covariance matrix following efficiency correction for the electron channel.

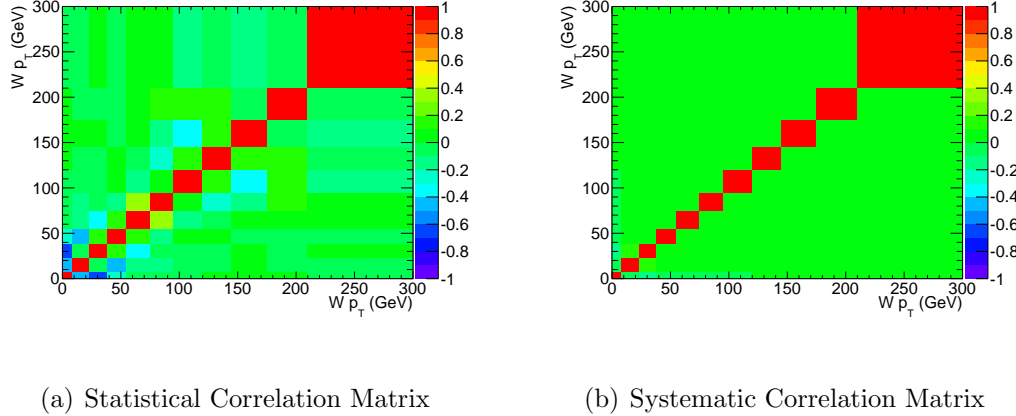


Figure 5.55: Statistical and systematic correlation matrices following efficiency correction for the muon channel.

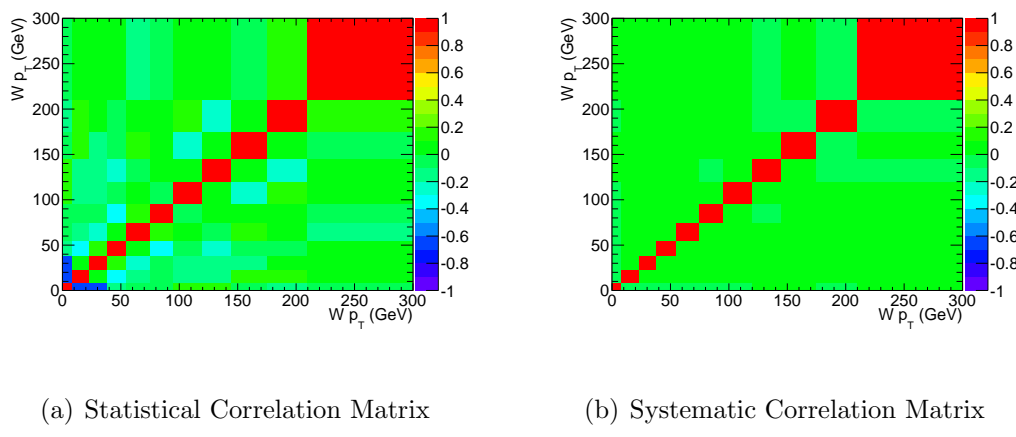


Figure 5.56: Statistical and systematic correlation matrices following efficiency correction for the electron channel.

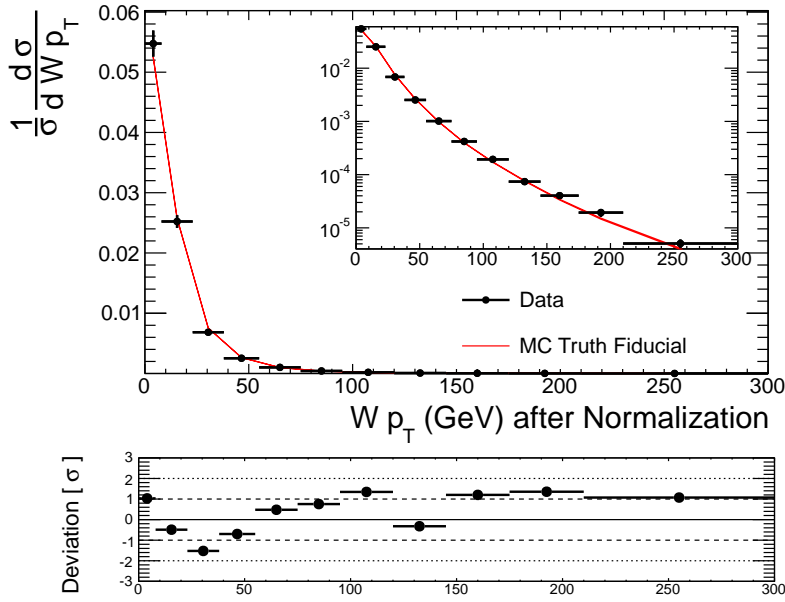


Figure 5.57: Muon sample after normalization compared with truth level PYTHIA signal Monte Carlo from events within the fiducial volume. The deviation is defined as the difference between the data and Monte Carlo divided by the sum in quadrature of their uncertainties.

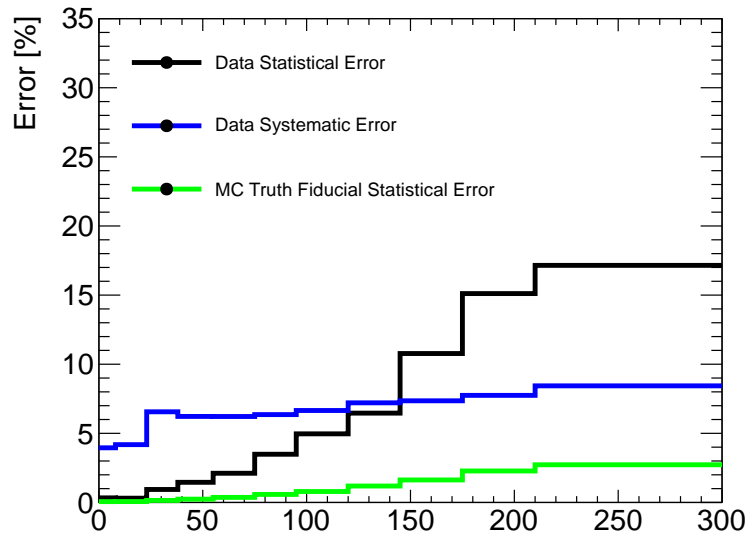


Figure 5.58: Diagonal elements of covariance matrix following normalization for the muon channel.

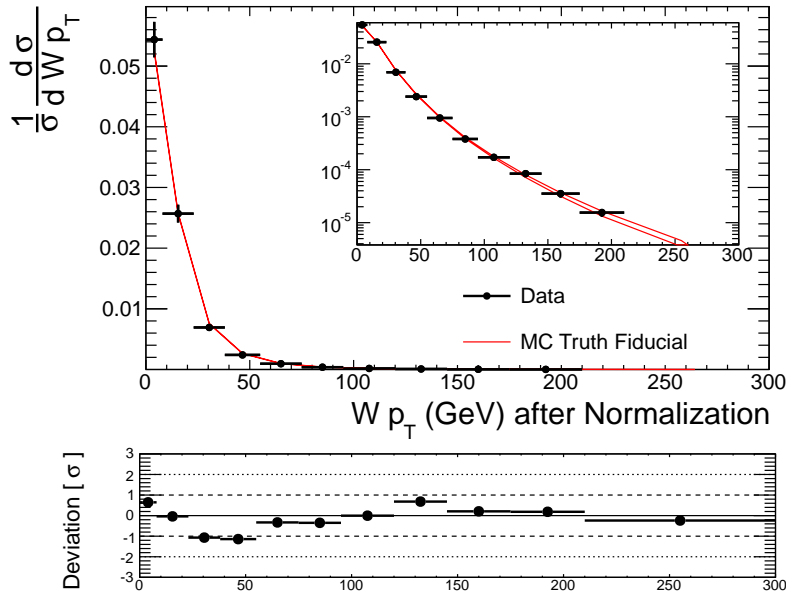


Figure 5.59: Electron sample after normalization compared with truth level PYTHIA signal Monte Carlo from events within the fiducial volume. The deviation is defined as the difference between the data and Monte Carlo divided by the sum in quadrature of their uncertainties.

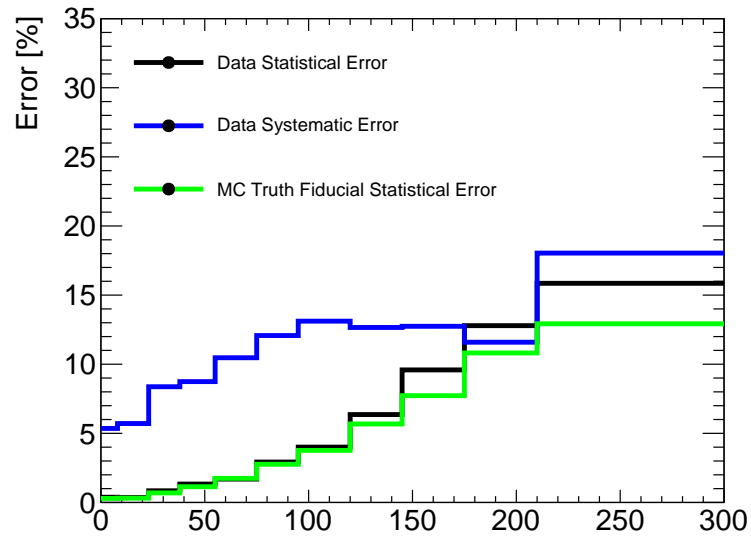


Figure 5.60: Diagonal elements of covariance matrix following normalization for the electron channel.

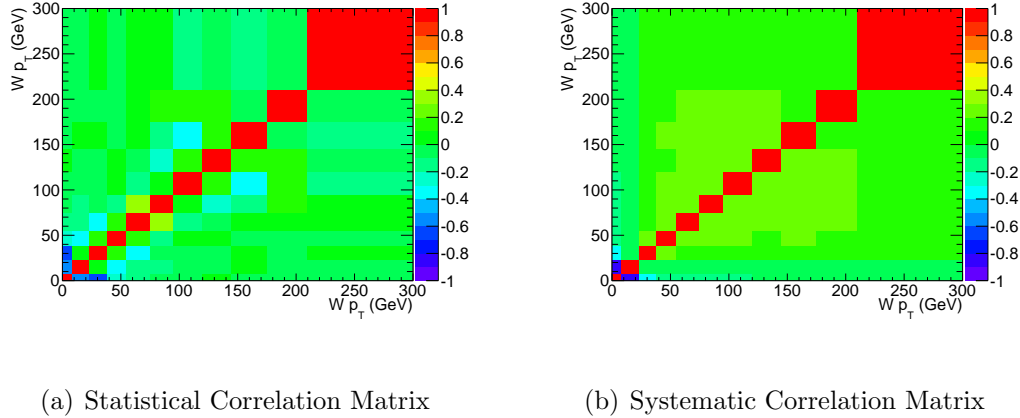


Figure 5.61: Statistical and systematic correlation matrices following normalization for the muon channel.

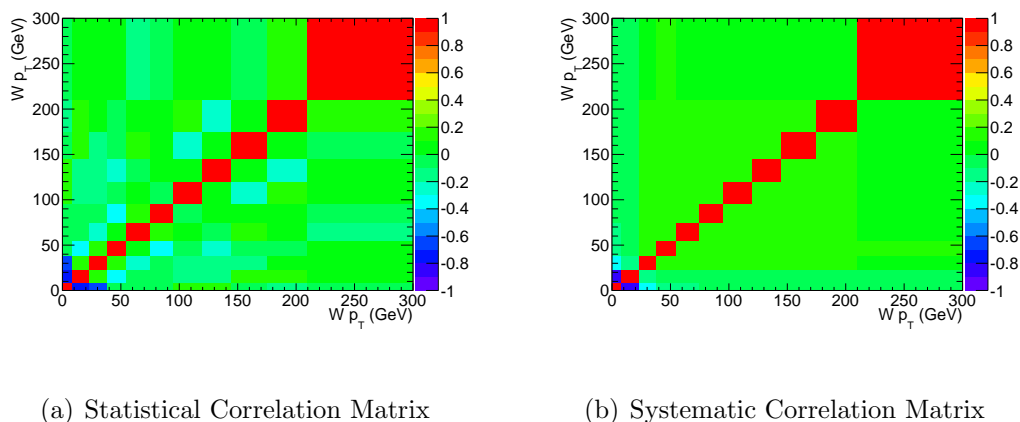


Figure 5.62: Statistical and systematic correlation matrices following normalization for the electron channel.

## 5.11 Conclusions

This thesis has presented a measurement of the  $Wp_T$  spectrum in proton-proton collisions at  $\sqrt{s} = 7$  TeV corrected back to the fiducial volume of the ATLAS detector in both the muon and electron channels. The observed data was found to be in good agreement with the theoretical predictions made by the PYTHIA generator tuned to the  $W$  and  $Z$  transverse momentum spectra at the Tevatron up to a  $Wp_T$  of 300 GeV. The results are statistically limited beyond 150 GeV, with a systematic uncertainty of less than 7% below 150 GeV. This measurement has the broadest  $p_T$  range, the largest statistics sample, and the best statistical power of any measurement of the  $Wp_T$  spectrum performed to date.

As this measurement is statistically limited at high  $p_T$ , the breadth of this measurement can be extended by increasing the size of the dataset used. This analysis used 125k  $W \rightarrow \mu\nu$  and 105k  $W \rightarrow e\nu$  from roughly  $30\text{ pb}^{-1}$  collected in 2010, but it is predicted that more than 30 times as much data will be collected in 2011. At lower  $p_T$ , the uncertainties are dominated by a 4 % systematic due to the parameterization of the resolution that was necessary in order to include data driven corrections using such a small  $Z \rightarrow \ell\ell$  sample. With a much larger control sample, it will be possible to increase the complexity of the parameterization and improve the quality of the fit, resulting in a smaller uncertainty. Use of the 2011 dataset, combined with improved techniques for estimating the QCD background shape, will likely result in measurements at the 2% level in the  $p_T$  region below 100 GeV and extending the high  $p_T$  region to beyond 500 GeV.

# Bibliography

- [1] ATLAS Experiment @ 2011 CERN. ATLAS Photos.  
<http://www.atlas.ch/photos/index.html>.
- [2] C. Balazs and C.P. Yuan. Soft gluon effects on lepton pairs at hadron colliders. *Phys. Rev.*, D56:5558–5583, 1997.
- [3] Interactions Image Bank. Illustration of particle detection in the subsystems of the ATLAS detector. (Courtesy CERN).  
[http://www.interactions.org/cms/?pid=2100&image\\_no=CE0155](http://www.interactions.org/cms/?pid=2100&image_no=CE0155).
- [4] V. Blobel. An Unfolding Method For High Energy Physics Experiments. arXiv:0208.022 [hep-ph].
- [5] J.M. Campbell et al. Next-to-leading order QCD predictions for  $W + 2\text{jet}$  and  $Z + 2\text{jet}$  production at the CERN LHC. *Phys. Rev.*, D68:094021, 2003.
- [6] J.M. Campbell, J.W. Huston, and W.J. Stirling. Title: Hard Interactions of Quarks and Gluons: a Primer for LHC Physics. arXiv:0611148 [hep-ph].
- [7] S. Catani et al. Vector boson production at hadron colliders: a fully exclusive QCD calculation at NNLO. *Phys. Rev. Lett.*, 103:082001, 2009.
- [8] CERN MultiMedia Productions. LHC Machine Outreach.  
<http://lhc-machine-outreach.web.cern.ch/lhc-machine-outreach/>.
- [9] The ATLAS Collaboration. Electron and Photon Reconstruction and Identification in ATLAS: Expected Performance at High Energy and Results at  $\sqrt{s} = 900$  GeV. ATLAS internal note: ATLAS-CONF-2010-005.
- [10] The ATLAS Collaboration. Expected Performance of the ATLAS Experiment - Detector, Trigger and Physics. arXiv:0901.0512 [physics.hep-x].
- [11] The ATLAS Collaboration. Luminosity Determination Using the ATLAS Detector. ATLAS conference note: ATLAS-CONF-2010-060.

- [12] The ATLAS Collaboration. Measurement of the cross-section for jets produced in association with a W -boson in pp collisions at  $\text{sqrt}(s) = 7 \text{ TeV}$ . ATLAS internal note: ATL-COM-PHYS-2010-756.
- [13] The ATLAS Collaboration. Measurement of the W Boson Transverse Momentum using Muons and Electrons in proton-proton collisions at  $\text{sqrt}(s) = 7 \text{ TeV}$  with the ATLAS detector. ATLAS internal note: ATL-COM-PHYS-2011-251.
- [14] The ATLAS Collaboration. Measurement of  $W \rightarrow \ell\nu$  charge asymmetry in proton-proton collisions at  $\sqrt{s} = 7 \text{ TeV}$  with the ATLAS detector. ATLAS internal note: ATL-COM-PHYS-2010-1032.
- [15] The ATLAS Collaboration. Muon definition for W, Z analysis based on Athena Release 15. ATLAS internal note: ATL-COM-PHYS-2010-1001.
- [16] The ATLAS Collaboration. Muon momentum resolution from p-p collision data. ATLAS internal note: IN PREPARATION,  
<https://svnweb.cern.ch/trac/atlasgrp/browser/CombPerf/MuonPerf/Notes/2010-Autumn/MuonMomentumResolutionNote/perf.pdf>.
- [17] The ATLAS Collaboration. Muon trigger efficiency measurements wtih Z bosons in proton-proton collisions at  $\text{sqrt}(s) = 7 \text{ TeV}$  with the ATLAS detector. ATLAS internal note: ATL-COM-PHYS-2011-049.
- [18] The ATLAS Collaboration. Total inclusive W and Z boson cross-section measurements, cross-section ratios and combinations in the electron and muon decay channels at 7 TeV based on  $300 \text{ nb}^{-1}$ . ATLAS internal note: ATL-COM-PHYS-2010-703.
- [19] The ATLAS Collaboration.  $W \rightarrow \mu\nu$  and  $Z \rightarrow \mu\mu$  cross-sections measurements in proton-proton collisions at  $\sqrt{s} = 7 \text{ TeV}$  with the ATLAS Detector. ATLAS internal note: ATL-COM-PHYS-2010-685.
- [20] The ATLAS Collaboration.  $W \rightarrow e\nu$  and  $Z \rightarrow ee$  Cross Section Measurements in Proton-Proton Collisions at  $\sqrt{s} = 7 \text{ TeV}$  with the ATLAS Detector. ATLAS internal note: ATL-COM-PHYS-2010-539.
- [21] The ATLAS Collaboration. *ATLAS Muon Spectrometer Technical Design Report*. CERN, Geneva, 1997.
- [22] The ATLAS Collaboration. *ATLAS Computing Technical Design Report*. CERN, Geneva, 2005.
- [23] The ATLAS Collaboration. The ATLAS Experiment at the Large Hadron Col- lide. *JINST*, 3:S08003, 2008.

- [24] The ATLAS Collaboration. *Expected performance of the ATLAS experiment: detector, trigger and physics*. CERN, Geneva, 2009.
- [25] The ATLAS Collaboration. Measurement of the  $W \rightarrow \ell\nu$  and  $Z/\gamma^* \rightarrow \ell\ell$  production cross sections in proton-proton collisions at  $\sqrt{s} = 7$  TeV with the ATLAS detector. *J. High Energy Phys.*, 12:060, 2010.
- [26] The CDF Collaboration. Measurement of the  $W$   $P(T)$  distribution in  $\bar{p}p$  collisions at  $\sqrt{s} = 1.8$  TeV. *Phys. Rev. Lett.*, 66:2951–2955, 1991.
- [27] The CDF Collaboration. Measurements of Inclusive  $W$  and  $Z$  Cross-sections in  $\bar{p}p$  collisions at  $\sqrt{s} = 1.8$  TeV. *J. Phys.*, G34:2457, 2007.
- [28] The CMS Collaboration. Measurements of inclusive  $W$  and  $Z$  cross sections in  $pp$  collisions at  $\sqrt{s} = 7$  TeV. *J. High Energy Phys.*, 01:080, 2011.
- [29] The D0 Collaboration. Measurement of the shape of the transverse momentum distribution of  $W$  bosons produced in  $p\bar{p}$  collisions at  $\sqrt{s} = 1.8$  TeV. *Phys. Rev. Lett.*, 80:5498–5503, 1998.
- [30] The D0 Collaboration. Extraction of the width of  $W$  boson from measurements of  $\sigma(p\bar{p} \rightarrow W + X) \times B(W \rightarrow e\nu)$  and  $\sigma(p\bar{p} \rightarrow Z + X) \times B(Z \rightarrow ee)$  and their ratio. *Phys. Rev.*, D61:072001, 2000.
- [31] The D0 Collaboration. A novel method for modeling the recoil in  $W$  boson events at hadron collider. *Nucl. Instrum. Meth.*, A609:250–262, 2009.
- [32] The NNPDF Collaboration. A determination of parton distributions with faithful uncertainty estimation. arXiv:0808.1231 [hep-ph].
- [33] The UA1 Collaboration. Studies of Intermediate Vector Boson Production and Decay in UA1 at the CERN Proton-Antiproton Collider. *Z. Phys.*, C 44:15, 1989.
- [34] The UA2 Collaboration. Measurement of the Transverse Momentum Distributions of  $W$  and  $Z$  Bosons at the CERN PPbar Collider. *Z. Phys.*, C 47:523, 1990.
- [35] J. Collins, D. Soper, and G. Sterman. Transverse Momentum Distribution in Drell-Yan Pair and  $W$  and  $Z$  Boson Production. *Nucl. Phys.*, B250:199, 1985.
- [36] G. Corcella et al. HERWIG 6: an event generator for Hadron Emission Reactions With Interfering Gluons. *JHEP*, 010:0101, 2001.
- [37] G. Cowan. *Statistical Data Analysis*. Oxford University Press, 1998.
- [38] G. D’Agostini. Improved Iterative Bayesian Unfolding. arXiv:1010.0632 [physics.data-an].

- [39] L. Evans and P. Bryant. LHC Machine. *JINST*, 3:S08001, 2008.
- [40] S. Frixione and B.R. Webber. Matching NLO QCD computations and parton shower simulations. *JHEP*, 06:029, 2002.
- [41] R. Gavin et al. FEWZ 2.0: A code for hadronic Z production at next-to- next-to-leading order. arXiv:1011.3540 [hep-ph].
- [42] Google, Inc. MapReduce: Simplified Data Processing on Large Clusters. <http://labs.google.com/papers/mapreduce.html>.
- [43] D. Griffiths. *Introduction to Elementary Particles*. Wiley-VCH, 2008.
- [44] The ATLAS Egamma Group. Efficiency Measurements. <https://twiki.cern.ch/twiki/bin/view/AtlasProtected/EfficiencyMeasurements>.
- [45] The ATLAS Egamma Group. Energy Resolution Recommendations. <https://twiki.cern.ch/twiki/bin/view/AtlasProtected/EnergyScaleResolutionRecommendations>.
- [46] The ATLAS Egamma Group. Object Quality Maps Usage. <https://twiki.cern.ch/twiki/bin/view/AtlasProtected/OQMapsUsage>.
- [47] The ATLAS Jet/EtMiss Group. How To Clean Jets. <https://twiki.cern.ch/twiki/bin/view/AtlasProtected/HowToCleanJets>.
- [48] The H1 and Zeus Collaborations. Combined Measurement and QCD Analysis of the Inclusive ep Scattering Cross Sections at HERA. arXiv:0911.0884 [hep-ex].
- [49] F. Halzen and A.D. Martin. *Quarks & Leptons: An Introductory Course in Modern Particle Physics*. Wiley, 1984.
- [50] P. C. Hansen. *The L-Curve and its Use in the Numerical Treatment of Inverse Problems*, pages 119–142. WIT Press, 2001.
- [51] A. Hocker and V. Kartvelishvili. SVD Approach to Data Unfolding. arXiv:9509.307 [hep-ph].
- [52] J. Kaipio and E. Somersalo. *Statistical and Computational Inverse problems*. Springer, 2005.
- [53] C. L. Lawson and R. J. Hanson. *Solving Least Square Problems*. Prentice-Hall Inc., 1974.
- [54] B. Malaescu. An Iterative, Dynamically Stabilized Method of Data Unfolding. arXiv:0907.3791 [physics.data-an].

- [55] M.L. Mangano et al. ALPGEN, a generator for hard multiparton processes in hadronic collisions. *JHEP*, 07:001, 2003.
- [56] A.D. Martin et al. Parton distributions for the LHC. arXiv:0901.0002 [hep-ph].
- [57] K. Melnikov and F. Petriello. Electroweak gauge boson production at hadron colliders through  $O(\alpha(s)^{**2})$ . *Phys. Rev.*, D74:114017, 2006.
- [58] P.M. Nadolsky et al. Implications of CTEQ global analysis for collider observables. arXiv:0802.0007 [hep-ph].
- [59] K. Nakamura et al. Review of Particle Physics. *J. Phys.*, G37:075021, 2010.
- [60] D.H. Perkins. *Introduction to High Energy Physics*. Cambridge University Press, 2000.
- [61] M.E. Peskin and D. V. Schroeder. *An Introduction to Quantum Field Theory*. Westview Press, 1995.
- [62] The LCG Project. *LHC Computing Grid Technical Design Report*. CERN, Geneva, 2005.
- [63] J. Pumplin et al. Inclusive Jet Production, Parton Distributions, and the Search for New Physics. arXiv:0303013 [hep-ph].
- [64] S. Schmitt. TUnfold Class. <http://root.cern.ch/root/html/TUnfold.html>. Unfolding software, part of the ROOT data analysis framework.
- [65] S. Schmitt. TUnfoldSys Class. <http://root.cern.ch/root/html/TUnfoldSys.html>. Unfolding with Systematic Errors software, part of the ROOT data analysis framework.
- [66] M. Schott and M. Bellomo. Staco Efficiencies based on Z Bosons with  $L = 42 \text{ pb}^{-1}$  and Release 15. <http://indico.cern.ch/conferenceDisplay.py?confId=110666>.
- [67] B. Smith. Muon ID Analysis Documentation. <https://twiki.cern.ch/twiki/bin/viewauth/Atlas/MuonIDAnalysis>.
- [68] B. Smith. Trigger Navigation Slimming Documentation. <https://twiki.cern.ch/twiki/bin/viewauth/Atlas/HLTTrigNavigationSlimming>.
- [69] B. Smith. Trigger Object Matching Documentation. <https://twiki.cern.ch/twiki/bin/view/Atlas/TriggerObjectsMatching>.
- [70] The ROOT team. Class Description for TDecompChol. <http://root.cern.ch/root/html/TDecompChol.html>.

- [71] The ROOT team. The ROOT Users Guide.  
<http://root.cern.ch/drupal/content/users-guide>.
- [72] R. M. Thurman-Keup et al.  $W$  boson physics at hadron colliders. *Rev. Mod. Phys.*, 73:267–306, 2001.
- [73] A. N. Tikhonov. On the Solution Of Improperly Posed Problems and the Method of Regularization. *Sov. Math*, 5:1035, 1963.
- [74] S. Torbjorn et al. PYTHIA 6.4 Physics and Manual. *JHEP*, 05:026, 2006.
- [75] Wikimedia Commons. Standard Model of Elementary Particles.  
[http://en.wikipedia.org/wiki/File:Standard\\_Model\\_of\\_Elementary\\_Particles.svg](http://en.wikipedia.org/wiki/File:Standard_Model_of_Elementary_Particles.svg).